KINETICS, MECHANISMS AND MODELLING OF CALCIUM TREATMENT OF STEEL

BY

DENNIS (D-Z.) LU, B.ENG.

A Thesis

Submitted to the School of Graduate Studies

in Partial Fulfilment of the Requirements

for the Degree of

Doctor of Philosophy

McMASTER UNIVERSITY

KINETICS, MECHANISMS AND MODELLING

OF CALCIUM TREATMENT OF STEEL

Doctor of Philosophy (1992) McMaster University

(Materials Science and Engineering) Hamilton, Ontario

CANADA

TITLE: Kinetics, Mechanisms and Modelling of Calcium Treatment of Steel

AUTHOR: Dennis (Ding-Zheng) Lu

B.Eng. Northeast University of Technology

Shengyang, Liaoling,

China

SUPERVISORS: Professors G.A. Irons and W-K. Lu

NUMBER OF PAGES: xxxvii, 382

ABSTRACT

Steel-clad calcium wire was fed into 40 kg heats of AISI steel with various sulphur and aluminum contents under argon atmosphere. Samples were taken continuously during and after calcium injection for chemical and inclusion analysis from more than twelve heats of injection. Calcium dissolution was found to be enhanced by instantaneous reactions with oxygen and sulfur in the boundary layer. The unreacted calcium diffuses through the gas-liquid film into the melt for oxide and sulfide inclusion modification. The overall interaction between oxides and sulfides with the bulk drives towards the equilibrium of (CaO) + $\underline{S}$ = (CaS) + $\underline{O}$. The system paths from the initial state to the final state were kinetically studied with the assistance of a_{CaS}-a_{MnS} diagrams, which were calculated by applying a regular solution model to the solid phase and an ideal model to the liquid phase of the CaS-MnS phase diagram at various steelmaking temperatures. A mathematical model for the multiphase kinetics was developed to interpret the calcium dissolution, deoxidation, desulphurization, oxide and sulfide inclusion modification during and after calcium injection. The implications for full-scale operation were discussed.

To Elise and My Mother

- D. Lu

ACKNOWLEDGEMENTS

The author wishes to express his sincere gratitude to Professor G.A. Irons for his guidance during the course of this project, and his countless efforts which led to the successful completion of this project. Thanks are also due to Professor W-K. Lu, whose direction and encouragement throughout this work were invaluable. The help from the other member of the supervisory committee, Professor A. Hrymak, is greatly appreciated.

Special thanks go to Mr. O. Kelly who operated and maintained the induction furnace, as well as assisted the experiment. Similar assistance from Dr. L-K. Chiang, M. Kozlowski, L. Matikainen and Y-F. Zhao with the experiments was also greatly appreciated.

The cooperation of Mr. M. Van Oosten for the chemical analysis is gratefully acknowledged. The ASA analysis by Om. Bagavar at Stelco, and SEM/EDS analysis by Mr. S. Koprich at Steltech and Dr. M. Shehata at CANMET are also very much appreciated.

The Educational Ministry of China, McMaster University are all greatly acknowledged for the scholarship they granted to the author during the study. The financial support from National Research Council of Canada and CANMET for this project is also highly appreciated.

TABLE OF CONTENTS

LIST OF SYMBOLS

a	activity based on pure solid as the standard state
$a_{Al_2O_3}$	activity of alumina
a_{CaO}	activity of calcium oxide
a_{CaS}	activity of calcium sulfide
a_{MnS}	activity of MnS
A_L	gas-liquid area, m^2
ASA	acid soluble aluminum
C	concentration of element in the melt, $mole/m^3$
Ca	calcium
$C_{Al,i}$	interfacial aluminum concentration at the inclusions, mole/m3
$C_{Al,ro}$	interfacial aluminum concentration at the free-surface, $mole/m^3$
$C_{Al_2O_3}$	amount of Al_2O_3 inclusion, in $mole/m^3$
CA_x	calcium aluminate
(Ca,Mn)S	calcium manganese sulfide
C_B	concentration of B in the bulk, $mole/m^3$
$C_{Ca,b}$	dissolved calcium concentration at the gas-liquid interface, $mole/m^3$
$C_{Ca,p}$	the equilibrium dissolved calcium concentration with (Ca,Mn)S, $mole/m^3$

$C_{Ca,r}$	dissolve calcium concentration at the reaction plane in the liquid film, mole/m^3
$C_{Ca,T}$	total calcium content, mole/m^3
$C_{Ca,x}$	dissolved calcium concentration at position x in the liquid film, mole/m^3
%Ca	dissolved calcium concentration in wt%
$\%Ca_r$	calcium wt% at the reaction plane in the film
$[\%Ca]^{SAT}$	the equilibrium calcium solubility, wt%
CFR	calcium feed rate, kg/tonne.min
C_G	concentration in gas phase, mole/m^3
C_o	oxygen concentration, mole/m^3
C_o^0	initial oxygen concentration in the bulk, mole/m^3
$C_{o,b}$	interfacial oxygen concentration in equilibrium with calcium bubble, mole/m3
$C_{o,p}$	equilibrium oxygen concentration with (Ca,Mn)S inclusion, mole/m^3
$C_{o,r}$	oxygen concentration at the reaction plane in the liquid film, mole/m^3
C_s	sulfur concentration, mole/m^3
C_s'	equilibrium sulfur at the slag-metal interface, mole/m^3
C_s^0	initial sulfur concentration in bulk, mole/m^3
$C_{s,b}$	interfacial sulfur concentration in equilibrium with calcium bubble, mole/m^3
$C_{s,p}$	equilibrium sulfur concentration with (Ca,Mn)S inclusion, mole/m^3

$C_{s,r}$	sulfur concentration at the reaction plane in the liquid film, mole/m^3
D_{Ca}	diffusivity of calcium in the steel, m/s
d_E	the equivalent diameter of the bubble, m
d_i	diameter of inclusion, μm
D_{Mg}	diffusivity of magnesium in the melt, m/s
D_O	diffusivity of oxygen in the melt, m/s
D_{O-Ag}	diffusivity of oxygen in silver, m/s
d_p	calcium wire penetration depth, m
D_S	diffusivity of sulfur in the melt, m/s
d_w	diameter of the calcium wire, m
E	cell emf, mv
E_{Ca}	the enhancement factor for calcium absorption
E_{Ca}^0	the initial enhancement factor
e	interaction coefficient
EDS	energy dispersive spectrum
F	Faraday's constant
f	Henry's activity coefficient
f_{Ca}	calcium activity coefficient
f_O	oxygen activity coefficient
f_S	sulfur activity coefficient
ΔG	free energy formation of oxide or sulfide, kcal/kg·mole
g	gravitational acceleration, m/s^2.
H	height of the melt, m
ΔH_{BP}	heat of evaporation of calcium, kcal/mole

H#R#	heat and run numbers
Ha	Hatta number ($(=D_L k_2 C_{BO})^{1/2}/k_L$)
h_{Al}	activity of aluminum in the melt using 1 wt% as the standard state
h_{Ca}	activity of calcium in the melt using 1 wt% as the standard state
$h_{Ca,i}$	the quilibrium acitivity of calcium with CA_x
h_{Ca}^{SAT}	the saturation calcium activity with 1 atm of calcium vapour
h_{Mn}	activity of manganese in the melt using 1 wt% as the standard state
h_o	activity of oxygen in the melt using 1 wt% as the standard state
h_o^*	theoretical oxygen activity from the pure oxygen ionic conductivity
h_o^0	the initial oxygen activity
$h_{o,i}$	the equilibrium activity of oxygen with CA_x
$h_{o,p}$	the equilibrium activity of oxygen with (Ca,Mn)S
h_s	activity of sulfur in the melt using 1 wt% as the standard state
h_s^0	the initial sulfur activity
$h_{s,i}$	the equilibrium activity of sulphur with CA_x
$h_{s,p}$	equilibrium activity of sulfur with (Ca,Mn)S
I_A/I_B	x-ray intensity ratio of element A to B
I_i, $I_{(i)}$	x-ray intensities from the sample and standard, respectively

K	the equilibrium constant
K_1	rate constant for calcium assimilation, s^{-1}
k_1	second-order reaction rate constant, s^{-1}
K_2	rate constant for calcium elimination, s^{-1}
$K_{2'}$	first-order rate constant for calcium elimination, s^{-1}
K_3	rate constant for desulphurization, s^{-1}
$K_{Al_2O_3}$	equilibrium constant for aluminum deoxidation
K_{CaO}	equilibrium constant for calcium deoxidation
K'_{CaO}	apparent solubility product based on the weight percent concentration ([%Ca]*[%O])
K_{CaS}	equilibrium constant for calcium desulphurization
K'_{CaS}	apparent solubility product ([%Ca]*[%S])
$k_{d,loc}$	local mass transfer coefficient based on surface renewal theory, m/s
k_{dis}	mass transfer coefficient for calcium dissolution, m/s
K_{evp}	rate constant for calcium vaporization or fading, s^{-1}
k_{evp}	mass transfer coefficient for calcium vaporization or fading. m/s
k_G	mass transfer coefficient in gas phase, m/s
K_H	Henry's equilibrium constant for calcium dissolution reaction
k_i	mass transfer coefficient at inclusions, m/s
k_iz	mass transfer rate constant at inclusions, s^{-1}
$k_{L,E}$	enhanced mass transfer coefficient, m/s

k_L	mass transfer coefficient for simple dissolution, m/s
k_{Lf}	mass transfer coefficient for the front of the bubble, m/s
k_{Lr}	mass transfer coefficient for the rear of the bubble, m/s
k_{Mg}	mass transfer coefficient of magnesium, m/s
k_{ovl}	the overall or mixed mass transfer coefficient, m/s
$k_{rm}z_{rm}$	rate constant of the inclusion removal, s^{-1}
$k_{ro}z_{ro}$	rate constant of reoxidation, s^{-1}
$k_{sl}z_{sl}$	rate constant of desulphurization by slag, s^{-1}
M_{Ca}	molar weight of calcium, g/mole
M_O	molar weight of oxygen, g/mole
[%M]	metallic element concentration wt% in bulk
N	mass transfer rate, mole/s
N'	mass transfer rate per unit gas-liquid interfacial area, mole/m^2.s
n_i	inclusion number per unit volume, no./m^3
$\%O_r$	oxygen wt% at the reaction plane in the liquid film
P	pressure, atm
P_{Ca}	calcium vapour pressure, atm
$P_{e'}$	equilibrium oxygen pressure from electron conductance, atm
$P_{O_2}^{I}$, $P_{O_2}^{II}$	the lower and higher oxygen pressure at cathode and anode, atm
Q	calcium gas flow rate, m^3/s

R	gas constant, 82 m^3.atm/mol.K
r	radius of the crucible, m
r_1	radius of depression, m
$r_{Al,CAx}$	aluminum flux into or out of CA_x, mole/s
$r_{Ca,CAx}$	calcium flux into CA_x inclusions, mole/s
$r_{Ca,diff}$	calcium diffusion rate through the liquid film, mole/s
$r_{Ca,diff}^{max}$	maximum calcium diffusion rate throught the liquid film, mole/s
$r_{Ca,reac}$	calcium reaction rate at the inclusions in the liquid film, mole/s
$r_{Ca,reac}^{max}$	maximum calcium reaction rate at the inclusions in the liquid film, mole/s
$r_{o,CAx}$	oxygen flux into or out of CA_x, mole/s
$\%S_r$	sulfur wt% at the reaction plane in the liquid film
SEM	scanning electron microscopy
SH	super heat of the melt
Sh	Sherwood number $Sh = k_L d_E / D_L$
T	temperature, ^0K
t	time, s
T_{BP}	boiling point of calcium, ^0C
U	mean radial velocity of the melt at the crucible surface, m/s
V	volume of the melt, m^3
v	calcium wire feed velocity, m/s
W_m	weight of the melt, kg

x	the arbitrary position in the liquid film, m
X	mole fracture of Al_2O_3 or CaO in CA_x, and CaS or MnS in (Ca,Mn)S
ZAF	x-ray correction for atomic number (Z), x-ray absorption in the specimen (A) and fluorescence effects (F)
z_L	calcium gas-liquid interfacial area per unit volume, m^2/m^3
z_{CA_x}	area per unit volume of CA_x inclusions. m^2/m^3
z_{CaO}	area per unit volume of CaO inclusions, m^2/m^3
z_{CaS}	area per unit volume of CaS inclusions, m^2/m^3

GREEK SYMBOLS

μ	viscosity, poise
υ	kinematic viscosity, m^2/s
δ_G	gas film thickness, μm
δ_L	liquid film thickness, μm
δ_r	distance of the reaction plane in from the gas-liquid interface, μm
Φ	rate of absorption per unit area ($mole/m^3.s$)
Ω	constant defined in Equation H.6
θ	exposure time or lifetime of a surface element, s
Θ	fraction of surface coverage
ε	stirring power per unit volume of the melt, $erg/m^3.sec$

ρ	density, g/m^3
ϕ	sulfur partition ratio between slag and melt

SUBSCRIPTS

Al	aluminum
B	component B in the liquid phase
b	bubble, or gas-liquid interface
BP	boiling point
Ca	calcium
CaO	calcium oxide
CaS	calcium sulphide
cell	the galvanic cell
diff	diffusion
dis	dissolution
evp	evaporation
G	gas phase
g-l	gas-liquid
i	inclusion
L	liquid phase
m	melt
o	oxygen
ovl	overall
r	reaction plane
reac	reaction
rm	removal

ro	reoxidation
s	sulphur
sl	slag
T	total
(v)	vapour phase
(%)	based on using 1 wt% as the standard state

SUPERSCRIPTS

Al	aluminum
C	carbon
Ca	calcium
Cr	chromium
eq	equilibrium
G	gas phase
max	maximum
Mn	manganese
Ni	nickel
O	oxygen
Si	silicon
t	time
^{0}	initial state
*	interfacial value

LIST OF FIGURES

LIST OF TABLES

CHAPTER 1

INTRODUCTION

Calcium-based additions are made to steels not only for deoxidation and/or desulphurization, but also for the control of inclusion composition and morphology due to its high affinity for oxygen and sulfur in the melt.

If enough calcium is added, the solid alumina (Al_2O_3) inclusions can be transformed into liquid calcium-aluminate (CA_x) inclusions. As a result, not only the volume fraction of remaining inclusions will be decreased, but also the nozzle clogging due to the precipitation of solid alumina inclusions during continuous casting will be prevented. If more calcium is added, the manganese sulphide (MnS) inclusions can also be modified to calcium-manganese sulphide (Ca,Mn)S. All of the above efforts result in a cleaner steel, and the improvement of the machinability and/or the mechanical properties of the final product.

However, excess addition of calcium in the melt with

high sulfur would result in the formation of solid calcium sulphide, which also precipitates on and clogs the nozzle during continuous casting. Therefore, the basic understandings of the thermodynamics and kinetics behind these treatments are needed, in order to achieve the optimum conditions for the reliable industrial performances.

Despite the fact that calcium treatment of steel is widespread, the results obtained are often erratic. While some of this may be attributed to variation in steelmaking practice, much of the problem is related to the fact that the mechanisms by which calcium dissolves, desulphurizes, deoxidizes and transforms sulphide and oxide inclusions are largely unknown.

There have been a number of studies on the thermodynamics of calcium treatment [1-6], but the inclusions observed in practice often differ from that expected from equilibrium. Therefore there is a need to study the kinetics of treatment to determine the way in which bulk concentrations change in the steel and the way inclusion distributions develop.

Few well-controlled injection experiments on calcium treatment of steel have been carried out. The current experiments were performed in the 40 kg furnace enclosed in a vacuum chamber, which was filled with argon following the pumping down of the air. The experimental conditions and

results can therefore be continuously and accurately measured and controlled. The present experiments have focused on the following three important parameters:

(a) the effect of the calcium injection rate,
(b) the effect of the initial sulphur content, and
(c) the effect of the initial oxygen/aluminum content.

The present results quantitatively demonstrate these and other important parameters' effects on the calcium absorption, desulphurization and deoxidation, and inclusion modification during and after calcium injection. A comprehensive mathematical model has been developed to study the kinetics for this multiphase system, and to quantitatively interpret the experimental results. The implications for full-scale operations are also discussed.

CHAPTER 2

LITERATURE REVIEW

2.1 CALCIUM METAL, ITS ALLOYS AND COMPOUNDS

Calcium is the fifth most abundant element in the earth's crust comprising 3.63% of the earth crust. It exists in nature mainly as calcium chloride and lime, which serve as the raw materials for making metallic calcium, calcium alloys and calcium compounds used for metallurgical purposes [7].

2.1.1 The Production of Calcium

There are generally two processes to obtain calcium metal: molten salt electrolysis and the thermal reduction process [7].

Electrolysis

The industrial production of calcium by electrolysis was started in France and Germany in 1920 and in the U.S.A. from

1939. In general, a cathode tip is dipped into the pure calcium chloride melt which serves as the electrolyte. After the electrical connection is made, calcium deposits onto the cathode, which is slowly raised in a way to just preserve the contact with the melt on salt. Successive layers of calcium precipitate onto the cathode tip to form a cylindrical block, which is then remelted and cast into billets. The purity of calcium made is generally 90-95% with Fe, Al, Mg, Si and $CaCl_2$ as the main impurities.

Thermal Reduction Process

In 1944, the New England Lime Co. of Canada succeeded in producing relatively pure calcium metal by thermally reducing lime with aluminum in a vacuum. At present, most calcium is produced by this method, which is an improved version of the Pidgen process for making magnesium. Having been loaded into a horizontal reaction vessel and exposed to temperatures of 1050-1200 ^0C and a vacuum of 10^{-3} torr, the mixture of CaO powder and Al turnings reacts to form Ca vapour and calcium aluminate according to the following reactions:

$$6CaO + 2Al = 3CaO \cdot Al_2O_3 + 3Ca \qquad (2.1)$$

$$5CaO + 2Al = 2CaO \cdot Al_2O_3 + 3Ca \quad (2.2)$$

$$4CaO + 2Al = CaO \cdot Al_2O_3 + 3Ca \quad (2.3)$$

The calcium vapour diffuses to the low temperature part of reaction vessel and condenses there. By this method, the purity of calcium reaches 99% with Mg and Al as the main impurities.

2.1.2 Chemical Properties of Calcium

Calcium is a silver white metal. Exposed to air, its surface is immediately covered by a grey oxide layer, which gradually transforms into hydroxide and carbonate [7]. With its strong reactivity like the rest of alkali metals, calcium can easily affiliate with O, N, H, S, P, Si, and halogen compounds. Reaction with oxygen starts at room temperature and with nitrogen at a temperature of 300 ^{0}C, while calcium chloride formation occurs around 400 ^{0}C. If Ca is heated in a CO_2 atmosphere, it changes to CaC_2. Reaction with hydrogen starts at 250 ^{0}C, resulting in the formation of calcium hydride CaH_2.

2.1.3 Physical properties of Calcium

The basic properties of calcium are shown in Table 2.1.[7]

TABLE 2.1

THE BASIC PROPERTIES OF CALCIUM [7]

atomic number	20
atomic weight	40.08
valency	2
atomic shell configuration	2-8-8-2 coordinated on K, L, M and N shell
atomic radius	1.97 Å
ionic radius	0.99 Å (Ca2+)
covalent radius	1.74 Å
isotopes	40,42,43,44,46,48
atomic volume	25.9 cm^3/g.atom
electrochemical equivalent	0.20762 mg/C
density	fcc: 1.55 g/cm^3 (20°C) bcc: 1.48 g/cm^3 (450°C)
melting point	850°C
boiling point	1483°C
crystal structure	fcc: (25-450°C) bcc,hcp (450-850°C)
thermal expansion coefficient	22*10^{-6} cm/cm/°C (0-300°C)
specific heat	0.157 cal/g (-850-20°C) 0.149 cal/g (20-100°C)
heat of melting	2070 cal/mole
heat of evaporation	36 kcal/mole (1483°C)
thermal conductivity	0.3 cal/cm.s.°C (0-100°C)
electric resistivity	3.43 $\mu\Omega/cm^3$ (0°C)

Boiling Point and Vapour Pressure

The boiling point and vapour pressure of calcium are of special importance for the application to steel refining. The values of the boiling point and the heat of evaporation measured by various investigators are given in Table 2.2 [8]. The average value of calcium's boiling point is 1483 °C.

TABLE 2.2

PUBLISHED VALUES OF THE BOILING POINT AND HEAT OF EVAPORATION OF CALCIUM [8]

Author(s)	year of publication	ΔH_{BP} kcal/mole	T_{BP} °C
H. Hartmann, R. Schneider	1929	40.30	1439
K. K. Kelley	1935	-	1487
J. F. Elliott, M. Gleiser	1960	35.84	1492
R. Hultgren	1963	36.39	1483
O. Kubaschewski, E. L. L. Evans	1967	36.00	1483
E.Schürmann,P.Fünders,H.Litterscheidt	1974	34.57	1511

The Ca vapour pressure and its dependence on temperature can be calculated from the following equation [9]:

$$\log P_{Ca}(atm) = -8082/T + 4.579 \qquad (1000\text{-}2000\ K) \qquad \textbf{(2.4)}$$

From the equation, the Ca vapour pressures P_{Ca} at 1550, 1600 and 1650 ^{0}C are 1.4, 1.846 and 2.31 atm respectively. Thus higher pressure systems are required in order to determine the solubility of calcium in liquid iron and steel at steelmaking temperatures.

2.1.4 Calcium solubility in Liquid Iron and Steel

Since early 1890, various researchers [10-13] tried but failed to determine the solubility of calcium in the iron and steel, even though small amounts of calcium were sometimes found in steel in the form of non-metallic inclusions.

It was Sponseller and Flinn [1] who succeeded in measuring the solubility of Ca in iron and various iron alloy melts. They claimed that the reason for the failure of the earlier investigators was the absence of a liquid layer of calcium in contact with the liquid steel. So they conducted experiments using titanium nitride crucibles under 13.4 atm pressure of argon to prevent the evaporation of Ca. As a result, they could obtain 2-phase Ca-Fe melts under equilibrium conditions. All experiments were kept for at least 3 minutes at 1607 ^{o}C to obtain the equilibrium. Solubility measurements were made for pure iron and Fe-C, Fe-Si, Fe-Al, Fe-Ni and Fe-Au alloys. For pure iron an apparent solubility of 0.032% Ca was obtained. It was also observed that additions of C, Si, Al and Ni to the

iron melt decreased the activity of Ca and therefore lead to an increase of Ca solubility. More recently their results were confirmed and expanded by others [4] under similar experimental conditions. Figure 2.1 shows both groups' [1,4] results of calcium solubility in pure iron as a function of temperature at 10 bar. It is seen that the solubility of calcium in liquid iron increases with temperature. The agreement between the two groups at 1600 °C is fairly good.

The dissolution of calcium vapour into a liquid iron may be written as:

$$Ca_{(v)} = \underline{Ca}_{(\%)} \qquad (2.5)$$

For the dilute solutions, the equilibrium constant for the above equation is given as:

$$K_{Ca} = \frac{h_{Ca}}{P_{Ca}} \qquad (2.6)$$

where

h_{ca} = calcium activity in the steel melt using 1wt% as the standard state

P_{ca} = calcium vapour pressure using 1 atmosphere as the reference state

K_{Ca} = equilibrium constant

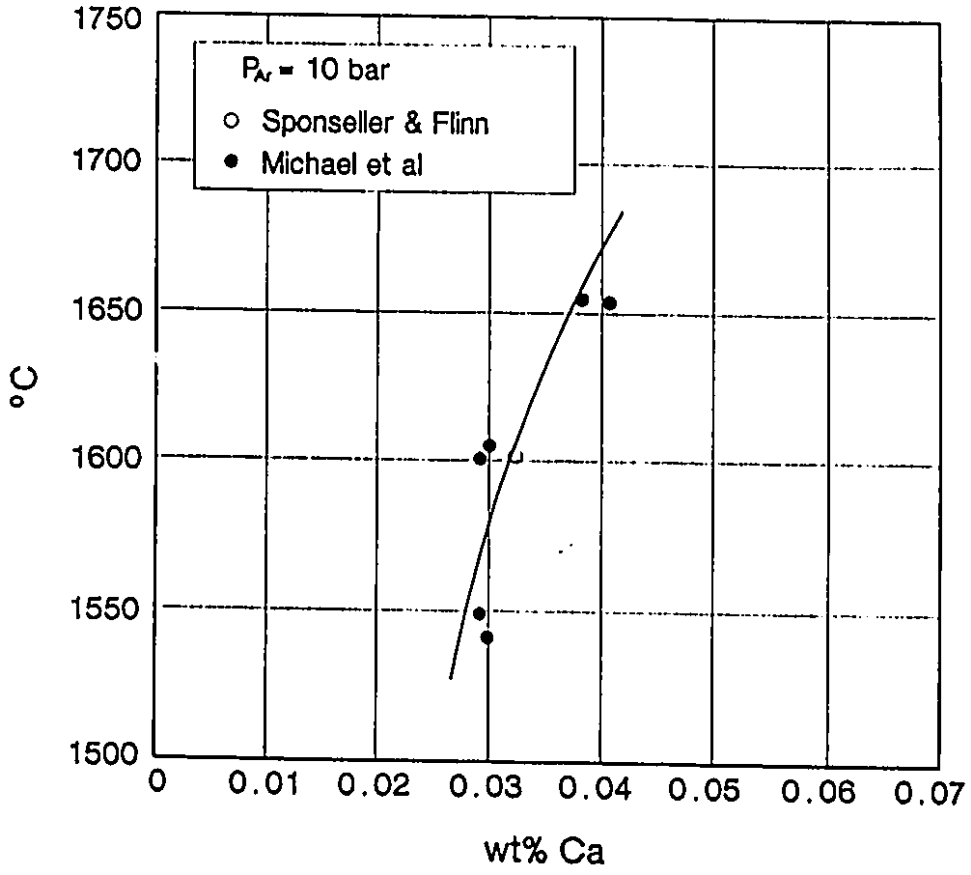

Figure 2.1 Calcium solubility in pure iron at 10 bar as a function of temperature [1,4]

By regression through the experimental data in Figure 2.1, one can derive the relationship of K_{Ca} against the inverse of the temperature as the following:

$$\log K_{Ca} = 4307.86/T - 4.0572 \qquad (1823\text{-}1923\,^{o}K) \qquad (2.7)$$

Since K_{Ca} is only a function of the temperature, it can be used to calculate the calcium activity from the known vapour pressure at a certain temperature, or to calculate the equilibrium pressure from its activity by equation 2.6.

Both groups [1,4] found that alloying elements such as carbon, silicon, aluminum and nickel increase the calcium solubility, while chromium significantly reduces calcium solubility. The interaction parameters e^{X}_{Ca} of the alloying elements in the iron are given in Table 2.3. The graphic expression is shown in figure 2.2.

From the data in Table 2.3, one can calculate the calcium activity for the particular experimental conditions according to the following equation:

$$\log h_{Ca} = \log[\%Ca] - 0.337[\%C] + 0.014[\%Cr] - 0.043[\%Ni] - 0.096[\%Si] - 0.054[\%Al] - 0.007[\%Mn] \qquad (2.8)$$

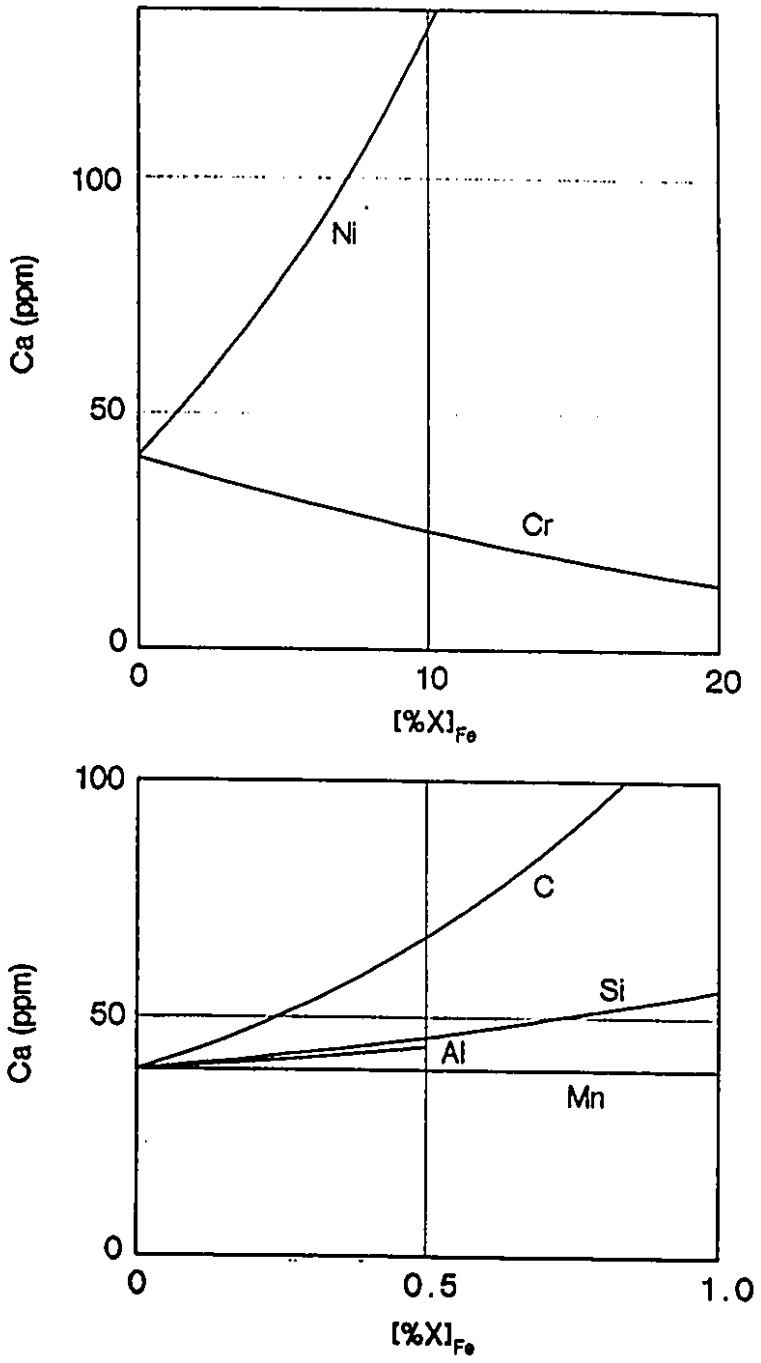

Figure 2.2 Influence of some alloying elements on calcium solubility in liquid steel at 1600 ^{0}C and 10 bar pressure [1,4]

TABLE 2.3

INTERACTION COEFFICIENTS e^{X}_{Ca} in iron at 1600 °C

e^{X}_{Ca}	Sponseller & Flinn	Kohler et al.
e^{Si}_{Ca}	-0.097	-0.096
e^{Al}_{Ca}	-0.072	-0.054
e^{Ni}_{Ca}	-0.044	-0.043
e^{Mn}_{Ca}	-	-0.007
e^{Cr}_{Ca}	-	+0.014
e^{C}_{Ca}	-0.337	-

No one has correctly estimated calcium solubility directly from an experiment conducted under normal conditions (1 atmosphere of calcium vapour at 1600 ^{0}C). Although some [2,14-15] tried to calculate the dissolved calcium content by subtracting the calcium combined with the inclusions from the total calcium, that dissolved calcium value could not be interpreted as the calcium solubility, since under normal conditions, equilibrium was not reached. Their results could be explained as the balanced calcium contents between calcium supply and calcium elimination.

In view of the negligible solubility of argon in liquid metals, variations in the pressure of argon should have a negligible effect on the calcium concentration in the iron-rich liquid, as long as the pressure is sufficient to permit the existence of the calcium-rich liquid [1]. However, at a pressure lower than its vapour pressure which is insufficient to maintain a calcium-rich layer, the calcium solubility is the function of the calcium gaseous pressure and the chemistry of the melt. For the present experimental conditions (at 1 atmosphere and 1600 ^{0}C), calcium solubility in 1045 steel is calculated according to equations 2.5-2.8. At 1600 ^{0}C, K_{Ca} is calculated to be 0.017 from equation 2.7. Substituting K_{Ca} into equation 2.6, the calcium activity h_{Ca} in equilibrium with 1 atm of calcium pressure is then 0.017. If h_{Ca} is inserted in equation 2.8 with the chemical compositions of AISI 1045 steel, the calcium solubility is calculated to be 0.024%.

2.1.5 Calcium Alloys and Compounds

The addition of calcium to steel melts can be made in its pure form, or in the form of alloys such as CaSi and CaSiMn or compounds such as CaC_2 and CaO.

Calcium can associate with Si, Al, Fe, Mn, Ni, Ba and the Rare Earth metals to form various kinds of binary, ternary and

multicomponent alloys. These alloys have relatively higher densities than that of molten iron and steel, and provide for a low vapour pressure of Ca. This is reported to allow a very stable Ca addition to steel and other metals. The most often-used and important ones are listed in Table 2.4 [16].

The most common calcium compounds used for the metallurgical purposes are CaO, $CaCO_3$, CaF_2, CaC_2, $CaCl_2$, $CaCN_2$ and CaS [17-18]. When calcium is added in the form of a compound that is stable [17] and largely insoluble in the steel at the treatment temperature, the violence of the reaction is greatly reduced. Thus, CaC_2, $CaCN_2$ and $CaCl_2$ may be introduced in the bath, where they react with sulfur and/or oxygen with a minimum of volatilization. These compounds are successfully employed to desulphurize pig iron, but for a number of reasons, not for steel treatment. CaS addition in the steel was recently found [18] useful as a refining agent to improve the machinability of the free-machining steel.

More recently, calcium metal, calcium alloys and compounds were together as a mixture or used in sequence to treat steels more effectively for desulphurization, dephosphorization, inclusion modification and other metallurgical purposes [19-20].

TABLE 2.4

COMPOSITION OF Ca ALLOYS (wt%) [7,16]

#-element	type of alloy	Ca	Si	Al	Mn	Fe	Mg	Ni	Ba	Rea
2-element	CaSi	60.64	33.66	1.15	0.20	2.93				
	$CaSi_2$	41.67	58.33							
	$CaNi_X$	8.9~25						75~91		
3-element	CaSiFe	>20	35~40			15~30				
	CaAlFe	19~33		8~22		56~57				
	CaSiMn	16~20	53~59		14~18					
	CaSiAl	18~22	60~62	10~20		4~5				
	CaSiBa	15~20	45~55						15~20	
	CaSiMg	24~29	48~56			Bal.[b]	5~12			
	CaSiRe[a]	18~24	50~55							10~20
4-element	CaSiAlFe	18~22	43~51	19~32		4~5				
	CaSiMnFe	>20	35~40		10~25	10~20				
	CaSiMgFe	12~16	50~57			22~28	2~5			
5-element	CaSiAlMnFe	15~20	30~45	5~10	10~25	10~25				
	CaSiBaAlFe	10~13	38~42	19~21		Bal.			9~12	
	CaSiMgAlFe	20	42	2		Bal.	12			

[a] Re: Rare Earth metals

[b] Bal: Balance

2.2 HISTORY ON CALCIUM APPLICATIONS IN STEELMAKING

Since Davy [21] discovered calcium in 1808 by isolating the element in its pure form, it took one century for it to be used in steelmaking, and it took nearly another century for

the process of calcium addition into steel to be fully-established, and to date our understanding of the process is still very limited.

Around the turn of the last century, calcium was able to be produced in the form of CaSi by the following two processes [7]: (1) the production of CaSi by Morehead and Chalmot in 1896, using a direct reduction of lime and quartz with coke or charcoal according to the reaction:

$$CaO + 2SiO_2 + 5C = Ca + 2Si + 5CO \qquad (2.9)$$

(2) Bozel and Wilson in 1908 used calcium carbide instead of lime as a starting material and produced CaSi according to the reaction:

$$CaC_2 + 2SiO_2 + 2C = Ca + 2Si + 4CO \qquad (2.10)$$

In 1906 Watts [11] added CaSi to a steel melt and found an improvement of the cleanliness of the steel. Thereafter, Goldschmidt [22] reported that CaSi is an effective agent for the deoxidation of the steel melts. Geilenkirchen [23] obtained similar results for a mixture of Al and CaSi. In the following years, the initial observations by Goldschmidt were confirmed by various experiments [24-25]. In 1931, pure Ca was

first tested for the deoxidation of steel [26]. Furthermore, Mantell and Hardy [27] reported that Ca additions may have various positive effects also in non-ferrous metals. These authors found that Ca removes bismuth from lead, reduces the hydrogen content, generally acts as a degassing agent and deoxidizer in a number of metals and improves their mechanical properties. At that time, Chipman [28] estimated through thermodynamic calculations that Ca can reduce the oxygen content in steel to 10^{-8}% in equilibrium with 1 atm of Ca vapour. However, several researchers [29-30] questioned the effectiveness of Ca deoxidation, because Ca has a low boiling point of 1439 ^{0}C and it is insoluble in steel. In 1940, with the simultaneous addition of Al and CaSi, it was found [31] that Ca can reduce the amount of harmful manganese sulfide and alumina clusters, change the shape and distribution of inclusions and improve the ductility, toughness and hot shortness of the steel products. Around 1950, doubts were raised again about the effects of Ca in steel due to its poor reproducibility which varies with operational parameters, and more importantly, with the methods of addition of Ca in the melt [32]. Thus for about half a century, various divergent opinions about the usefulness of Ca existed and impeded its industrial applications in steel. The historic development of this period is summarized in several papers [13,33].

However from 1960, stimulated by the explosive world wide

growth of the steel industry, extensive research on the basic thermodynamics of Ca deoxidation, desulphurization, and inclusion modification has been done. Modern and sophisticated methods of Ca addition into the steel melt have been developed to increase the efficiency and reproducibility of the process. Calcium addition has become a routine to ensure the stable castibility by eliminating the solid aluminate inclusions which otherwise would cause nozzle clogging during continuous casting. Finally, calcium treatment of steel has established itself as a recognized refining method to ensure cleaner and higher quality steels. Recent developments are contained in a series of conferences [34] and the most comprehensive study on the subject is presented in the first international symposium devoted to calcium treatment [35].

2.3 METHODS OF CALCIUM ADDITION TO STEEL

In view of the limited solubility of calcium in steel and the violent reaction taking place, the method of addition of calcium is very important to its retention in steel and its effectiveness on the final products. With the advance of the technology, the methods of calcium addition have improved over the century. The early forms of addition were simple, but suffered from lower calcium retention in steel. Modern

processes are equipped with sophisticated units to achieve higher calcium yield.

2.3.1 Early Addition Methods

Over the first half of the century, various methods were attempted with variable success [36]. Listed below are some of the conventional methods for adding calcium to steel:

1) Tap the molten steel onto the calcium alloy placed in the bottom of the ladle.
2) Add the calcium alloy to the surface of the molten steel in the ladle.
3) Add the alloy in lump form attached to the end of a metal rod plunged deeply into the ladle.
4) Add the alloy in expanded metal screens attached to the end of a long weighted bar quickly lowered by a crane into the melt.
5) Add the alloy in a large sealed steel pipe with holes drilled in the side. The pipe is plunged deep into the melt until agitation ceases usually after 15-30 seconds.
6) Briquette calcium metal with sponge iron or steel chips.
7) Shoot slugs of the alloy by air pressure deep into the melt.

8) Wrap the alloy in bags and add to ladle stream

The conventional calcium addition methods often result in short contact time or small contact area between the evolved calcium gas and the melt, and the calcium yield and reaction efficiency are also very low.

2.3.2 Powder Injection Method

In the middle of 1960's, Thyssen-Nuederrhein (TN) Company succeeded in developing an industrial process for calcium-argon blow [37]. It is a pneumatic injection process in which powdered calcium or other reagents are injected by an carrier gas, deep into the melt through a lance. The equipment used for TN injection method is schematically in figure 2.3. It consists of three main parts:

(1) Main support unit and the lance: This is the frame work of the unit to support the whole system, and controls the movement of the lance, which carries the gas-powder mixture into the melt.
(2) Powder dispenser: It sits directly on top of the lance, to store and controls the flow of powdered reagents.
(3) Carrier gas supply unit: which supplies the carrier

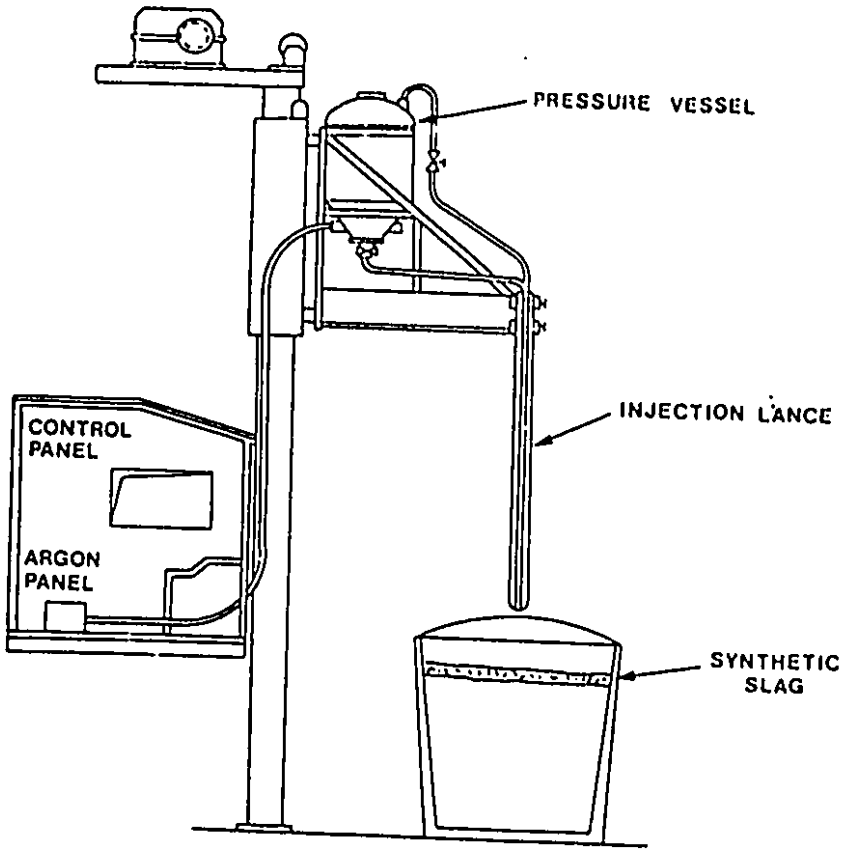

Figure 2.3 TN powder injection system [37]

gas with adjustable pressure and flow rates. The carrier gases can be an inert gas such as argon or nitrogen which has limited reaction with the melt.

However this simple pneumatic dispenser system was upgraded and improved to a complete ladle metallurgical system with multi containers and computerized facility by Scandinavian Lancers System in 1972 [38]. The injection system is schematically shown in figure 2.4. By comparison with TN process, Scandinavian Lancers System is more flexible and automatically controlled, and it can also inject several different types of powder reagents in sequence.

2.3.3 Wire Feeding Method

The technology of adding Al wire to a steel melt is well known and is widely used for adjustment of the soluble Al content because of the high and controlled yield of the addition method [39]. In recent years, it has been used for adding calcium in a similar way [40-41]. Extensive research has been done on the dissolution of both Al and Ca wires during their additions to steel [42-43]. An acceleration transducer was also used to measure the vibration caused by calcium evaporation on its addition to the steel melt [44].

Figure 2.5 shows the outline of a feeding process, in

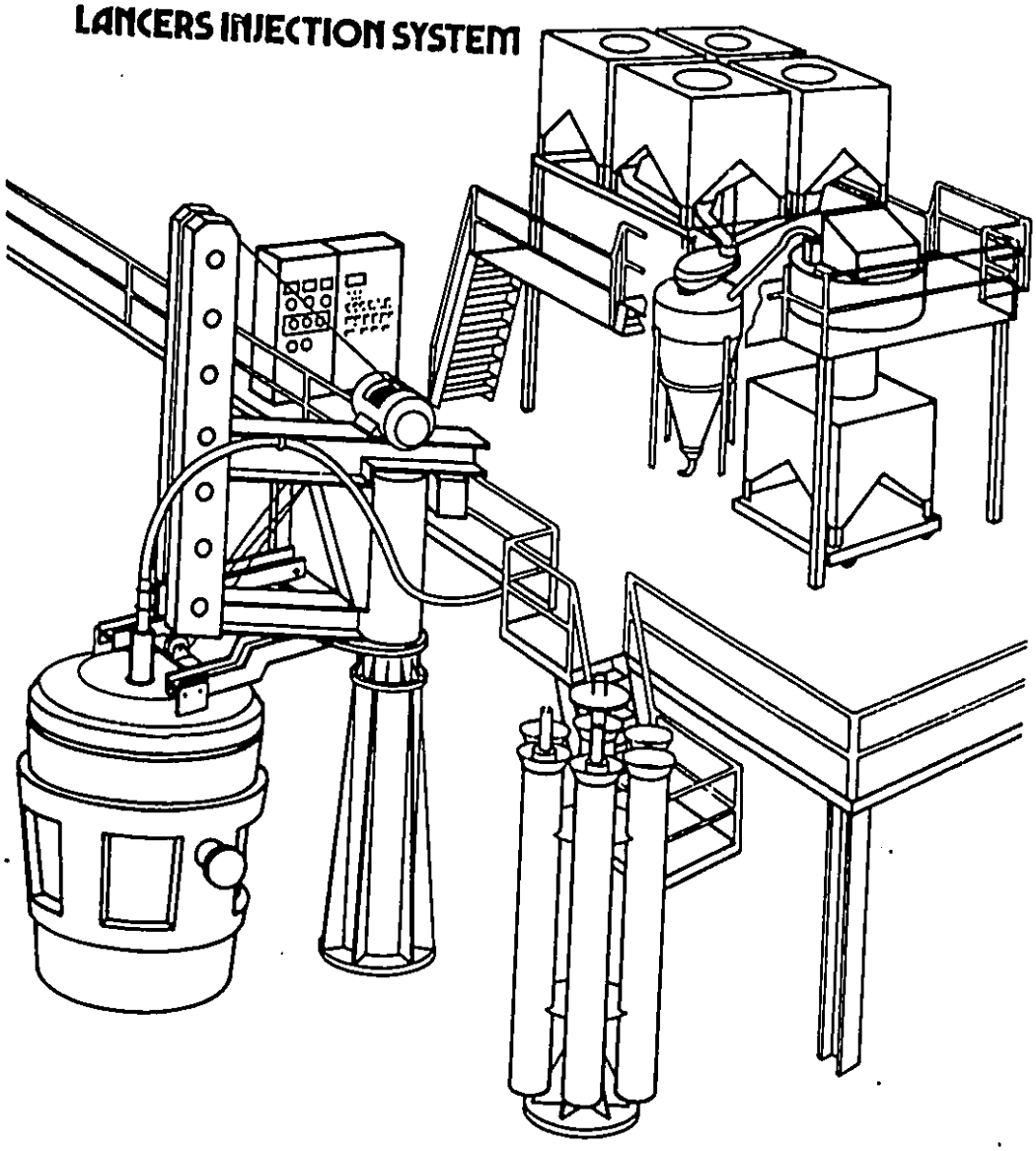

Figure 2.4 Scandinavian Lancers injection system [38]

which iron-clad calcium wire is continuously fed to the ladle by a wire feeder. Calcium and calcium alloy cored wires are derived from the welding technology. Such wires were developed with feeders, generally, for treatment in full ladle, in bottom pouring and in tundish of casters. The survey of the technique and the results was made recently [45].

Even though calcium wire is more expensive than calcium powder, by comparison, the process of calcium powder injection has the following disadvantages over wire injection process:

1) Larger loss of the temperature.
2) The treatment is made mainly in ladle, at relatively large flow rates making it difficult to be used in small ladles and in the tundish of casters.
3) Low calcium recovery compared to calcium wire injection.
4) More complex and hard to control.
5) Higher capital costs.

Therefore, this simple and easy-control feature of calcium wire injection has gained its wide applications in secondary steelmaking, especially for refining in small or medium size refining vessels.

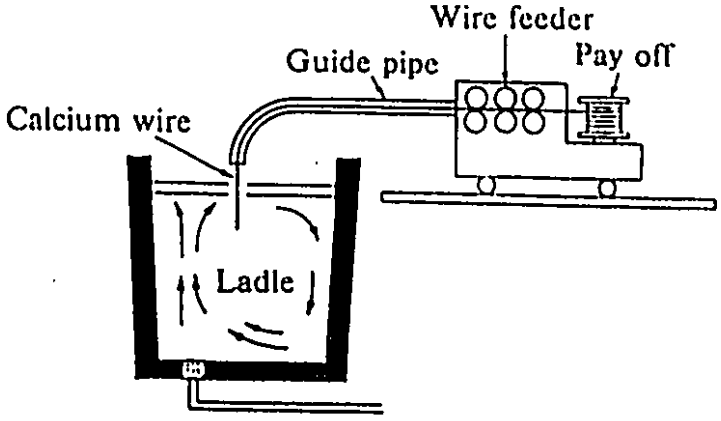

Figure 2.5 Calcium wire feeding process [45]

2.3.4 Wire Lance Injection

In 1983, Pfizer Inc, began field testing a new process, which combines features of Powder Injection and Wire Injection methods [46], and it is called the Wire Lance Method (WL process). As shown in figure 2.6, a calcium wire is fed into the steel melt through a ceramic lance, which is submerged about 2 meters below the liquid free-surface. Prior to feeding the wire, the lance is purged with an inert gas and the gas flow continues during the wire injection period. Basically a modification over the simple Wire Feeding Method, the WL process claims the following advantages [46]:

1) The wire enters the melt at a depth determined by the lance immersion and therefore sufficient ferrostatic pressure can be provided to avoid "boiling" of calcium at the location where the wire dissolves into the steel melt.
2) Protected by the steel sheath, calcium core starts to react with the liquid steel only about 1 second after the wire entered the melt. Therefore, calcium reaction takes place far from the lance and is not influenced by the gas bubbles rising from the lance tip to the melt surface.
3) In contrast to the Powder Injection process, the inert carrier gas has no carrier function, and its

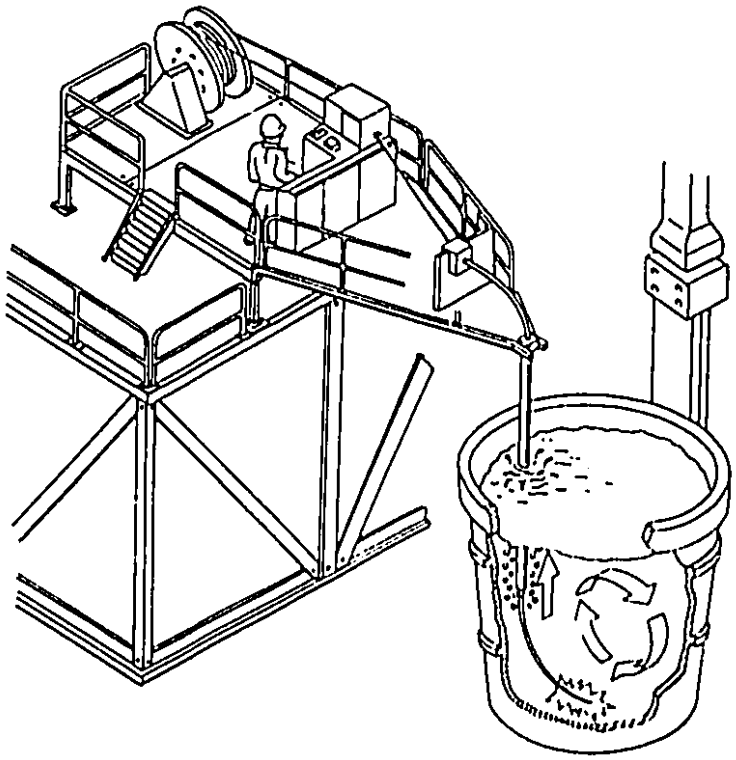

Figure 2.6 Wire lance method [46]

flowrate can be adjusted solely for maximum stirring and purging of the melt.

4) Calcium vapour bubbles created when calcium raises above the critical vaporization depth will be small and well dispersed. Emerging bubbles will create little disturbance and this reaction of the steel with the atmosphere will be small.

It is claimed that the even dispersion of small liquid calcium and long contact of calcium with the melt deep below the steel melt surface, ensures a maximum calcium-steel interaction. Figure 2.7 compares the calcium yield for the Wire Feeding and Wire Lance methods [46]. A much better yield is achieved, if calcium wire is added through the lance deep into the steel melt. The improvement is especially profound for small additions.

The three modern addition methods of calcium described above are all based on the same principle: To introduce calcium or calcium alloy as deep as possible into the melt to ensure calcium contact and react effectively with the steel melt for as long as possible. Since the calcium yield or recovery is still low (<50%) and cost of the process installation and operation is still relatively high, that same problem will provide the same incentives for the future innovation for adding calcium to steel.

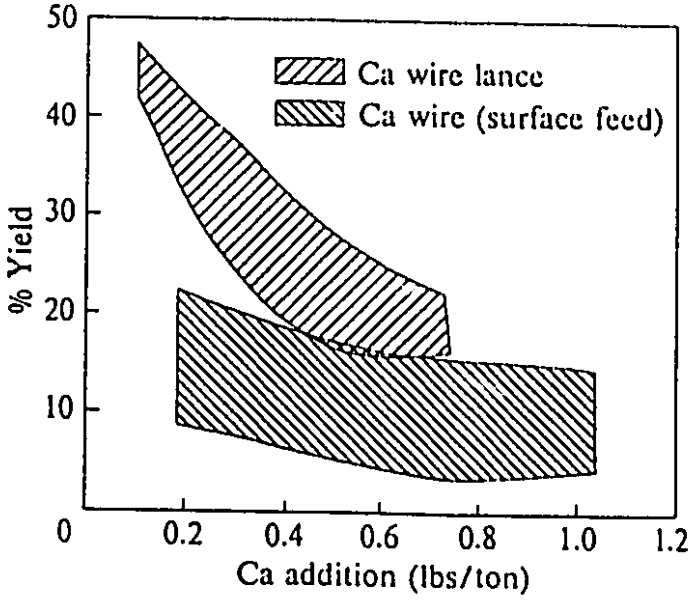

Figure 2.7 Comparison of calcium yield between wire lance method and wire feeding method [46]

2.4 DEOXIDATION,DESULPHURIZATION & REMOVAL OF OTHER IMPURITIES

The main feature for calcium application in steel is its high reactivity with oxygen, sulfur and other impurity elements such as P and N. The calcium reaction products are therefore more stable than those of most other metals.

2.4.1 Thermodynamics of Calcium Oxides and Sulfides

The standard free energy of formation for calcium oxide and for sulfide is shown in figure 2.8 in comparison to those of Mg and Mn [47]. It is recognized that the equilibrium activities of oxygen and sulfur with calcium are smaller than those with magnesium and manganese. So that calcium would have a higher degree of deoxidation and desulphurization when it is added to molten steel. As the oxides are thermodynamically more stable than the sulfides, it is expected that upon a Ca treatment, calcium oxide is formed initially, and calcium sulfide forms after the free oxygen of the melt has reached a certain value. The following equations show the common reactions of Ca with O and S, and their standard free energy of formation corresponding to each reaction [48-49], where <> denotes solid phases, {} denotes liquid phases and () denotes gas phases.

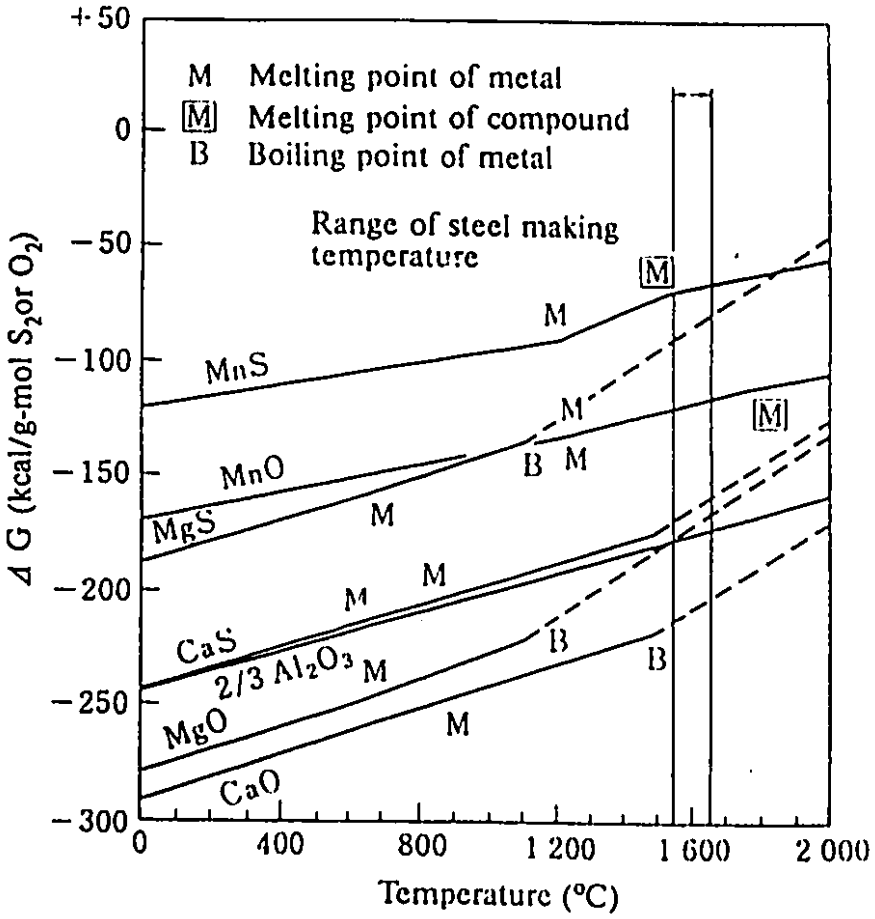

Figure 2.8 Formation free energy of oxide and sulfide of Ca, Mg and Mn [47]

$$2\langle Ca\rangle + (O_2) = 2\langle CaO\rangle$$

$$\Delta G^0 = -302{,}650+47.32T\pm 3kcal \quad (298\sim 1{,}124K), \tag{2.11}$$

$$2\langle Ca\rangle + (O_2) = 2\langle CaO\rangle$$

$$\Delta G^0 = -307{,}100+51.28T\pm 3kcal \quad (1{,}124\sim 1{,}760K), \tag{2.12}$$

$$2(Ca) + (O_2) = 2\langle CaO\rangle$$

$$\Delta G^0 = -380{,}200+93.24T\pm 5kcal \quad (1{,}760\sim 2{,}500K), \tag{2.13}$$

$$2\langle Ca\rangle_\alpha + (S_2) = 2\langle CaS\rangle$$

$$\Delta G^0 = -258{,}870+45.62T\pm 2kcal \quad (298\sim 673K), \tag{2.14}$$

$$2\langle Ca\rangle_\beta + (S_2) = 2\langle CaS\rangle$$

$$\Delta G^0 = -259{,}100+45.92T\pm 2kcal \quad (673\sim 1{,}124K), \tag{2.15}$$

$$2\langle Ca\rangle + (S_2) = 2\langle CaS\rangle$$

$$\Delta G^0 = -263{,}560+49.88T\pm 3kcal \quad (1{,}124\sim 1{,}760K), \tag{2.16}$$

$$2(Ca) + (S_2) = 2\langle CaS\rangle$$

$$\Delta G^0 = -336{,}710+91.44T\pm 5kcal \quad (1{,}760\sim 2{,}000K). \tag{2.17}$$

However, the validity of the value of the free energy of CaO formation was questioned recently [6]. Kay and Subramanian derived the standard free energy change from the data of Edmunds and Taylor [50], who measured the CO partial pressure equilibrated with CaO, CaC_2 and C. Their data showed a large discrepancy in the enthalpy term from the previously accepted JANAF [49] data. The comparison is made in Table 2.5. More recently Wakasugi and Sano [51] confirmed the uncertainty of ΔG^0 of CaO formation. Their data is also included in Table 2.5.

TABLE 2.5

COMPARISON ON FREE ENERGY OF CaO FORMATION

ΔG^0 (J) $Ca(l) + \frac{1}{2}O_2(g) = CaO(s)$	Reference
-641837 + 107T	Kubaschewski & Alcock [48]
-642000 + 111 T	JANAF [49]
-564000 + 108T	Kay & Subramanian* [6]
-628000 + 118T	Wakasugi & Sano [51]

* calculated based on Edmunds and Taylor's data [50].

2.4.2 Deoxidation

The deoxidation reaction by calcium in equilibrium with the melt is given by:

$$CaO_{<S>} = \underline{Ca} + \underline{O} \qquad (2.18)$$

The equilibrium constant K_{CaO} for equation 2.18 can be evaluated based on Henrian activities of Ca and O, assuming pure CaO is formed, i.e. $a_{CaO} = 1$:

$$\log K_{CaO} = \log h_{Ca} + \log h_{o} \qquad (2.19)$$

There are two ways to determine the value of the calcium deoxidation equilibrium constant K_{CaO}: one is through the thermodynamic calculation and the other is from the experimental measurement.

Thermodynamic Calculation:

If one combines the reactions of calcium and oxygen dissolution in steel, and calcium oxide formation, one would have equation 2.18. An example of the rearrangement of the equations involved and the calculation of K_{CaO} is shown in Table 2.6 [6].

TABLE 2.6

THERMODYNAMIC CALCULATION OF K_{CaO} AND K_{CaS}

Reaction	ΔG^0 (J)	Reference
$Ca(l) + \frac{1}{2}O_2(g) = CaO(s)$	-564000+108T	6,50
$CaO(s) + \frac{1}{2}S_2 = CaS(s) + \frac{1}{2}O_2$	91383-5.02T	52
$Ca(l) = \underline{Ca}_{1w/o}$	120133-35.53T	4
$\frac{1}{2}O(g) = \underline{O}_{1w/o}$	-117876-2.88T	53
$\frac{1}{2}S(g) = \underline{S}_{1w/o}$	-131754+22.03T	53
$CaO(s) = \underline{Ca} + \underline{O}$	566257-146.41T	6
$CaO(s) = \underline{Ca} + \underline{S}$	460996-116.48T	6

The results calculated by different authors [6,51,53-56] are shown in Table 2.7. It can be seen that there is a couple of order magnitude of difference in K_{CaO} and K_{CaS} values. This is maybe due to the uncertainty in the free energy of CaO formation, as suggested by Kay and Subramarian [6].

Experimental Measurements

If only first order interaction is considered and self interactions along with all other elements effects are neglected (which may be justified for all systems with strong i-j interaction) the two activity coefficients f_O and f_{Ca} for h_o and h_{Ca} in equation 2.19 are given by:

$$\log f_O = e_O^{Ca} * [\%Ca] \qquad (2.20)$$

TABLE 2.7

LITERATURE SURVEY OF SOLUBILITY PRODUCTS OF Ca OXIDE AND SULFIDE, AND INTERACTION COEFFICIENTS

K_{CaO}	e_O^{Ca}	K_{CaS}	e_S^{Ca}	T (°C)	K_{CaS}/K_{CaO}	Ref.
Thermodynamic Calculations						
$5.5*10^{-11}$	-	$2.1*10^{-9}$	-	1600	38.18	53
$1.5*10^{-11}$	-	$3.8*10^{-10}$	-	1600	25.33	54
$4.5*10^{-11}$	-700	-	-	1600	-	55
$7.0*10^{-9}$ [a]	-	$1.96*10^{-7}$ [a]	-	1600	28.00	6
$5.5*10^{-9}$	-	-	-	1600	-	56
$3.94*10^{-10}$	-	-	-	1600	-	51
Experimental Measurements						
$6*10^{-9}$	-535	-	-	1600	-	2
$1.5*10^{-10}$	-535	-	-	1550	-	57
$2.5*10^{-9}$	-535	$7.9*10^{-8}$	-100	1600	31.60	58
$4.5*10^{-8}$	-150	$3.2*10^{-7}$	-110	1600	7.11	59
$7.0*10^{-7}$	0	$1.7*10^{-5}$	0	1600	24.28	54

[a] These values are used in the present research

$$\log f_{Ca} = e_{Ca}^{O} * [\%O] \qquad (2.21)$$

equations (2.20)-(2.21) then yield:

$$\log K_{CaO} = \log([\%Ca]*[\%O]) + e_{O}^{Ca}*[\%Ca] + e_{Ca}^{O}*[\%O] \qquad (2.22)$$

Introducing K'_{CaO} (the apparent solubility product) based on weight percent concentrations:

$$K'_{CaO} = [\%Ca]*[\%O] \qquad (2.23)$$

and also using the relation:

$$e_{O}^{Ca} = (M_{Ca}/M_{O}) * e_{Ca}^{O} \qquad (2.24)$$

After rearranging, we have:

$$\log K'_{CaO} = \log K_{CaO} - e_{O}^{Ca}*([\%Ca]+2.505[\%O]) \qquad (2.25)$$

If one plots log K'_{CaO} against ([%Ca]+2.505[%O]) and obtains a linear relationship, the intercept would be log K_{CaO} and the slope would be e_{O}^{Ca}. The results from several works [2,54,57-59] are plotted in figure 2.9, according to equation (2.25). They fit together unexpectedly well with each other. However, they do not exhibit a straight line behaviour. That

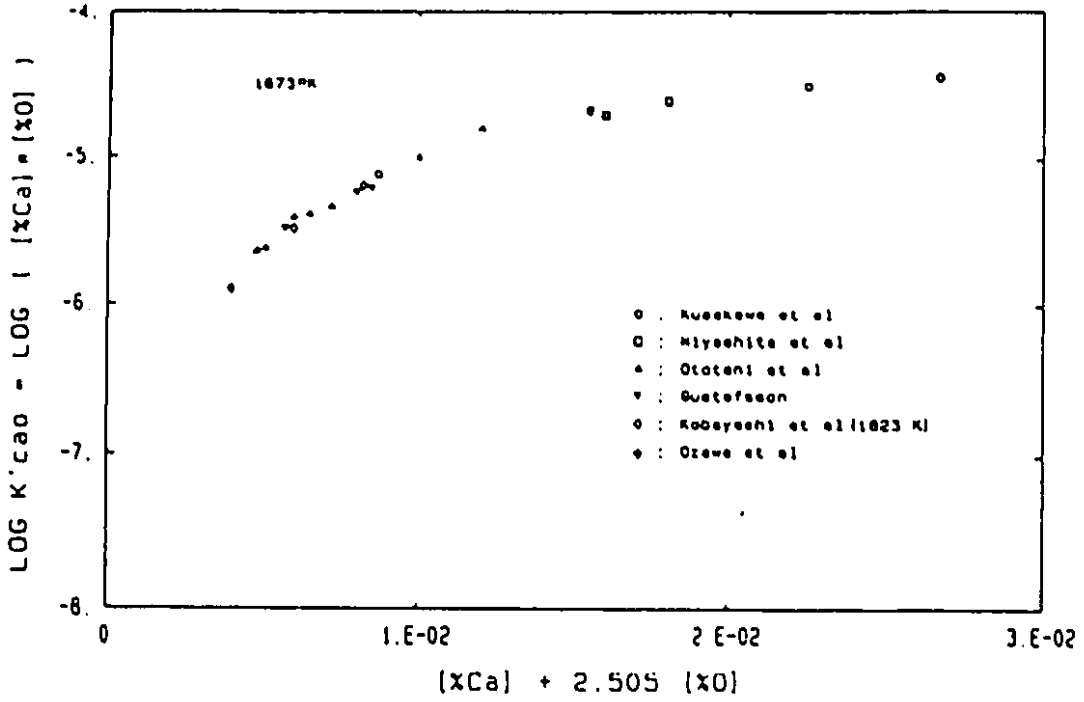

Figure 2.9 Concentration dependence of solubility product in Fe-Ca-O system [2,54,57-59].

is why there are very unrealistically large negative values of e_{Ca}^{O} and e_{O}^{Ca} from most of the experiments.

From Table 2.7, it shows that the activity solubility products, $h_{Ca}h_{O}$ and $h_{Ca}h_{S}$, obtained from the experiments are much higher than that expected from the thermodynamic calculations. As suggested by Kay and Subramanian [6], this discrepancy might come from some errors in the generally established free energy of formation of CaO, as discussed earlier. Their data after some correction on ΔG^{0}, is much close to the actual experimental results. So that their values ($K_{CaO}=7*10^{-9}$ and $K_{CaS}=1.96*10^{-7}$ at 1600 ^{0}C) [6] are used for the present research.

2.4.3 Desulphurization

The calcium desulphurization reaction can be written by:

$$CaS_{(s)} = \underline{Ca} + \underline{S} \qquad (2.26)$$

Assuming for pure CaS formed, i.e. $a_{CaS} = 1$, the equilibrium constant, K_{CaS}, for equation (2.26) can be given by:

$$\log K_{CaS} = \log h_{Ca} + \log h_{S} \qquad (2.27)$$

Similar to the deoxidation, there are two ways to obtain K_{CaS}: Thermodynamic calculation and experimental measurement.

Thermodynamic Calculation:

The basic process of thermodynamic calculation of K_{CaS} is similar to that of calculating K_{CaO}. If one combines the reactions of calcium deoxidation, calcium and sulfur dissolution, with the equation of oxide and sulphide in equilibrium with their gas phases (Equ. 2 in Table 2.6), one would obtain the calcium desulphurization equation 2.26. the detailed calculation and results are shown in Tables 2.6 and 2.7.

Experimental Measurements

Similarly, introducing K'_{CaS} as the apparent solubility of sulfide based on the weight percent concentrations:

$$K'_{CaS} = [\%Ca] * [\%S] \qquad (2.28)$$

The same principle as in deoxidation can be used to evaluate K_{CaS} and e_S^{Ca} by the following equation, if a linear relationship exists.

$$\log K'_{CaS} = \log K_{CaS} - e_S^{Ca} * ([\%Ca] + 1.25[\%S]) \qquad (2.29)$$

According to most data, K_{CaS} is usually one magnitude smaller than K_{CaO}, which means at normal experimental conditions (h_s and h_o are in the same order of magnitude) deoxidation always precedes desulphurization by calcium. In other words, it is quite difficult to study reaction (2.26) alone and to obtain the K_{CaS} and e_S^{Ca} values from equation (2.29). The combination of equations (2.19)-(2.25) and (2.27)-(2.29) will result in the following equations after rearranging:

$$logK'_{CaS}+2.5e_O^{Ca}*[\%O]-logK_{CaS}-e_S^{Ca}([\%Ca]+1.25[\%S]) \quad (2.30)$$

$$logK'_{CaO}+1.25e_S^{Ca}*[\%S]-logK_{CaO}-e_O^{Ca}([\%Ca]+2.5[\%O]) \quad (2.31)$$

Since e_S^{Ca} and e_O^{Ca} are included in the left side of the equations, an iteration procedure has to be applied, if two graphs show the linear relationship. This method was used by Gustafsson [51] and his results are given in Table 2.7.

The second way to determine K_{CaS} is called indirect determination method. As mentioned in the literature [52] equilibrium between liquid metal and the crucible produces a desulphurization of the bath by lime refractory. By combining equations 2.19 and 2.27, one would have:

$$K_{CaS} = K_{CaO}\frac{h_s}{h_o} \quad (2.32)$$

At 1600 ^{0}C, the equilibrium ratio of h_s/h_o was found to be 19, which is also the ratio between K_{CaS} and K_{CaO}. K_{CaS} fully depends on the accuracy of K_{CaO} value and the extent of bath contamination by other elements. Their results are also shown in Table 2.7.

2.4.4 Dephosphorization and Removal of Other Impurities

Dephosphorization is one of the most important steps in the pretreatment of hot metal and the production of ferroalloys and stainless steel, and, in the latter case, dephosphorization by conventional oxidation refining is impossible because of the preferred oxidation of the more-reactive alloying elements present. Investigations conducted over the last decade have shown that effective dephosphorization can be achieved by adding metallic calcium or calcium compounds to the melt [54] to produce Ca_3P_2 as the main product of dephosphorization.

Besides Phosphorus, Ca and other alkaline earth metals (X = Ca, Ba, Mg) can also react with other elements of Va group of periodical classification (Y = N, P, As, Sb, Bi) to form X_3Y_2 compounds:

$$X_3Y_{2(S)} = 3X + 2Y \qquad (2.33)$$

$$K_{X_3Y_2} = \frac{a_X^3 . a_Y^2}{a_{X_3Y_2}} \qquad (2.34)$$

Experimental investigations [60] show that calcium additions in steel remove these elements (see Figure 2.10). However, the amounts of calcium necessary are about ten times higher than those used for oxide or sulfide shape control. Table 2.8 shows the solubility products of calcium phosphorite and nitride, and Figure 2.11 shows their stabilities relative to calcium oxide and sulphide. It can be seen that they are less stable than oxide and sulphide.

TABLE 2.8

SOLUBILITY PRODUCTS OF Ca PHOSPHORITE AND NITRIDE

$K_{Ca_3P_2}$	e_P^{Ca}	$K_{Ca_3N_2}$	e_N^{Ca}	T (°C)	Ref.
$7.0*10^{-14}$	-3.1	-	-	1600	Han [56]
$1.4*10^{-11}$	-	$1.2*10^{-11}$	-	1600	Nadif [54]

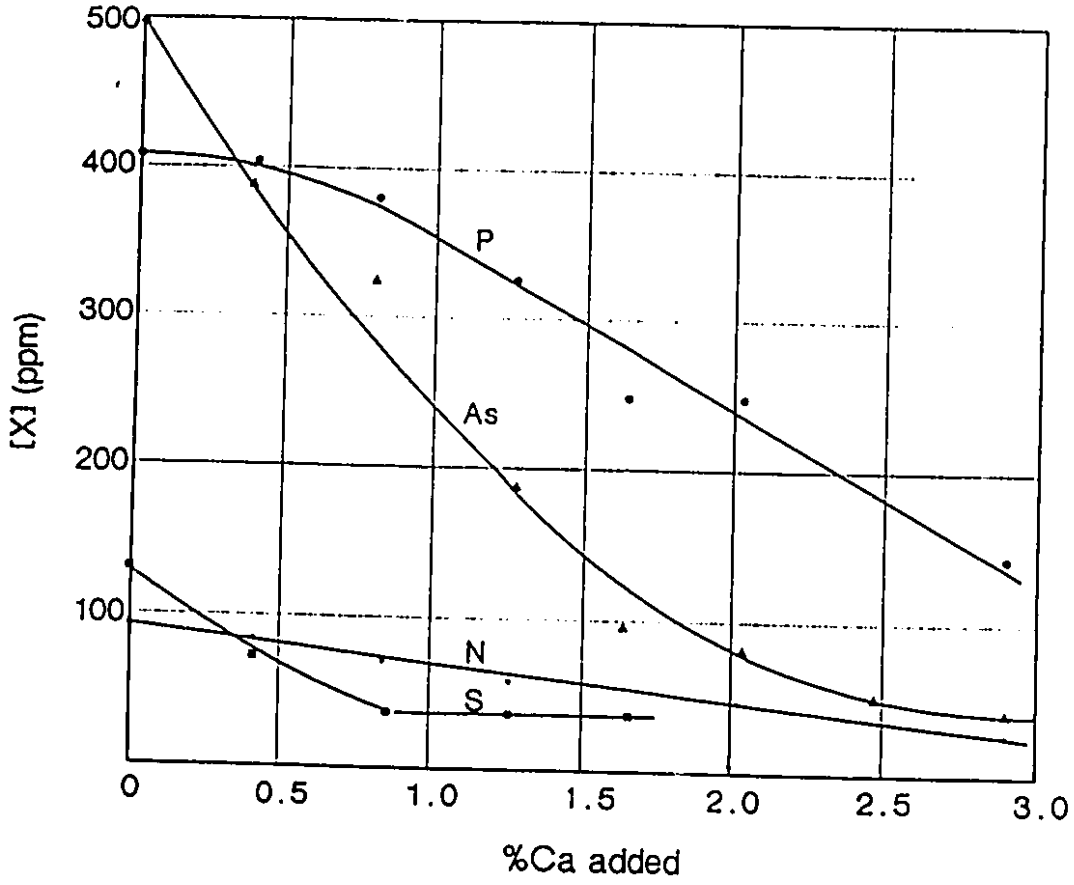

Figure 2.10 Evolution of non metallic elements in Si-killed steel during Ca treatment [54]

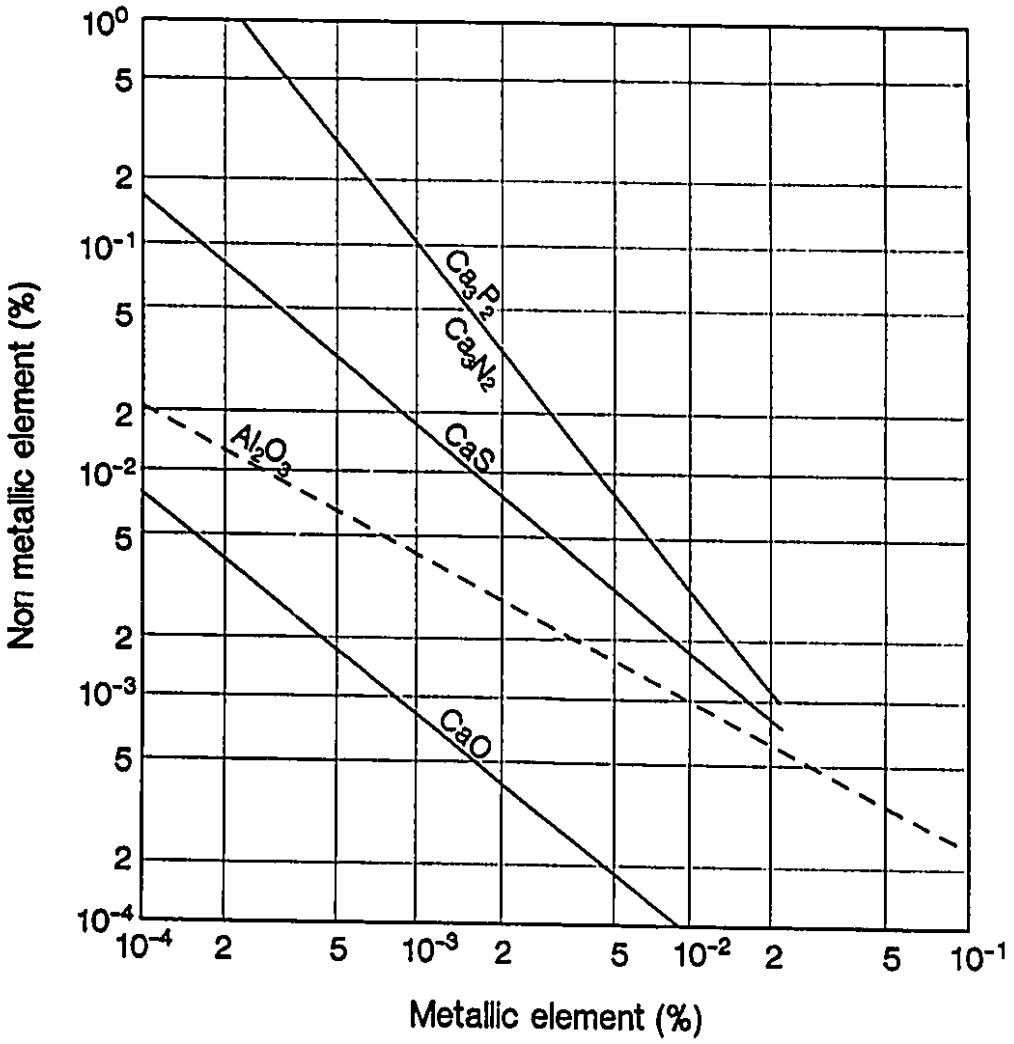

Figure 2.11 Relative stability of various Ca Compounds in liquid steel at 1600 °C [54]

2.5 INCLUSION MODIFICATION BY CALCIUM

Calcium-based additions are made to steels not only for deoxidation and desulphurization, but also for the control of inclusion composition and morphology.

Calcium converts the solid alumina inclusions into liquid calcium-aluminate inclusions [3,6,53]. As a result, not only will the volume fraction of remaining inclusions be decreased, but also the nozzle clogging, due to the precipitation of solid alumina inclusions during continuous casting, will be prevented [61]. Calcium can also modify MnS into (Ca,Mn)S [62-66]. However with the addition of too much calcium, solid (Ca,Mn)S may form and contribute to unnecessary nozzle clogging in the tundish [67-69].

2.5.1 Oxide Inclusion Modification

Al_2O_3 inclusions will change to various kinds of calcium-aluminate during calcium addition to steel. The different phases of calcium-aluminate are shown in the $CaO-Al_2O_3$ binary phase diagram in figure 2.12 [70]. The activities of CaO and Al_2O_3 at each phase are given in Figure 2.13 [53].

The Al_2O_3 inclusion modification reaction by calcium can be written by:

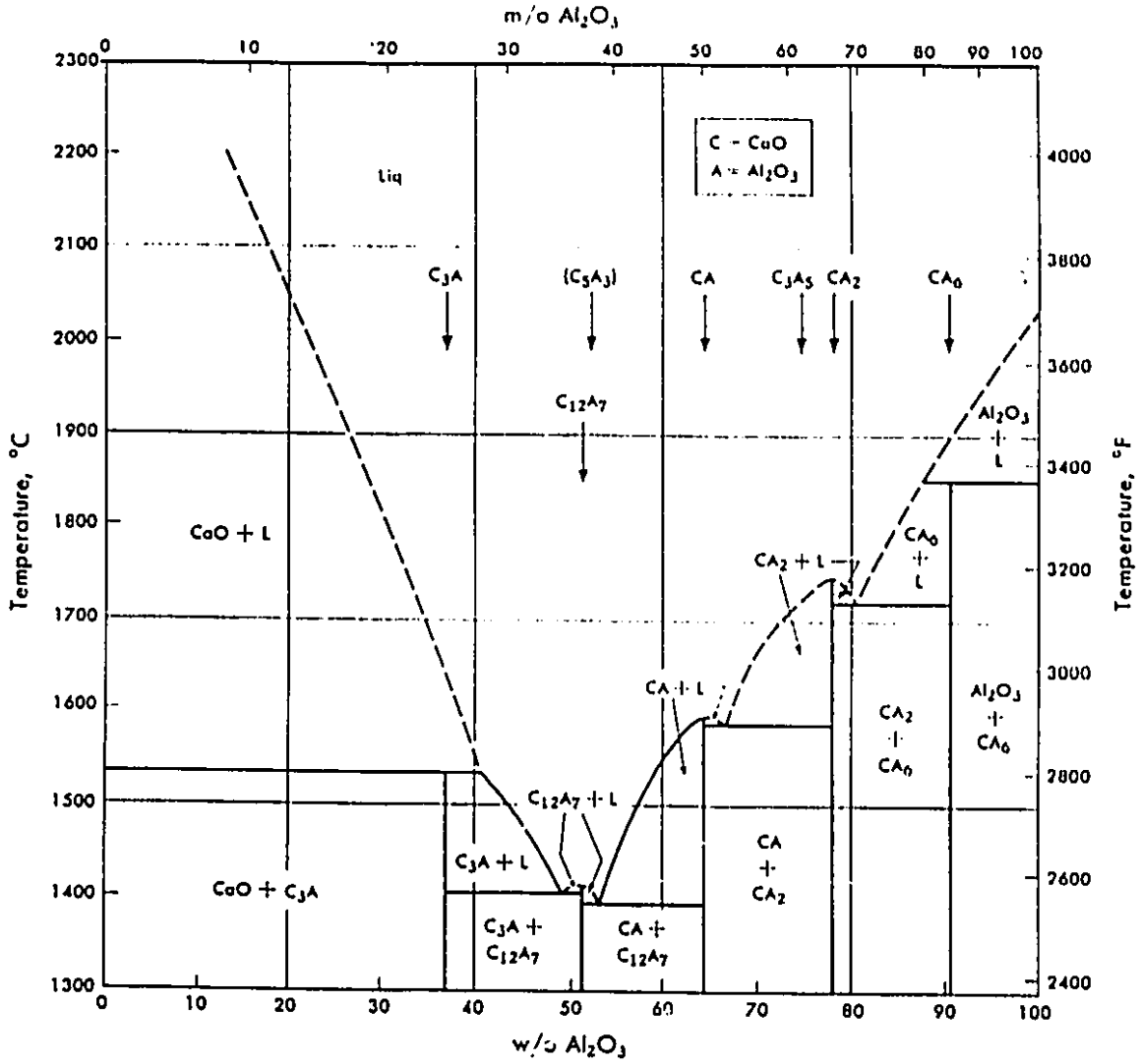

Figure 2.12 The $CaO-Al_2O_3$ system [53]

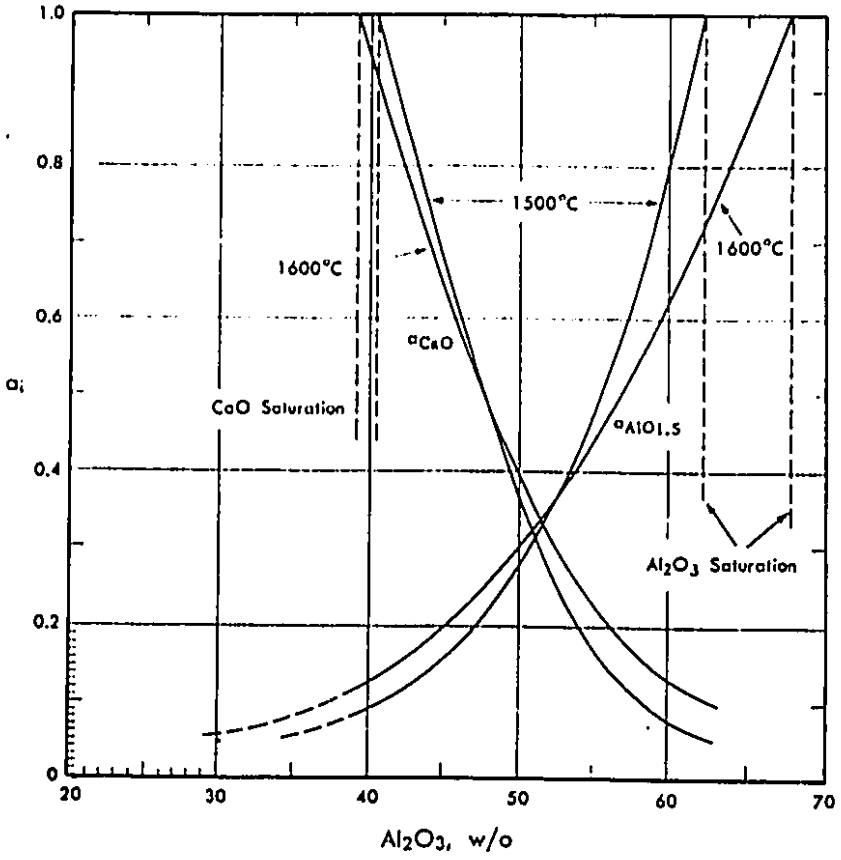

Standard states
CaO: Pure solid CaO in equilibrium with melt.
Al_2O_3: Pure solid Al_2O_3 in equilibrium with melt.

Figure 2.13 CaO and Al_2O_3 activities at 1500 to 1600 °C [53]

$$Al_2O_{3(s)} = 2\underline{Al} + 3\underline{O} \qquad (2.35)$$

combining with equation (2.18), we would have:

$$\underline{Ca} + \frac{1}{3}(Al_2O_3) = (CaO) + \frac{2}{3}\underline{Al} \qquad (2.36)$$

where the underlined symbols denote species dissolved in the steel, and the species within the parentheses are the components of the calcium aluminate. Then the equilibrium constant for the above equation is:

$$K = \frac{a_{CaO}}{a_{Al_2O_3}^{1/3}} \frac{h_{Al}^{2/3}}{h_{Ca}} \qquad (2.37)$$

The composition of the $CaO{\cdot}xAl_2O_3$ (CA_x in short) depends on the bath chemistry. As the ratio of the activity of calcium to the activity of aluminum increases, the equilibrium deoxidation product will shift from alumina to calcia. Figure 2.14 shows the change in the composition of the inner and outer parts of the inclusions, which formed after a Ca addition [71]. With increasing Ca amount the MnS and Al_2O_3 clusters are reduced and replaced by calcium aluminates, which have a core consisting of $CaO{\cdot}2Al_2O_3$, $3CaO{\cdot}5Al_2O_3$ and an outer layer of (Ca,Mn)S. If the residual Ca in the steel rises above 30 ppm, the MnS portion is replaced by CaS and the core consists of the CaO rich $CaO{\cdot}Al_2O_3$ compound.

Hilty and Farrell [72] also found that the CaO content of CA_x increases with increases of the total calcium in the melt.

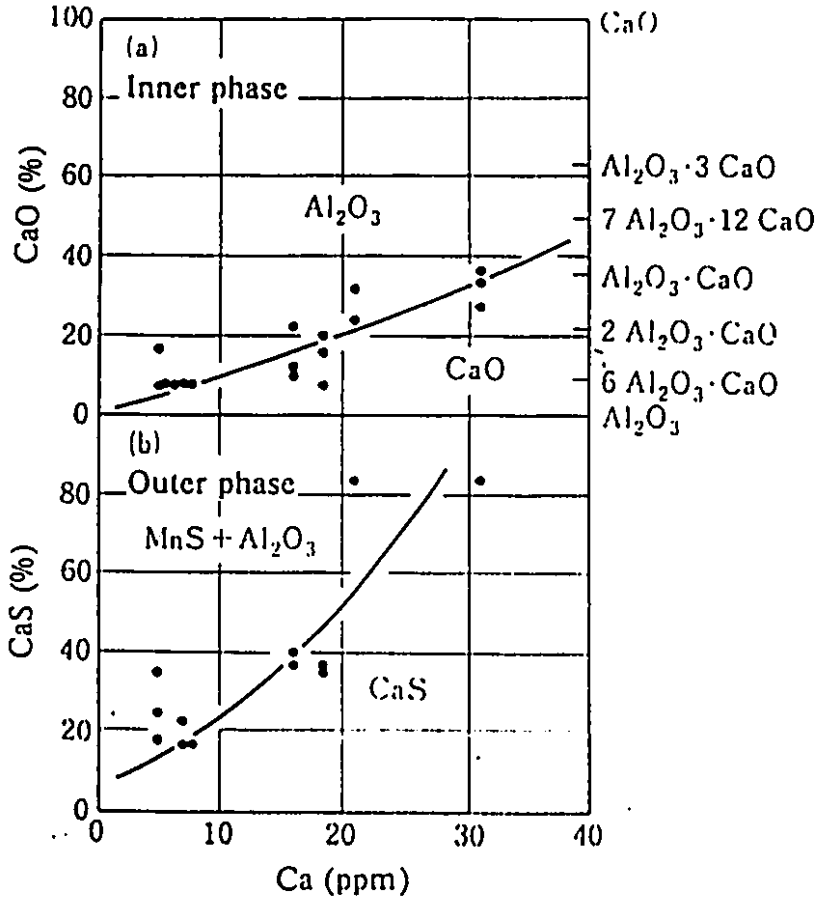

Figure 2.14 Effect of Ca content in the steel on the composition of non-metallic inclusions [71]

However, they found that high sulfur retarded the speed of this transformation. For example, at 50 ppm of Ca, calcium aluminate consists of $CaO.Al_2O_3$ at 0.005% S, and only of $CaO.2Al_2O_3$ at 0.015%S. Recently, Weh et al. [73-74] found that both high Al and S contents retarded the modification of aluminate inclusions by calcium.

The control of the composition of precipitation inclusions in ladle treatment processes has been the subject of several thermodynamic investigations [3,6,53]. Kay and Subramanian [6] developed phase stability diagrams to explain the relative behaviour of calcium in the ladle treatment of steel, while Faulring and Ramalingam [3] constructed the precipitation diagram for the Fe-O-Al-Ca system using the thermodynamic calculation results from Table 2.7. Some of the calculations from both groups [3,6] are shown in Table 2.8.

TABLE 2.9

BULK CONTENTS IN EQUILIBRIUM WITH DIFFERENT CA_x PHASES [3,6].

h_{Al} = 0.05, T = 1550 °C

CA_x phases	a_{CaO}		a_{Al2O3}		h_s		h_o		h_{Ca}	
	Kay & Subramanian	Faulring & Ramalingam	Kay & Subramanian	Faulring & Ramalingam	Kay & Subramanian	Faulring & Ramalingam	Kay & Subramanian	Faulring & Ramalingam	Kay & Subramanian	Faulring & Ramalingam
Al_2O_3-CA_6	0.003	0.018	1.000	1.00	3.85	-	$2.81*10^{-4}$	$1.57*10^{-4}$	$1.77*10^{-8}$	$3.83*10^{-9}$
CA_6-CA_2	0.043	0.048	0.631	0.83	$2.09*10^{-1}$	-	$2.41*10^{-4}$	$1.39*10^{-4}$	$3.27*10^{-7}$	$1.14*10^{-8}$
CA_2-CA	0.100	0.068	0.414	0.71	$7.80*10^{-2}$	-	$2.09*10^{-4}$	$1.24*10^{-4}$	$8.72*10^{-7}$	$1.81*10^{-8}$
CA-$C_{12}A_7$	0.150	0.07	0.275	0.70	$4.53*10^{-2}$	-	$1.83*10^{-4}$	$1.23*10^{-4}$	$1.50*10^{-6}$	$1.85*10^{-8}$
$C_{12}A_7$-C_3A	1.000	1.00	0.017	0.02	$2.69*10^{-3}$	-	$7.21*10^{-5}$	$1.15*10^{-5}$	$2.53*10^{-5}$	$2.86*10^{-6}$

The major difficulty encountered by these authors was that the thermodynamic predictions made for the systems involving calcium did not correlate well with actual industrial practice. For example, from Table 2.8, less than 1 ppm calcium in the melt will modify aluminate to liquid calcium aluminate, if the system is in equilibrium. However, solid aluminate inclusions were found in the experiments[61,75-76], even though the calcium content was up to 100 ppm in the bulk. This discrepancy may come from the uncertainty in measuring the dissolved calcium in the melt. There is also an uncertainty as to whether the system is in equilibrium during continuous calcium addition to the melt. Thus a kinetic study of the process is very important to determine how far away the system from the equilibrium.

2.5.2 Sulfide Inclusion Modification

Calcium treatment of steel is widely practised to modify both oxide and sulphide inclusions. The transformation of manganese sulphide by calcium to CaS is an important factor contributing to surface quality, machinability, and nozzle clogging during continuous casting.

Sulphide inclusions with varying amounts of Mn and Ca in solid solution have been observed in different grades of calcium treated steel [62-66]. Church et al.[77] were among the

early ones to find (Ca,Mn)S inclusions in vacuum-degassed, bearing steel. Salter and Pickering [78] reported an extensive solid solubility range in the ternary system: MnS, CaS, and FeS, containing up to 19% MnS and 4% FeS in CaS. A continuous series of solid solution was not found, so they concluded that there is a miscibility gap in the system. Kiessling and Westman [79] observed the approximate extent of the miscibility gap. This gap was also observed by Skinner and Luce [80] in solid solutions of (Ca,Mg,Mn,Fe)S. It was Leung and van Vlack [81] who constructed a complete phase diagram for the CaS-MnS binary system (Figure 2.15), among other chalcogenide systems. From Figure 2.15, it is seen that sulfide is liquid from pure MnS up to 70% CaS in (Ca,Mn)S, while it becomes solid when CaS is over 70%, at the steelmaking temperature of 1600 °C.

The overall sulfide reaction involving calcium can be written as follows:

$$\underline{Ca} + \underline{Mn} + \underline{S} = (Ca,Mn)S \qquad (2.38)$$

The composition of (Ca,Mn)S is a function of the equilibrium concentrations of S, Ca and Mn in the melt. (Ca,Mn)S can form directly in the melt or form during solidification. The (Ca,Mn)S inclusions may exist as a single phase inclusion, however they usually occur surrounding calcium aluminate inclusions.

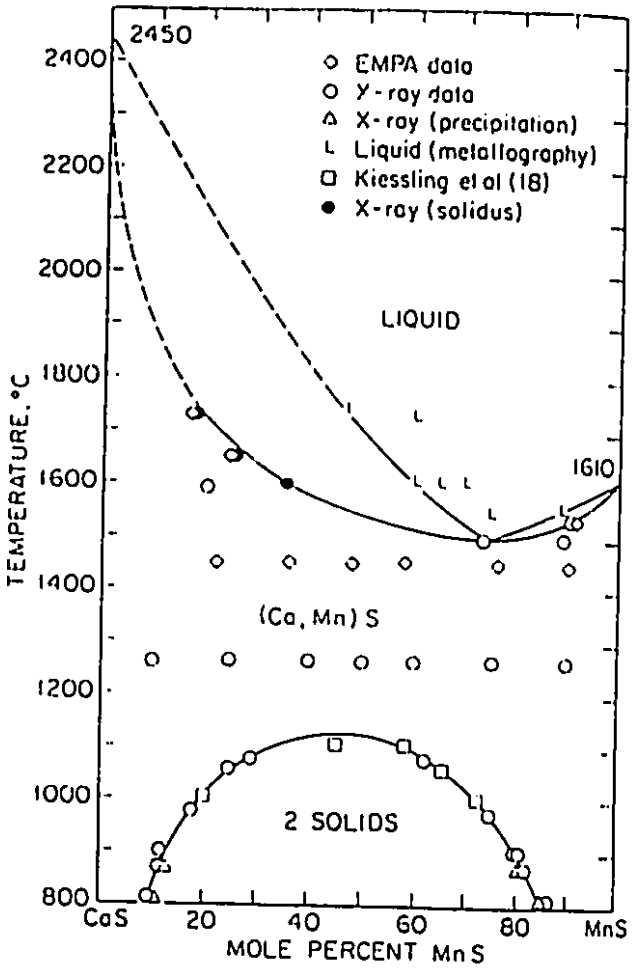

Figure 2.15 The CaS-MnS system [81]

However, the activities of CaS and MnS as the function of (Ca,Mn)S composition are still unknown. Without these basic thermodynamic data, the study on CaS-MnS system would be impossible or incomplete. The mechanism of sulphide modification or shape control by calcium is still very unclear. Following are some various proposals for the (Ca,Mn)S formation [82-85].

1) Sulfur is absorbed by the CA_x compounds, which form after Ca oxidation and have a strong desulphurization power. During solidification, the $CaO-Al_2O_3$ inclusions act as nuclei for the crystallization of the dissolved Ca and S either on the particles [82].
2) Initially single phase $CaO-Al_2O_3$-CaS compounds with a homogeneous CaS content exist in the melt. During solidification the CaS precipitates because of the reduced solubility in $CaO-Al_2O_3$, whereby the ring shaped layer is attributed to the effects of the surface tension [83].
3) Agglomeration of $CaO-Al_2O_3$ and CaS particles by diffusion and collision [84].
4) In the case of a high Ca addition to the steel, the CaO of the core and the CaS content of the outer layer may increase to such an extent that the particles transform into single phase $CaO.Al_2O_3$-CaS

compounds [85].

Recently there was a confirmation [86] of the precipitation of the complex sulfides on calcium aluminates in a Ca-doped steel. Reaction between oxides and sulfides, and recrystallization of oxides were also studied [87] during solidification or heat treatments prior to the hot rolling. However, the actual mechanism of sulfide modification and shape control by calcium still needs to be clarified.

2.5.3 Influence of Inclusion Composition on Nozzle clogging

The clogging of the tundish nozzle during continuous casting is one of the big problems in modern steelmaking. One method to avoid nozzle clogging is to ensure inclusions with melting points lower than the steel melt temperature by changing their composition through a suitable selection of the deoxidizer materials. For instance if Ca is added to an Al deoxidized steel, liquid calcium aluminates are formed. It was reported [88] that by controlling their composition nozzle clogging could be prevented effectively.

Figure 2.16 shows the amount of steel, which could be cast prior to nozzle clogging, as a function of the Ca/Al ratio [88] in pilot-scale tests. Depending on the composition of the deoxidation, the ingot weights exhibit drastic changes.

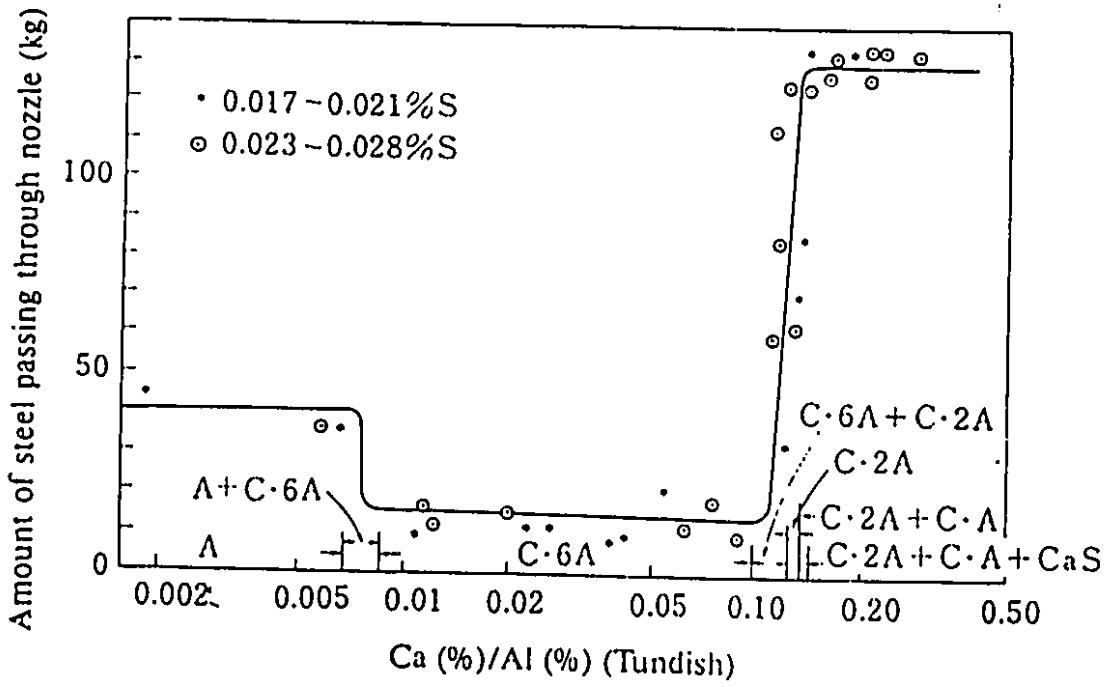

Figure 2.16 Effect of Ca on the flow of an Al-killed steel melt through the tundish nozzle [88]

For instance, in the case of Ca/Al < 0.115, the initial melt velocity was very high, but due to the accumulation of $CaO \cdot 6Al_2O_3$ in the nozzle, the final ingot weight was rather small. As the solidification temperatures of Al_2O_3 and $CaO \cdot 6Al_2O_3$ are 2,050 °C and 1,850 °C respectively, these solid particles can attach themselves to the nozzle wall and thereby cause complete clogging of the nozzle. For Ca/Al between 0.1 and 0.14 the nozzle becomes increasingly less obstructed, ensuring a freer flow of the steel melt from the tundish. The inclusions precipitated at the nozzle wall consisted of complex $CaO \cdot 6Al_2O_3$ plus $CaO \cdot 2Al_2O_3$ compounds and nozzle clogging diminished with decreasing amounts of $CaO \cdot 6Al_2O_3$. When the Ca/Al ratio was increased above 0.14, the major part of the inclusions consisted of low melting point $CaO \cdot 2Al_2O_3$ and $CaO \cdot Al_2O_3$. As a result, nozzle clogging was prevented and the casting time decreased correspondingly as more molten steel went through the nozzle.

However, it was found [89] that in iron containing aluminum, the calcium concentration can be too high, so that solid sulfide may form. In iron containing silicon without aluminum, with similar calcium contents, solid calcium silicates and calcium sulfides may form. As a result, the castibility of steel may actually decrease by too much calcium addition.

Therefore, it is necessary to control the amount of calcium addition for the specific melt compositions to completely convert solid Al_2O_3 into liquid calcium-aluminate, and to avoid the formation of solid calcium sulfide inclusions, in order to ensure the steady castibility of steel.

2.6 FLUID DYNAMICS

2.6.1 Calcium Gas-liquid Interfacial Area

For aluminum wire injection, Mucciardi et al [43] have obtained an empirical equation to predict the wire penetration depth in the melt.

$$d_p = \frac{145.4 * d_w^{0.86} * v^{0.52}}{SH^{0.34}} \qquad (2.39)$$

where d_p is the wire penetration depth in the melt, d_w is the diameter of the wire, v is the wire feeding velocity, and SH is the superheat of the molten steel. It can be seen that the wire penetration depth is approximately proportional to the square root of the wire feeding rate.

There is no empirical equation available to estimate the penetration depth for calcium wire injection into molten

steel. However, an accelerometer was used [44] to "view" the violent calcium gas-liquid interactions in molten steel. Both calcium and aluminum wires exhibited similar kind of oscillation during their injection. This periodic oscillation was found to be caused by the heat transfer between the wire and the surrounding hot melt. At 1600 ^{0}C, feeding 0.005-m diameter steel-clad Ca wire at speed of 0.01 m/s, there was lack of bubbling and deep penetration. However, at the same injection rate, the calcium wire, whose surface was coated with a thermal resistance, was found to penetrate the melt deeper. Ca vapour bubbles were produced at a relatively constant rate and did not resurface. Since both aluminum and calcium are exothermal on their reaction with the melt, the above empirical equation can be used to roughly estimate the calcium wire penetration depth.

2.6.2 Fluid Dynamics of Inclusions in the Melt

Inclusion movement in the induction furnace and other metallurgical vessels has been the subject of much research [90-96]. Most of the studies show that the concentration of inclusions (or total oxygen for oxides) decreases exponentially with time down to a constant plateau value. This is found for various kinds of agitation: electromagnetic, [90-92] mechanical [93] and gas purging [94].

The physical significance of the first order removal of inclusions was suggested [90] as the transport of inclusions across the boundary layer at the crucible wall or at the slag-metal interface. For oxide inclusions, this exponential expression may be interpreted as the removal rate of total oxygen content with time [90].

$$\frac{dC_0}{dt} = - k_{rm} z_{rm} C_0 \qquad (2.40)$$

or

$$C_0 = C_0^0 \exp(-k_{rm} z_{rm} t) \qquad (2.41)$$

where C_0 is the total oxygen (or oxide inclusion volume) at time, t, C_0^0 is the initial total oxygen, and the inclusion removal rate constant, $k_{rm}z_{rm}$, is a function of inclusion composition and size, the stirring intensity and the density of steel. Engh et al [90] obtained an empirical expression of $k_{rm}z_{rm}$ for the inclusions with a radius, r, in the induction furnace.

$$k_{rm} z_{rm} = \frac{0.29 * 10^{-2} \epsilon r^2}{\nu^2 \rho} \qquad (2.42)$$

where ϵ is the stirring power per unit volume of the melt, ϱ is the steel density and ν is the kinetic viscosity. $k_{rm}z_{rm}$ may vary with specific experimental conditions, the exponential expression for inclusion removal is still valid.

2.7 MASS TRANSFER WITH GAS-LIQUID-SOLID REACTIONS

Mass transfer with gas-liquid-solid reactions has been well-studied in chemical Engineering [97-101] . In general, there are two main distinct types of gas-liquid-solid reactors, in terms of the gas absorption and reaction in the heterogenous system. One type of reactors has no or negligible reaction(s) in the gas-liquid film, and its gas absorption process is called physical absorption. The other kind of reactors accompanies by the reaction between the gaseous, A, and a liquid reagent, B, in the gas-liquid film, and its absorption process is called chemical absorption. The concentration profiles for both physical and chemical absorptions in the three-phase reactors are schematically shown [99] in Figure 2.17.

If the reaction involves a gaseous, A, and a liquid reactant, B, to form the product, C:

$$A_{(g)} + B_{(l)} = C \qquad (2.43)$$

For physical absorption, this reaction only occurs at the solid interfaces as shown in Figure 2.17 (above), while in chemical absorption case, the reaction can take place in gas-liquid interface, within the gas-liquid film and on the solid interfaces as seen in Figure 2.17 (below). The difference is that chemical absorption results in the enhancement of the absorption of the gaseous A.

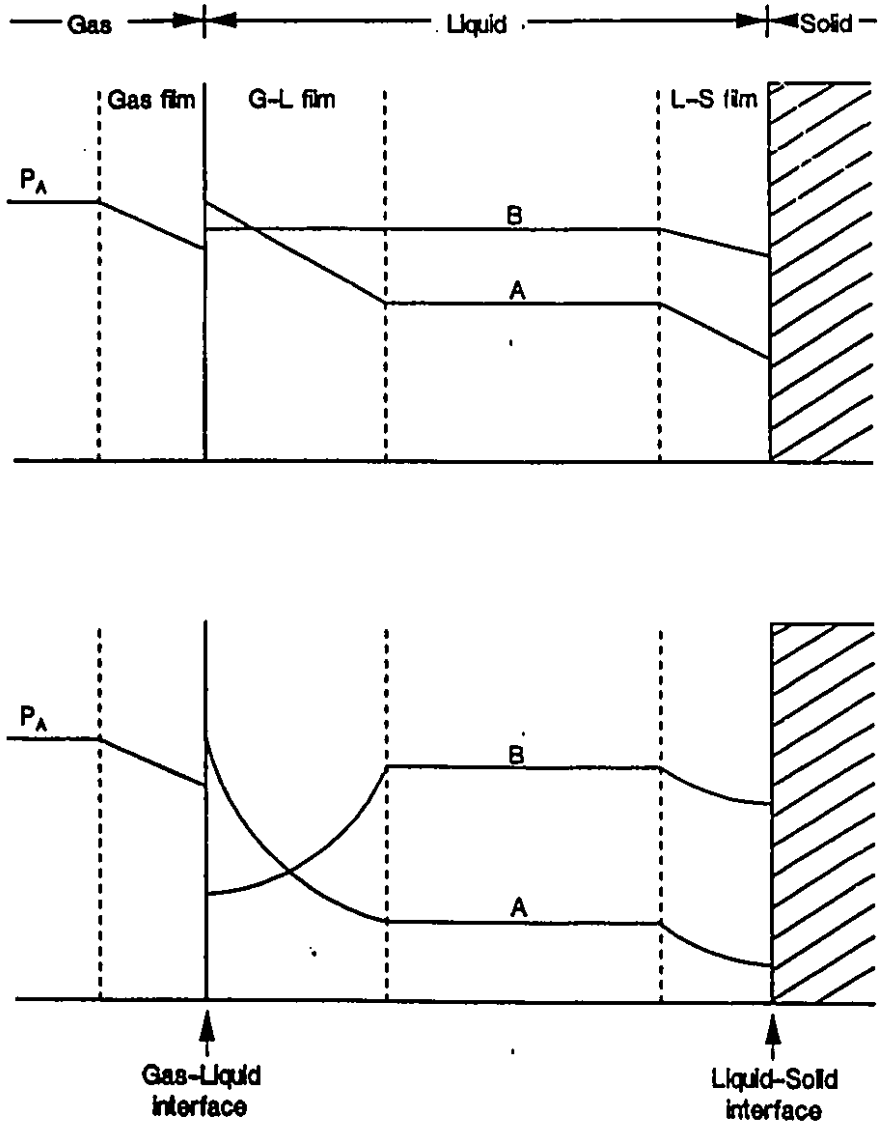

Figure 2.17 Concentration profiles of physical absorption (TOP) and chemical absorption (BOTTOM) in gas-liquid-solid reactors [99].

Gas-liquid, liquid-solid and liquid-liquid mass transfer are considered separately below.

2.7.1 Gas-Liquid Mass Transfer

2.7.1.1 Physical Absorption

The overall processes of dissolution, adsorption at the heterogeneous interfaces or evaporation are usually considered to consist of several consecutive steps in physical absorption or evaporation:

1. Transport through the gas or liquid boundary
2. Adsorption on the gas-liquid surface
3. Transport through the liquid or gas boundary

Each of these steps is considered separately in the following review for the case of calcium dissolution and evaporation.

If we consider first physical absorption, whereby gas dissolves in the liquid without reacting or dissociating, the basic representation of the solute gas is based upon the concept of additivity of a gas-phase resistance and a liquid-phase resistance, assuming that the interfacial resistance can be neglected [100]. The rate of absorption is then:

$$N = N'z = \frac{k_G z}{RT}(P-P_i) = k_L z(C_A^*-C_A) \qquad (2.44)$$

where z is the interfacial area between gas and liquid per unit volume of the system, N' is the average rate of transfer of gas per unit area, p and p_i are the partial pressures of soluble gas in the bulk gas and at the interface, C_A^* is the concentration of dissolved gas corresponding to equilibrium with p_i, and C_A is the average concentration of dissolved gas in the bulk liquid. k_G is the gas side mass transfer coefficient and k_L is the physical liquid side mass transfer coefficient that applies in the absence of chemical reaction. When a carrier gas (for example argon gas) is used in calcium powder injection, the mass transfer resistance of both liquid phase and gas phase has to be considered.

Liquid phase control

The mass transfer rate through the liquid boundary is:

$$N = k_L z(C_A^*-C_A) \qquad (2.45)$$

The mass transfer coefficient, k_L, depends on the character of the gas formed including its geometry and velocity [102].

A) Single Bubbles

For spherical cap bubbles, Higbie's penetration theory [103] can be applied to obtain the approximate mass transfer coefficient [104-105]:

$$k_L = 2\left(\frac{D_L}{\pi\,\theta}\right)^2 \qquad (2.46)$$

where D_L is the diffusivity in the liquid, and the "lifetime" or the exposure time is suggested [104] as:

$$\theta = \frac{\textit{Length of the bubble spherical surface}}{\textit{mean velocity over the bubble}} = 0.0716\, d_E^{1/2} \qquad (2.47)$$

d_E is the equivalent bubble diameter. Thus the mass transfer coefficient is:

$$k_L = 0.716\, g^{1/4}\, D_L^{1/2}\, d_E^{-1/4} \qquad (2.48)$$

By assuming potential flow over the front of or upper surface of the bubble, the theoretical value of the mass transfer coefficient for the front of the bubble has been well established to be [106-108]:

$$k_{Lf} = 0.951\, g^{1/4}\, D_L^{1/2}\, d_E^{-1/4} \qquad (2.49)$$

Transfer from the rear of the bubble is not as well understood. Weber [108] used penetration theory to relate the mean mass transfer rate from the rear:

$$k_{Lr} = 0.29\ g^{1/4}\ D_L^{1/2}\ d_E^{-1/4} \qquad (2.50)$$

B) Gas cavity or dimple

Mass transfer at the gas-liquid interface in the cavity formed by the jet was studied by Wakelin [109], who obtained the following equation for the local mass transfer coefficient based on the surface renewal theory:

$$k_{d,loc} = \left(\frac{2D_{O\text{-}Ag}U_r r}{\pi}\right)^{1/2}\left(\frac{1}{r_1}\right) \qquad (2.51)$$

where r = radial distance from the jet axis in the liquid

U_r = radial liquid velocity at the surface

$D_{O\text{-}Ag}$ = diffusivity of oxygen in silver, $9*10^{-9}$ m^2 sec^{-1}

r_1 = radius of depression

His model applied quite well to the mass transfer between an impinging oxygen get and the liquid silver at 1000 ^{0}C [110].

Adsorption

It has been known that sulphur, oxygen, selenium and tellurium are very surface active elements in liquid iron[111]. The fractional surface coverage, θ_i, is described by Langmuir's Adsorption Isotherm [112]:

$$K_i = \frac{\theta_i}{(1-\theta_i)z_i} \qquad (2.52)$$

It has been shown that the surface-active elements hinder dissolution of nitrogen in proportion to the surface coverage θ_i, at the high surface coverage in inductively-stirred crucibles [112].

Gas phase control

The mass transfer rate through the gas phase boundary is:

$$N' = k_G(C - C_G^*) \qquad (2.53)$$

where C_G and C_G^* are the bulk in the gas phase and surface contents.

Mixed control

For the case of gas and liquid phase mixed control [102, 113], the overall transfer rate is given by:

$$N' = k_L \left(1+\frac{K_H\, k_L}{k_G}\right)\left(C_L^G - C_L\right) = k_{ovl}\left(C_L^G - C_L\right) \qquad (2.54)$$

where k_{ovl} is the overall or the mixed mass transfer coefficient.

The concentration in the gas phase is converted to the equivalent liquid concentration C_L^G by:

$$K_H = \frac{C_L}{C_G} \qquad (2.55)$$

From the previous survey on the calcium solubility, 0.024% Ca (C_L=21.6 mol/m^3) in steel is in equilibrium with 1 atm of pure calcium gas. Then the equivalent liquid concentration C_L^G is 6.5 mol/m^3, according to Equation 2.6. So that K_H is calculated to be 3.32.

But there have been no experimental investigations to determine a gas phase mass transfer coefficient [114]. However, the coefficient can be estimated by assuming that the circulation within the bubble is the same as the liquid-phase circulation [115]:

$$\frac{k_L}{k_G} = \left(\frac{D_L}{D_G}\right)^{1/2} \qquad (2.56)$$

Using estimates of $1*10^{-4}$ m^2/s for the diffusivity of calcium in argon from the Chapman-Enskog Theory [116] and $3*10^{-9}$ m^2/s for the diffusivity of calcium in liquid steel (see Appendix B), the ratio of mass transfer coefficients is estimated as:

$$\frac{k_G}{k_L} = 547.33 \qquad (2.57)$$

After inputting those values in equation 2.54, the overall or mixed mass transfer coefficient is then:

$$k_{ovl} = \left(1 + \frac{3.32}{547}.33\right)^{-1} k_L \approx k_L \qquad (2.58)$$

It can be seen that the overall transfer step is mainly controlled in the liquid phase.

2.7.1.2 Calcium Vaporization Kinetics

Liquid phase control

In the induction coil, the flow is usually in the shape of a single toroid, up-welling at the center and going down at

the sides [117-119]. The vaporation rate of a dissolved element (e.g. Mg and Ca) through the free-surface of the melt can be expressed as:

$$N' = k_{evp}([\%Ca] - [\%Ca]^*) \qquad (2.59)$$

[%Ca] and [%Ca]* are respectively the bulk and surface contents. The mass transfer coefficient k_{evp} depends on the rate of bath surface renewal. Machlin [120] applied Higbie's [103] penetration theory and assumed the "lifetime" θ of a surface element is equal to the average distance from the center of the melt to the edge of the crucible, divided by the average velocity <U> of the melt at the surface:

$$k_{evp} = 2\left(\frac{D_L}{\pi\,\theta}\right)^{1/2} = 2\left(\frac{2\,D_L\,\langle U\rangle}{\pi\,R_c}\right)^{1/2} \qquad (2.60)$$

The surface velocity can either be measured directly or calculated by solving the turbulent electromagnetically driven fluid flow equations [117-119].

Gas phase control

The overall transfer rate expression is similar to equation (2.54).

$$N' = k_{evp}\left(1 + \frac{k_H\, k_{evp}}{k_{G'}}\right)\left(C_L - C_L^G\right) - k_{ovl}\left(C_L - C_L^G\right) \qquad (2.61)$$

where $k_{G'}$ is the calcium mass transfer coefficient in the argon atmosphere. The calcium concentration in the argon phase can be regarded as zero, i.e. $C_L^G \approx 0$. Applying the same expressions for k_H and the ratio of $k_L/k_{G'}$ from equations 2.55 and 2.56 to the above equation, we would have:

$$N' \approx k_{evp}\, C_L \qquad (2.62)$$

So that the overall vaporation process for calcium is controlled in the metal phase. Based on this theory, Joyant and Gatellier [121] obtained the calcium diffusivities from the experiment on calcium decrease after injection, and their results are shown in Table 2.9. From Table 2.9, there is nearly two orders of magnitude of difference in D_{Ca} between pure Fe and Fe-20%Ni system. Although this may be explained by the different experimental systems, it is rather reasonable to consider that some errors in measuring the dissolved calcium content in the melt account for this difference. Since some calcium is tied up in the non-metallic inclusions, using total calcium to estimate the calcium diffusivity, D_{Ca}, from equation (2.62) would create the errors.

TABLE 2.10

EXPERIMENTAL RESULTS OF DIFFUSION COEFFICIENT OF CALCIUM IN DIFFERENT IRON ALLOYS AT 1600 °C [121]

System	D_{Ca} (m^2/s)
Fe	$2 * 10^{-10}$
Fe - 10%Ni	$4 * 10^{-9}$
Fe - 20%Ni	$8 * 10^{-9}$

2.7.1.3 Chemical Absorption

The theory of gas absorption with chemical reaction, namely chemical absorption, has been well developed in chemical engineering [122-127]. In the metallurgical system, Turkdogan et al. [128] were the first ones to discover that the chemical reaction formation of iron oxide fume at gas-liquid film contributed to the enhancement of iron vaporization in a vacuum. Recently, Zong and Yoon [129] succeeded in applying the gas-liquid reaction theory to explain the decarburization phenomena in converter oxygen steelmaking. However the application of gas-liquid reaction to the metallurgical processes is still very limited.

The chemical system that has received the most attention is the one [123] in which the absorption of a gas A undergoes an irreversible second-order reaction with a reactant B dissolved

in the liquid (both film and bulk). For the present, the gas will be taken as consisting of pure A, so that complications arising from gas film resistance can be avoided. The stoichiometry of the reaction is represented by:

$$A(g) + yB(l) - Products \qquad (2.63)$$

for which the simplest form of the rate equation will be

$$-r_A = k_2 C_A C_B , \qquad r_B = y r_A \qquad (2.64)$$

If steady-state conditions are assumed in the film, material balance for the two reactants yields:

$$D_A(d^2C_A/dx^2) - k_2 C_A C_B = 0 \qquad (2.65)$$

$$D_B(d^2C_B/dx^2) - y k_2 C_A C_B = 0 \qquad (2.66)$$

Here x is the distance in the liquid from the interface, and D_A and D_B are the diffusivities of A and B in the liquid.

Boundary conditions at the gas-liquid interface at x = 0 are

$$C_A = C_A^* \qquad (2.67)$$

$$dC_B/dx = 0 \qquad (2.68)$$

at the linear edge of the liquid film ($x = \delta_L$), the boundary condition for component B is:

$$C_B = C_{B0}\ , \qquad x = \delta_L \qquad (2.69)$$

To obtain the boundary condition for component A, it must be assumed that A reacts within the film while the rest is transferred across the film and reacts in the bulk of the liquid. If z is the specific interfacial area per unit volume of the reactor space and ß is the liquid holdup, the volume of this bulk liquid may be written as $ß/z - \delta_L$. The boundary for component A thus becomes:

$$-D_A(dC_A/dx)_{x=\delta_L} = k_2 C_{A0} C_{B0}(ß/z - \delta_L) \qquad (2.70)$$

Typical concentration profiles are shown in Figure 2.18. For the absorption with reaction, the concentration profile of A in the liquid boundary is represented by the solid curve and the effective mass transfer coefficient is represented by slope ij. Therefore, the overall mass transfer rate of A through the gas-liquid interface is given as follows:

$$N = -r_A.z = -z.D_A\left.\frac{dC_A}{dx}\right|_{x=0,\,t=t} = -\frac{1}{y}r_B.z \qquad (2.71)$$

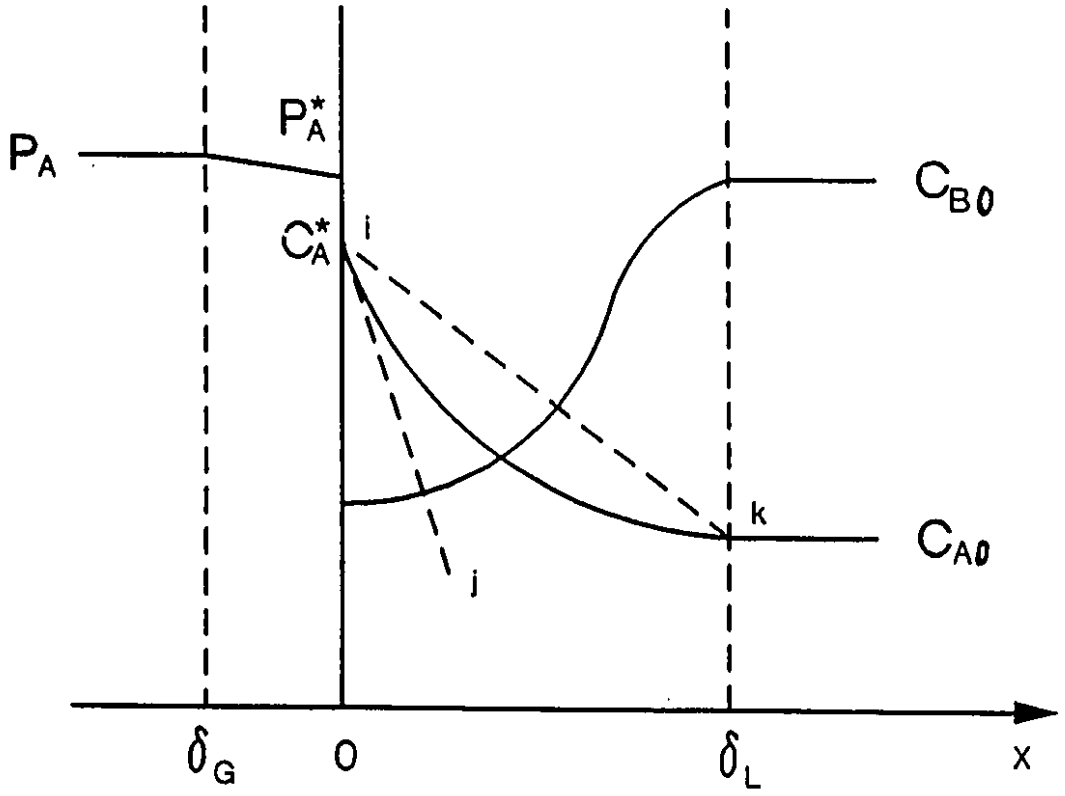

Figure 2.18 Concentration profiles of chemical absorption in liquid film [123].

For the absorption without chemical reaction, the concentration profile of A is linear and represented by the dashed line ik, and the effective mass transfer coefficient is represented by slope ik. Therefore, the mass transfer rate of A through the gas-liquid boundary is:

$$N_p = \frac{k_G \cdot z}{R \cdot T}(P_A - P_A^*) = k_L \cdot z \cdot (C_A^* - C_{A0}) \qquad (2.72)$$

In figure 2.18, enhancement factor, E, which means increased ratio of absorption rate by chemical reaction to physical absorption, is given as:

$$E = \frac{N}{N_P} = \left. \frac{\left. \frac{dC_A}{dx} \right|_{x=0}}{\frac{C_{A0} - C_A^*}{\delta_L}} \right|_{t=t} = \frac{slope(ij)}{slope(ik)} \qquad (2.73)$$

Although the general solution of equation (2.71) does not exist, the chemical absorption rate, N, can be expressed partially in special cases. Nine reaction regimes (including physical absorption) are classified by the dimensionless groups such as Ei and Ha as shown in Table 2.10 [123]. It indicates that the thermodynamic and hydrodynamic parameters, including concentration of reactant B in the bulk of the liquid and rate constant for second-order chemical reaction, determine the kinetic regime.

REGIME2.DRW

TABLE 2.11

REACTION REGIMES OF GAS ABSORPTION FOR IRREVERSIBLE SECOND-ORDER REACTION [A(g) + yB(l) = PRODUCTS] [123]

Reaction Site(s)	Reaction Speed and Regimes	Interface Conc. by Two-Film Theory	Rate Equations
	Chemical Absorption		
Reaction Confined to Film	A: Instantaneous reaction (Ha > 10 Ei)	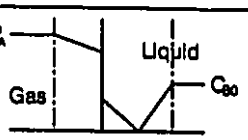	$\phi = \frac{P_A/He + D_B/D_A C_{B0}/\gamma}{1/k_L + 1/He\ k_L}$
	B: Instantaneous & high C_{B0} (Ha > 10 Ei)	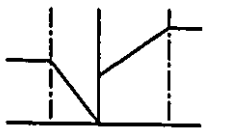	$\phi = k_g P_A$
	C: Fast reaction (Ha > 3)		$\phi = \frac{P_A}{1/k_g + He/E\ k_L}$
	D: Fast and high C_{B0} (3 < Ha < Ei/2)	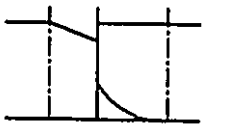	$\phi = \frac{P_A}{1/k_g + He/\sqrt{D_A k_1 C_{B0}}}$
Reaction In both Film & Bulk	E: Intermediate reaction (0.3 < Ha < 3)	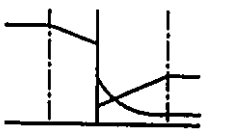	no expression developed
	F: Intermediate & high C_{B0} (0.3 < Ha < 3)	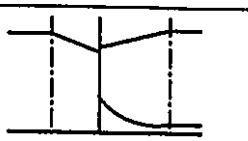	no expression developed
Negligible Reaction In Film	G: Slow reaction & diff. (0.02 < Ha < 0.3)	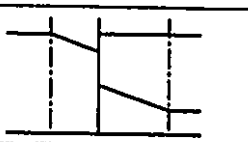	$\phi = \frac{P_A}{1/k_g + He/k_L + He\ z/\beta k_1 C_{B0}}$
	H: Very slow reaction (Ha < 0.02)	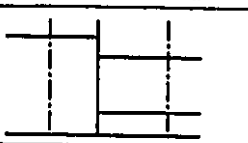	$\phi = k_2 C_A C_{B0} \beta$
	Physical Absorption		
	!: Diffusional process only	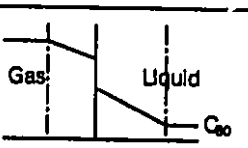	$\phi = \frac{P_A - He\ C_{A0}}{1/k_g + He/k_L}$

2.7.2 Liquid-Solid Mass Transfer

The rate of precipitation on inclusions in liquid steel should normally be diffusion-controlled, since rates of chemical reaction are very fast at high temperature. Consequently, the dimensionless mass transfer to a spherical inclusion particle should be given by the well-known Ranz-Marshall relation [130]:

$$Sh = \frac{k_i\, d_i}{D_L} = 2 + 0.6 Re^{1/2} Sc^{1/3} \qquad (2.74)$$

For micro-size inclusions, the terminal settling velocity is negligible and furthermore, the scale of turbulence in inductively-stirred melts (with the extra stirring form the Ca gas bubbling) is 10 to 100 larger than the inclusions [131]. Consequently inclusions must appear as being stagnant to the adjacent liquid even though they are being carried around the melt. As an order-of-magnitude approximation, the Sherwood number will take its limiting value, 2, for radial diffusion. Combining this with the number of inclusions per unit volume, n_i, the rate constant of precipitation on inclusions is:

$$k_i z_i = 2\, \pi\, D_L\, d_i\, n_i \qquad (2.75)$$

2.7.3 Liquid-Liquid Mass Transfer

The kinetics of sulfur transport between slag and molten iron has been the subject of many studies [132-135]. The overall transport process may involve the following three elementary steps:

1) Transfer of sulfur from the metal phase to slag/metal interface.

$$N_S = k_L z (C_S - C_S^*) \qquad (2.76)$$

2) Chemical reaction at the slag/metal interface

$$N_S = k_f z C_S^* - k_b z C_{S,sl}^* \qquad (2.77)$$

3) Transfer of sulfur from the slag/metal interface to the slag phase

$$N_S = k_{sl} z (C_{S,sl}^* - C_{S,sl}) \qquad (2.78)$$

where C_S is the sulfur concentration in the metal phase and $C_{S,sl}$ is the concentration in slag. C^* is the interfacial concentration. k_L and k_{sl} are the mass transfer rate constants in the metal and slag, respectively. k_f and k_b are the forward and backward reaction rates. z is the slag-metal interfacial area per unit volume of metal.

Rearranging Equations 2.76 and 2.78 gives

$$N_S/k_L z = C_S - C_S^* \tag{2.79}$$

$$N_S/k_f z = C_S^* - k_b/k_f C_{S,sl}^* \tag{2.80}$$

$$N_S/k_s z = C_{S,sl}^* - C_{S,sl} \tag{2.81}$$

Introduce ϕ, the partition ratio which is given as:

$$\phi = k_f/k_b \tag{2.82}$$

At steady state, one can combine Equations 2.77 and 2.80, one would get:

$$N_S = \frac{z(C_S - C_{S,sl}/\phi)}{(1/k_L+1/k_f+1/\phi k_{sl})} = \frac{z(C_S - C_{S,sl}/\phi)}{1/k_{ovl}} \tag{2.83}$$

where the term $(C_S - C_{S,sl}/\phi)$ represents the driving force in terms of concentration. For the high temperature metallurgical systems, the chemical reactions are so fast that equilibrium can be assumed to be attained [114]. Therefore, the overall mass transfer rate constant can be simplified as:

$$1/k_{ovl} = 1/k_L + 1/\phi k_{sl} \tag{2.84}$$

Whether the overall mass transfer is controlled by the transport in metal or slag side depends on the values of k_L and k_{sl}, which are the mass transfer coefficients in the metal and slag phases respectively, and on the partition ratio, ϕ,

which is a function of slag composition and oxygen potential in the metal.

2.8 MECHANICAL PROPERTIES OF CALCIUM TREATED STEEL

The improved cleanness through the deoxidizing and desulphurizing effect of calcium, and the modification of oxide and sulfide inclusions, results in an improvement in the mechanical properties of steel, particularly transverse ductility and toughness.

The main improvements in mechanical properties by calcium are higher impact strengths particularly at low temperatures, a raising of the impact self energy [136-138], and higher ductility, especially in the transverse direction [63,139]. There is some evidence to show that yield strength and tensile strength are improved slightly [63,140], but the general finding is that Ca has little effect on tensile properties [141]. Additionally, Ca treatment has been observed to improve the deep drawing performance of low carbon strip and to reduce strain aging [142]. More recently a marked improvement was found [143] in hot workability in high nitrogen stainless steel with calcium addition.

2.9 CALCIUM FREE-CUTTING STEELS

Free-cutting steels are those whose cutting properties are improved by the presence of S (Se,Te) or Pb inclusions.

Calcium free-cutting steels were first developed in Germany [144-145], and were later introduced to Japan and other countries [7]. Calcium free-cutting steels not only have excellent machinability at high cutting velocities, but also show no deterioration of the general materials properties. This is in contrast to the conventional sulfur and lead free-cutting steels: in the sulfur free-cutting steels, the strength of the materials is lowered, while lead free-cutting steels show a loss in abrasion and fatigue properties and in high temperature strength. Thus calcium free-cutting steels quickly gained their wide applications, especially in making automobile parts.

The unique effect of calcium addition in free-cutting steels is associated with the modification of the hard alumina inclusions by calcium to the low-melting calcium aluminate inclusions which deform more easily and form a protective layer on tools during chip formation [65,68]. Therefore calcium free-cutting steels are also called deoxidation-controlled free-cutting steels.

CHAPTER 3

OBJECTIVES OF THE RESEARCH

From the previous review, it can be seen that there is a great deal of literature [1-22] which qualitatively show the positive effects of calcium addition in the steel on deoxidation, desulphurization, desiliconization, dephosphorization and inclusion modification and on the quality improvement of the final steel products.

Carlsson et al. [23-24] were the first ones to report the negative uses of calcium in steel. They found that the total oxygen content as well as the number of inclusions increased during CaSi injection, whereas the opposite was true for CaO + CaF_2 injection. That means the calcium-treated steel is "dirtier" than the untreated steel. Large calcium aluminate inclusions (>100 μm) were sometimes found [25] to remain in the final products after calcium treatment. It was also reported [26] that excess addition of calcium in the melt would result in the formation of solid calcium aluminate or sulfide inclusions which cause nozzle clogging during casting [27-28].

However, there is no generally accepted model which could be used to explain quantitatively those phenomena, and the mechanisms by which calcium dissolves, desulphurizes, deoxidizes and transforms sulphide and oxide inclusions are still unknown. There is also a large discrepancy and controversy over the thermodynamic data of calcium deoxidation and desulphurization with a couple of order of magnitude differences on K_{CaO} and K_{CaS} (see Table 2.7) among the different authors, and the inclusions observed in practice often differ from that expected from equilibrium. Therefore there is a need to study the kinetics of treatment to determine the way in which bulk concentrations change in the steel and the way new inclusion distributions develop.

The kinetics and mechanisms for calcium addition in steel can only be understood if one continuously monitors what happens during and after injection. The present experiments were designed to be able to continuously and accurately observe and measure the process during and after calcium injection in a well-controlled system. That made it possible for the following objectives to be studied in detail in the present research:

1) The mechanism and kinetics of calcium absorption;
2) Ca evaporation/elimination kinetics;
3) Deoxidation kinetics;

4) Desulphurization kinetics;

5) The kinetics and mechanism of inclusion modifications for both oxides and sulfides;

6) The system kinetic path and effect of various parameters.

The unique feature of calcium treatment of steel is that calcium is a strong reagent, but only with a very limited solubility in steel. So that the first most important question of all needed to be answered is how calcium comes into the bulk during its continuous injection. Once one knows where the calcium is, one would know where the deoxidation, desulphurization, and inclusions modification reactions take place. The continuous calcium distribution in different phases can then be monitored, and the kinetic path of the system can also be traced during and after the process.

CHAPTER 4

APPARATUS AND PROCEDURE

4.1 APPARATUS

4.1.1 Furnace System

A general view of the vacuum induction furnace unit is schematically shown in Figure 4.1. An induction furnace is enclosed in a vacuum chamber which is equipped with a calcium wire feeder, an alloy addition chamber, a furnace atmosphere oxygen analyzer, an argon inlet, a viewing window and a sampling port. Each of the main components is described below:

The vacuum chamber measures 1 meter in diameter and 2 meters in length. It is well sealed by high vacuum grease, around the door, ports and equipment connections.

Fifty kg capacity magnesium oxide crucibles were used to melt the charge materials. The crucibles measured 18 centimetres in diameter and 33 centimetres in height.

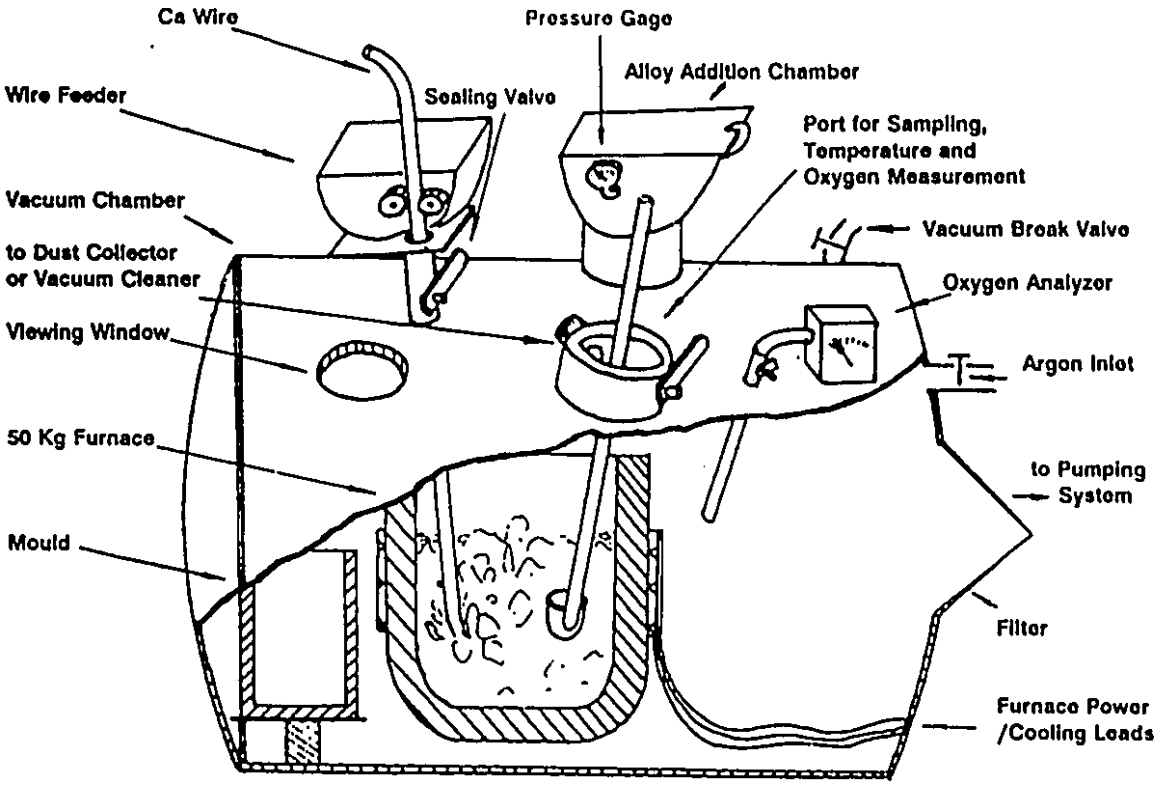

Figure 4.1 Schematic view of the vacuum furnace facility showing the injection of Ca wire into the melt

Typically two-third of the crucible was filled with 40 kg of the melt during the melting operation.

The sampler used was a cone-type dipper, measuring 0.04 metres in diameter and 0.025 metres in height. Tilting the sampler not only made the samples easier to take out, but also prevented the formation of cavities in the samples during cooling.

The alloy addition chamber on the top of the furnace enables 6 different types of alloys to be added under a vacuum or argon atmosphere simultaneously or individually.

The pumping system consists of the following pumps: roughing, booster, holding and diffusion. Under the present conditions, the first three pumps were powerful enough to meet the experimental requirements.

The wire feeder was originally a welding machine with a feeding rate of 0.02 to 0.5 m/s. For the present situation, the allowed calcium feed rate varies from 0.02 to 0.12 m/s, or from 0.7 to 4.2 Kg Ca/t min.

The induction power varied from 50 to 60 kW during melting, from 30 to 40 kW during the calcium wire injection, and about 20 kW during the holding period after calcium

addition.

4.1.2 Oxygen Measurement

Oxygen measurement includes the oxygen potential of the argon atmosphere in the chamber and oxygen activity in the melt.

The furnace atmosphere was continuously monitored by a portable oxygen analyzer (model 320P-4) with an integral pump from Teledyne Analysis Instruments. Oxygen is sensed utilizing a Cell which samples oxygen from the atmosphere surrounding the measuring probe and generates a proportional electric current. The generated current is amplified and read out on a built-in meter. The specifications for the analyzer are given in Table 4.1.[146]

TABLE 4.1

THE SPECIFICATIONS FOR THE OXYGEN ANALYZER

Ranges	0-5, 0-10, 0-25% O_2
Sensitivity	0-5% of full scale
Accuracy	±1% of full scale at constant temperature; ±5% of reading or ±1% of full scale
Operating T	30-125 °F

The Celox oxygen probe (Celox2/C11) from Electro-Nite, used in the present study to measure the oxygen activity in

the melt, is a commercial, single use electrochemical oxygen cell. The cell consists of a ZrO_2 solid electrolyte partially stabilized with MgO and a Cr/Cr_2O_3 reference electrode. The galvanic cell can be represented by:

$$\{Mo\}\ Cr,\ Cr_2O_3 \ \vert\ ZrO_2\ (MgO)\ \vert\ [O]_{Fe},\ Fe_{(s)}$$

The galvanic cell reaction can be written by:

$$2Cr_{(s)} + 3[O]_{1w/o} = Cr_2O_{3(s)} \qquad (4.1)$$

The theoretical oxygen activity from the pure oxygen ionic conductivity is given by:

$$\log h_o^{\bullet} = \frac{-(13580-10.08E)}{T} + 4.62 \qquad (4.2)$$

In practice, the electronic conductivity can not be ignored. Wagner gave the following expression for the oxygen voltage when the electronic conductivity was considered:[147]

$$E = \frac{R\,T}{n\,F} \ln \frac{P_e^{1/4} + P_{O_2}^{II\,1/4}}{P_e^{1/4} + P_{O_2}^{I\,1/4}} \qquad (4.3)$$

where:

$P_{O_2}^{I}$, $P_{O_2}^{II}$ = the lower and higher oxygen pressure at cathode and anode.

$P_{e'}$ = equivalent oxygen pressure from electron conductance.

$P_{e'}$ is a function of temprature and the chemical compositions of the solid electrolyte [148-151]. For the composition of the ZrO_2 electrolyte (2.4%MgO, 0.2%CaO, 0.3%SiO_2, 0.15%Al_2O_3, and 0.05%Fe_2O_3) used in the present experiments, the following relationship is used to calculate $p_{e'}$ [151]:

$$\log p_{e'} = -74370/T + 24.42 \qquad (4.4)$$

There are two ways to correct Equation (4.3) depending on the relative levels of oxygen potential at cathode and anode.

A. When the oxygen pressure of Cr_2O_3 is higher than the partial oxygen pressure in equilibrium with the melt

$P_{O_2}^{II} = P_{O_2}^{(Cr+Cr_2O_3)}$, and $P_{O_2}^{I} = P_{O_2}^{[O]}$, from equation (4.3), one would have the following expression for the actual oxygen activity, a_o:

$$h_o = \left[(h_o^*)^{1/2} + \frac{K^{1/4}(1-e^{EF/RT})}{e^{EF/RT}} P_{e'} \right]^2 \qquad (4.5)$$

where K is the equilibrium constant for the following equation:

$$O_2 - 2[O] \qquad (4.6)$$

Since $(1-e^{EF/RT})<0$, the result will show a positive deviation, if the electron contribution is ignored. This is shown by the left half diagram of Figure 4.2, where the solid line represents ionic conductance only and the broken curve includes both ionic and electronic conductance.

B. When the oxygen pressure of Cr_2O_3 is lower than the partial oxygen pressure in equilibrium with the melt

The expression for the actual oxygen activity in this case is given as:

$$h_o = \left[(h_o^*)^{1/2} + (e^{(EF/RT)}-1) K^{1/4} P_e^{1/4} \right]^2 \qquad (4.7)$$

Since $(e^{EF/RT} -1)>0$, the negative deviation will result from ignoring the electron conductance. This is shown by the right half diagram of Figure 4.2.

At high temperatures, due to temperature gradient across the liquid-solid boundary at the probe, the measured oxygen activity has to be calibrated, and this was done by a joint effort of Hoogovens steelworks with C. R. M and Electro-Nite [152]. Their recommended equation is used for the present experiment:

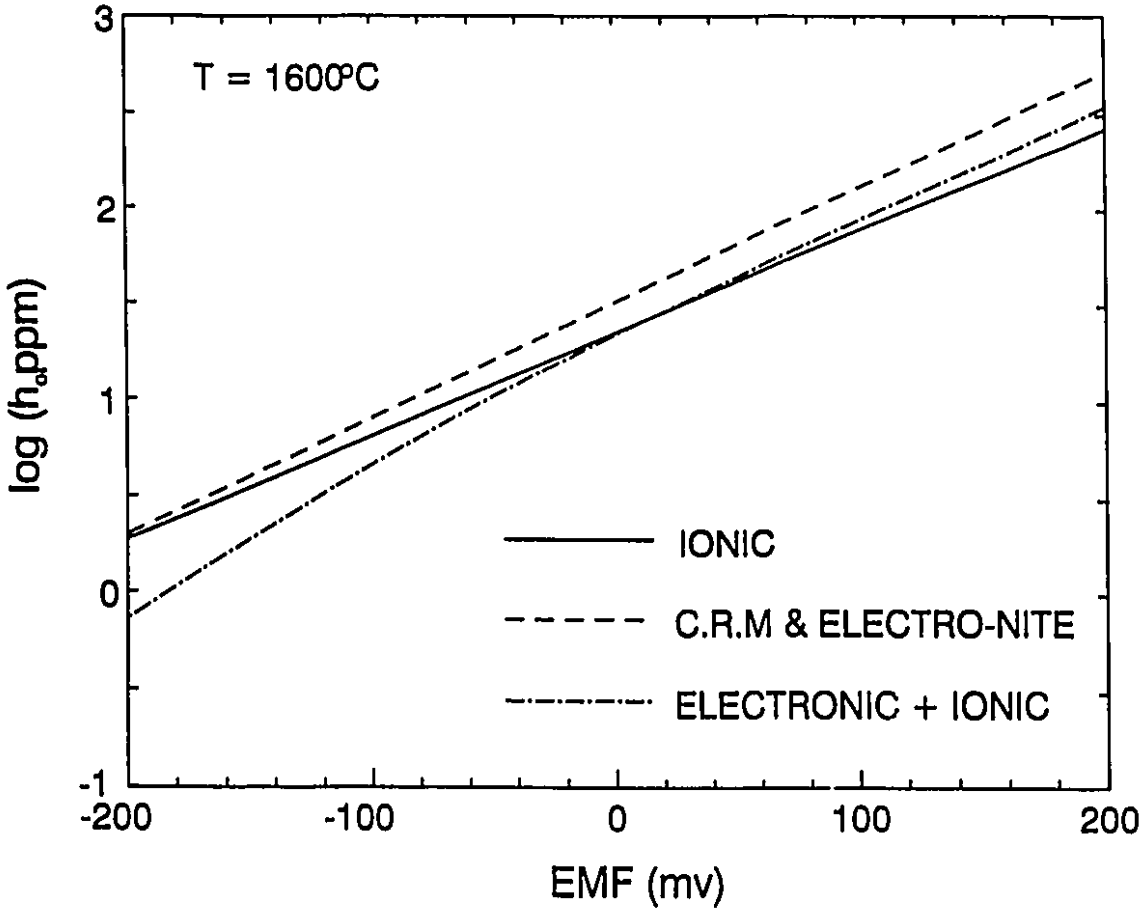

Figure 4.2 Comparison for different contributions to the oxygen activity.

$$\log h_o = 1.36 + 0.0059\,[E + 0.54(T - 1550) + 0.00021E(T - 1550)] \quad (4.8)$$

where T is the temperature in ^{0}C.

Figure 4.2 compares the calibration line (the broken line) with the theoretical calculation (the dashed line from the electron and ionic conductance). It can be seen that at lower oxygen activity (h_o<10 ppm), the two lines deviate. Since most of the present oxygen levels are around 10 ppm or above, errors are of the order of 30%.

4.2 MATERIALS

The steel used for the experiments was AISI 1045 steel, which was kindly provided by Stelco Inc.. Its nominal composition is shown in Table 4.2.

TABLE 4.2

CHEMICAL COMPOSITIONS OF 1045 STEEL FROM STELCO INC.

X	C	Mn	P	S	Si	Cu	Ni	Cr	Mo	ASA[a]
%	0.45	0.75	0.08	0.017	0.25	0.015	0.011	0.027	0.003	0.027

[a] ASA: Acid Soluble Aluminum

The calcium wire was provided by Pfizer Inc. Pure calcium powder was wrapped in a thin layer of steel pipe. The unit calcium weight of the wire was 23.1 grams per meter with the outside diameter of 5 mm.

The cover slag from Foseco was mainly a two component system made of 70%CaF_2 and 30%CaO, which has a high sulfur capacity [C_s = (%S) * (P_{O_2}/P_{S_2}) = 0.0316].

4.3 EXPERIMENTAL DESIGN

The experimental design is shown in Table 4.3. The three important independent variables were considered to be the sulfur content, the acid soluble aluminum and the calcium feed rate. The principle of the original design was to study the effect of the change of the individual variable on the process, while the other two independent variables were fixed. There were two levels of sulfur: 0.017% and 0.005%, three levels of acid soluble aluminum: 0.01, 0.05 and 0.10% ASA, and three Ca wire feed rates: 0.02, 0.06 and 0.10 m/s. Generally 10 m, (0.231 kg Ca), was fed, so that the injection time varied inversely with the feed rate.

TABLE 4.3

EXPERIMENTAL DESIGN

Exp. No.	Initial S (%)		Initial Al (%)		Wire Feed Rate (m/s)		Heat No.
	target value	actual value	target value	actual value	target value	actual value	
1	0.017	0.0280	0.10	0.127	0.02	0.020	H3R1
2	0.017	0.0140	0.05	0.046	0.02	0.022	H4R1
3	0.017	0.0140	0.01	0.010	0.02	0.026	H6R1
4	0.107	0.0154	0.01	0.004	0.10	0.103	H9R1
5	0.107	0.0120	0.01	0.002	0.06	0.062	H8R1
6	0.005	0.0004	0.10	0.125	0.02	0.020	H9R3
7	0.005	0.0106	0.05	0.073	0.02	0.028	H7R2
8	0.005	0.0013	0.01	0.010	0.02	0.023	H9R2
9	0.005	0.0080	0.01	0.031	0.10	0.112	H5R1
10	0.005	0.0089	0.01	0.002	0.06	0.062	H8R2
11		0.0030		0.078		0.058	H6R2
12		0.0189		0.000		0.067	H7R1

4.4 EXPERIMENTAL PROCEDURE

The flow-chart of the experimental procedure is summarized in Figure 4.3.

Bar was charged to the crucible for melting, before the door of the vacuum chamber was closed and sealed with high vacuum grease. As the steel was heated, the air was pumped out of the furnace. Close to the melting point of the steel, the chamber was back-filled with argon. Argon was continually flushed through the furnace when the sampling port was open. After melt-down, the power was adjusted to maintain 1600 °C. Additions (aluminum, sulfur and slag) were made through the alloy addition chamber. An initial oxygen probe measurement,

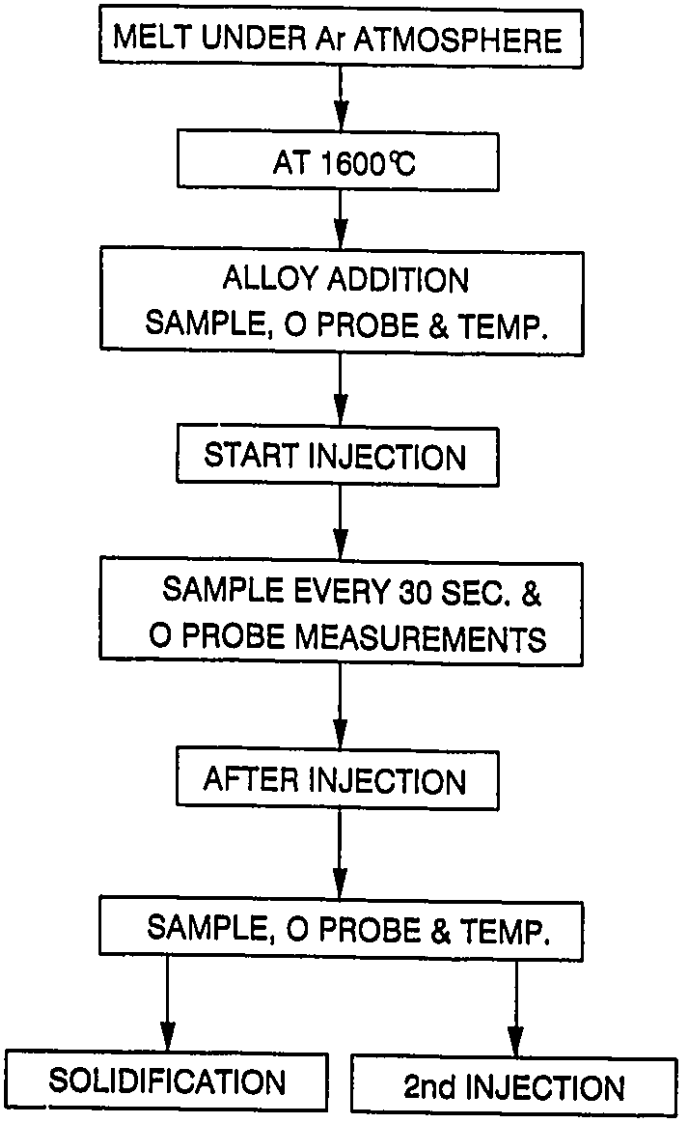

Figure 4.3 Flow-chart for the experiment procedure

chamber oxygen reading and an ingot dip sample were taken. The Ca wire feeding time varies between 1.2 to 7 minutes depending on the feed rate, but samples were also taken for 30 minutes after the injection. The temperature reading from the oxygen probes were double-checked by single-use thermocouple. Oxygen measurements in the furnace atmosphere were taken frequently throughout the experiment.

A second injection usually followed the first one, in which case the starting sulphur content would be significantly lower. For the second injection, the melt would be deoxidized with aluminum. After the injections were finished, the ingot would be solidified in the crucible. A new crucible was used for each melt because the splash around the perimeter of the crucible was hard to dislodge.

The total about half-hour duration of calcium injection and holding period was recorded in detail via a tape recorder. The ingot dipper sample taken were sectioned into several pieces: one solid disk for ICAP analysis for total of 24 elements, two pieces for optical spectrometer or SEM analysis for inclusions, two dopes of (1 gram each) drilling chips for N_2, O_2 and sulfur analysis and around 1 gram drilling for ASA ICP analysis.

4.5 CHEMICAL ANALYSIS PRINCIPLE AND EQUIPMENT

4.5.1 Nitrogen and total oxygen

The simultaneous determination of nitrogen and total oxygen is performed on a Leco microprocessor controlled instrument (model TC-136) [153]. The analysis of oxygen is accomplished by heating a sample of the specimen in a graphite crucible where oxides are reduced by excess carbon to form CO. Then, total oxygen in the sample is converted to CO and subsequently oxidised to CO_2 by sweeping the CO over copper oxide using a helium gas stream. The presence of CO_2 is used to change the thermal conductivity in a thermal conduction cell based on a thermistor device. This represents one arm of a wheatstone bridge. The output of a digital voltmeter can be calibrated directly as a total oxygen percentage by using calibration standards. During heating, nitrogen is also liberated and carried away with CO by helium. After CO_2 is absorbed by copper, the remaining gas volume is nitrogen. The specifications of the instrument are shown in Table 4.4.[153]

TABLE 4.4

SPECIFICATIONS OF LECO INSTRUMENT FOR N_2 AND O_{TOT}

Analysis time	15 seconds for O_2 30 seconds for N_2
Ranges (1 g sample) Nitrogen (low) Nitrogen (high) Oxygen	 0.00001% to 0.1 % N_2 0.01% to 0.5% N_2 0.00001% to 0.2% O_2
Sensitivity	0.1 ppm
Accuracy N_2 (low) N_2 (high) O_2	 $\pm$0.0001 or $\pm$1% N_2 present $\pm$0.0002 or $\pm$1% N_2 present $\pm$0.0002 or $\pm$1% O_2 present

The standard used is 460 $\pm$ 5 ppm O_2 and 31 $\pm$ 1 ppm N_2.

4.5.2 Sulfur Analysis

There are several ways to determine Sulfur content in steel. The most common one is the combustion analysis. This was done on a Leco 518 titrator [154].

A weak HCl solution is put into a titration vessel where KI and starch solutions are added. Then a very small amount of the standard KIO_3 solution is added, and free I_2 is released, which is indicated by the starch turning blue.

$$KIO_3 + 5KI + 6HCl = 6KCl + 3I_2 + 3H_2O \qquad (4.9)$$

An automatic buret containing the KIO_3 is then refilled to the zero or starting point. The sample is next combusted in oxygen where sulfur in the sample goes to SO_2 and/or SO_3 depending on the combustion conditions:

$$S + O_2 = SO_2 \qquad (4.10)$$

SO_2 is then conducted to the titration vessel where it reacts with the free iodine and ties it up as a compound, HI:

$$SO_2 + I_2 + 2H_2O = H_2SO_4 + 2HI \qquad (4.11)$$

More KIO_3 is added to form more free iodine and to bring the solution back to its original colour until all the SO_2 is out of the sample and has been titrated. The amount of KIO_3 used is then read in the buret directly in percent sulfur, which is then corrected by a titration factor from the sulfur standard and the sample weight.

The standard deviation is $\pm$ 0.0003% for a 0.026% standard with a titration factor of 1.14.

The alterative method for analyzing the sulfur content

in steel is by Plasma Spectrometric as mentioned later. However, its resolution for sulfur analysis is not as high as that of the iodometric titration method.

4.5.3 Acid Soluble Aluminum (ASA)

The commonly accepted concept of ASA is considered to be the dissolved aluminum in the steel. In fact some aluminum compounds in steel such as aluminum nitride are also acid soluble. So ASA is not actually equal to, but is related to the dissolved aluminum. The accuracy of analyzing it depends on the bath chemistry and the standards available and technique to measure.

A variety of techniques are available [155], but in general a certain weight (usually 1 gram) of sample is dissolved in a dilute acid mixture (HCl and HNO_3 are commonly used). This was the procedure used by Stelco, who kindly performed these analyses. Ideally, the aluminum combined with the inclusions is supposed to precipitate out from the solution. After filtration, the solution is ready for absorption analysis.

There are two commonly used ways to analyze the ASA content. The first one is the classical Atomic Absorption Analysis. The basic principle is that, if an element is

dissociated from its chemical bonds into an un-ionised ground state it can selectively absorb radiation over a narrow bandwidth. Excitation is usually caused by burning in a flame and the emission lines are provided by a low pressure rear or argon lamp with a cathode of the element being sought. The degree of absorption of resonance lines can be determined by a photodetector.

The second method uses an Inductively Coupled Argon Plasma (ICAP). The liquid sample is aspirated into the induction coil zone where it is excited by the high temperature argon plasma, and the concentration is determined according to the intensity of that element's specific wavelength after calibration with standards. Most of the ASA were kindly analyzed on Stelco's ICP. The standard deviation is $\pm$ 0.001% for a 0.06% ASA standard [155].

4.5.4 Total Aluminum and Calcium

Both elements can be analyzed by the atomic absorption analysis method. At the present research, the samples were dissolved in solutions to analyze the calcium content in steel on ICAP. The results were not satisfactory due to the lack of the standards. Alternative methods have to be used.

One of the unique features of the present ICAP 7000 is its Solid Sampling ICAP system [156]. The main principle is shown in Figure 4.4. About 2 millimetres diameter area of the solid sample surface is sparked by a tungsten electrode and carried to the plasma by argon. The following sequences would be same as discussed above (4.5.3).

The reliability of all the chemical analysis results are based on the accuracy and ranges of the standards available. Several solid disks of calcium treated steel standards were purchased from Brammer Standards whose concentrations are close to the present experimental ranges. The calibrations were done for a total of 24 elements including total aluminum and calcium by using NITS (former NBS) steel disk standards as well as the Brammer calcium treated steel standards. Excellent analytical results were achieved and agreed well with the results obtained from the same samples by Algoma Steel Inc., using the atomic absorption method. The ranges and deviation of some related elements are listed in Table 4.5.

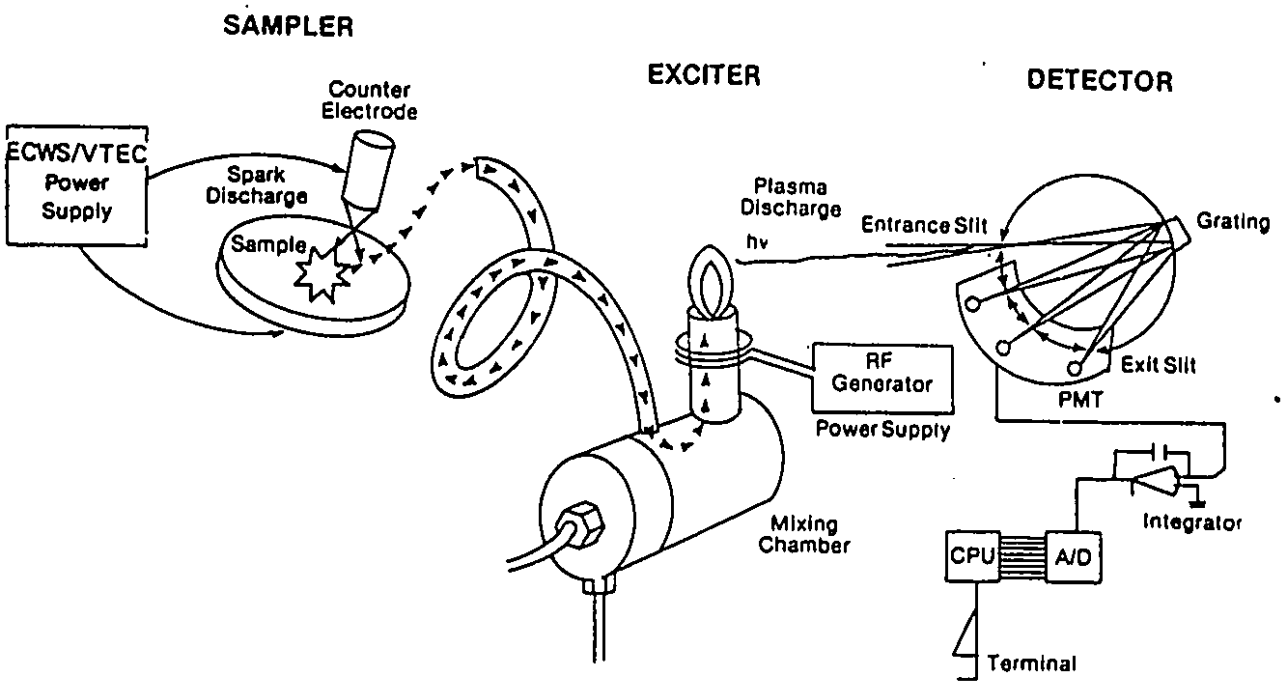

Figure 4.4 SS 7000 ICAP analysis system

TABLE 4.5

SPECIFICATIONS OF ICAP FOR SOME ELEMENTS

Element	Range wt%	Relative standard deviation
Ca	0 - 0.02	± 5.0 %
Si	0 - 1.28	± 1.2 %
Mn	0 - 1.50	± 9.0 %
Al_{tot} [a]	0 - 0.24	± 3.0 %
Cr	0 - 2.70	± 2.5 %

[a] Al_{tot}: total aluminum

4.6 INCLUSION ANALYSIS

Quantitative inclusion analysis according to size and composition were performed by Stelco Inc. and CANMET. Both of their systems consist of a scanning electron microscope and a Link System (860 Series 2) Analyzer equipped with both DIGIMAP and DIGISCAN hardware [157].

4.6.1 LINK System

As schematically illustrated in Figure 4.5, the Link System combines three analytical tools under computer control: 1) the scanning electron microscope, which is widely used in materials science because of the ease of sample preparation, high resolution, large depth of field, and sharp secondary electron images; 2) energy dispersive x-ray spectroscopy, which adds to the SEM the extra dimension of x-ray microanalysis; and 3) computer control of the electron beam via the digital scan generator, which allows rapid measurement of the size, shape and chemistry of individual features in the SEM images [157-158].

Software has been developed to provide quantitative composition, size, and shape data for a number of applications, including inclusion metallography [159-160]. The present software used, DIGISCAN/FDC allows features in a field of view in the scanning electron microscope to be detected, sized and chemically classified. Data may be collected from more than one field and the area of the total field occupied by each class is printed. This software may also be used in conjunction with stage automation (MULTIPOINT) and detected features may be analyzed quantitatively when used in conjunction with ZAF-4/FLS.

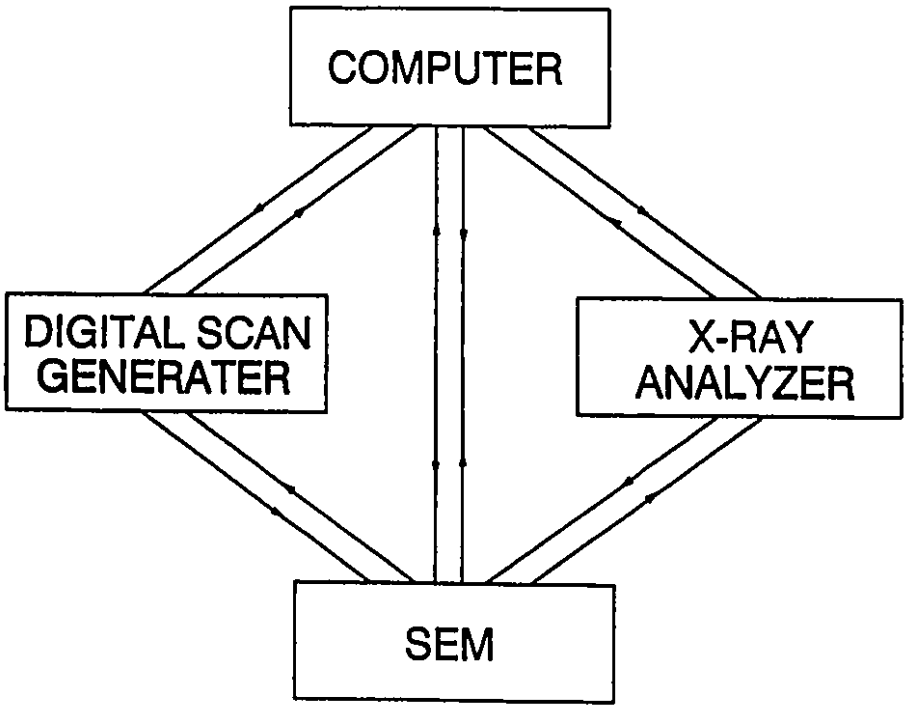

Figure 4.5 Basic components of a LINK System

4.6.2 Principles of Image Analysis by DIGISCAN/FDC

A backscattered electron image is obtained from an area of interest. Those features of interest may be selected using an adjustable comparator with upper and lower thresholds are seen as white areas whilst all parts of the image whose grey levels are outside this range are set to black. The program allows these thresholds to be set in a variety of ways. Once the thresholds have been set the beam is driven from the Link digital beam control system and a grid of points superimposed on the thresholded image. As the beam scans, regions seen as white (by inspection of the comparator output) are stored. The beam is then driven back and scans over each particle in turn and x-ray data collected. i.e. Features are detected during the first scan and the chemical information obtained whilst the beam scans over each feature.

All the relevant size and chemical information is stored in a file to which data from subsequent fields may be added. Once all data have been collected, a statistical summary of the results is printed and a histogram displayed. This summary indicates the number of features in each chemical class and size range specified by the user. The area% occupied by each chemical class and each size range are also printed. The criterion used for size determination is also selected by the user.

The flow chart of running DIGISCAN on the Link System is illustrated schematically in Figure 4.6,[157] for the inclusion detection and classification.

4.6.3 Classification of Inclusions

Before the system can be used to chemically classify material, two files must be created; the first contains the 'window' information and eV/channel. These windows denote the regions in the x-ray spectrum to be used for each element of interest (and its background). The second file lists the various chemical categories into which features are to be sorted.

Setting Windows

When the electron beam is positioned on an inclusion in a Fe matrix, a spectrum obtained shows the peaks of each element present including the background contribution. It is necessary to know what other elements are present so that background windows could be selected properly together with the spectrums windows for all elements in the inclusion. Correction for background and overlap contributions have to be made, before the integral for all element windows are summed and each integral is calculated as a percentage of this total. The exact composition of the inclusion is then determined by

flow.drw

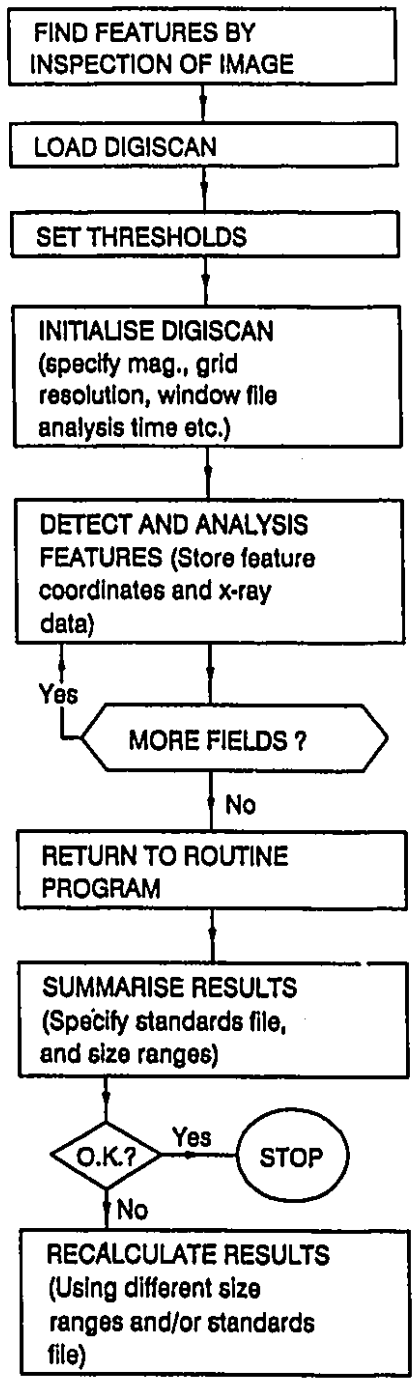

Figure 4.6 Running DIGISCAN - flow chart

a simple ratio technique.

Standards File

The standard file defines the permissible lower and upper concentration limits for the elements in each category, or classification of inclusions. The maximum number of standards or chemical categories which may be defined in one standards file is 32.

In the present work, the major elements in the inclusions detected in concentrations greater than 5% were Fe, Ca, Al, Mn and S (There were trace amounts of P, N, Si, Ti, Mg and so on). The inclusions were divided into 8 categories or classes according to Table 4.6. The 5% threshold was chosen as the lower limit for classification of the major components. The right-hand column of Table 4.6 identifies the phases which fall into each classification.

All of the inclusions found in this study were spherical and less than 20 μm in diameter. Typically the inclusions were composed of more than one phase, so that the designation in Table 4.6 apply to the average inclusion composition. The lower resolution, or the the smallest feature to be detected for the present conditions is about 0.2 μm.

TABLE 4.6

DESIGNATIONS OF INCLUSION CLASSIFICATIONS

Element / Designation	Ca	Al	Mn	S	Stoichiometric Compounds
	%				
MnS	0-5	0-5	5-100	5-100	MnS
Al_2O_3	0-5	5-100	0-5	0-5	Al_2O_3
CaS	5-100	0-5	0-5	5-100	CaS
CaO	5-100	0-5	0-5	0-5	CaO
(Ca,Mn)S	5-100	0-5	5-100	5-100	CaS + MnS *
CA_x	5-100	5-100	0-5	0-5	CA_6,CA_2,CA $C_{12}A_7$ & C_3A #
$CaS{\cdot}CA_x$	5-100	5-100	0 5	5-100	CaS + CA_x
$CaMnS{\cdot}CA_x$	5-100	5-100	5-100	5-100	(Ca,Mn)S + CA_x

* see CaS-MnS phase diagram, Figure 2.15.

\# see $CaO-Al_2O_3$ phase diagram, Figure 2.12.

4.6.4 Analysis and Inclusion Area

Once a window file and standards file have been created and thresholds set, the system can be used for detection and analysis of features in an image. For the present inclusion size range, the operational parameters including grid resolution, size limits and analysis time are shown in Table 4.7.

TABLE 4.7

OPERATIONAL PARAMETERS OF LINK SYSTEM FOR INCLUSION ANALYSIS

Screen width = 117000 μm	Sampling count = 1	Areamax (grid pts) = no limit	Window info. file = CaIncl.
10 Scan lag (grid pts) = 0.2	Field width = 58.5 μm	Protect zone = 2.5 μm	Calibration standard = Co
No. of grid point/line = 256	Thresholds = 0-108	No.of diam. projections = 20	Magnification = 2000
Point spacing = 0.229 μm	Areamin (grid pts) = 2	EDX:dwell/feature = 100 mS	Results file = H7R2

As the beam scans the inclusions which appear as white (the matrix is black), each inclusions' size, shape and chemistry are stored in a output file. For each sample, at least 40 fields were analyzed for all the inclusion features, and the statistical printout is given including the size distribution and area% of each class of inclusion as well as of the total inclusions.

4.6.5 Quantitative Inclusion Composition with ZAF-4/FLS

DIGISCAN can also be used in conjunction with DIGIPOINT and MULTIPOINT to detect the features, and the centre of the gravity of the feature will be analyzed and stored in a file. The information is then passed to ZAF-4/FLS quantization routines for the detailed quantitative analysis of the inclusion composition.

The concentration of the element, i, in the sample, is determined by a ratio technique [161]:

$$\frac{C_i}{C_{(i)}} \propto \frac{I_i}{I_{(i)}} = k_i \qquad (4.12)$$

where C_i and $C_{(i)}$ are the concentration of element i in the sample and standard, and I_i and $I_{(i)}$ are the measured intensities from the sample and standard, respectively. Once the k_i value is obtained, it must be corrected for several effects including (1) differences between specimen and standard for electron scattering and retardation, i.e., the so-called atomic number effect expressed by the factor Z_i; (2) absorption of x-rays within the specimen, A_i; (3) fluorescence effects, F_i, and in a few specific cases, continuum fluorescence. A common form of the correction equation is:

$$C_i = (ZAF)_i k_i \qquad (4.13)$$

This method is often referred as the ZAF method.

This ratio technique is often used to measure the concentration ratio of the two elements A and B in the same specimen, i.e., C_A/C_B:

$$\frac{C_A}{C_B} = K_{AB}\frac{I_A}{I_B} \qquad (4.14)$$

where K_{AB} is the Cliff-Lorimer calibration factor from the standard, and I_A and I_B are the measured intensities of elements A and B in the specimen, respectively. If one measures all the elemental ratios in the feature, and adds them up to 1, each elemental concentration will be known.

CHAPTER 5

EXPERIMENTAL RESULTS

More than twelve injections were conducted. The initial injections produced a great amount of fine calcium oxide (lime) dust during injection. A dust collector had to be installed near the sampling port, and protection equipment (mask with a thermal-insulating suit) was used for extra safety. There was a large amount of splashed molten steel, especially at higher injection rates, which stuck to the sides of the crucible above the melt surface. It made it virtually impossible to cast the melt after refining. Most of the heats were therefore cooled inside the crucibles and taken out afterwards by destroying the crucibles. A new crucible had to be used for every injection. In some heat a second injection followed after the first injection. However, the amount of charge had been reduced and the initial chemistry for the second injection was not that precise on the target.

A tape recorder was used to record the procedures. Usually a sample was taken for about every half minute during

injection and for about couple of minutes after injection. The time interval to take the samples during injection shortens with the increase of the calcium wire feed rate, so that at least 5 samples and 3 oxygen activity measurements were taken to study the kinetics during injection, and at least 3 samples and 2 oxygen measurements before injection and during the holding period.

Only one heat has no top slag. The slag of the rest heats was immediately pushed aside on the touch of calcium wire on the surface of the melt, due to the vaporization of calcium. Which resulted in 20% of slag coverage around the crucible. No slag entrapment was found from the samples taken, which means there was no intensive mixing between slag and melton metal.

The calcium wire penetration depth in the melton metal was also measured. The measurement system consists of a fast speed camcorder and an electric circuit. The electric circuit comprises of a Mo wire, which is inserted in the melt, the calcium wire, a light bulb and several batteries. When the calcium wire touches the melt surface, the circuit is closed and light bulb is lighted up and recorded in the camcorder. When the calcium wire penetrates to a certain depth in the melt, it vaporizes. The first calcium bubbling occurs at the melt surface is visually seen from the video recording. The

time interval between the lighting-up and bubbling is how long for calcium wire to take to penetrate in the melt. The testing was successful. The time interval for the first calcium bubble to erupt after the penetration of the wire in the melt is about half a second at a feed rate of 0.02 m/s. The calcium wire penetration depth in the melt at that speed is about 0.01 m.

A summary of the initial experimental conditions for the injections and some of the results are shown in Table 5.1. The results for the bulk chemical analysis will first be presented, followed by the micro-analysis of the inclusions.

5.1 BULK CHEMICAL RESULTS

The typical concentration changes of calcium, sulfur, total oxygen, oxygen activity and aluminum as a function of time during and after injection are shown in Figure 5.1 (one heat without top-slag) and Figure 5.2 (with top-slag). More raw data is given in Appendix A. The change of the individual element for each case (with or without top slag) is discussed below in detail:

TABLE 5.1

SUMMARY OF SOME EXPERIMENTAL PARAMETERS AND RESULTS

Heat & Run (No)	Weight of Melt (kg)	Ca Feed Rate (kg/T Min)	Inj. Time (min)	Ca Fed (g)	Initial Conditions							
					Total Al (%)	ASA (%)	Oxygen Activity (ppm)	Total Oxygen (%)	Chamber Oxygen (%)	Sulphur Content (%)	Feseco Slag (g)	Initial Temp (°C)
H3R1	36.86	0.795	6.35	176.00	0.1339	0.127	2.47	0.0025	1.50	0.028	0	1582
H4R1	37.20	0.842	4.75	144.78	0.0403	0.046	4.20	0.0025	0.08	0.014	250	1600
H5R1	32.00	4.851	1.16	180.07	0.0278	0.031	8.38	0.0044	0.22	0.008	675	1598
H6R1	40.00	0.906	6.00	217.60	0.0137	0.010	18.6	0.0028	0.07	0.018	250	1585
H6R2	35.00	2.289	2.70	216.44	0.0844	0.078	*	0.0022	0.20	0.003	250	1644
H7R1	41.00	2.299	2.93	277.20	/	/	185.09	0.0095	0.06	0.0189	250	1640
H7R2	38.00	1.036	4.18	164.80	0.0767	0.073	4.88	0.0040	0.30	0.0106	250	1635
H8R1	41.00	2.11	1.90	164.70	/	0.002	35.78	0.0047	0.05	0.012	250	1612
H8R2	38.00	2.25	2.13	182.87	/	0.002	11.62	0.0036	0.70	0.0089	250	1626
H9R1	41.00	3.48	1.83	261.25	0.0028	0.004	61.58	0.0032	0.08	0.0154	250	1642
H9R2	38.00	0.835	4.75	150.76	0.0084	0.010	26.40	0.0049	3.00	0.0013	250	1601
H9R3	33.00	0.832	5.95	163.28	0.1220	0.125	1.47	0.0029	2.40	0.0004	250	1605

Note: * Not measured
/ Below level of detection

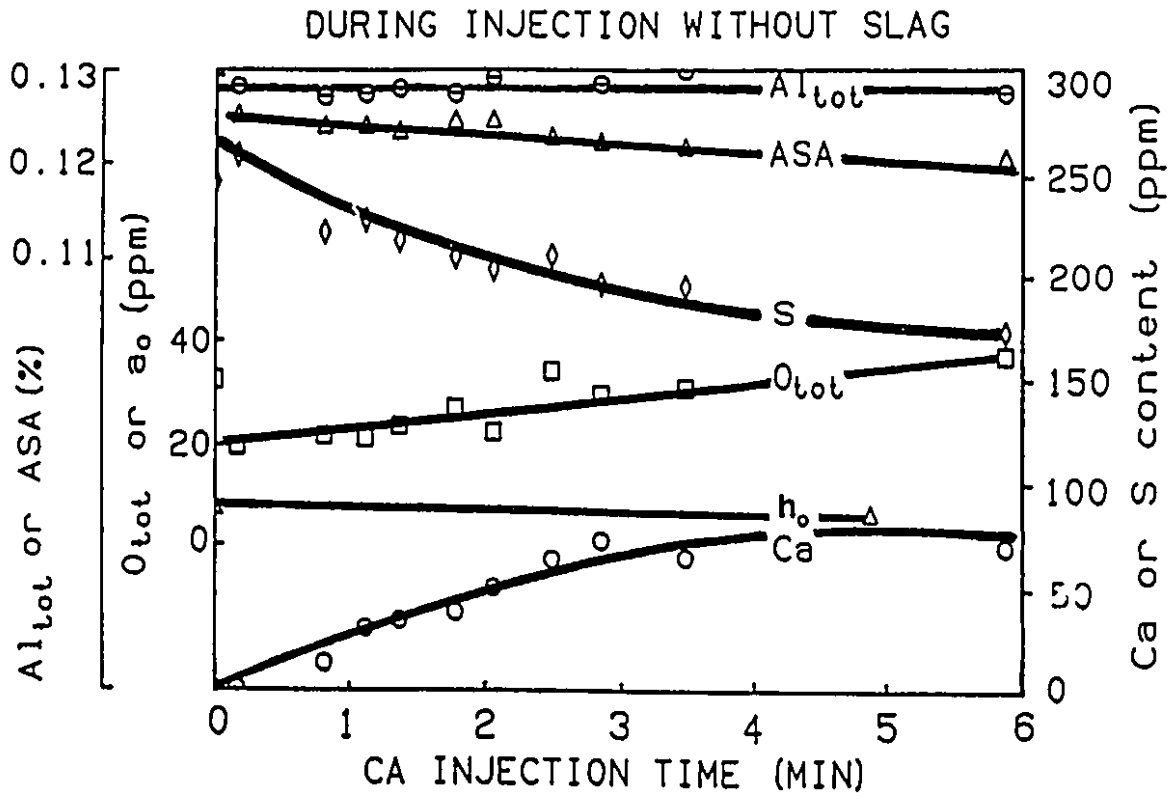

Figure 5.1 The changes of total calcium, oxygen activity, h_o, total oxygen, sulfur content, acid soluble aluminum and total aluminum content for H3R1 (without top slag)

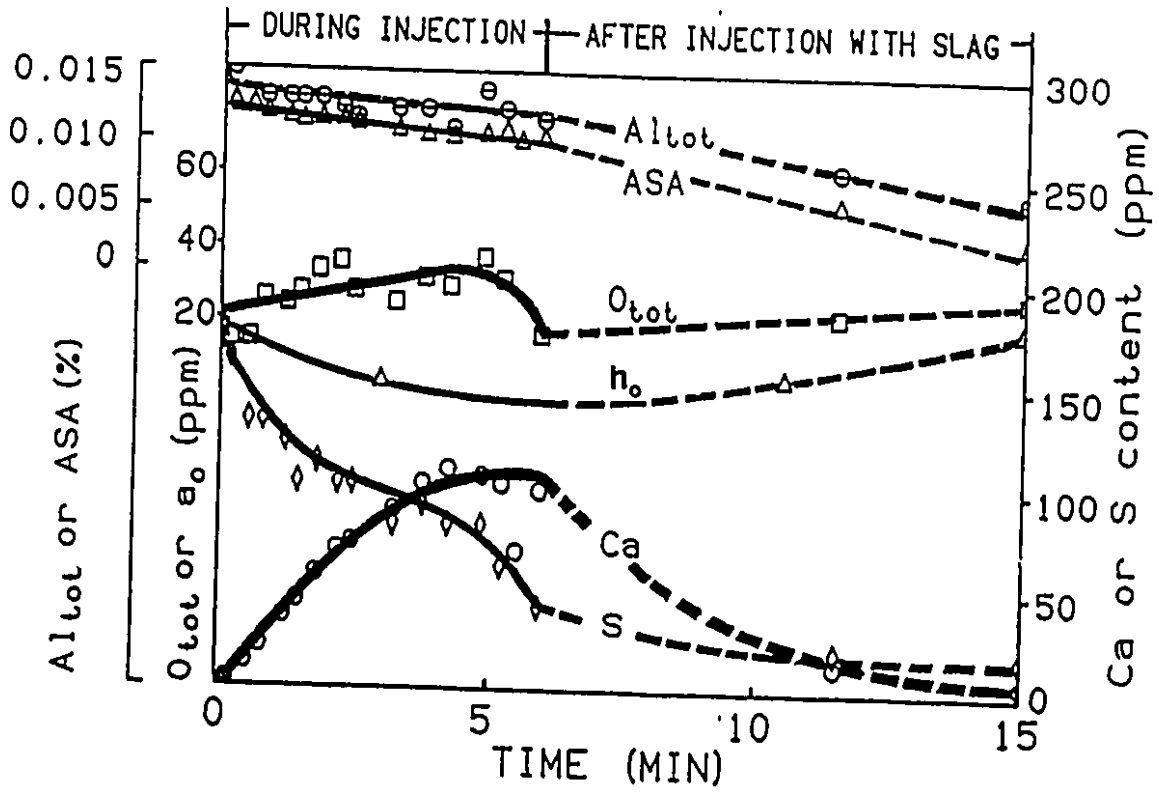

Figure 5.2 The changes of total calcium, oxygen activity, h_o, total oxygen, sulfur content, acid soluble aluminum and total aluminum content for H6R1 (with top slag)

Without Top Slag

There is only one heat (H3R1) with no top slag. At calcium wire feed rate of 0.8 kg Ca/T min, the total calcium increases very rapidly at the beginning of the injection, slows down in the middle of the injection, and then finally levels off at about 80 ppm at the late stage of injection.

Although there is no top slag, the sulfur decreases immediately at the beginning of calcium injection. The average desulphurization rate by calcium for the period of 6 minutes injection is about 15 ppm/min, when the initial sulfur is 0.028%.

The acid soluble aluminum (ASA) decreases continuously, and the total oxygen increases. This indicates that reoxidation occurs during injection, because the interfacial oxygen activity in equilibrium with the partial pressure of oxygen in the chamber (about $1*10^{-4}$ atm) exceeds the oxygen activity in the bulk.

Usually the oxygen activity increases with the falling ASA in the melt according to Al-O equilibrium. However, at the present condition, both ASA and oxygen activity decrease during injection. Which indicates the deoxidation rate by the calcium is faster than the reoxidation rate from the free

surface of the melt.

Total aluminum analysis measures both the dissolved aluminum and the aluminum tied up in the inclusions. Although the portion of aluminum in the inclusions increases due to the reoxidation, the total aluminum remains constant.

With Top Slag

H6R1 is a typical heat, which has 250 grams of top slag before calcium injection. The raw data of other heats is given in Appendix A.

A. During calcium injection period

At a slightly higher calcium feed rate (0.036 kg Ca/min) than that (0.032 kg Ca/min) of the heat (H3R1) without top slag, the changing pattern during injection for all the elements, except the total aluminum, is similar to that in H3R1. The total calcium content increases to approximately 100 ppm, and remains constant. The oxygen activity decreases slightly to approximately 10 ppm, while the total oxygen content increases from 20 to 35 ppm. There is a considerable amount of desulphurization in this heat starting with 0.015% S. However, the total and acid soluble aluminum contents decrease indicating that dissolved aluminum is being consumed,

and that inclusions are being eliminated from the melt to the slag.

B. During the holding period

After injection (keeping the temperature constant and holding the liquid for around 30 minutes), calcium decreases rapidly. After 15 minutes of holding, around 100 ppm of calcium was almost reduced to zero.

The oxygen activity increases due to the reoxidation, and the sulfur tends to be constant.

Both total and acid soluble aluminum still decrease, while the total oxygen increases slightly. This indicates both reoxidation and inclusion flotation continue to occur during the holding period right after calcium injection.

5.1.1 Al Predeoxidation

Various amounts of Al were added to predeoxidize the steel before calcium injection. The Al-O equilibrium reaction is given as:

$$Al_2O_3 = 2\underline{Al} + 3\underline{O} \qquad (5.1)$$

the equilibrium constant is then:

$$K_{Al_2O_3} = \frac{h_{Al}^2 \, h_O^3}{a_{Al_2O_3}} \qquad (5.2)$$

If assume pure Al_2O_3 is formed, h_{Al} and h_O should exhibit a straight linear relationship at certain temperature. The experimental h_{Al}-h_O relationships before calcium injection are shown in Figure 5.3. The linear regression from Figure 5.3 gives the following equation:

$$\log h_{Al} = -1.52 \log h_O - 5.65 , \qquad r^2 = 0.98 \qquad (5.3)$$

where h_O is taken from the oxygen probe readings, and h_{Al} is calculated from the dissolved aluminum and the interactions from the other elements by the following equation. Where the values of interaction coefficients, e_{Al}^i are taken from [53].

$$\log h_{Al} = \log[\%ASA] + 0.045[\%ASA] + 0.056[\%Si] + 0.091[\%C]$$

$$+ 0.012[\%Mn] + 0.025[\%Cr] - 6.6[\%O] + 0.03[\%S] \qquad (5.4)$$

This assumes ASA is the dissolved aluminum content. As discussed in section 4.3.3, in fact some aluminum compounds in steel such as aluminum nitride are also acid soluble. But the common accepted concept ASA is considered to be the dissolved aluminum.

From these results at 1600 ^{0}C, the product of $K_{Al_2O_3} = h_{Al}^2 * h_O^3$ from Figures 5.3 equals $5 * 10^{-13}$, which is very close

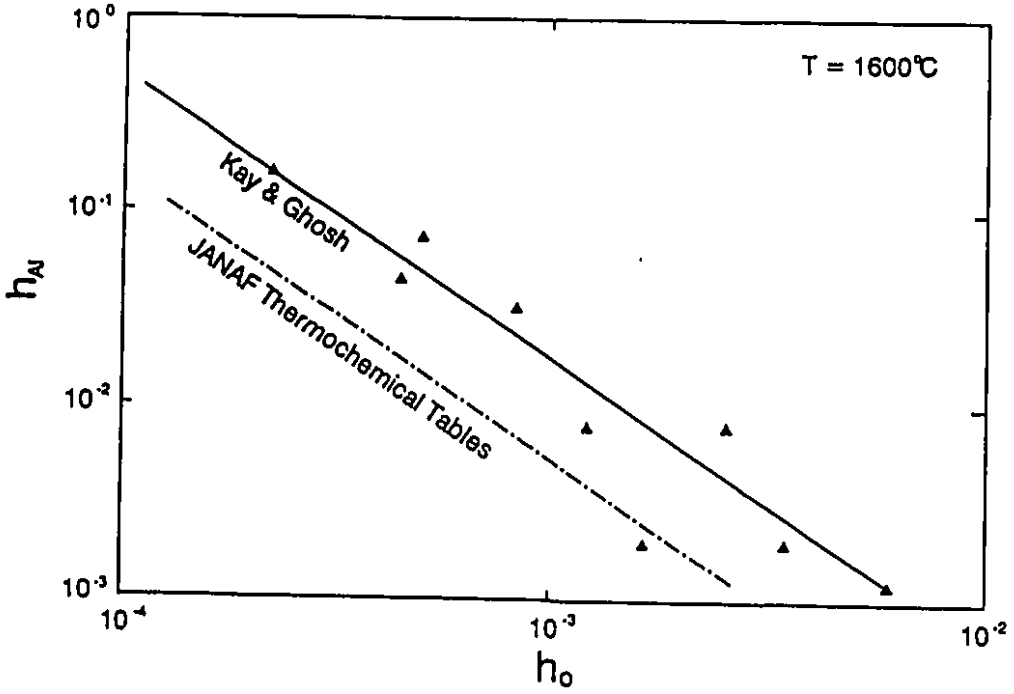

Figure 5.3 The relationship between aluminum activity and oxygen activity before calcium injection. The lines are the thermodynamic equilibrium data from different authors.

to work of Kay and Ghosh [162] ($K_{Al_2O_3}$ = 5.15 *10^{-13} at 1600 ^{0}C).

The consistent relation between h_{Al} and h_O suggests that the results from the oxygen probe are reliable.

5.1.2 Calcium Assimilation Rates

Typically the total calcium content increased rapidly at the beginning of injection, and reached a steady-state value as shown in Figures 5.4 and 5.5. One can also see that both the pick-up rate and steady-state value increase with the calcium feed rate for the same initial aluminum and sulfur contents. Higher injection rate generates deeper penetration of the wire and larger gas-liquid contact area, thus increases the calcium pick-up rate.

The individual effect of the initial sulfur or oxygen on calcium assimilation is quite scattering as shown in Figure 5.6. However, It is also found that the calcium pick-up rate increases with the initial sulfur and dissolved oxygen contents in the melt as shown in Figures 5.7 and 5.8. Figure 5.7 shows that at the same initial aluminum (oxygen) content and calcium feed rate, the calcium pick-up rate increases with the initial sulfur content. Figure 5.7 shows that at the same injection rate, the calcium assimilation rate increases with the summation of both sulfur and oxygen contents. Only the

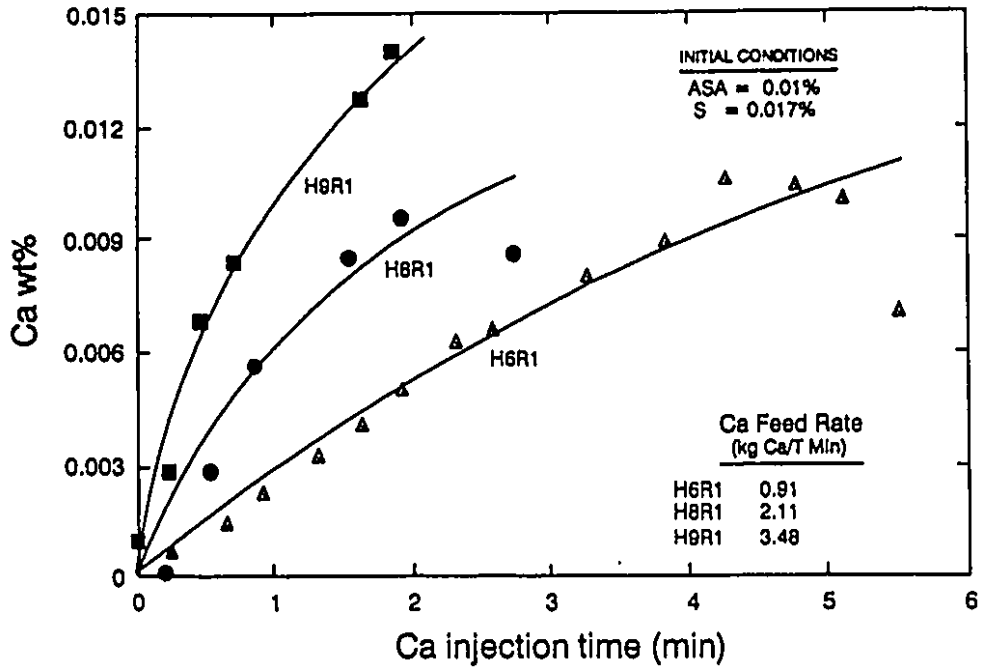

Figure 5.4 The effect of the calcium wire feed rate on the rate of total calcium content pick-up in the steel for three different injections with the same initial sulfur content, 0.017% and acid soluble aluminum content, 0.01%.

CFR1.drw

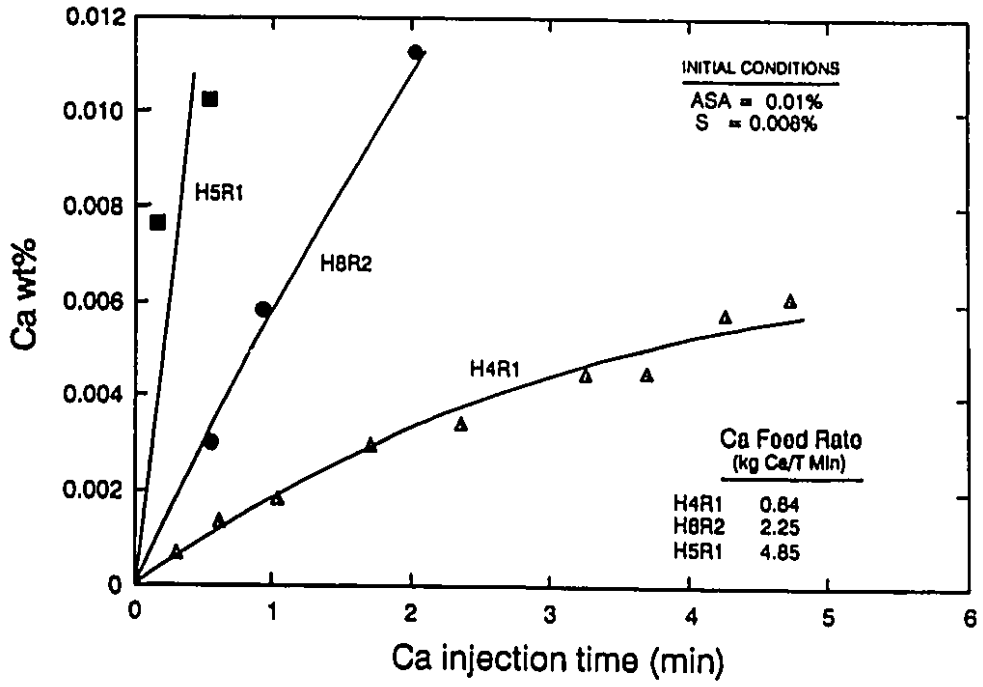

Figure 5.5 The effect of the calcium wire feed rate on the rate of total calcium content pick-up in the steel for three different injections with the same initial sulfur content, 0.008% and acid soluble aluminum content, 0.01%.

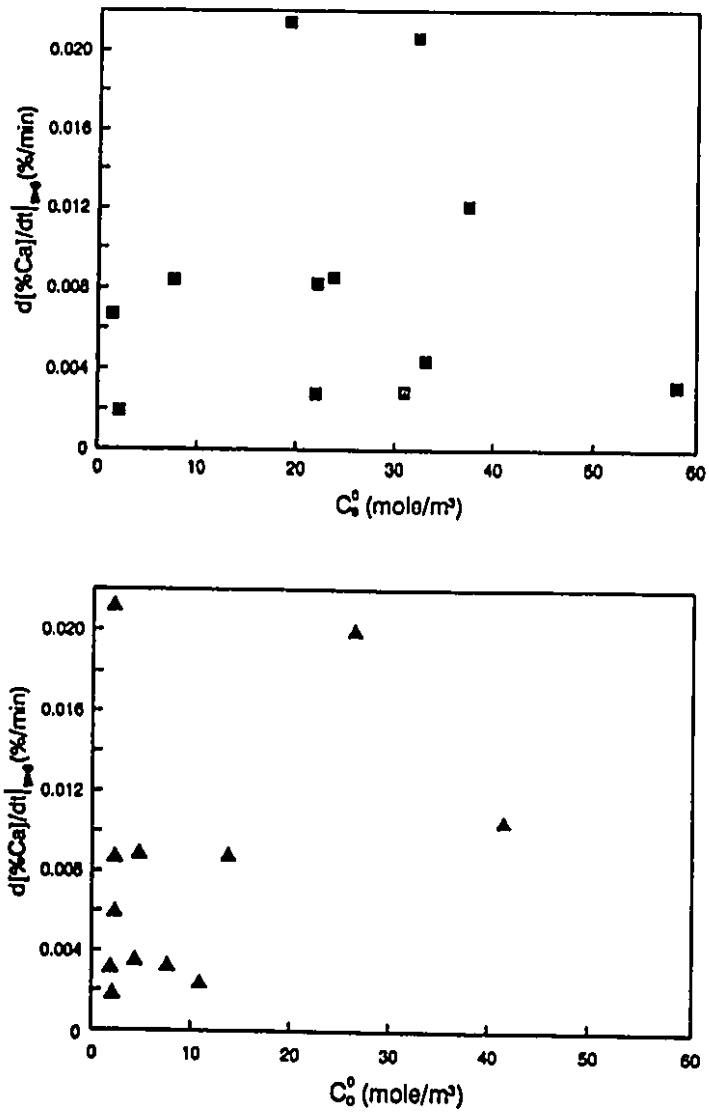

Figure 5.6 The scattering relationship between the initial calcium pick-up rate (%/min) and the individual initial sulfur (TOP) or initial oxygen content (BOTTOM).

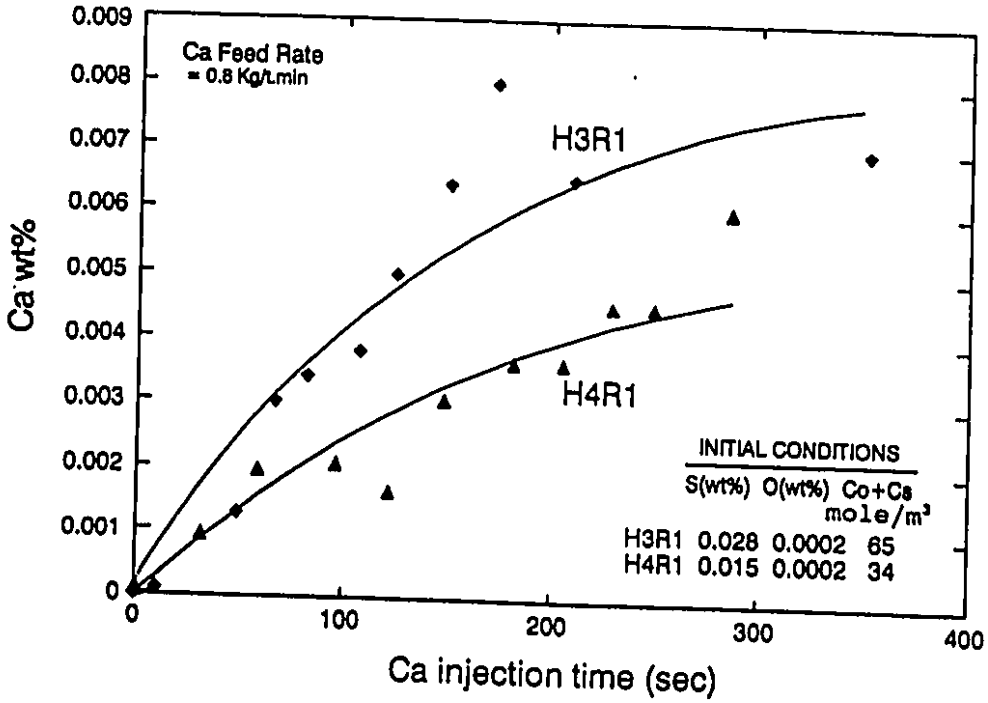

Figure 5.7 The effect of the initial sulfur content on the rate of total calcium content pick-up in the steel for two different injections with the same injection rate, 0.8 kg Ca/t.min, and initial dissolved oxygen activity, 2 ppm.

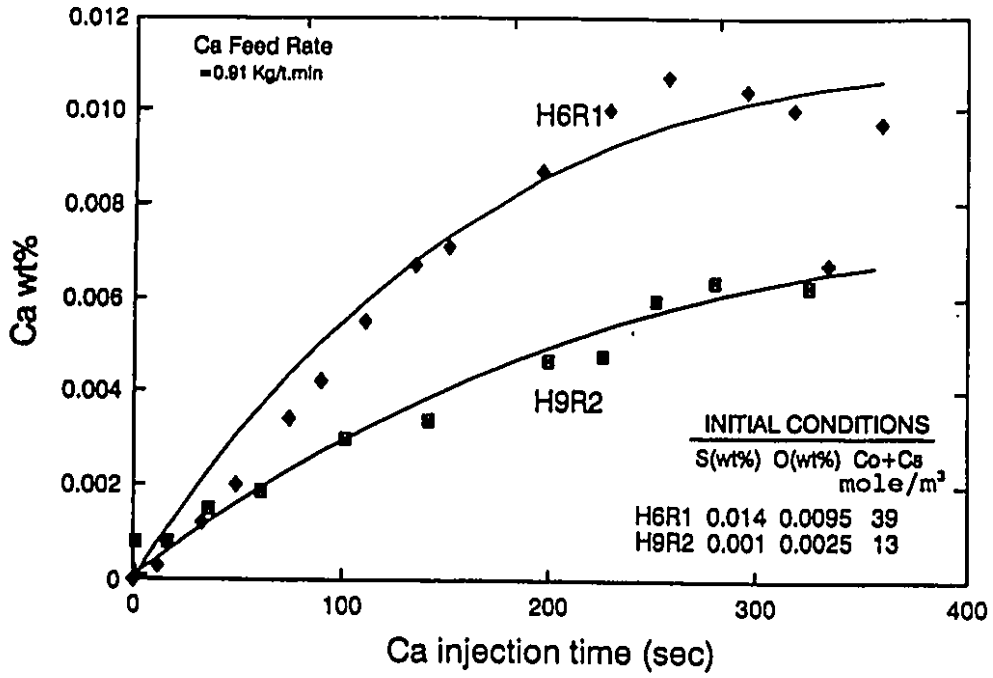

Figure 5.8 The effect of the summation of the both initial sulfur and dissolved oxygen contents on the rate of total calcium content pick-up in the steel for two different injections with the same injection rate, 0.91 kg Ca/t.min.

summation of both oxygen and sulfur shows a strong enhancement to the calcium assimilation rate as shown in Figures 5.7 and 5.8.

The initial tangent of the calcium content - time curve can be used to represent the initial calcium pick-up rate, $d[\%Ca]/dt|_{t=0}$. The unit is in wt% Ca/min. It is assumed as the dependent variable, and the rest of the parameters (Ca feed rate, oxygen and/or sulfur contents, temperature, bath weight, chamber oxygen as listed in Table 5.1) are the independent variables. It is found that calcium feed rate, and the dissolved oxygen and sulfur are the most significant independent variables by using the stepwise multiple linear regression of the MINITAB software. The linear regression equation is:

$$d[\%Ca]/dt|_{t=0} = -(4.904\pm1.17)*10^{-3}+(5.539\pm3.70)*10^{-3}*[CFR] + (5.04\pm2.11)*10^{-5}*\left[(C_0^0+C_S^0)\right] \qquad (5.5)$$

the regression correlation coefficient r = 0.962, and where $d[\%Ca]/dt|_{t=0}$ is the initial calcium assimilation rate in wt%Ca/min. CFR is the Ca Feed Rate in Kg Ca/t·min. $(C_o^0+C_s^0)$ are initial oxygen and sulfur molar concentrations (mole/m^3).

Again it is proved that the individual initial oxygen or

sulfur content was not found to be significant to the initial calcium assimilation rate, which is in consistent with Figure 5.6. The combined term ($C_o^0+C_s^0$) used as an independent variable, and their physical significance is further discussed in Chapter 6 (section 6.2).

Assume that the total calcium in the melt is the dissolved calcium, for a simple dissolution process, the rate of dissolved calcium increase can be expressed as [119]:

$$\frac{d\%Ca}{dt} = K_1(\%Ca^{SAT} - \%Ca) - K_2(\%Ca) \qquad (5.6)$$

where the first term is calcium dissolution and the second term is its elimination, and K_1 and K_2 are the rate constants for calcium dissolution and elimination, respectively. The equilibrium solubility of calcium, $\%Ca^{SAT}$, in AISI 1045 steel was estimated to be 0.024% [6].

The analytical solution for the above equation is:

$$\%Ca = \frac{K_1 * \%Ca^{SAT}}{K_1 + K_2}\left(1 - e^{-\frac{t}{K_1 + K_2}}\right) \qquad (5.7)$$

At initial condition t=0, K_1 can be calculated from the initial slope of Ca-t curve by the following equation.

$$\left.\frac{d\%Ca}{dt}\right|_{t=0} = K_1 * \%Ca^{SAT} \qquad (5.8)$$

At steady-state (calcium curve becomes flat) d%Ca/dt=0, equation 5.6 becomes:

$$K_1(\%Ca^{SAT}-\%Ca^{STD}) = K_2*\%Ca^{STD} \quad (5.9)$$

where $\%Ca^{STD}$ is the steady-state calcium content, so that from the above equation, the apparent value of K_2 can also be obtained. The values of both K_1 and K_2 are shown in Figure 5.9. This diagram shows that calcium pick-up rate, K_1, increases rapidly with feed rate while the elimination rate, K_2, is relatively independent of the calcium feed rate. However, the dependence of K_1 on calcium feed rate is quite scattering. For example, at same 0.9 kg Ca/T.min calcium injection rate, K_1 varies from 0.001 s^{-1} for one injection to 0.0045 s^{-1} for the another injection. This scatter is due to the effect of the initial sulfur and oxygen on the calcium pick-up rate.

5.1.3 Calcium Fading Rates

During the holding period, the calcium content decreased rapidly with time. When the calcium content is plotted in logarithm scale against time, a straight line with the slope K_2' is obtained, as shown in Figure 5.10. That means the calcium content after injection follows the first-order decay. Its rate of decay can then be expressed by the following equation:

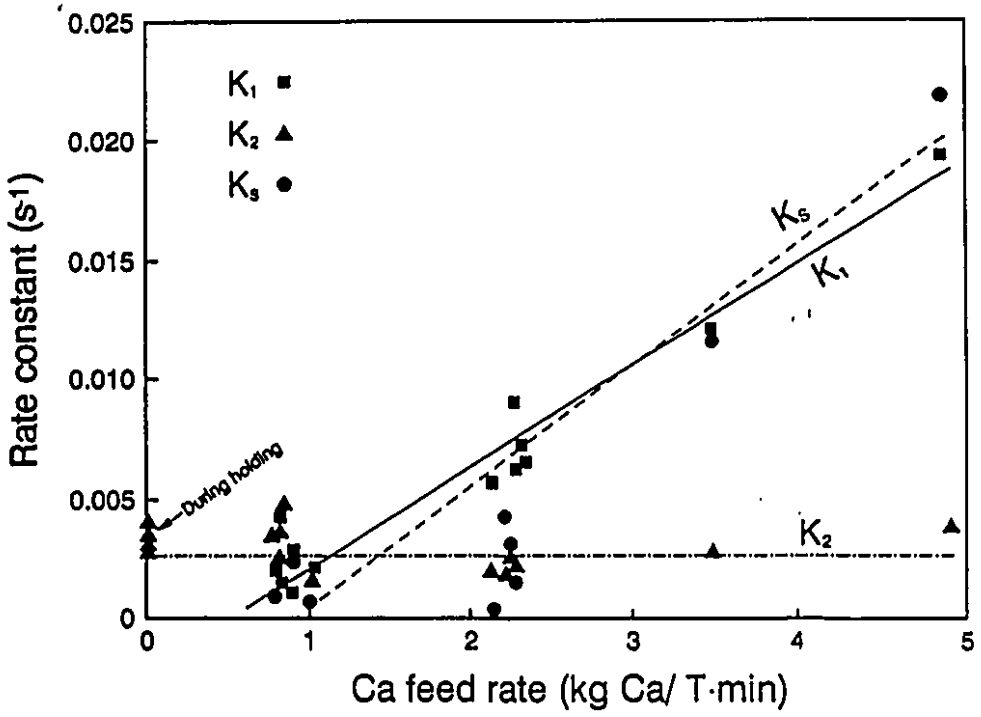

Figure 5.9 The apparent rate constants for calcium absorption, K_1, and calcium elimination, K_2, and desulphurization, K_3, as a function of the calcium feed rate.

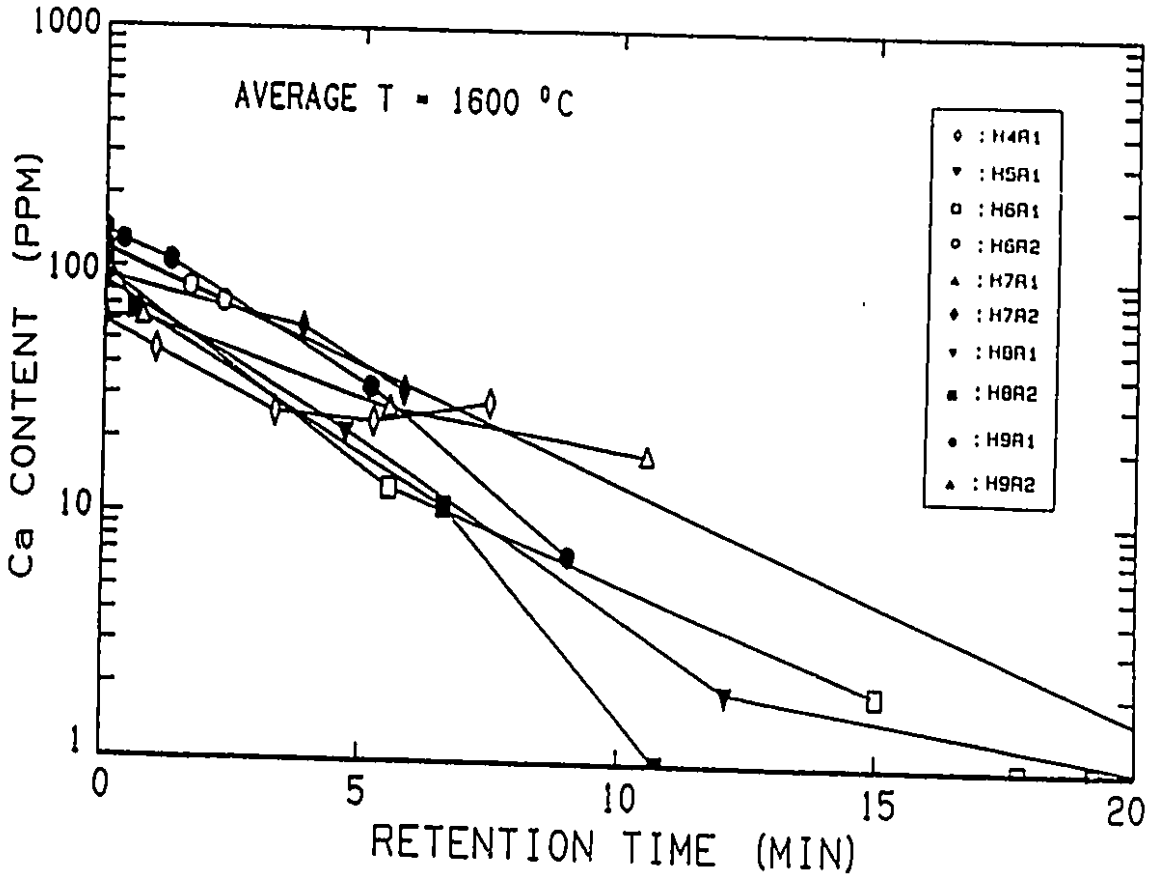

Figure 5.10 The logarithm of the total calcium content as a function of time during the holding period after calcium injection.

$$\frac{d\%Ca}{dt} = -K_2'(\%Ca) \qquad (5.10)$$

The average slope of these lines yields an apparent, first-order rate constant K_2' of $5\pm2.5*10^{-3}$ s^{-1}, which agrees well with the elimination rate constants in Figure 5.9 extrapolated to zero feed rate. That indicates the calcium decay theory for both injection and holding periods obeys the same principle.

According to Machlin's Model [117] for the vaporization of a dissolved element from the inductively stirred melts, the calcium vaporization rate constant, k_{evp}, can be calculated by equation 2.60.

$$K_{evp} = 2\left(\frac{2D_{Ca}\langle U\rangle}{\pi R_c}\right)^{\frac{1}{2}} \qquad (5.11)$$

On the basis of the similarity of the experimental conditions (size of crucible and the induction power input) of Irons' work [119], the mean radial velocity is estimated to be 0.20 m/s. The k_{evp} value is then calculated as $4.1*10^{-4}$ s^{-1} for the present conditions (R_c = 0.09 m and D_{Ca}= 10^{-9} m^2/s). This value of K_{evp} based on the molecular diffusion is more than one order of magnitude smaller than the actual rate constant K_2'. This means that the actual decay of the total calcium is other than the molecular diffusion. It may be due to the flotation of calcium containing inclusions from the melt. This will be further discussed with regard to the mechanism in the

following chapter.

5.1.4 Deoxidation and Desulphurization Rates

The dependence of desulphurization and deoxidation on the calcium feed rate and the initial ASA (or initial oxygen activity) is shown in Figures 5.11 and 5.12 respectively. Figure 5.11 shows both deoxidation and desulphurization rates increase with the calcium feed rate, and Figure 5.12 shows both rates increase with the increase of the initial ASA content (or the decrease of the initial oxygen activity), for the same calcium feed rate.

The sulfur content is plotted in logarithm scale in Figure 5.13. The rate of desulphurization is close to the first order expression:

$$\frac{d\%S}{dt} = -K_S(\%S) \qquad (5.12)$$

where K_S is the rate constant for desulphurization. This rate constant increases rapidly with calcium feed rate as shown in Figure 5.9, and furthermore is very similar for the observed K_1 values. However, the dependence of K_S is also quite scattering, especially at the lower initial ASA content (the higher a_o). The desulphurization also appears to depend on the oxygen content in the melt. This close relationship will be discussed with respect to the mechanism in section 6.2.

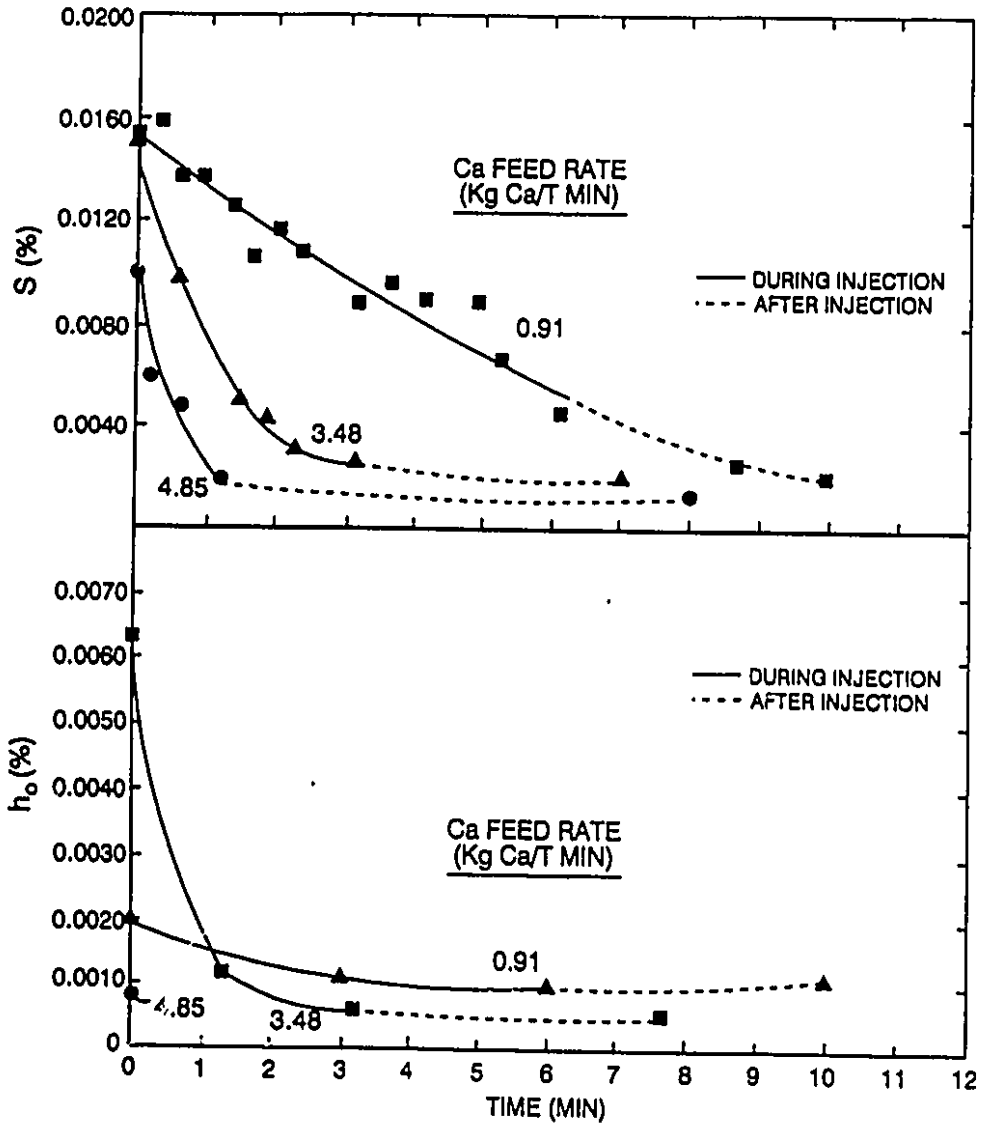

Figure 5.11 The effect of calcium feed rate on the desulphurization (TOP) and changes in oxygen activity (BOTTOM).

SOaL.DRW

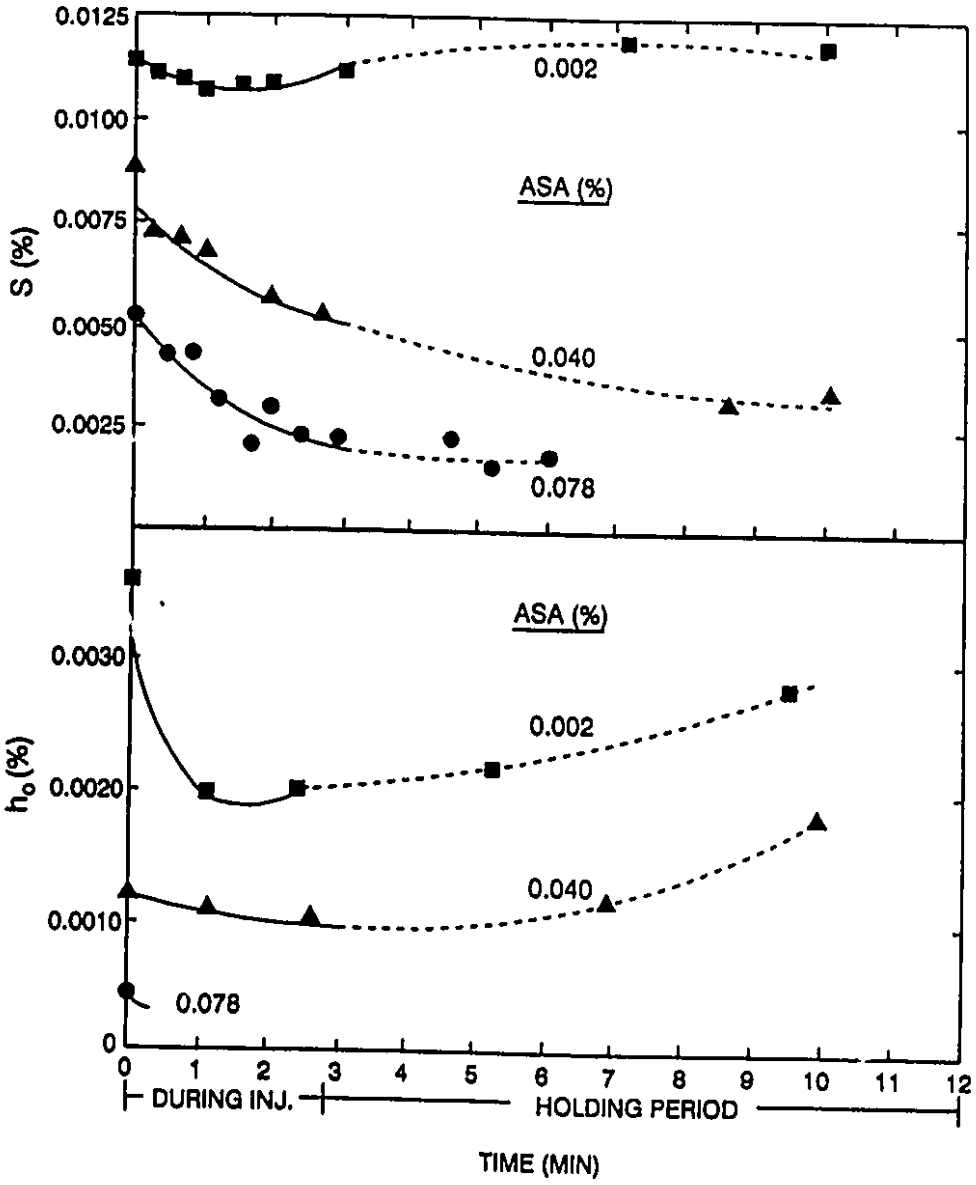

Figure 5.12 The effect of acid soluble aluminum on the desulphurization (TOP) and changes in oxygen activity (BOTTOM).

logS.DRW

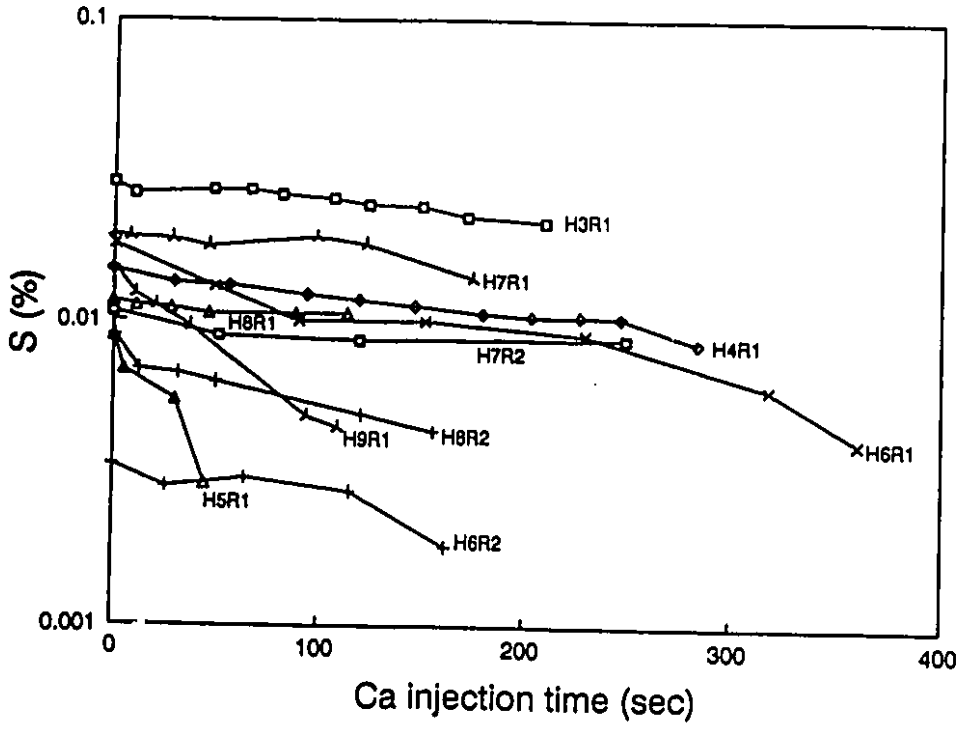

Figure 5.13 The logarithm of the sulfur content as a function of time during injection, showing the first-order kinetics.

5.2 INCLUSION DISTRIBUTION AND CHEMICAL ANALYSIS

Qualitatively, two heats (H2R1 and H3R1) with relatively high initial ASA (0.13%) and sulfur (0.028%) contents were examined under the normal SEM (without LINK System) and the optical microscope to study the changing patterns of Al_2O_3 inclusions. Some of those inclusion pictures with the energy levels of the significant elemental x-ray peaks are shown in Figures 5.14-15. There is very little change of Al_2O_3 with calcium addition in the melt, even though the total calcium reached 60 ppm. In other words, at higher initial ASA and sulfur contents, aluminum oxide modification by calcium is very slow or limited. The mechanism is discussed in the next chapter.

For the cases where both initial ASA and S contents are modest, about eight samples from each of the four complete heats (H6R1, H6R2, H7R1 and H7R2) were examined quantitatively for inclusion distributions and chemical compositions. Six samples with the same bulk total calcium content, but three with different ASA contents, and the other three with different S contents, from three different heats (H6R1, H7R2 and H9R1) were also analyzed in detail to study the effect of the different ASA and S contents in the bulk on the inclusion chemistry and distribution.

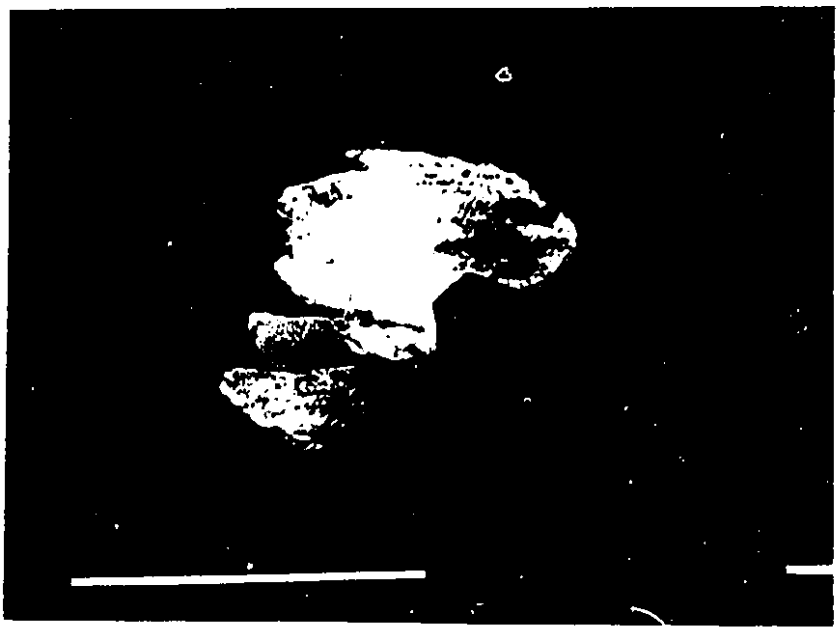

H2S3P3 Spectrum:		Al_2O_3
Energy	Counts	X-Ray Lines
1.5	63062	A1 KA1, A1 KA2, BR LA1, BR LA2, BR LB1, YB MA1, YB MA2.
6.40	635	Fe KA1, Fe KA2.

Figure 5.14 The SEM photo and x-ray energy level of Al and Fe (matrix) spectrums of Al_2O_3 inclusion during injection in H2R1. The sample contains 0.13% ASA, 0.03% S and 0.005% Ca.

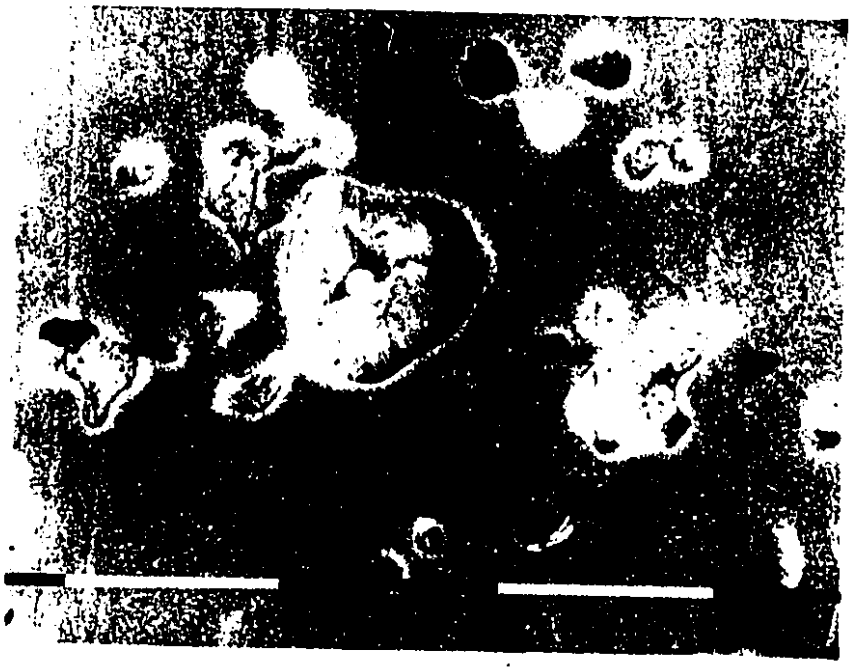

H3S6P3 X2980 1 Bar = 10 μm

H2S6P3 Spectrum:		Al_2O_3
Energy	Counts	X-Ray Lines
1.49	3584	A1 KA1, A1 KA2, BR LA1, BR LA2.
6.40	55968	Fe KA1, Fe KA2.
7.05	7384	Fe KB1.

Figure 5.15 The SEM photo and x-ray energy level of Al and Fe (matrix) spectrums of Al_2O_3 clusters during injection in H3R1. The sample contains 0.128% ASA, 0.028% S and 0.006% Ca.

Under the LINK System, 40 fields for each sample were examined under the magnification of 2000, in order to obtain a reasonably accurate statistical analysis. A statistical summary of the inclusion size distribution and area fraction for total and each inclusion class, from a typical sample is shown in Table 5.2. In the same sample, several different types of inclusions were found. For example, there were pure CaS (Figure 5.16) and CaO (Figure 5.17), coexisting with unmodified MnS (Figure 5.18) and Al_2O_3. However, complex oxy-sulfides $CaS{\cdot}CA_x$ (Figure 5.19) and $(Ca,Mn)S{\cdot}CA_x$ (Figure 5.20), and pure (Ca,Mn)S were also present.

5.2.1 Area and Volume Fractions of Inclusions

Table 5.2 did not show the volume fraction of inclusion, however it can be calculated using Underwood's method [163] for the spherical particle distributions. The basic principle lies in relating the number of sections observed on the plane of polish in unit area to the number of spheres in unit volume: The particles sizes may be broken down into n groups, and the term Δ is used as the ratio of the maximum diameter D_{max} to n. The intersection of particles of the jth group (diameters equal to $j\Delta$) may form sections of the ith group (diameters ranging between $(i-1)\Delta$ and $i\Delta$). By successive substitution of integer values of j and i, with the coefficients provided in reference[163], the numbers and volume

TABLE 5.2

STATISTICAL SUMMARY OF INCLUSIONS FROM A TYPICAL SAMPLE

Heat no. = H6R1, Sample no. = 11, X-Ray window file = MnSAlCa, Standards file = Mac, 20 Fields analyzed.

MEAN DIAMETER DISTRIBUTION (μm)		
BIN	RANGE (μm)	AREA%
1	0 to 0.5	0.0221
2	0.5 to 1.0	0.0301
3	1.0 to 1.5	0.0135
4	1.5 to 2.0	0.0119
5	2.0 to 2.5	0.0106
6	2.5 to 3.0	0.0104
7	3.0 to 3.5	0.0083
8	3.5 to 4.0	0.0000
9	4.0 to 4.5	0.0000
10	greater than 4.5	0.0000
Total		0.1068

CHEMICAL CLASSIFICATION:	
INCLUSION CLASS	AREA %
1: MnS	0.0053
2. CaS	0.0234
3. CaO	0.0212
4. Al2O3	0.0058
5. (Ca,Mn)S	0.0217
6. CAx	0.0014
7. CaS·CAx	0.0084
8. (Ca,Mn)S·CAx	0.0043
9. unclassified	0.0153
Total	0.1068

HISTOGRAM SUMMARY

CLASS	BIN NO. = 1	2	3	4	5	6	7	8	9	10
MnS	32	9	2	1	0	0	0	0	0	0
CaS	18	30	7	1	2	1	0	0	0	0
CaO	97	26	2	0	0	0	1	0	0	0
Al2O3	36	12	1	0	0	0	0	0	0	0
(Ca,Mn)S	19	22	2	3	1	2	0	0	0	0
CAx	6	6	0	0	0	0	0	0	0	0
CaS·CAx	5	4	3	2	1	0	0	0	0	0
(Ca,Mn)S·CAx	1	3	2	0	1	0	0	0	0	0
unclassified	94	22	1	0	0	0	0	0	0	0
Total	308	134	20	7	5	3	1	0	0	0

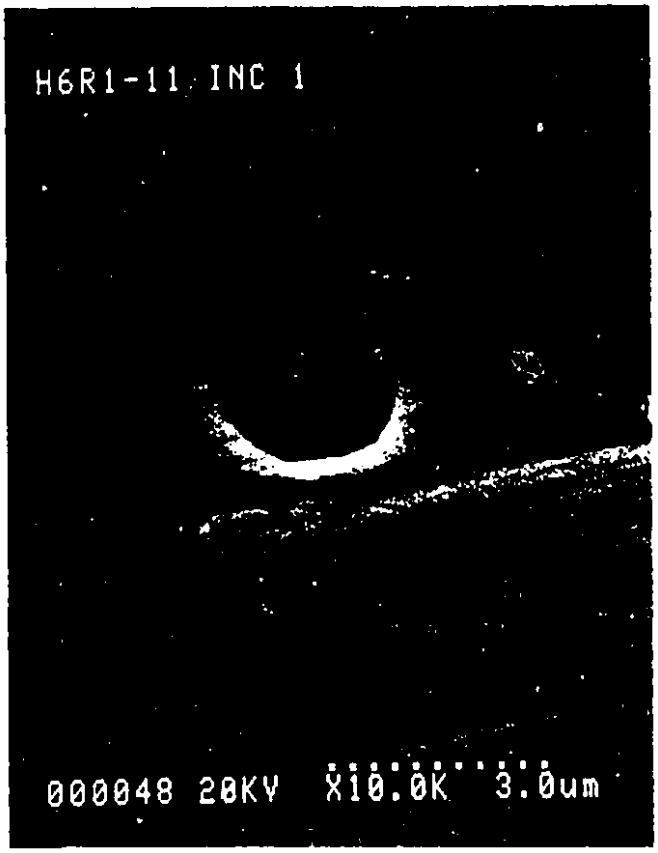

Incl Spectrum: CaS (trace of MnS)

ELMT	ZAF	%ELMT	ATOM.%
CaK : 0	0.924	49.34	44.40
AlK : 0	0.803	4.25	4.67
MnK : 0	0.789	5.19	3.41
S K : 0	0.987	40.42	45.46
SiK : 0	0.718	0.18	0.43
MgK : 0	0.699	0.62	1.63
TOTAL		100.0	100.0

Figure 5.16 An SEM photo of CaS inclusion and its quantitative composition from ZAF analysis.

Inc2 Spectrum: CaO

ELMT	ZAF	%ELMT	ATOM.%
CaK : 0	1.225	76.86	95.27
AlK : 0	0.576	0.45	0.83
MnK : 0	0.758	3.00	2.72
S K : 0	1.287	0.00	0.00
SiK : 0	0.717	0.67	1.18
MgK : 0	0.647	0.00	0.00
TOTAL		80.98	100.0

Figure 5.17 An SEM photo of CaO inclusion and its quantitative composition from ZAF analysis.

Inc3 Spectrum: MnS

ELMT	ZAF	%ELMT	ATOM.%
CaK : 0	0.994	0.43	0.47
AlK : 0	0.615	0.21	0.33
MnK : 0	0.912	62.86	49.72
S K : 0	0.934	36.51	49.48
SiK : 0	0.950	0.00	0.00
MgK : 0	0.484	0.00	0.00
TOTAL		100.0	100.0

Figure 5.18 An SEM photo of MnS inclusion and its quantitative composition from ZAF analysis.

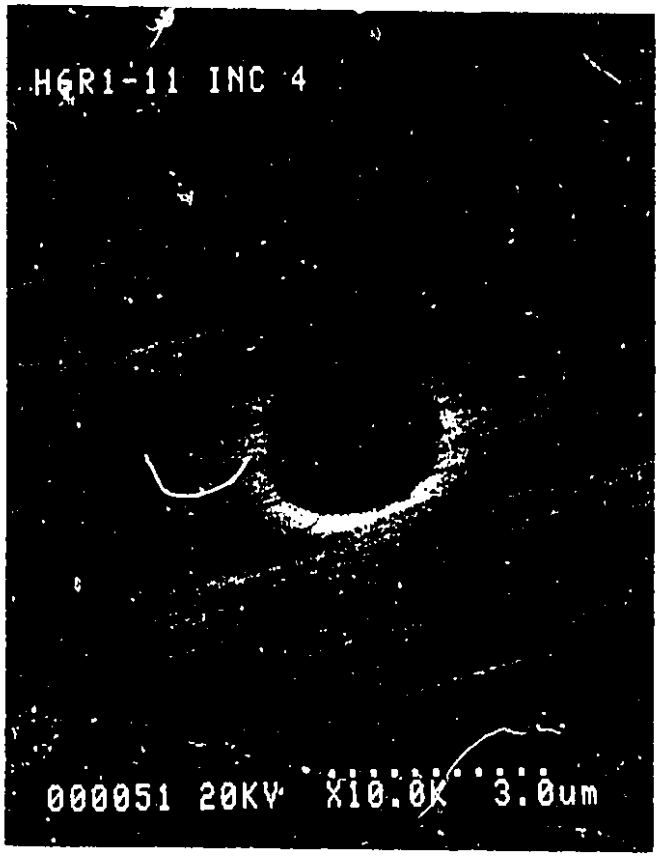

Inc4 Spectrum: $CaS{\cdot}CA_x$

ELMT	ZAF	%ELMT	ATOM.%
CaK : 0	0.928	49.90	43.91
AlK : 0	0.809	9.90	12.94
MnK : 0	0.788	3.48	2.24
S K : 0	0.951	35.22	38.74
SiK : 0	0.716	0.74	1.20
MgK : 0	0.720	0.75	0.97
TOTAL		100.0	100.0

Figure 5.19 An SEM photo of $CaS{\cdot}CA_x$ inclusion and its quantitative composition from ZAF analysis.

Inc5 Spectrum: (Ca,Mn)S·CA_x

ELMT	ZAF	%ELMT	ATOM.%
CaK : 0	0.927	20.48	17.05
AlK : 0	0.758	38.66	47.82
MnK : 0	0.829	17.58	10.68
S K : 0	0.783	22.94	23.88
SiK : 0	0.798	0.24	0.55
MgK : 0	0.744	0.10	0.02
TOTAL		100.0	100.0

Figure 5.20 An SEM photo of (Ca,MnS)·CA_x inclusion and its quantitative composition from ZAF analysis.

of particles in unit volume for spheres can be calculated, in relating to the number of sections in unit area.

Total Inclusions

The area and volume fractions of the total inclusions as a function of time, for heats of H6R1, H6R2, H7R1 and H7R2 are presented in Figures 5.21 - 5.24. It can been seen that in all those heats both area and volume fractions start to increase with the injection time, reach maximum values and then decrease again. Both those maximum values occur at shorter times for increased calcium feed rate. This means the inclusion generating rate is faster than the elimination rate at the beginning of injection, and the reverse is true at the later stage of injection. After injection, the area and volume fractions of the total inclusions decrease as inclusions flotation becomes the dominating factor.

Each Inclusion Type

The most striking feature of the present inclusion image is the coexistence of several different types of inclusions found in the same sample. Figure 5.25-28 show the changes of area and volume fraction of the various types of inclusions including Al_2O_3, MnS, CA_x, CaS, CaO, (Ca,Mn)S and (Ca,Mn)S·CA_x as a function of time. In all the heats examined, the original

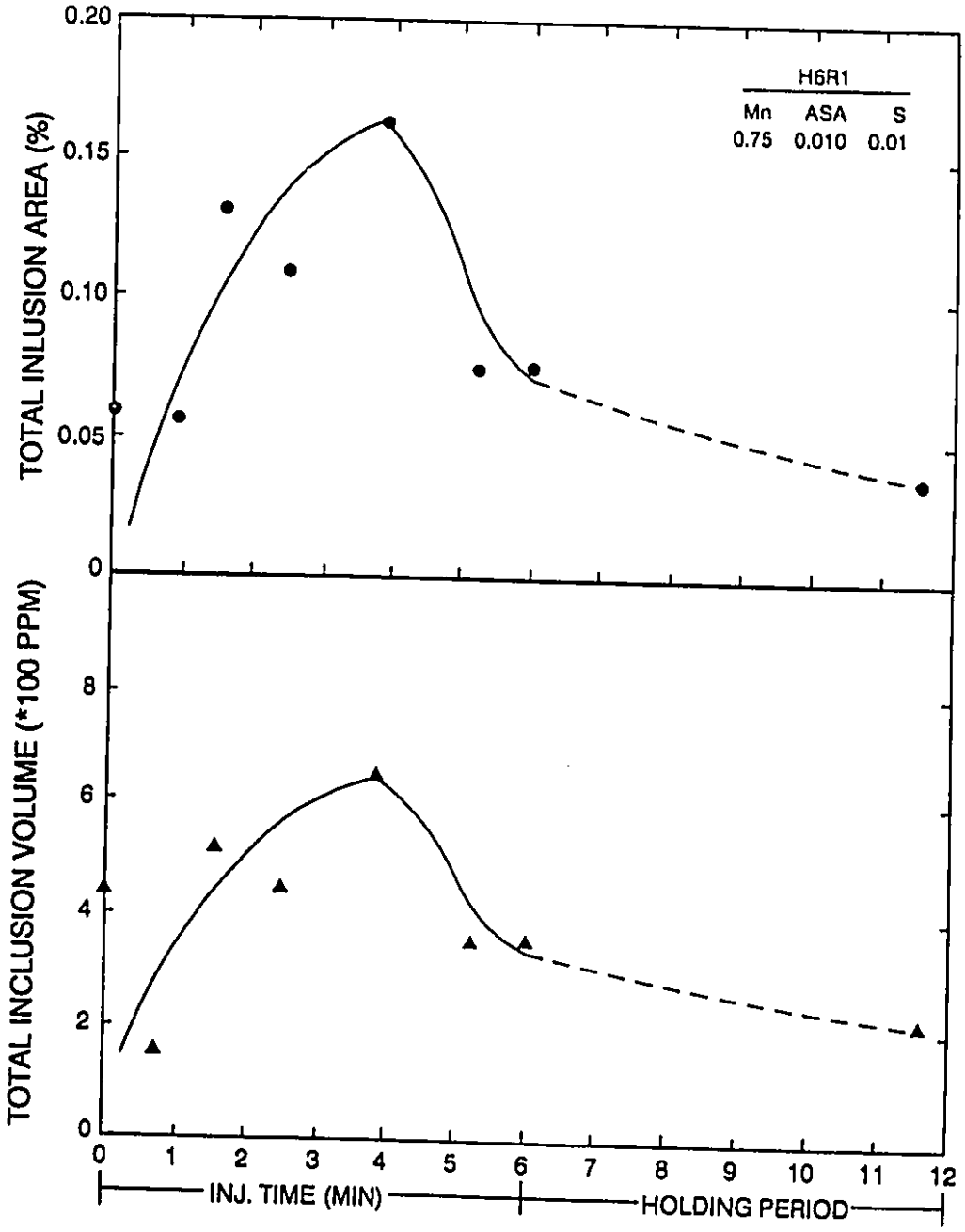

Figure 5.21 The changes of the total inclusion area fraction (TOP) and calculated volume fraction (BOTTOM) during and after injection for H6R1.

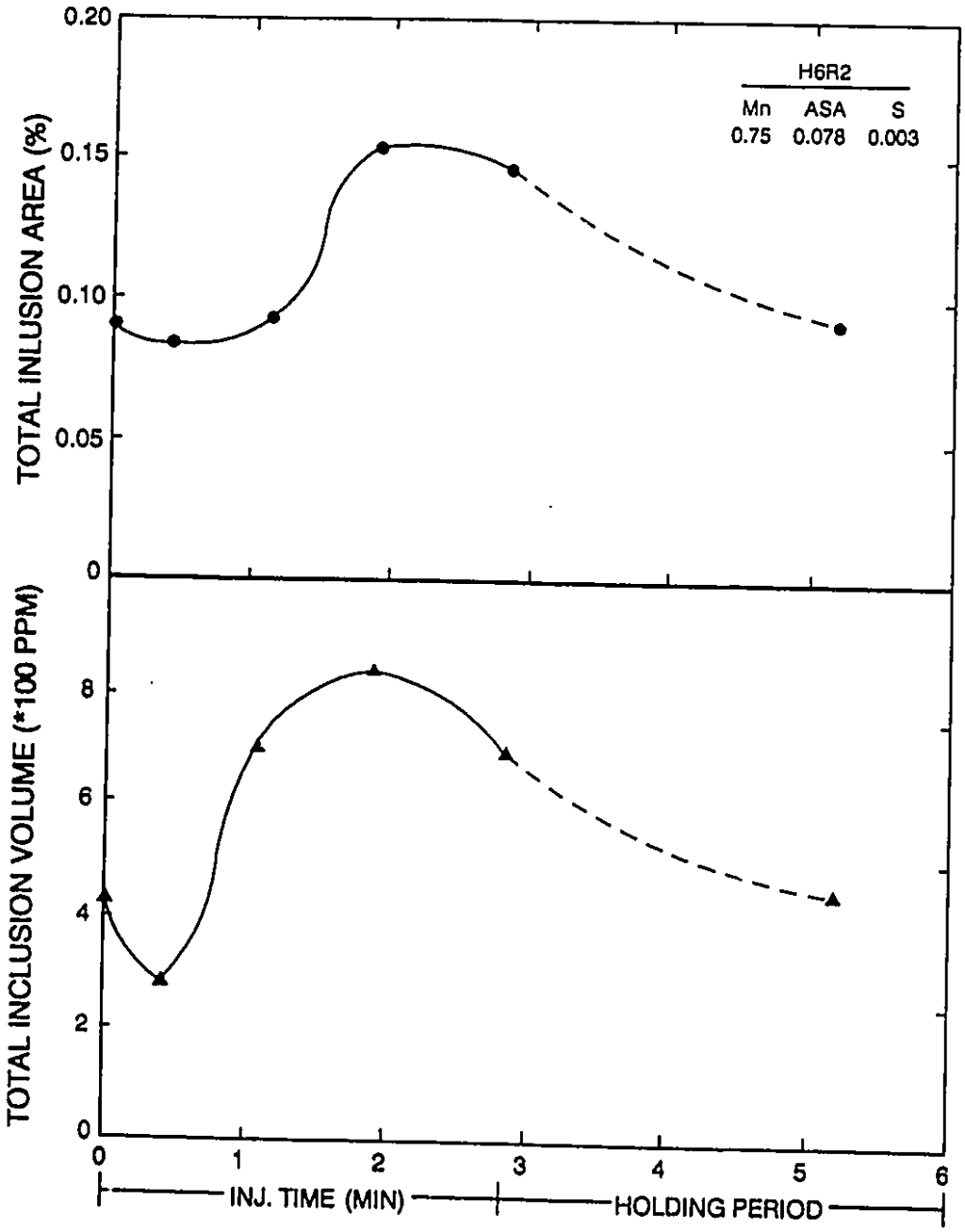

Figure 5.22 The changes of the total inclusion area fraction (TOP) and calculated volume fraction (BOTTOM) during and after injection for H6R2.

H71AREAV.DRW

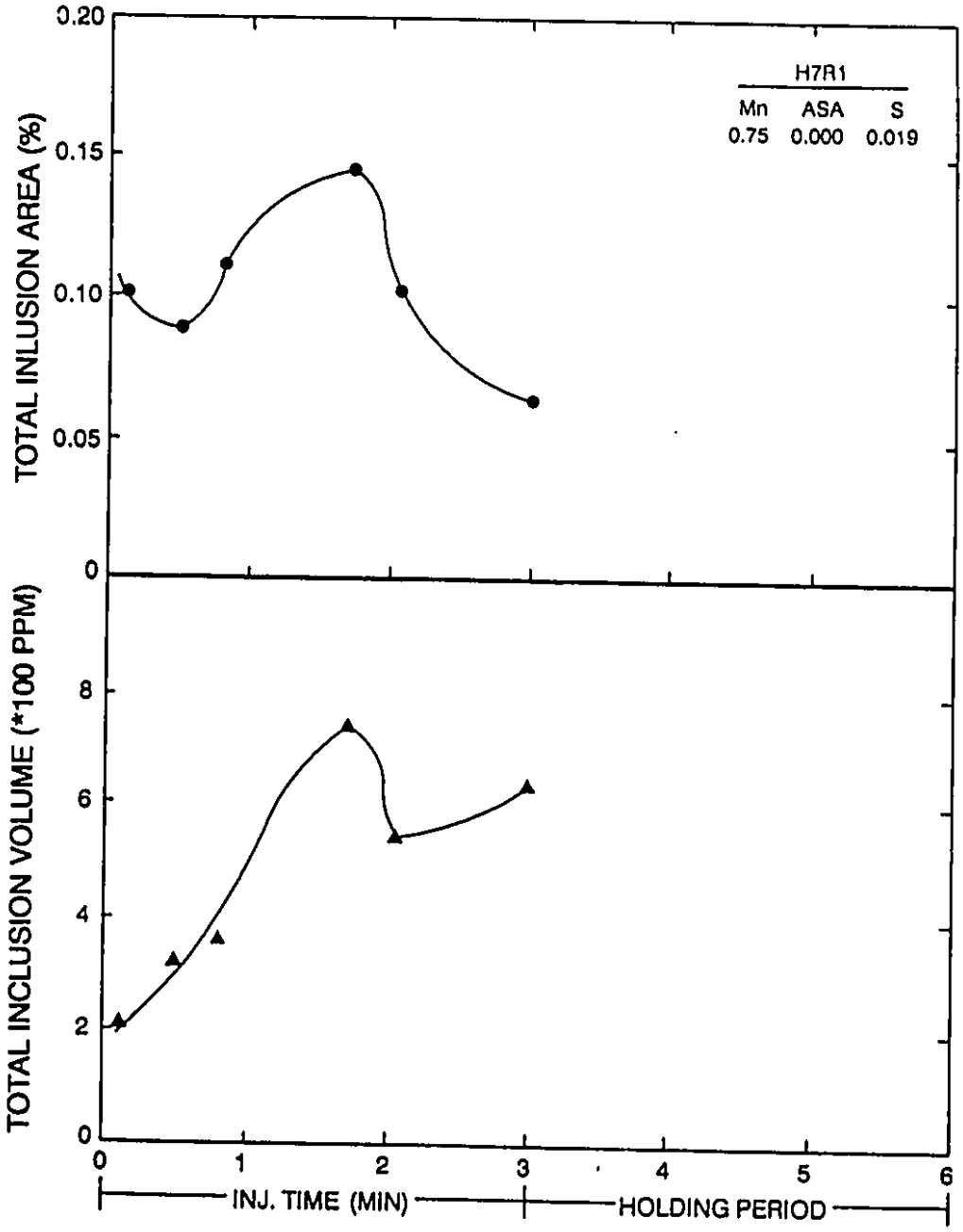

Figure 5.23 The changes of the total inclusion area fraction (TOP) and calculated volume fraction (BOTTOM) during and after injection for H7R1.

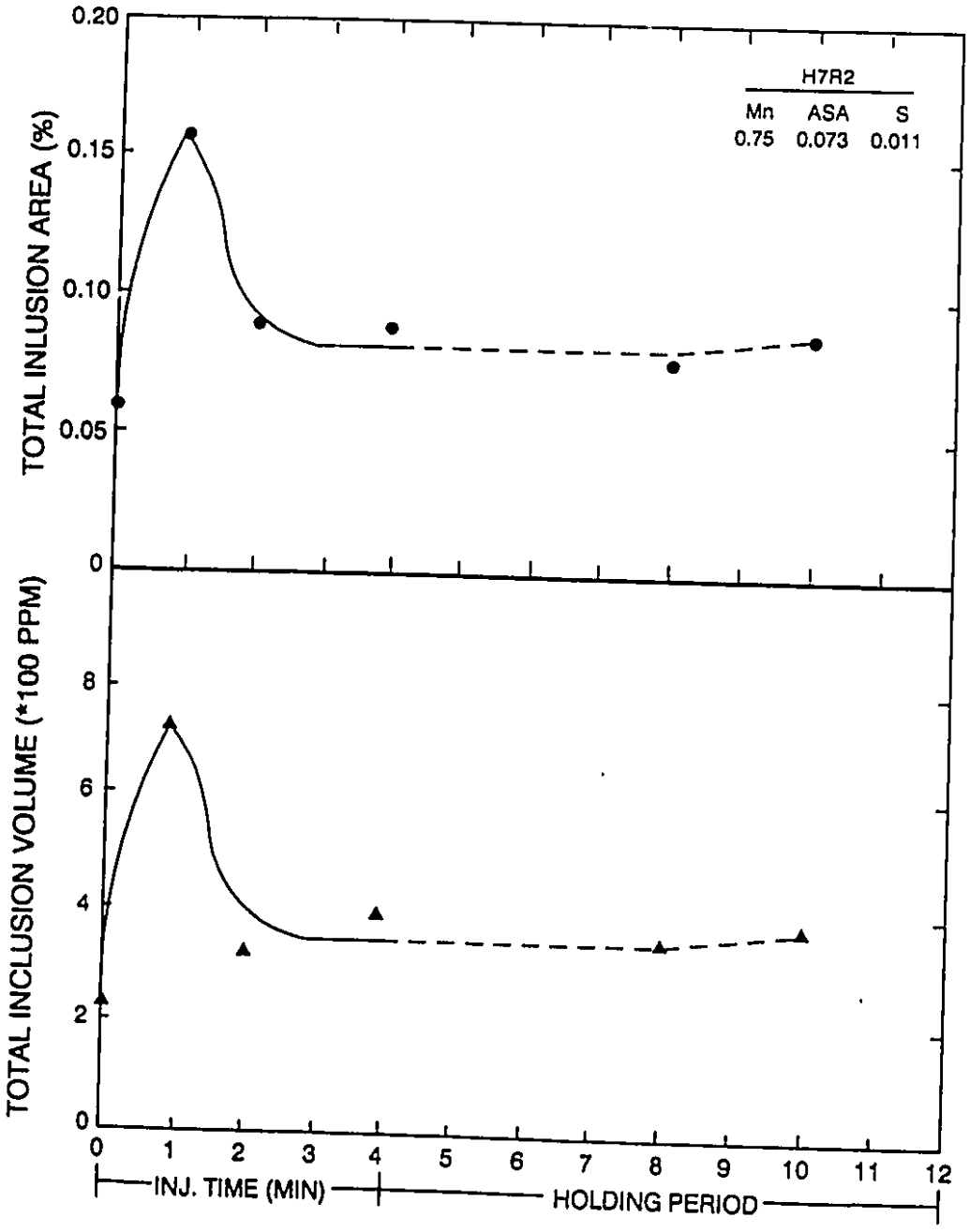

Figure 5.24 The changes of the total inclusion area fraction (TOP) and calculated volume fraction (BOTTOM) during and after injection for H7R2.

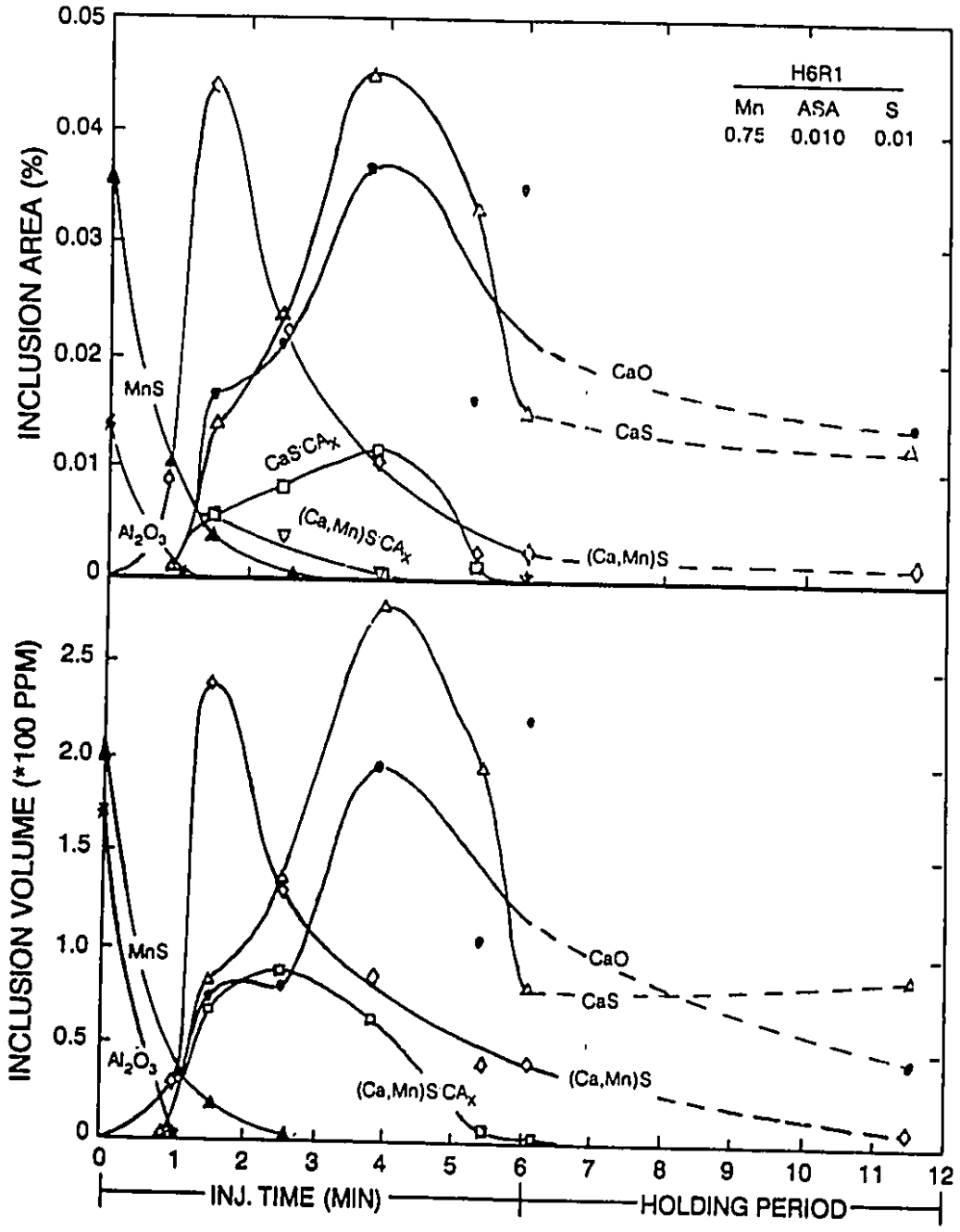

Figure 5.25 The changes of area fraction (TOP) and volume fraction (BOTTOM) of the each inclusion type during and after injection for H6R1.

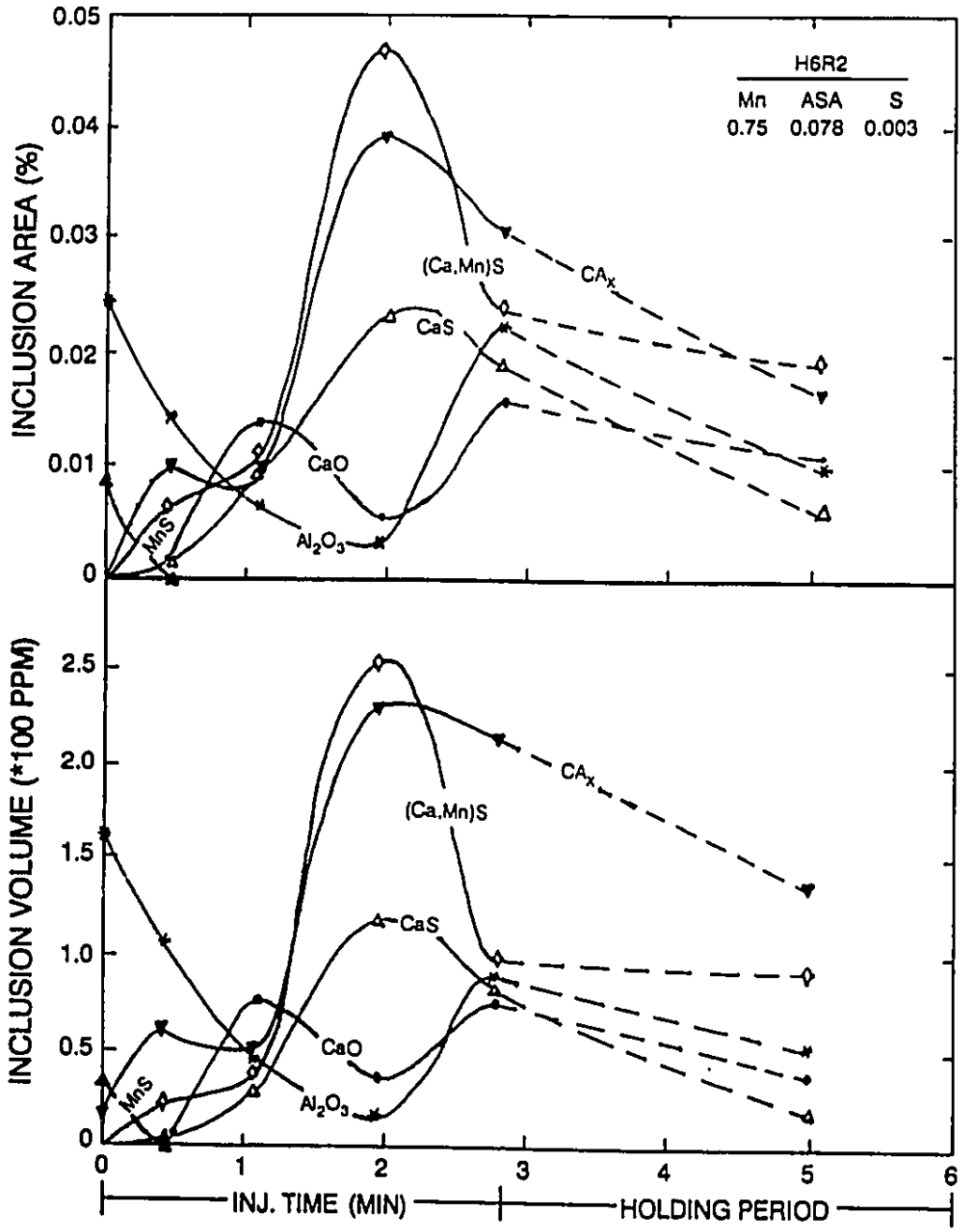

Figure 5.26 The changes of area fraction (TOP) and volume fraction (BOTTOM) of the each inclusion type during and after injection for H6R2.

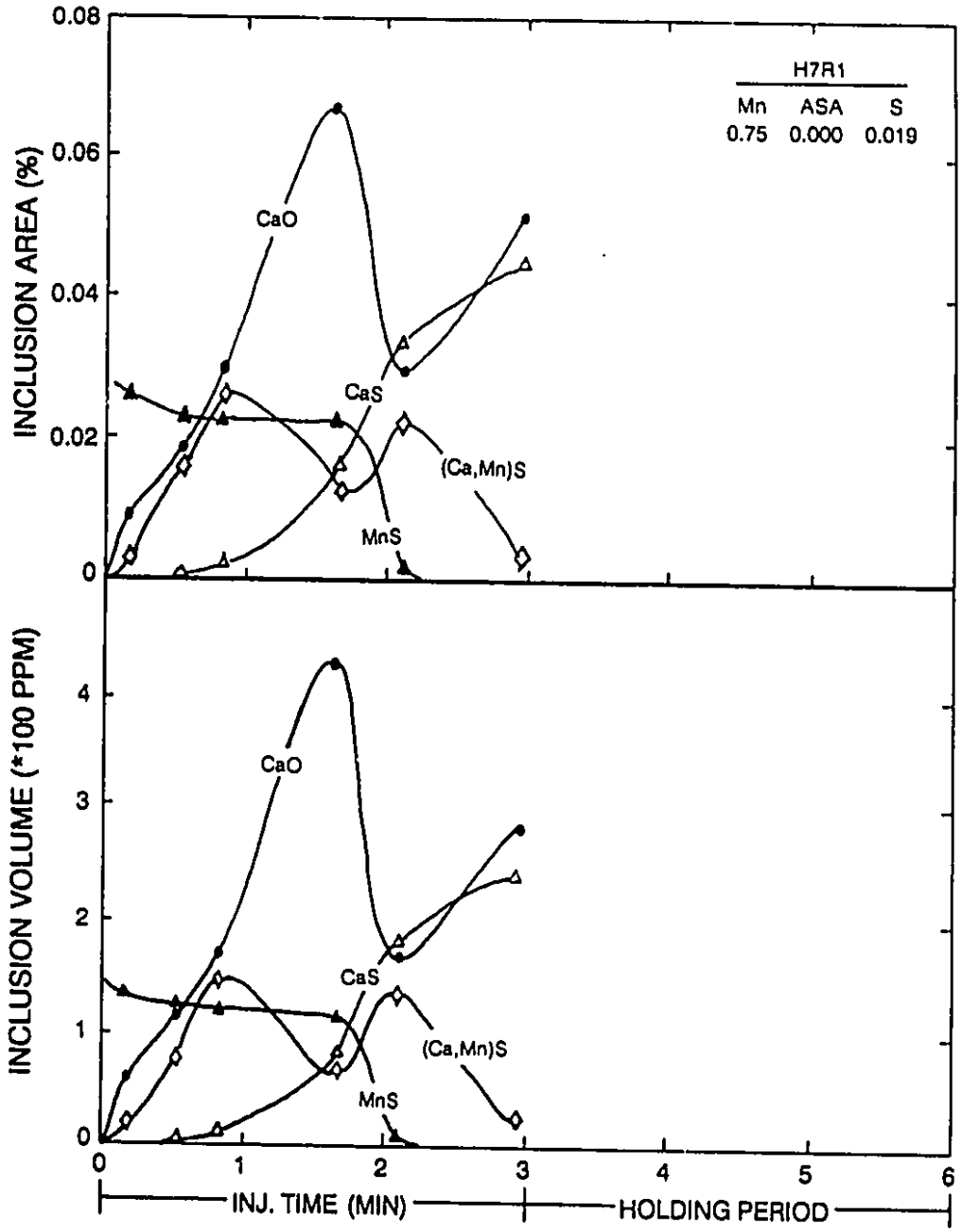

Figure 5.27 The changes of area fraction (TOP) and volume fraction (BOTTOM) of the each inclusion type during and after injection for H7R1.

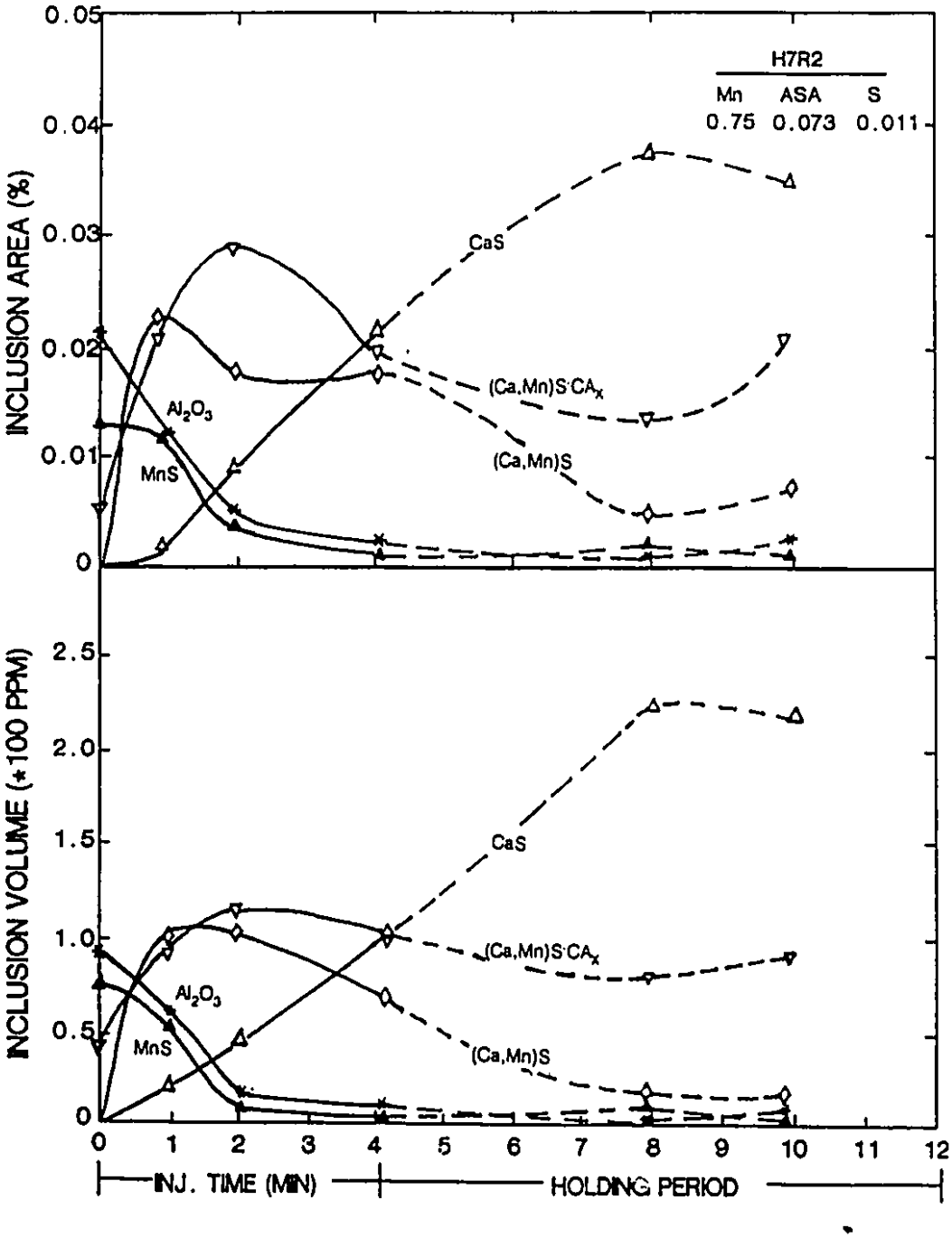

Figure 5.28 The changes of area fraction (TOP) and volume fraction (BOTTOM) of the each inclusion type during and after injection for H7R2.

Al_2O_3 and MnS inclusions decrease as expected with the injection time. The dominant feature of these diagrams is the rapid increase and then decrease of (Ca,Mn)S, and pure CaO and CaS inclusions. The peak of (Ca,Mn)S usually occurs at shorter times. As will be discussed later this is probably due to the formation of CaO and CaS at the injection point, while (Ca,Mn)S inclusions form on them in the bulk. In H7R1 (Figure 5.27) with a lower initial h_s/h_o ratio, larger amount of pure CaO than CaS were formed, while in H7R2 (Figure 5.28) with higher initial h_s/h_o, more CaS, (Ca,Mn)S and (Ca,Mn)S·CA_x inclusions were generated. The calcium aluminate CA_x and its oxy-sulfide (Ca,Mn)S·CA_x also increase at initial stage of injection, reach to a maximum near middle of injection, and decrease at later stage of injection. After injection, most inclusion contents decrease with the holding time.

Effect of Total Ca, ASA and S Contents

The effect of the total calcium content on the area fraction of each inclusion type is shown in Figure 5.29. For H6R1, MnS, Al_2O_3 and (Ca,Mn)S containing inclusions decrease, while CaS, CaO and CaS·CA_x inclusions increase with the increase of the total calcium content in the melt.

For three different injections with similar sulfur and calcium contents, the effect of acid soluble aluminum is seen

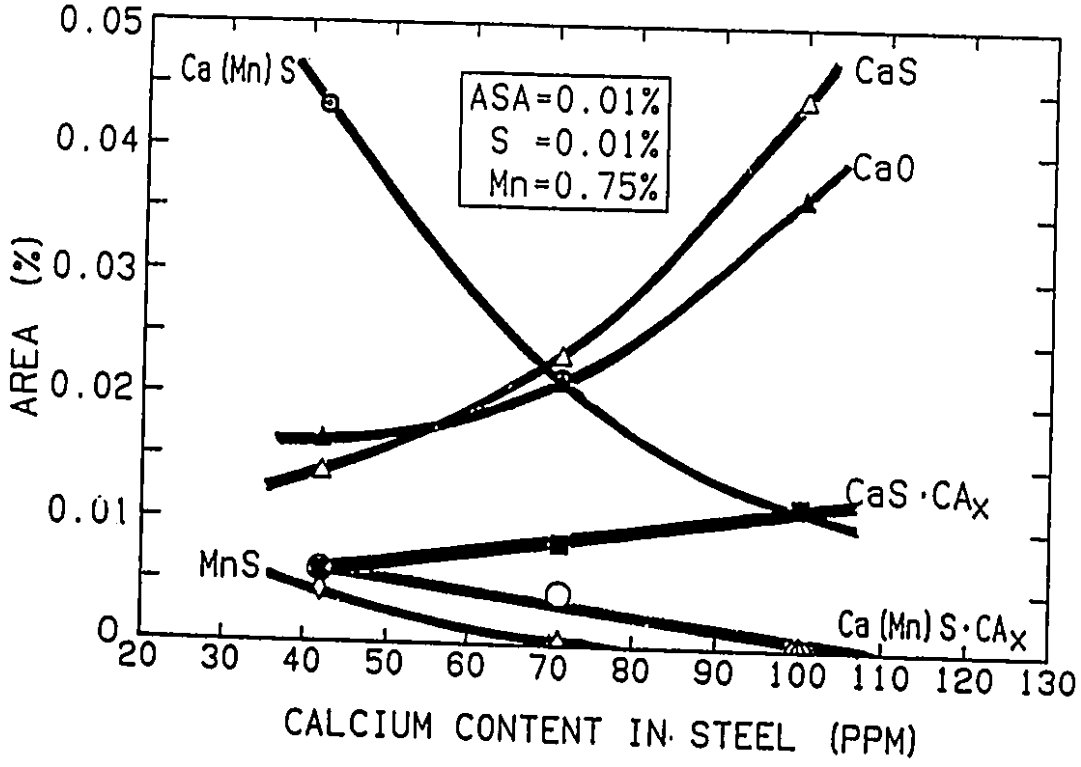

Figure 5.29 The area of each inclusion type as a function of the total bulk calcium content of the steel for injection H6R1.

in Figure 5.30. Increased acid soluble aluminum increases both aluminum activity and decreases oxygen activity. This favours the formation of aluminates and sulphides.

For the same bulk ASA, Ca and Mn contents, the effect of S content on inclusion distributions is shown in Figure 5.31. CaS, (Ca,Mn)S and $CaS{\cdot}CA_x$ inclusions increase with increasing S content in the bulk, while CaO inclusion decreases and then increases again.

5.2.2 Inclusion Numbers

The changes of the total inclusion numbers per volume (no./m^3) as a function of time are shown in Figures 5.32 and 5.33. In general, the numbers of total inclusions show the similar patterns as the inclusions area and volume fractions. For H6R1 and H7R2, the total numbers of inclusions increase at the beginning of injection, reach to a maximum value and then decrease at the later stage of injection. For H6R2 and H7R1, the number of inclusions increases at the beginning of injection, decreases during the middle and increases again at the later stage of injection. However, the number of inclusions for all the four heats shows the continuous decline during the holding period after injection.

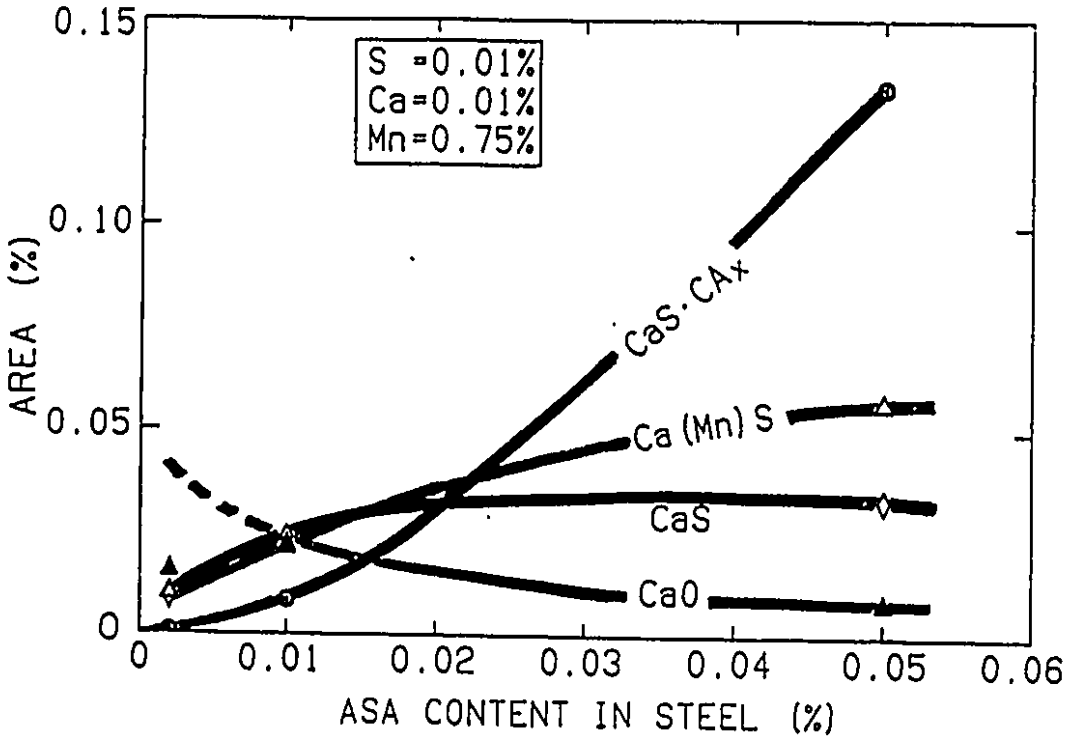

Figure 5.30 The effect of the acid soluble aluminum content on the area of each inclusion type.

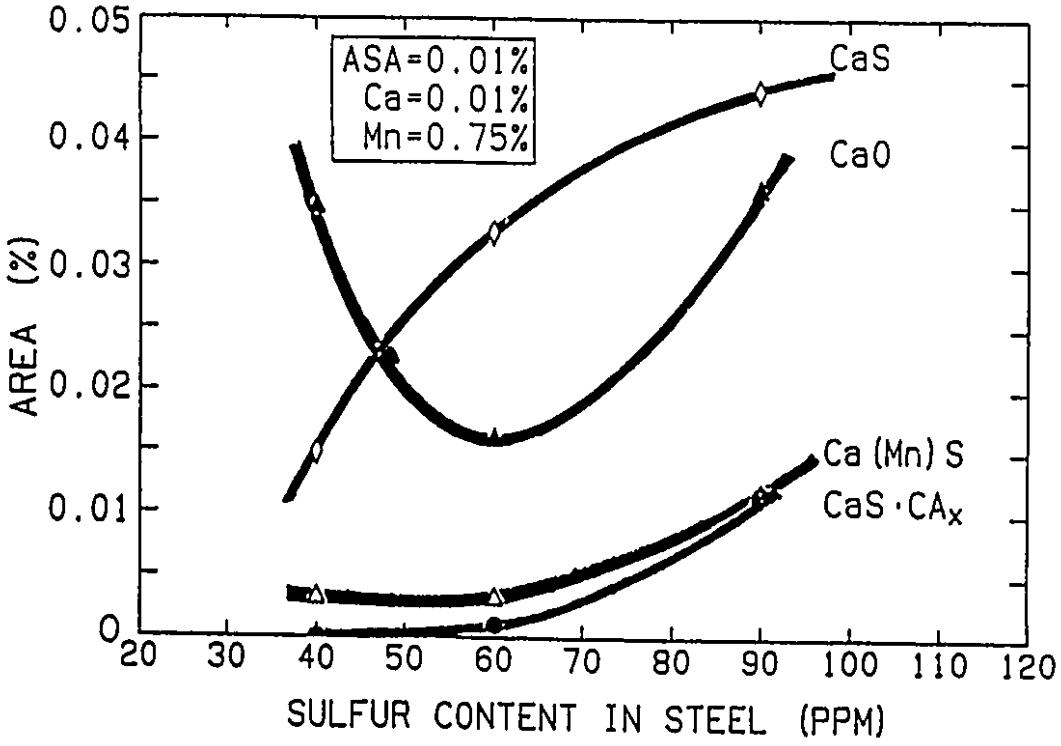

Figure 5.31 The effect of sulfur content on the area of each inclusion type for injection H6R1.

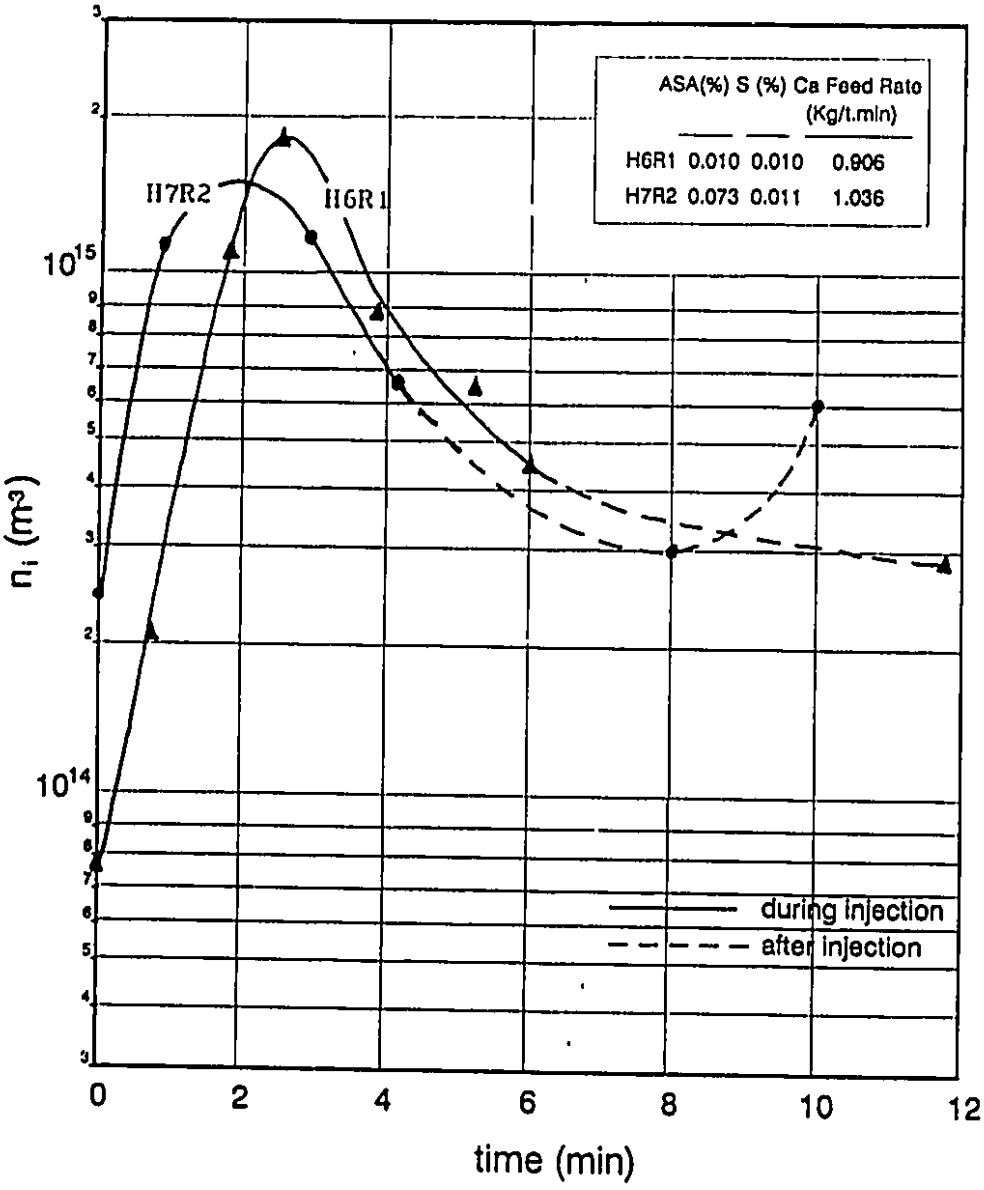

Figure 5.32 The changes of the total inclusion numbers per volume, (no./m^3), for two different injections with the similar initial sulfur content, 0.01%, and Ca injection rate, 1 kg /t.min.

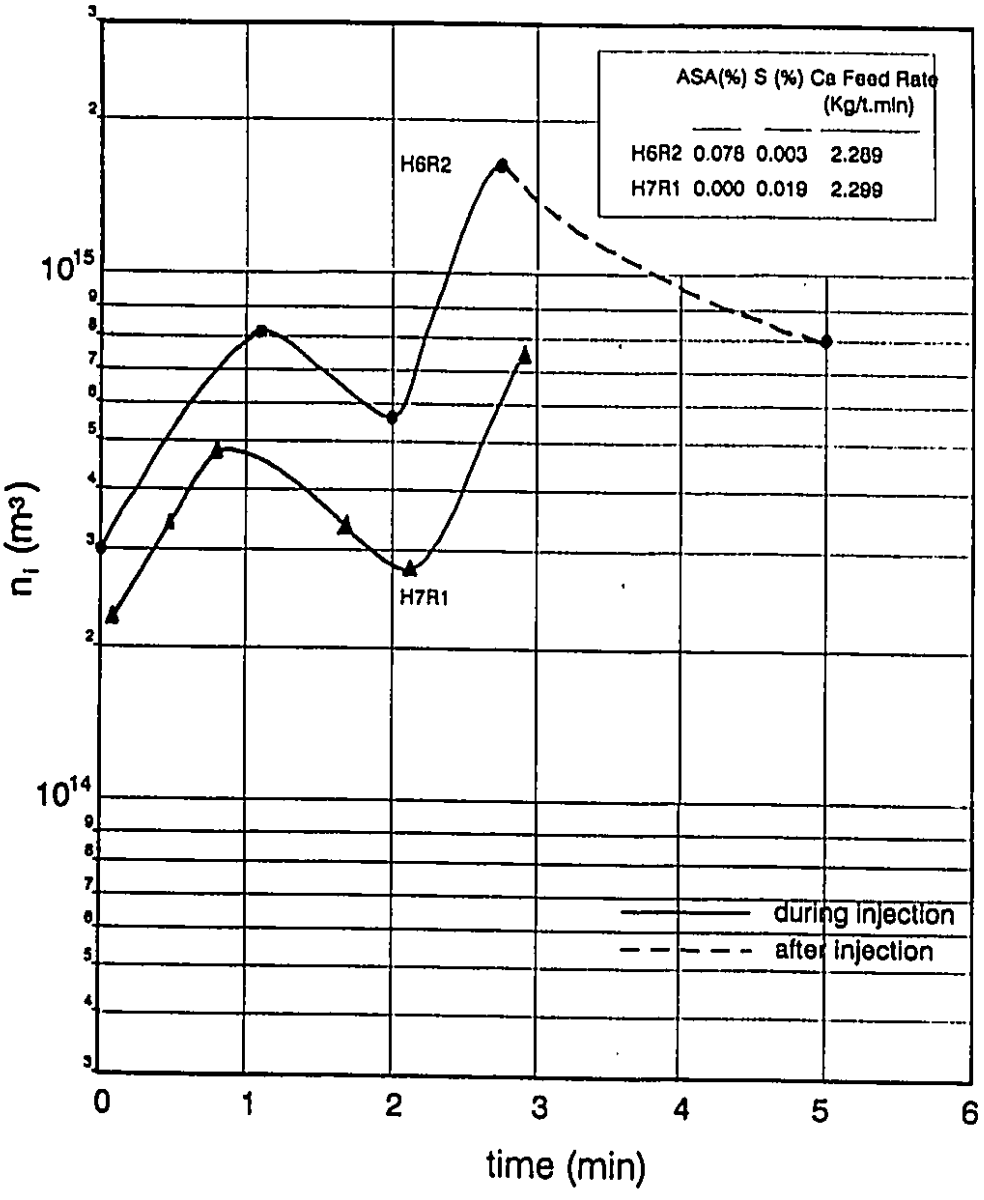

Figure 5.33 The changes of the total inclusion numbers per volume, (no./m^3), during and after injection, for two different injections with the similar calcium injection rate, 2.29 kg Ca/t.min.

The most significant inclusions contributing to this dramatic change of inclusion numbers are pure CaO and CaS. Their numbers were singled out to be plotted in Figures 5.34-5.37, together with the changes of the dissolved sulfur and oxygen in the melt as a function of time. For H7R1 (Figure 5.36) with higher initial oxygen activity than the sulfur content, more deoxidation than desulphurization occurred and more CaO than CaS formed during the course of calcium injection. While for H7R2 (Figure 5.37) with higher initial sulfur content than oxygen, more desulphurization than deoxidation occurred, and more CaS than CaO formed during injection. The pattern that emerged from those diagrams is that the numbers of CaO and CaS formed are directly related to the reduction of the dissolved oxygen and sulfur in the melt, respectively. Higher initial h_s/h_o results in the formation of larger numbers of calcium sulfide inclusions than oxide inclusions. This direct linkage will be addressed later in the mechanisms of Ca absorption, deoxidation and desulphurization in section 6.1 and 6.2.

5.2.3 Inclusion Size Distribution

All of the inclusions found in this study were spherical and less than 20 μm in diameter. The lower limit of size detection of the present instruments is about 0.2 μm. A typical size distribution of inclusions as a function of time

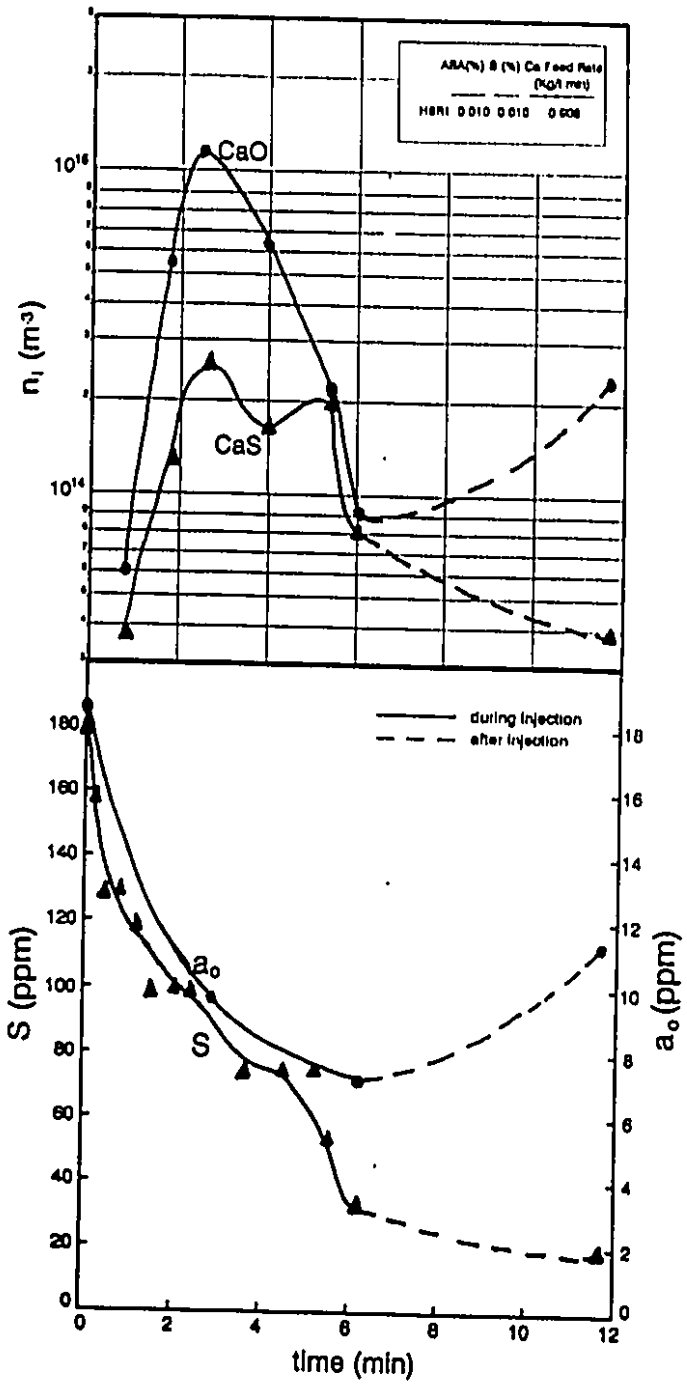

Figure 5.34 The changes of CaO and CaS inclusion numbers per volume (TOP) in comparison with changes of sulfur and oxygen activity (BOTTOM) for H6R1.

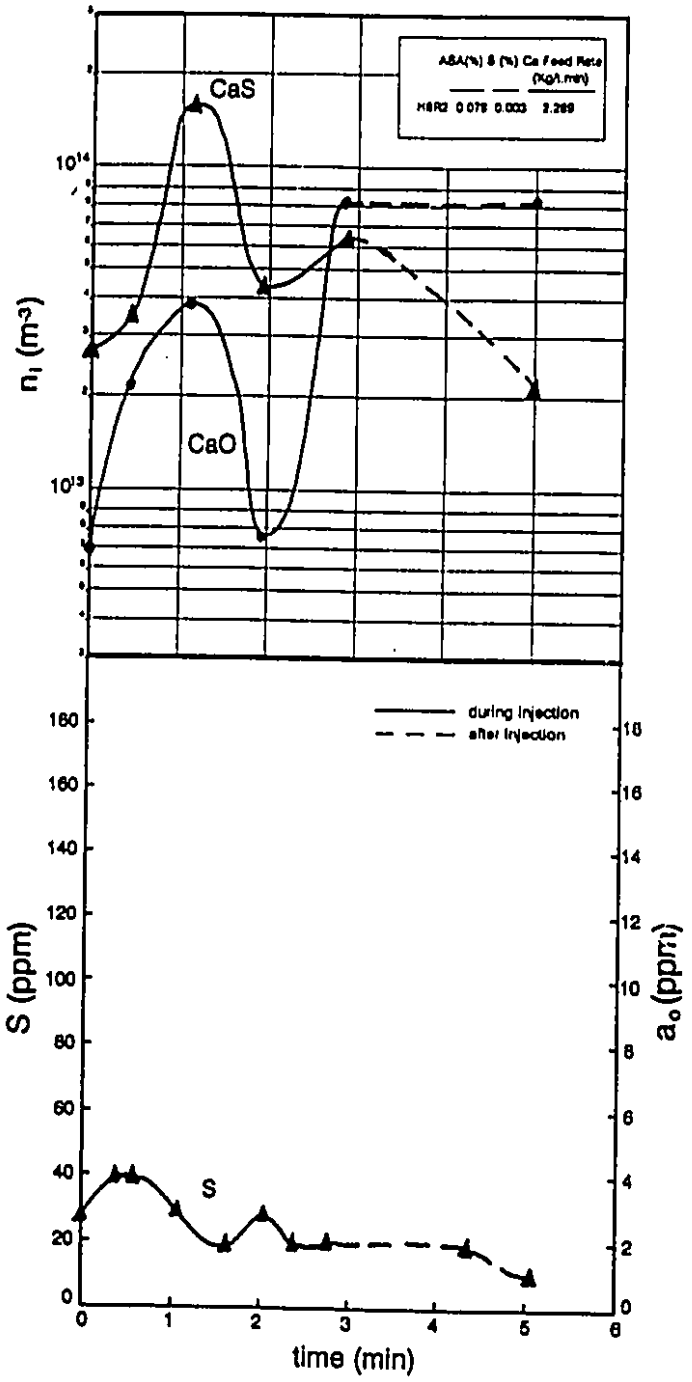

Figure 5.35 The changes of CaO and CaS inclusion numbers per volume (TOP) in comparison with changes of sulfur and oxygen activity (BOTTOM) for H6R2.

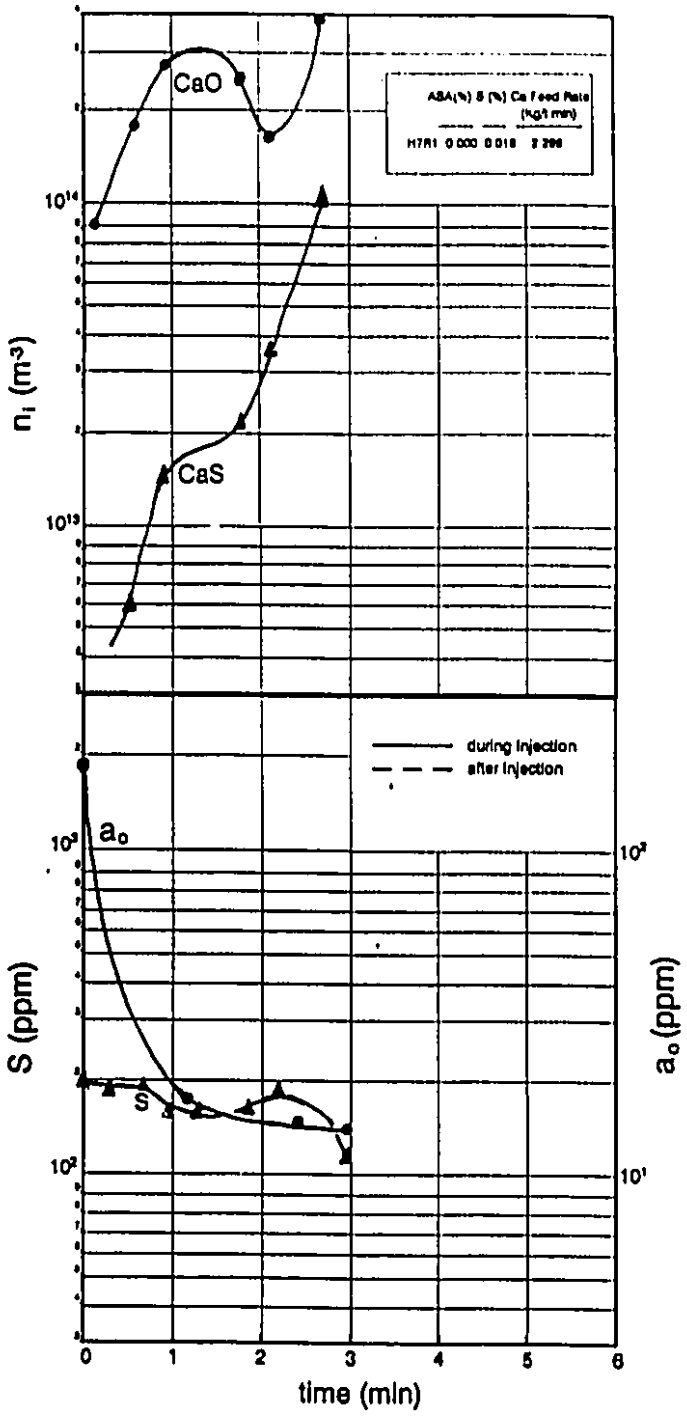

Figure 5.36 The changes of CaO and CaS inclusion numbers per volume (TOP) in comparison with changes of sulfur and oxygen activity (BOTTOM) for H7R1.

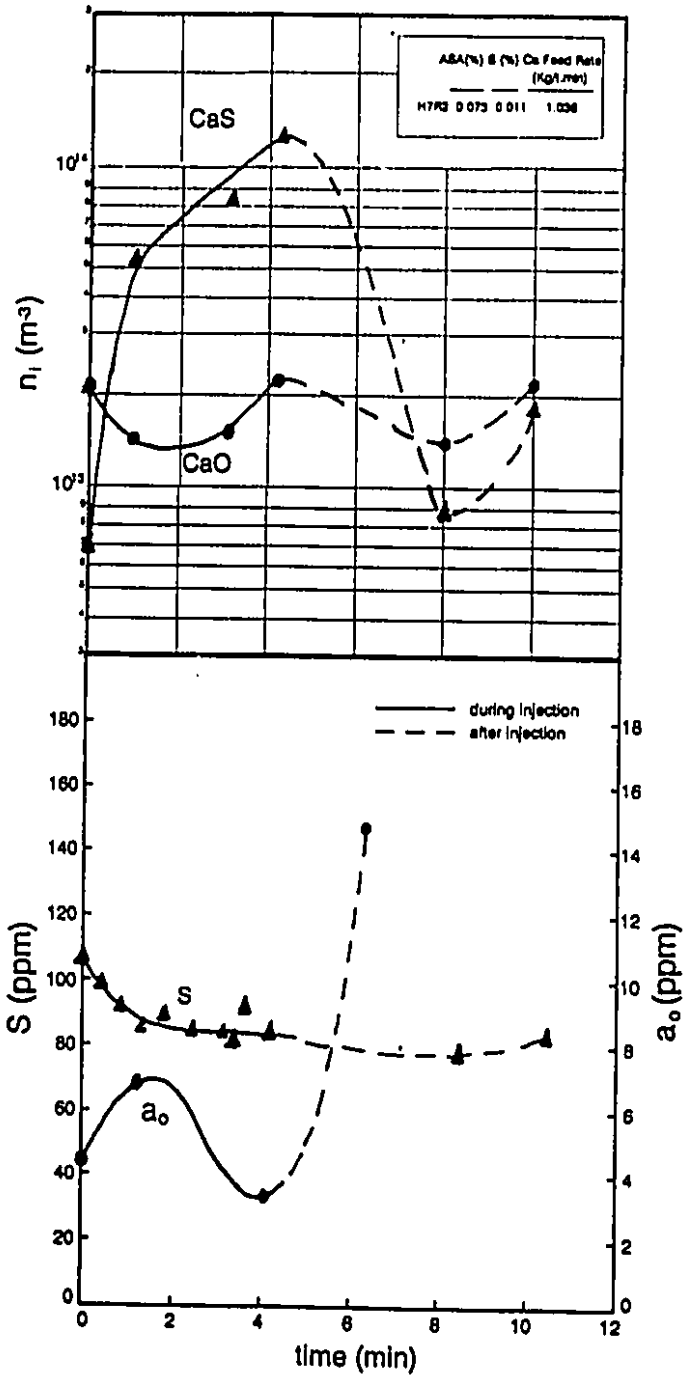

Figure 5.37 The changes of CaO and CaS inclusion numbers per volume (TOP) in comparison with changes of sulfur and oxygen activity (BOTTOM) for H7R2.

during and after injection is shown in Figure 5.38. It is seen that the inclusion size is relatively small at the beginning of injection (1.5 min), it increases and reaches to a maximum value at the middle of injection (2.87 min), then decreases at the later injection stage (6 min), and continues to decrease through the holding period (12 min). In general, the inclusion size also shows a peak during the injection. That same pattern coincides with the changes of numbers of inclusions, and area and volume fractions of inclusions.

5.2.4 Inclusion Chemistry

Table 5.3 shows the EDS inclusion analysis results for a typical sample analyzed for more than 20 fields (94 μm * 94 μm, each field). The EDS analysis gives each element's atomic percentage in the inclusion which needs to be converted to oxide and sulphide compositions. Typically the inclusions were composed of more than one phase, so that the inclusion analysis represents the average inclusion composition. The general formula for the oxide and sulfide components in the complex oxy-sulfide inclusions for the particular elemental constituents can be written as:

$$(CaO{\cdot}xAl_2O_3{\cdot}ySiO_2{\cdot}zMnO)\cdot\underline{rCaS{\cdot}qMnS}$$

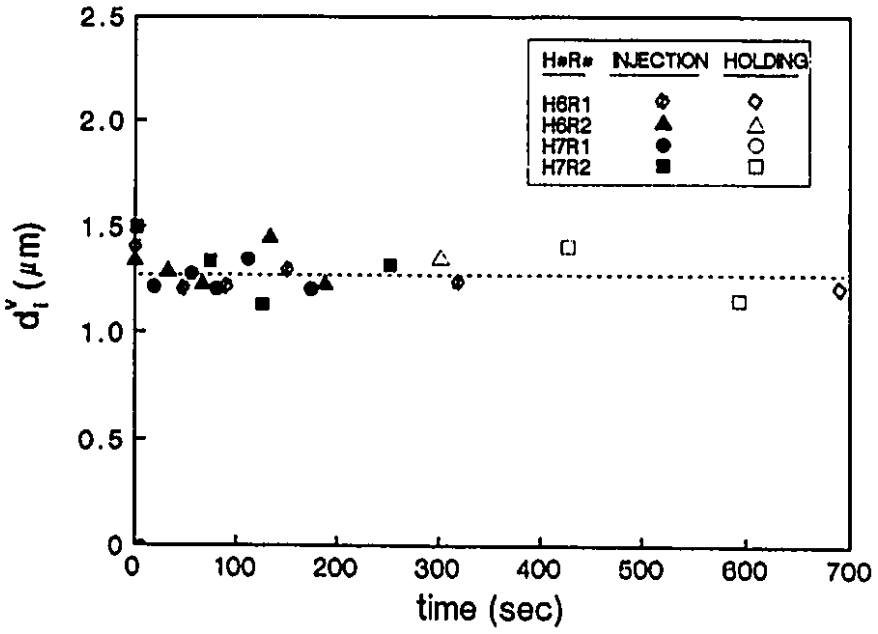

Figure 5.38 Change of the average volumetric diameter of inclusions during and after injection for the four injections analyzed by SEM.

TABLE 5.3

EDS INCLUSION ANALYSIS RESULTS OF A TYPICAL SAMPLE

HEAT NO. = H6R1, SAMPLE NO. = 11					
Inclusion no.	EDS Element Analysis (at %)	Calculated Oxides and Sulfides (mole %)	CA_x * Composition	CM_y + Composition	Inclusion
Inc1	Ca = 44.40 Al = 4.67 Mn = 3.41 S = 45.46 Si = 0.43	Al_2O_3 = 4.62 CaO = 4.65 SiO_2 = 0.85 MnO = 0.00 CaS = 83.14 MnS = 6.74			CaS (traces of MnS)
Inc2	Ca = 95.27 Al = 0.83 Mn = 2.72 S = 0.00 Si = 1.19	Al_2O_3 = 0.42 CaO = 95.65 SiO_2 = 1.20 MnO = 2.73 CaS = 0.00 MnS = 0.00			CaO
Inc3	Ca = 0.47 Al = 0.329 Mn = 49.72 S = 49.49 Si = 0.00	Al_2O_3 = 0.33 CaO = 0.93 SiO_2 = 0.00 MnO = 0.46 CaS = 0.00 MnS = 98.28			MnS
Inc4	Ca = 43.91 Al = 12.94 Mn = 2.24 S = 38.74 Si = 1.20	Al_2O_3 = 12.02 CaO = 13.77 SiO_2 = 2.23 MnO = 0.00 CaS = 67.82 MnS = 4.16	$CA_{0.87}$		CaS CAx
Inc5	Ca = 17.05 Al = 47.82 Mn = 10.68 S = 23.88 Si = 0.55	Al_2O_3 = 45.81 CaO = 7.38 SiO_2 = 1.05 MnO = 0.00 CaS = 25.29 MnS = 20.47	$CA_{6.2}$	$CM_{0.81}$	(Ca,Mn)S CAx
Inc6	Ca = 0.00 Al = 95.11 Mn = 2.21 S = 0.00 Si = 2.68	Al_2O_3 = 90.24 CaO = 0.00 SiO_2 = 5.35 MnO = 4.41 CaS = 0.00 MnS = 0.00			Al_2O_3
Inc7	Ca = 28.65 Al = 4.30 Mn = 20.30 S = 42.28 Si = 2.10	Al_2O_3 = 4.04 CaO = 12.54 SiO_2 = 3.95 MnO = 0.00 CaS = 41.31 MnS = 38.16		$CM_{0.02}$	(Ca,Mn)S

* CA_x: $CaO \cdot xAl_2O_3$

\+ CM_y: $CaS \cdot yMnS$ or (Ca,Mn)S

Where the term in the parenthesis is the oxide phase and the underlined term is the calcium-manganese sulfide. During the calculation process, Mn and Ca have first to be used for satisfying the stoichiometric requirement by S in the sulfide phase. The extra Ca and Mn values are used to for calculating the oxide components in the oxide phase. Based on 1 mole of CaO, the relative molar coefficients (x, y, z, r and q) in the general formula can be calculated from the EDS analytical results. Then the mole% of each component in either oxide or sulfide phase is determined (if the inclusion is an oxy-sulfide inclusion, the computed value represents the average mole% of each component). The detailed calculation for the mole% of each component of an oxy-sulfide inclusion $(Ca,Mn)S{\cdot}CA_x$ (inclusion #5 in Table 5.3) is shown in Table 5.4.

5.2.4.1 Pure CaO and CaS

This is probably the first time that large amounts of pure CaO and CaS inclusions have been found in the melt. Some of the typical inclusions photos and SEM x-ray EDS spectrums are given in Figures 5.39 and 5.40. It can be seen that the major x-ray peak shown from the inclusion CaO is the Ca peak (Figure 5.39). The oxygen peak is not shown in the x-ray spectrums, because it is a light element and the present SEM is incapable of detecting its signal.

TABLE 5.4

CALCULATION OF MOLE % OF EACH COMPONENT IN INCLUSION #5

Inclusion Formula	$CaO{\cdot}xAl_2O_3{\cdot}ySiO_2{\cdot}zMnO{\cdot}rCaS{\cdot}qMnS$
Relative molar ratio of each component to another: $CaO/Al_2O_3/SiO_2/MnO/CaS/MnS$	1/2x/y/z/r/q (Based on 1 mole CaO)
Molar% of the above ratios from EDS	3.85/47.82/0.55/0/13.2/10.68
the calculated values of x to q in the formula	x = 47.82/(2*3.85) = 6.21 y = 0.55/3.85 = 0.143 z = 0 r = 13.2/3.85 = 3.43 q = 10.68/3.85 = 2.77
the calculated mole% of the each component in the inclusion #5 shown in Table 5.3	X_{CaO} = 1/(1+x+y+z+r+q) = 7.38 % X_{Al2O3} = x/(1+x+y+z+r+q) = 45.81 % X_{SiO2} = y/(1+x+y+z+r+q) = 1.05 % X_{MnO} = 0 X_{CaS} = r/(1+x+y+z+r+q) = 25.29 % X_{MnS} = q/(1+x+y+z+r+q) = 20.47 %

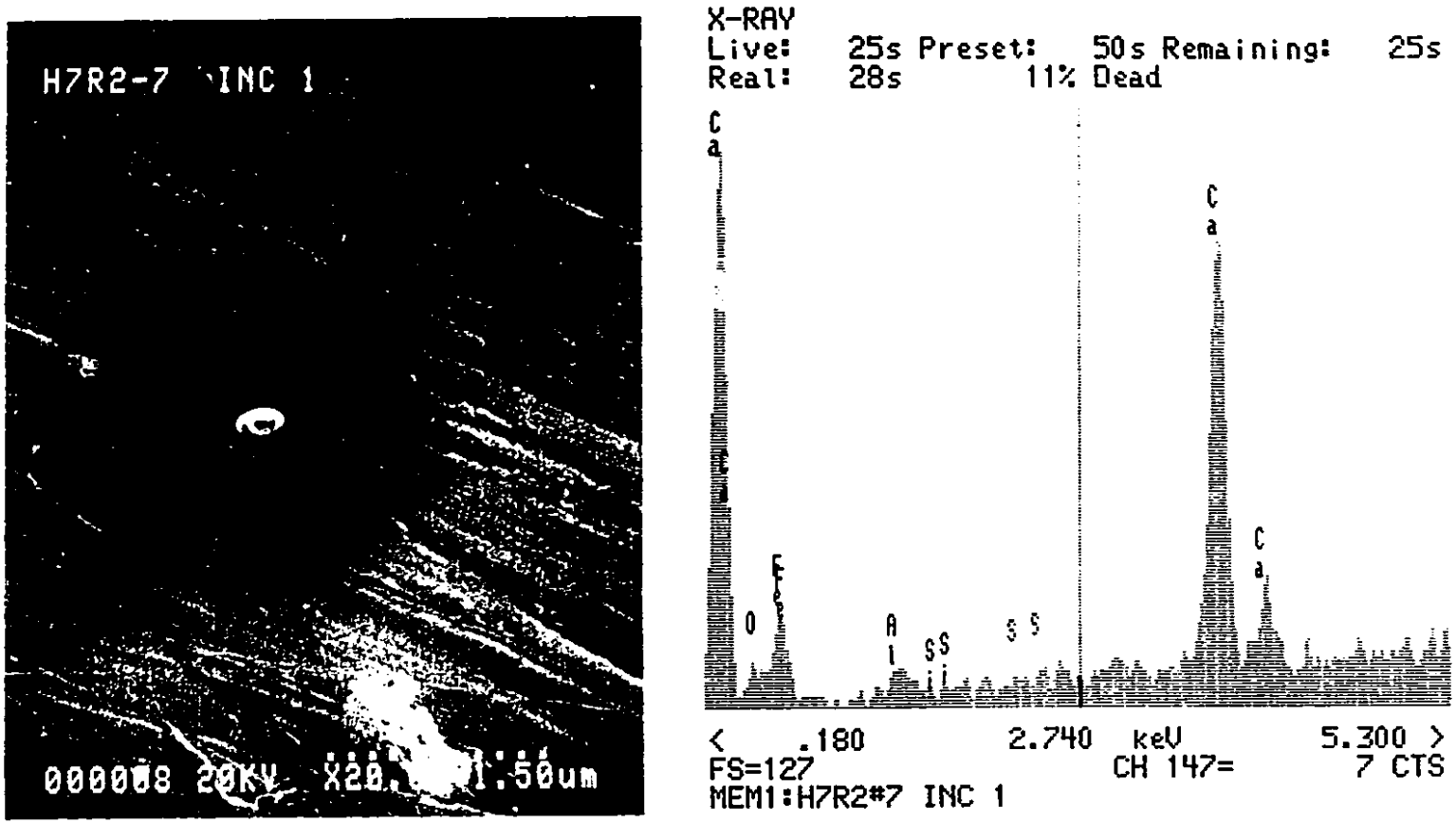

Figure 5.39 A typical CaO inclusion photo and its x-ray spectrum from H7R2 sample 7.

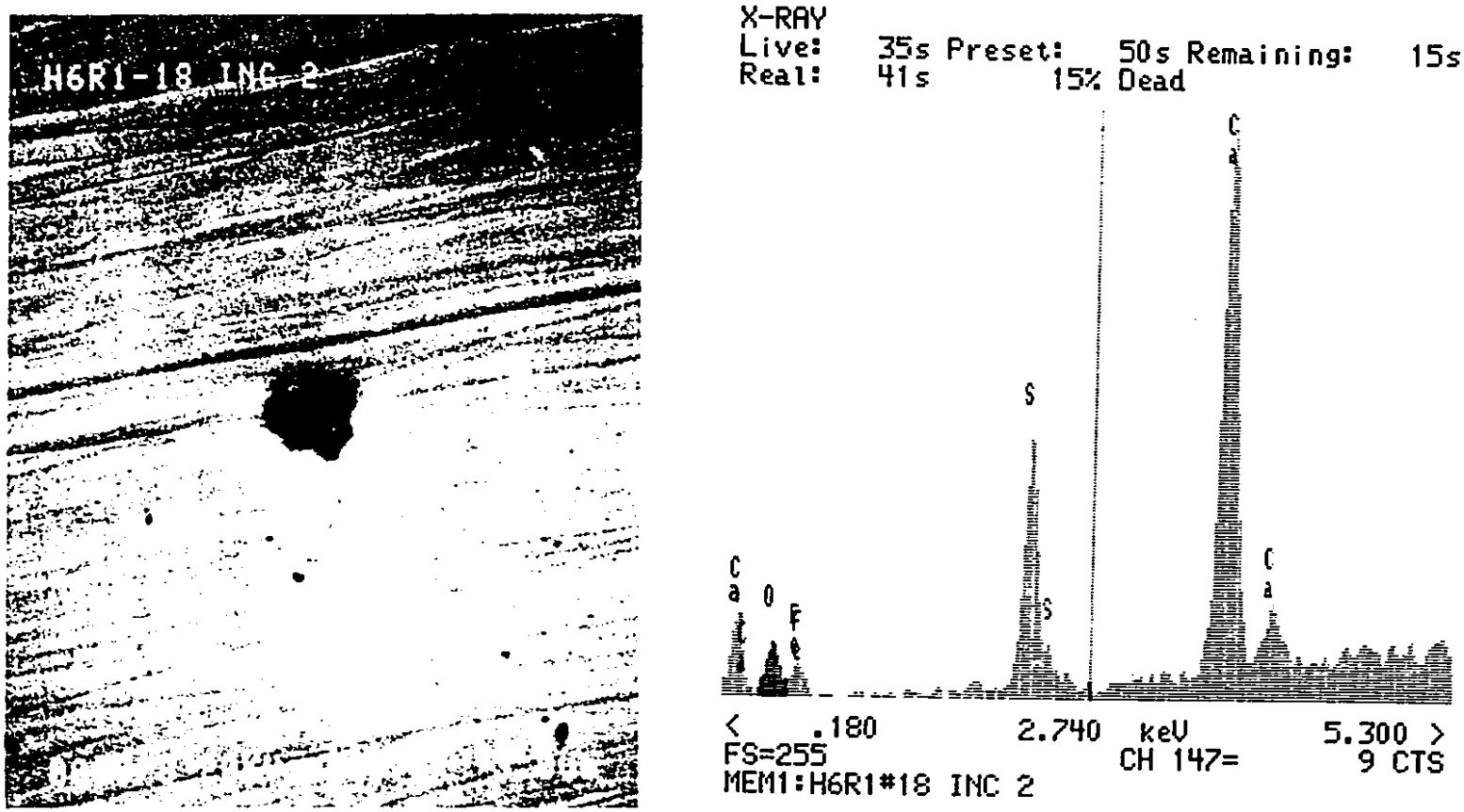

Figure 5.40 A typical CaS inclusion photo and its x-ray spectrum from H6R1 sample 18

5.2.4.2 Calcium Aluminate - CA_x

The composition of CA_x inclusions during the course of injection and the subsequent holding period is shown in Figure 5.41. Alumina inclusions are transformed to CaO-rich CA_x during the injection which is followed by some reversion in the holding period. The bulk calcium content of the steel is also super-imposed. It is clear from the this diagram that for even one injection condition that there is no unique relation between total calcium in steel and the extent of transformation of alumina inclusions. For example, 20 ppm Ca early in the injection corresponds to an average inclusion composition near CA_2, while in the holding period 20 ppm calcium corresponds to C_3A.

For the same injection rate, Figures 5.42 and 5.43 show the effect of the different injection conditions on the CA_x composition during the injection and the subsequent holding period. From Figure 5.42, H6R1 has lower initial ASA content than H7R2 does, and the CA_x formed in H6R1 is richer in CaO than the CA_x formed in H7R2 at the same injection time. In other words, lower initial ASA content favours oxide modification by calcium addition. In Figure 5.43, H7R1 has no Al predeoxidation and higher initial S content compared with H6R2, so that the oxide formed in the melt during injection is mainly pure CaO.

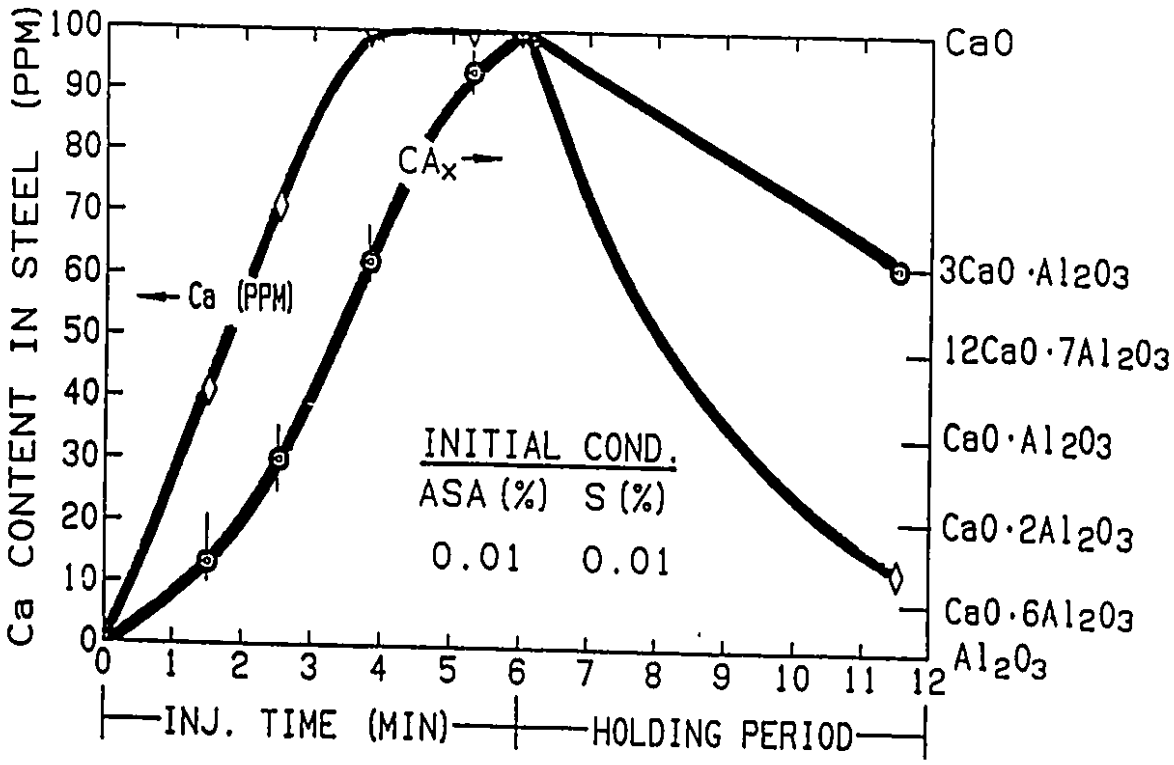

Figure 5.41 The calcium oxide percentage of the calcium aluminate inclusions, CA_x, during and after injection H6R1. The total calcium content of the steel is also shown for the same samples.

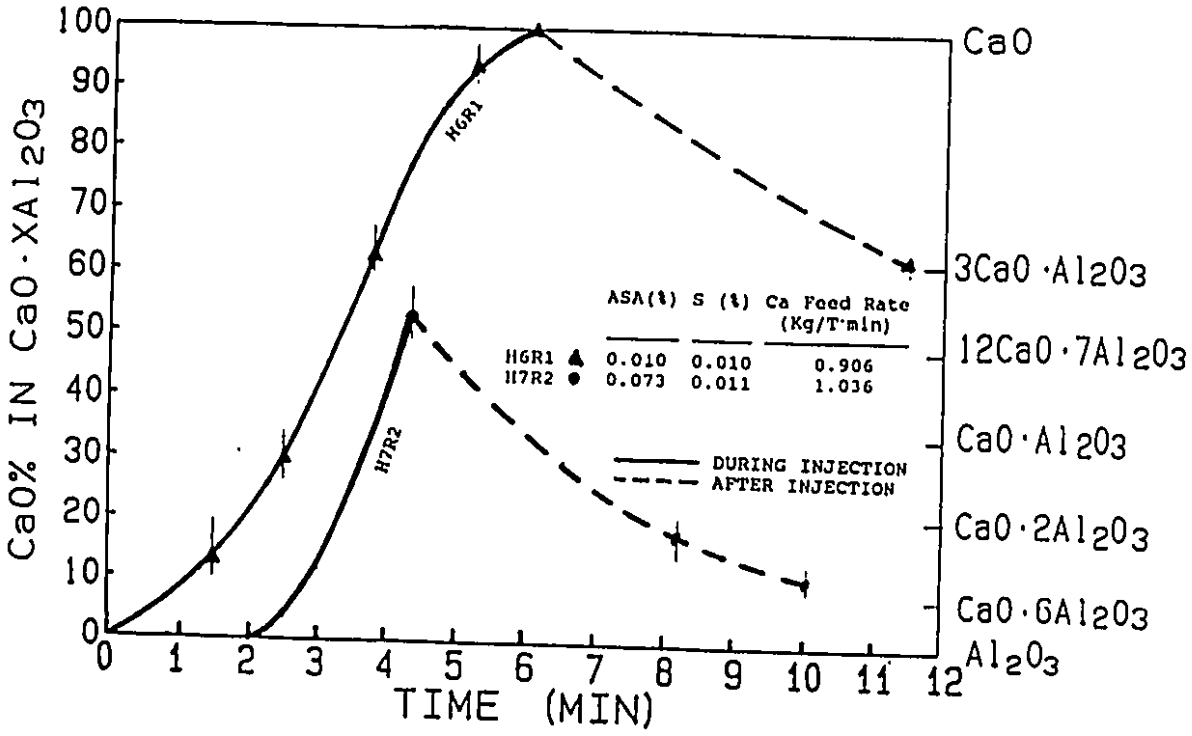

Figure 5.42 The modification of the Al_2O_3 inclusion towards calcium-rich aluminate during injection, and the reverse of the modification after injection for two different injections with the similar initial sulfur content, 0.01%, and injection rate, 1 kg/t.min, but with different initial ASA, contents.

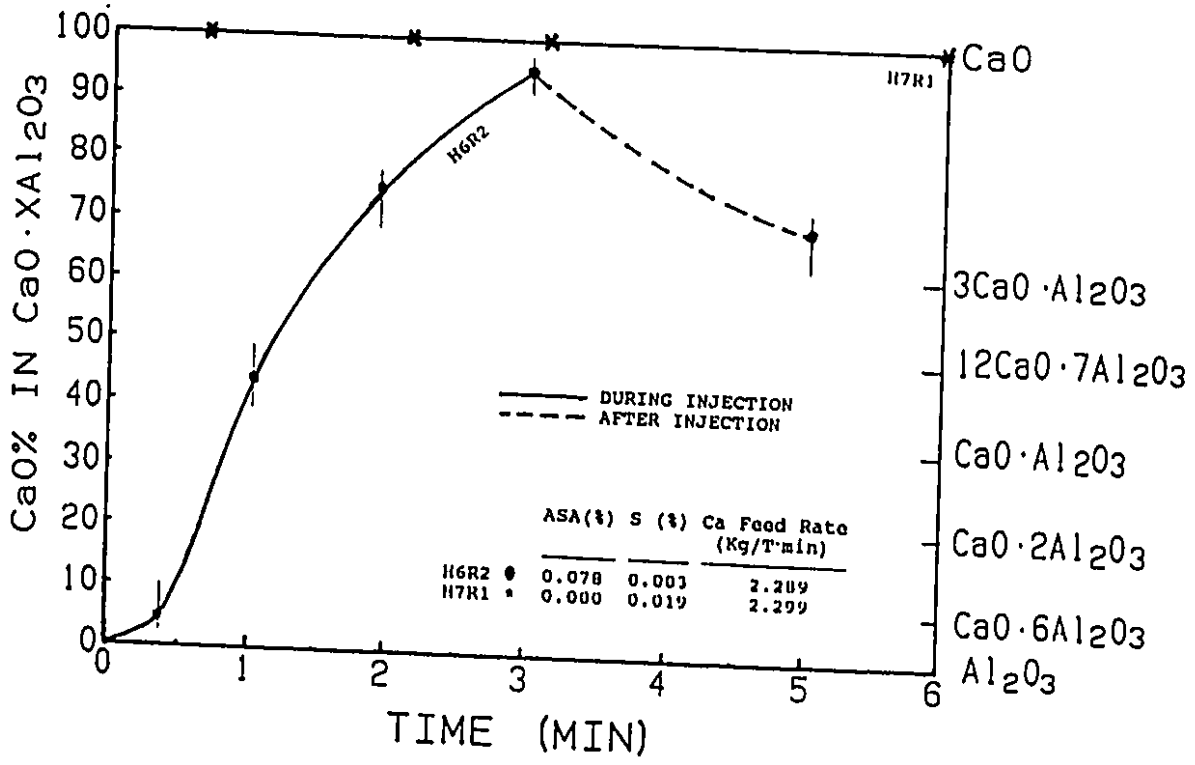

Figure 5.43 The modification of the Al_2O_3 inclusion towards calcium-rich aluminate during injection, and the reverse of the modification after injection for two different injections with the similar injection rate, 2.29 kg/t.min, but with different initial S and ASA contents (H7R1 has no Al predeoxidation).

For different injections with similar bulk calcium and sulphur contents the effect of the acid soluble aluminum content on the calcium content of the calcium aluminates is shown in Figure 5.44. The increased aluminum activity at higher ASA increases the aluminum content of the calcium aluminates.

For the same bulk total calcium and ASA contents, the effect of the sulfur content on the calcium aluminates is shown in Figure 5.45. The lower sulfur increases the calcium content of the calcium aluminates.

In Figure 5.46 the CaO wt% in CA_x inclusions is plotted against the bulk total calcium content for all the four heats examined in details. In general, increasing bulk total calcium content increases the calcium content in the calcium aluminate inclusions. However the effect is not solely from the bulk total calcium in the diagram, a simple pattern is not shown here. The mechanism in section 6.3.1 verifies these findings.

5.2.4.3 Calcium manganese sulfide - (Ca,Mn)S

The composition of (Ca,Mn)S inclusions during the course of injection and the subsequent holding period is shown in Figures 5.47 and 5.48 for the similar injection rates, but

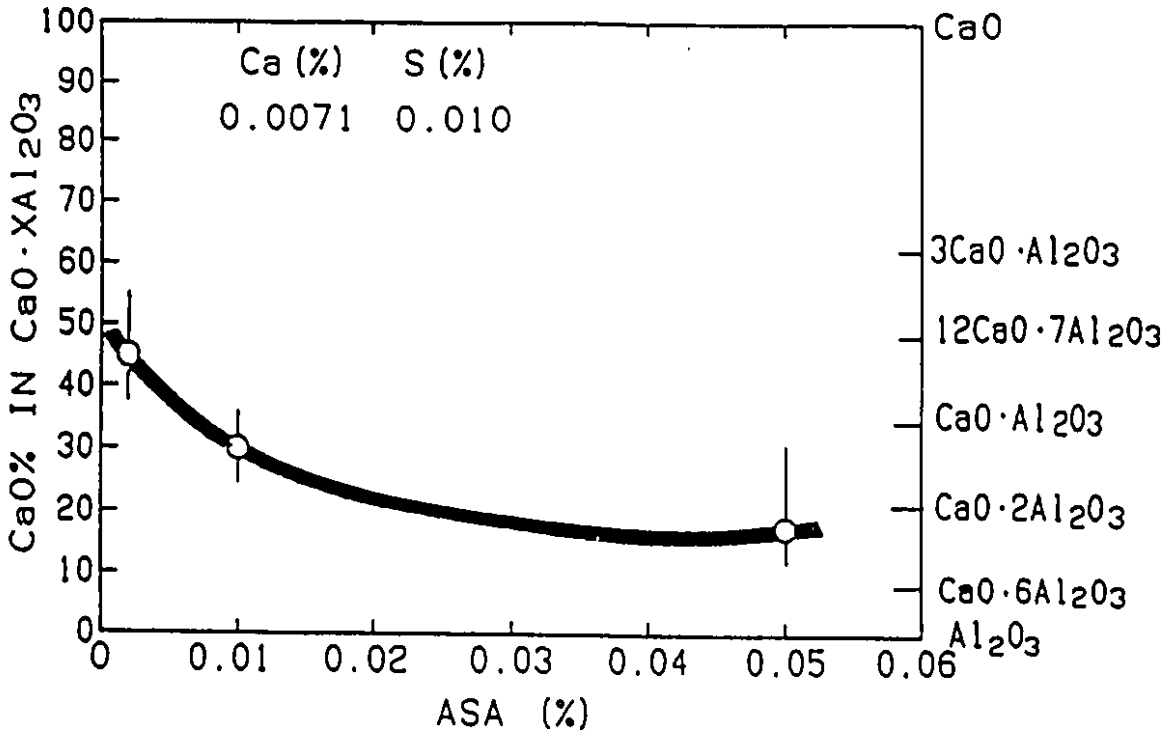

Figure 5.44 The effect of the acid soluble aluminum content on the calcium oxide percentage of the calcium aluminate inclusions, CA_x, for three different injections with the same total calcium and sulfur content in the steel.

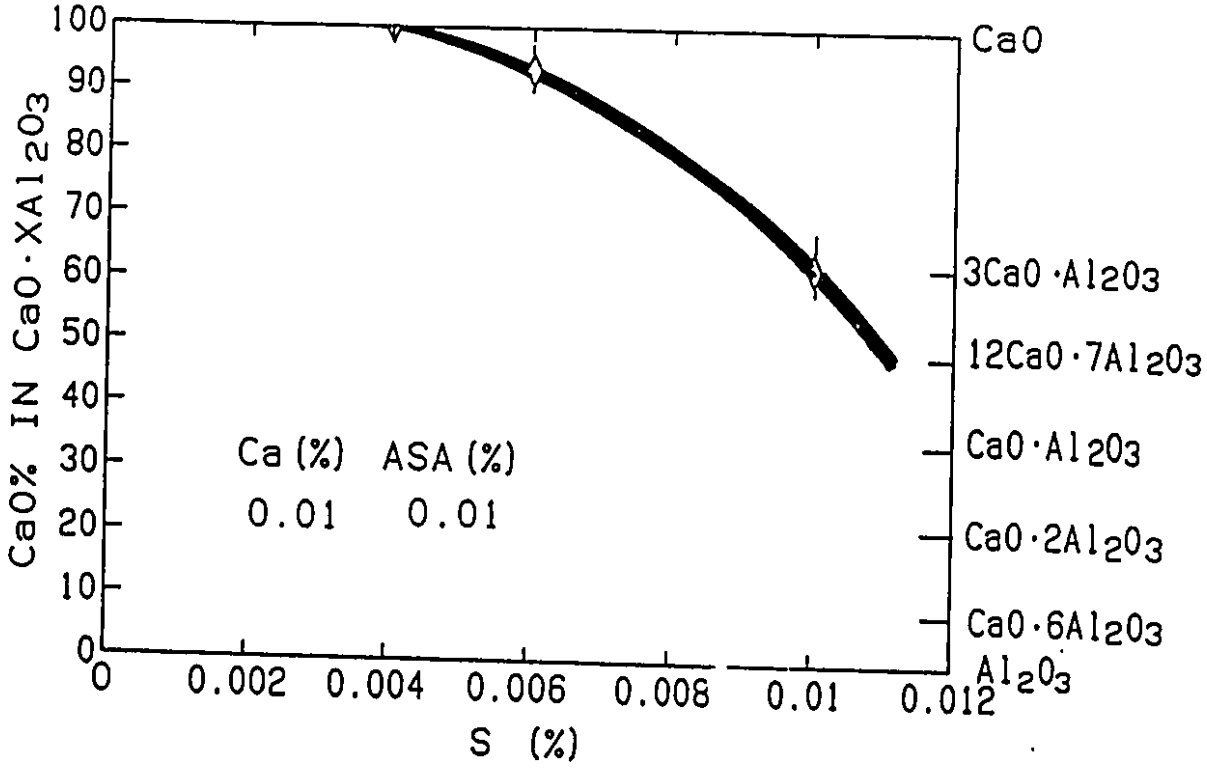

Figure 5.45 The effect of the sulfur content on the calcium oxide percentage of the calcium aluminate inclusions, CA_x, for H6R1 with the same total calcium and acid soluble aluminum content in the steel.

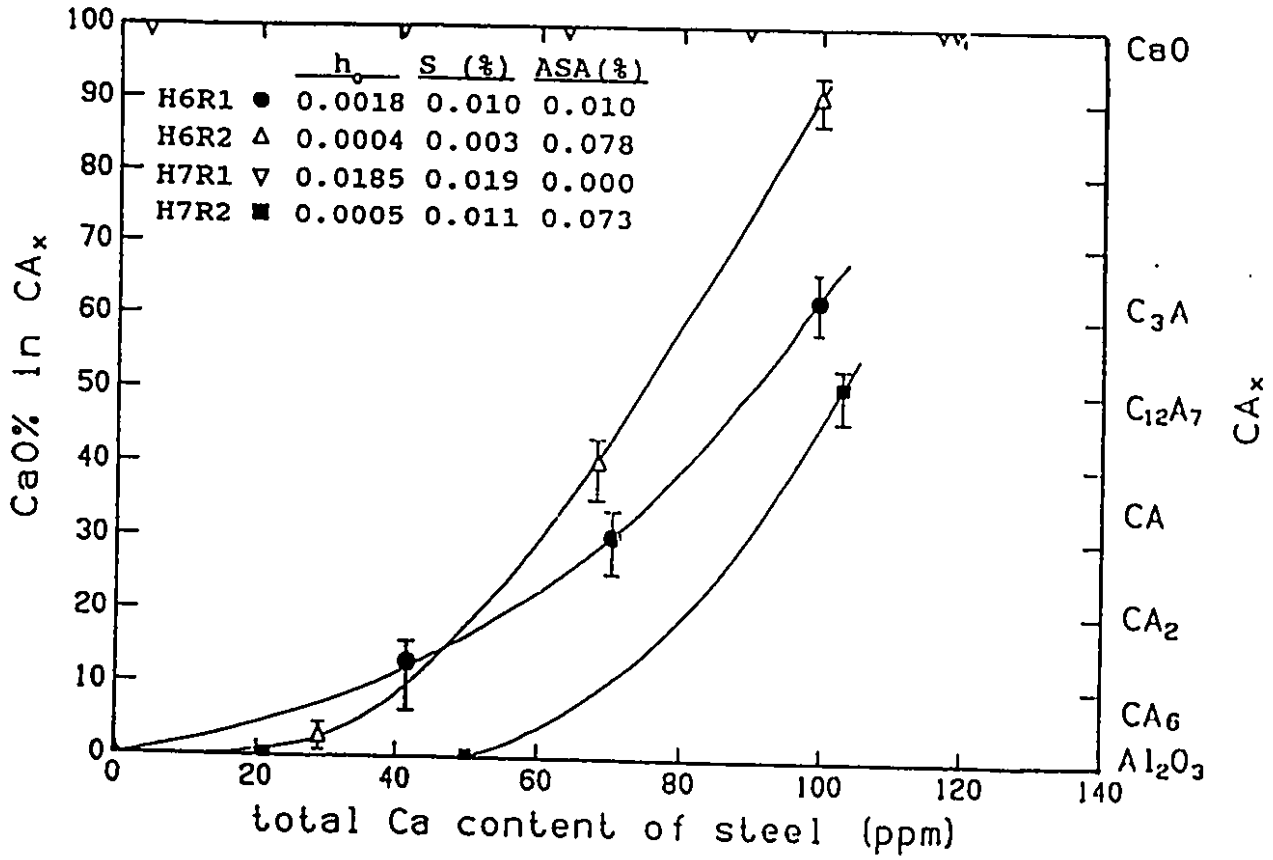

Figure 5.46 The modification of alumina inclusions towards calcia-rich aluminates by the injection of calcium

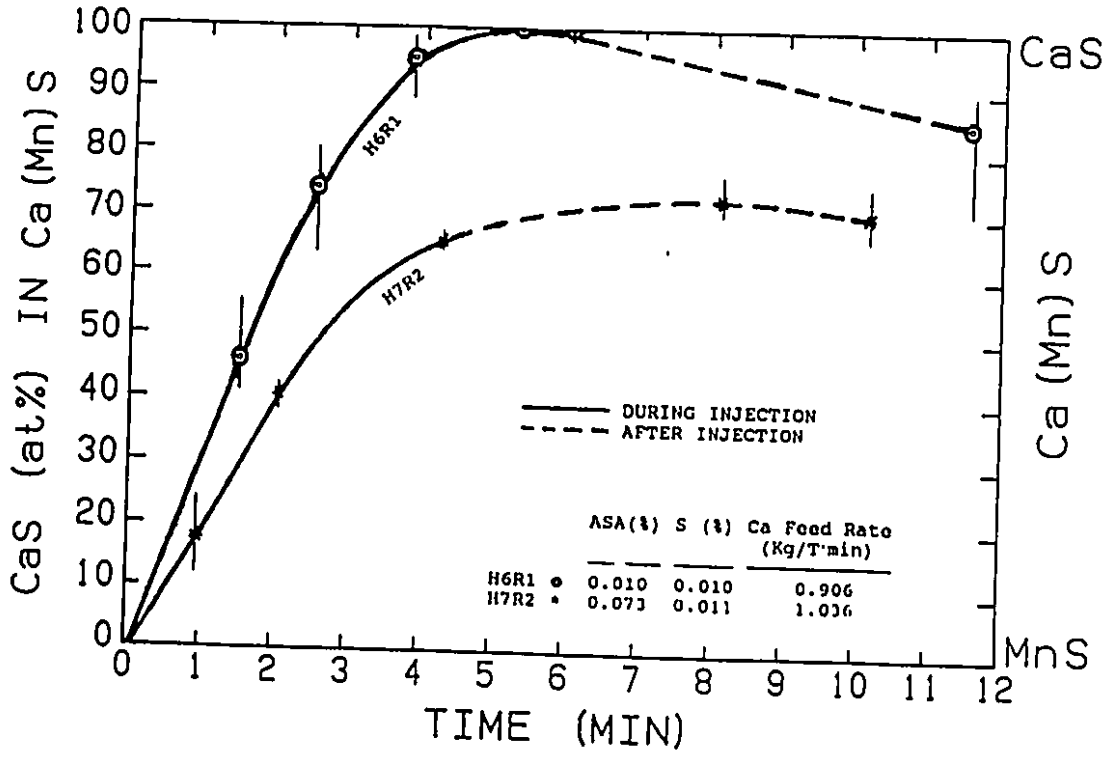

Figure 5.47 The modification of manganese sulfide inclusion towards calcium sulfide during and after injection for two different injections with the similar initial sulfur content, 0.01%, and injection rate, 1 kg/t.min, but with the different initial ASA contents.

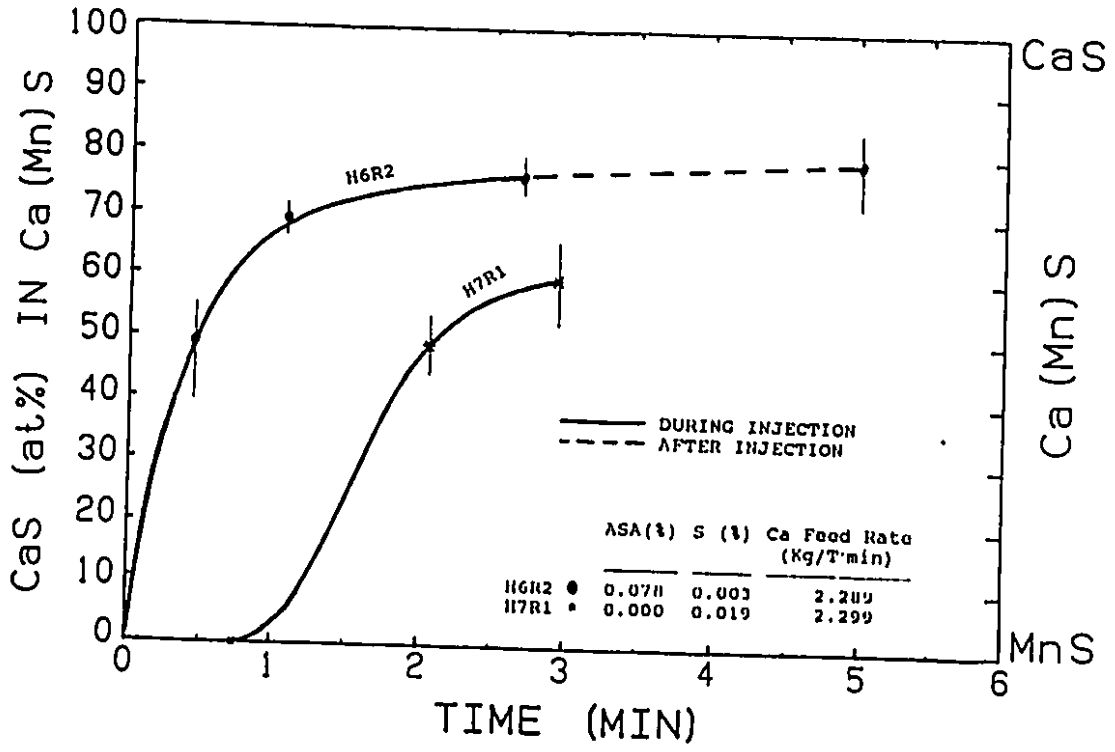

Figure 5.48 The modification of manganese sulfide inclusion towards calcium sulfide during and after injection for two different injections with the similar injection rate, 2.29 kg/t.min, but with different initial S and ASA contents. (H7R1 has no As predeoxidation)

with different initial conditions. Manganese sulphide inclusions are transformed to calcium sulphide during the injection which is followed by some reversion in the holding period. Higher initial ASA (lower dissolved oxygen) and lower initial S contents need shorter injection time to reach certain calcium content in (Ca,Mn)S inclusions.

For different injections with similar bulk calcium and sulphur contents the effect of the acid soluble aluminum content on the calcium content of (Ca,Mn)S inclusion is shown in Figure 5.49. The increased aluminum activity at higher ASA increases the calcium content of (Ca,Mn)S inclusion. Figure 5.50 shows that solid (Ca,Mn)S (CaS at% > 0.75) can form at much higher aluminum content.

For the same bulk total calcium and ASA contents, the effect of the sulfur content on (Ca,Mn)S is shown in Figure 5.50. The lower sulfur seems to increase the calcium content of the (Ca,Mn)S inclusion, but the degree of its effect is not clear from this diagram.

In Figure 5.51 the CaS at% in (Ca,Mn)S inclusions is plotted against the bulk total calcium content for all the four heats examined in detail. In general, increasing bulk total calcium content increases the calcium content in (Ca,Mn)S inclusions. However, similar to Figure 5.46, a

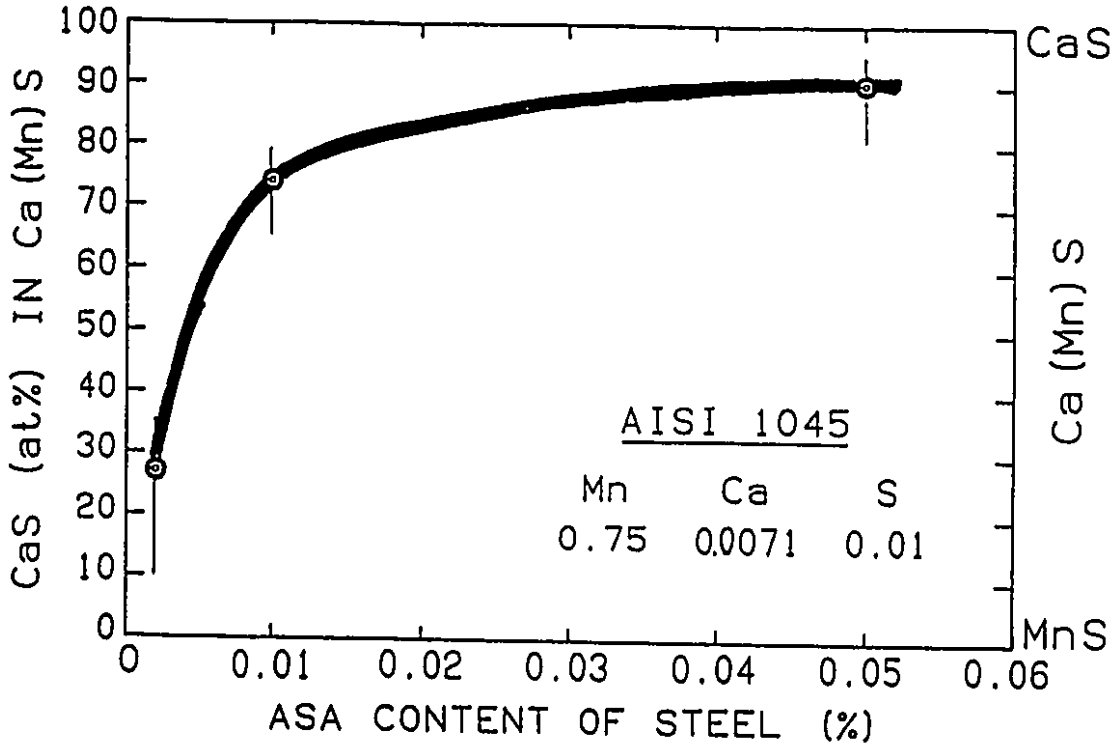

Figure 5.49 The effect of the acid soluble aluminum content on the CaS (mole %) component of the calcium manganese sulfide inclusions, for three different injections with the same sulfur and total calcium content in the steel.

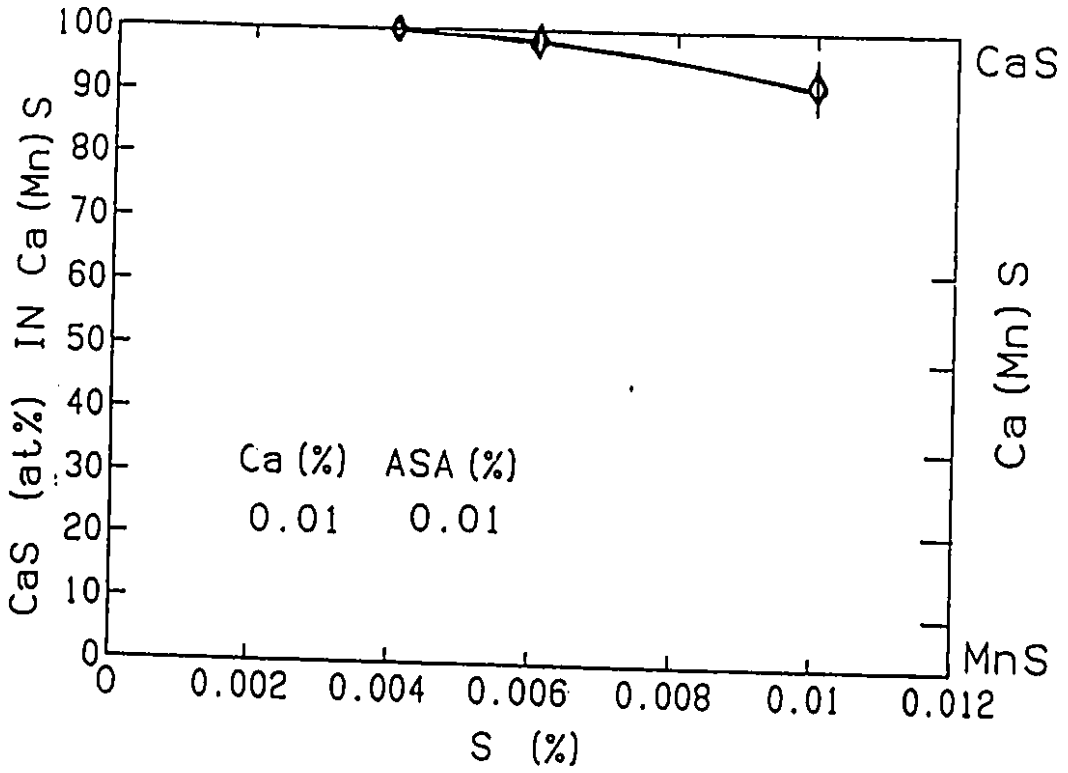

Figure 5.50 The effect of the sulfur content on the CaS (mole %) component of the calcium manganese sulfide inclusions for H6R1 with the same total calcium and acid soluble aluminum content in the steel.

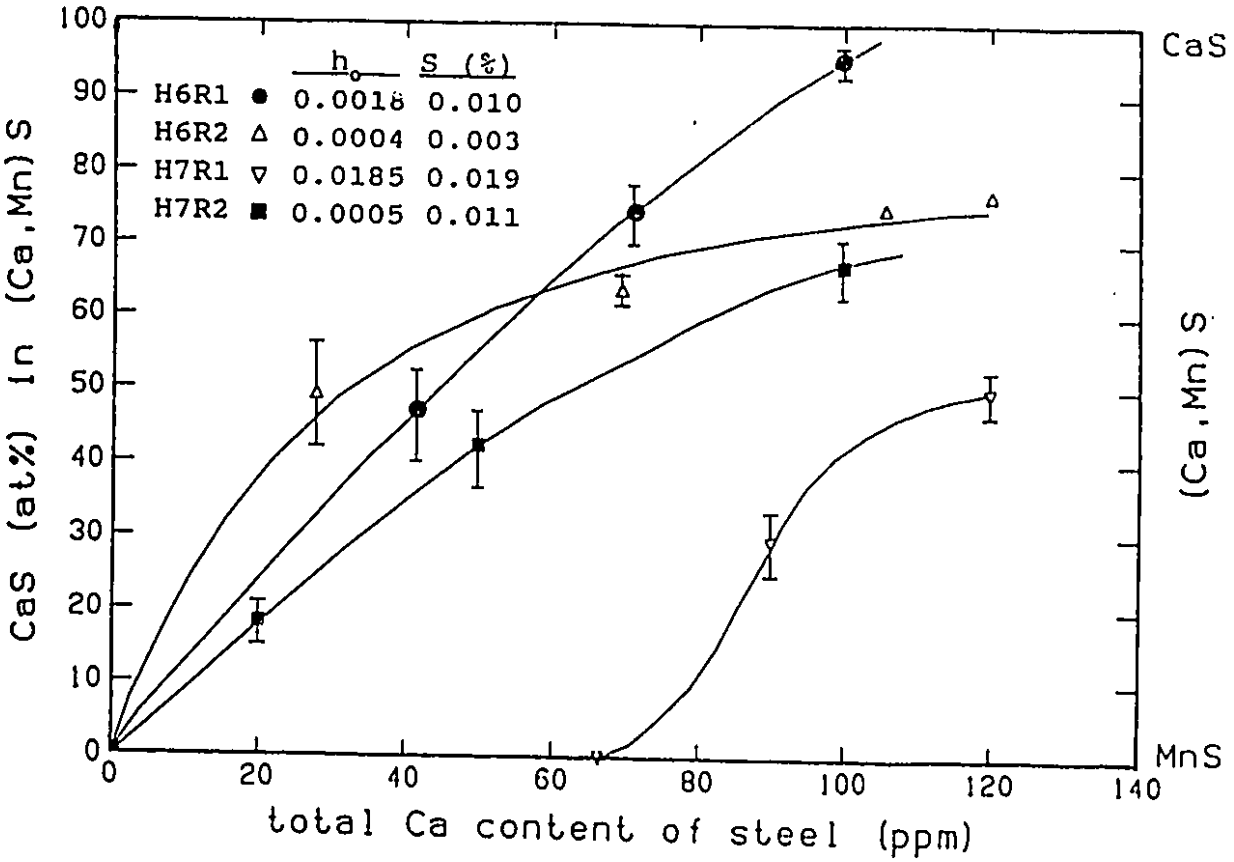

Figure 5.51 The modification of MnS inclusions towards calcium-rich (Ca,Mn)S by the injection of calcium.

simple pattern is not shown, because the effect on (Ca,Mn)S is not solely from the calcium in the diagram. The kinetics and mechanism for both oxide and sulphide modification and their relationship are discussed in section 6.3.

5.3 COMPARISON BETWEEN BULK CHEMICAL AND INCLUSION ANALYSIS

In principle it is possible to calculate the content of each element contained as inclusions from the number, size and composition of the inclusions. The contents of each in inclusions can be subtracted from the total bulk analysis to obtain the content of the element dissolved in the steel. There are a number of difficulties in actually performing this calculation. First of all, there are uncertainties in the number, size and composition of the inclusions because it is only practical to analyze a small fraction of the sample. (In the present study, 40 fields each measuring 94 μm by 94 μm each were taken from one polished sample). Another problem is that there is a distribution of particle sizes which are randomly sectioned, but it is more likely that a smaller cross-section is cut. Therefore a statistical correction procedure is required to adjust the observed particle distribution. In the present case, Underwood's procedure is used [163].

The results of this calculation are compared with the

chemical analysis results in Figures 5.52 - 5.54. The calcium content in inclusions is compared with the bulk total calcium contents in Figures 5.52. Results from all the four heats indicate that the agreement between the total calcium content from bulk chemical analysis and the calcium content calculated from the inclusion distribution is surprisingly good. This means most of calcium is tied up in the inclusions, and the dissolved calcium is almost negligible by comparison. Since Equations 5.6 and 5.11 are based on the assumption that the total calcium in the melt is the dissolved calcium, Equations 5.6 and 5.11 are incorrect to be used for explaining the calcium absorption and its vaporization. An alternative mechanism is thus presented in section 6.2.

Figure 5.53 shows the comparison between the oxygen content combined in the inclusions and the oxygen content from subtracting the dissolved (converted from oxygen activity) oxygen from the total oxygen. The agreement is fair, even though there is some scatter due to the uncertainty in inclusion analysis. For sulfur, there are three components: one is the total sulfur which can be chemically analyzed, one is the sulfur combined in the inclusions, and the third is the dissolved sulfur which is the difference of above two and can not be directly measured. Figure 5.54 shows the progress of these three sulfur contents as a function of injection time. Both the total sulfur and the dissolved sulfur contents

Ca%H1.DRW

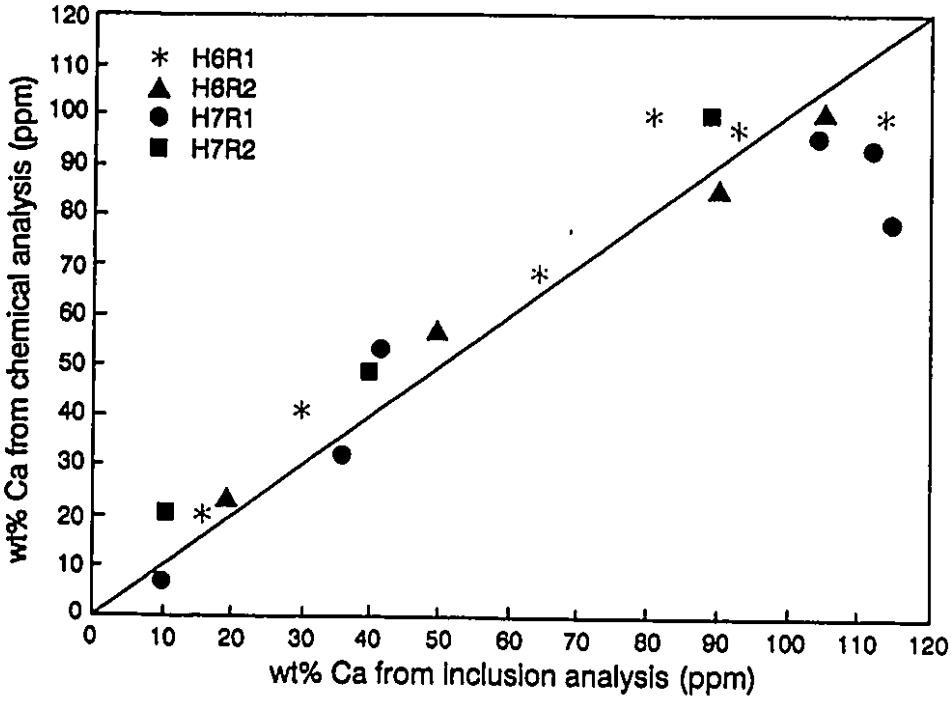

Figure 5.52 The comparison on wt%Ca between the bulk chemical and inclusion analysis during and after injection for H6R1, H6R2, H7R1 AND H7R2.

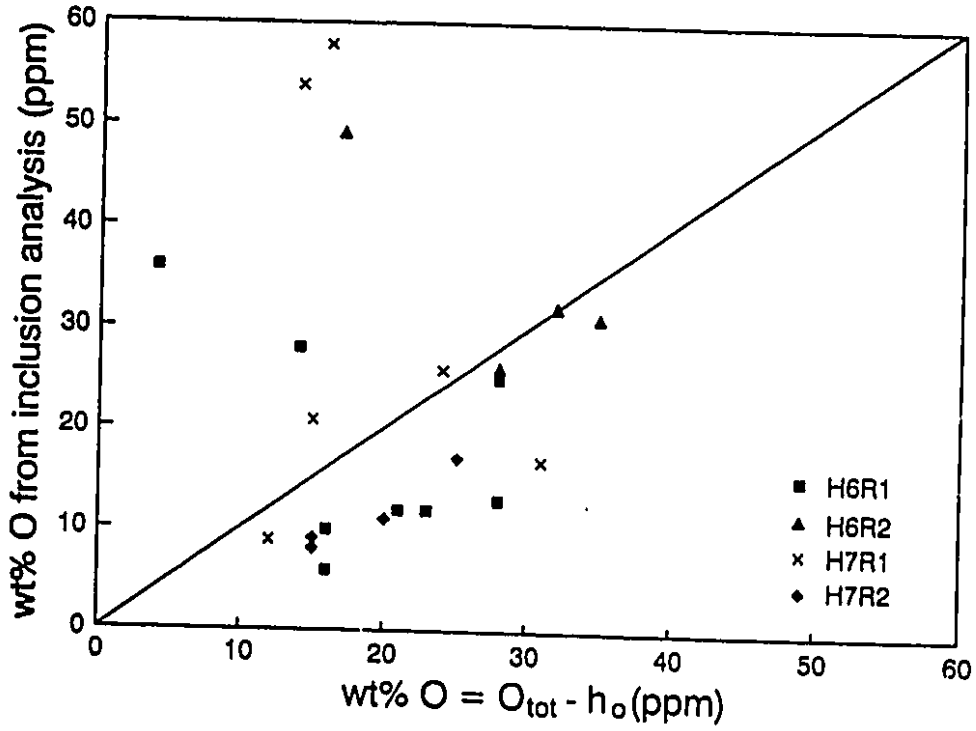

Figure 5.53 The comparison on wt%O between the bulk chemical and inclusion analysis during and after injection for H6R1, H6R2, H7R1 AND H7R2.

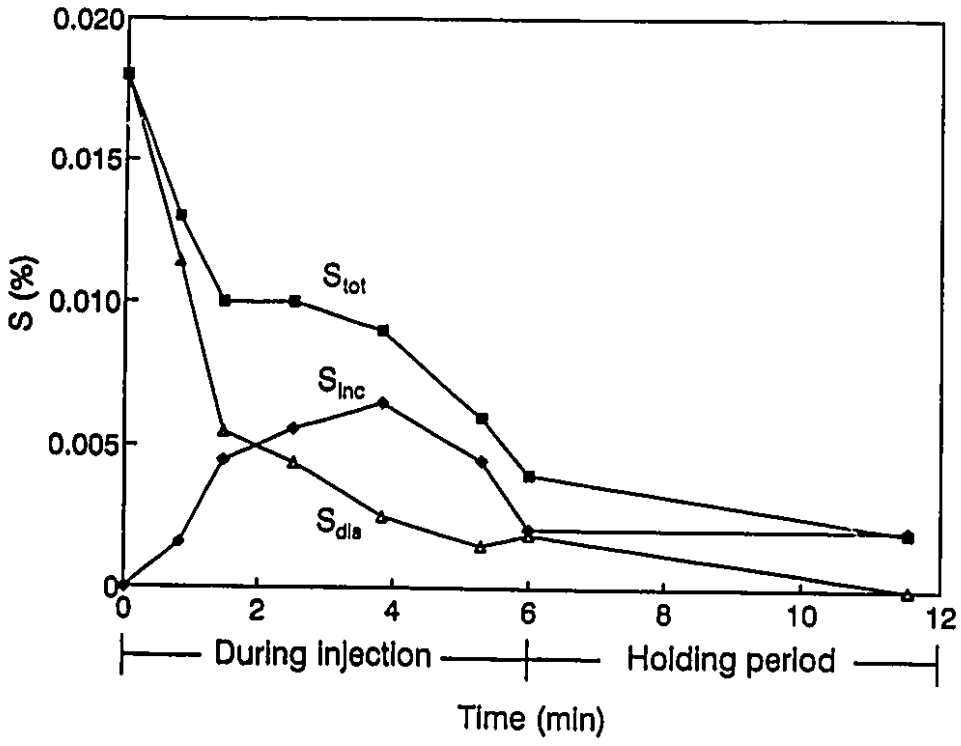

Figure 5.54 The change of total sulfur, sulfur in the inclusions, and the dissolved sulfur contents during and after injection for H6R1.

continue to decrease, while the sulfur in the inclusions increases at the beginning of injection, reaches to a maximum and then decreases at the later stage of injection.

5.4 CALCIUM RECOVERY

Calcium recoveries are often quoted for industrial processes as the calcium retained in the melt compared to the calcium injected into the steel, it is also called calcium efficiency:

$$CALCIUM\ RECOVERY = \frac{\%Ca - \%Ca_{INITIAL}}{\%Ca_{ADDED}} \qquad (5.13)$$

In industrial precesses this can only be done by comparing calcium before and after injection. In the present experiments the calcium recovery was calculated at each sampling time based on the total calcium content. The results for three different injection rates are shown in Figure 5.55. The peak is due to the fact that the calcium content increases rapidly at the beginning, but levels off (Figures 5.4 and 5.5) even though calcium is still being fed. The peak is higher and occurs at shorter times for increased feed rate because K_1 increases with feed rate (Figure 5.9). Therefore both the feed rate and the sampling time influence the observed values

for calcium recovery. Furthermore, the extent of inclusion modification cannot be deduced from calcium recoveries based on total calcium content as Figure 5.41 demonstrates. In summary, calcium recoveries must be carefully interpreted, and comparisons between widely different practices may not yield a useful measure of the effectiveness of inclusion modification by the different techniques.

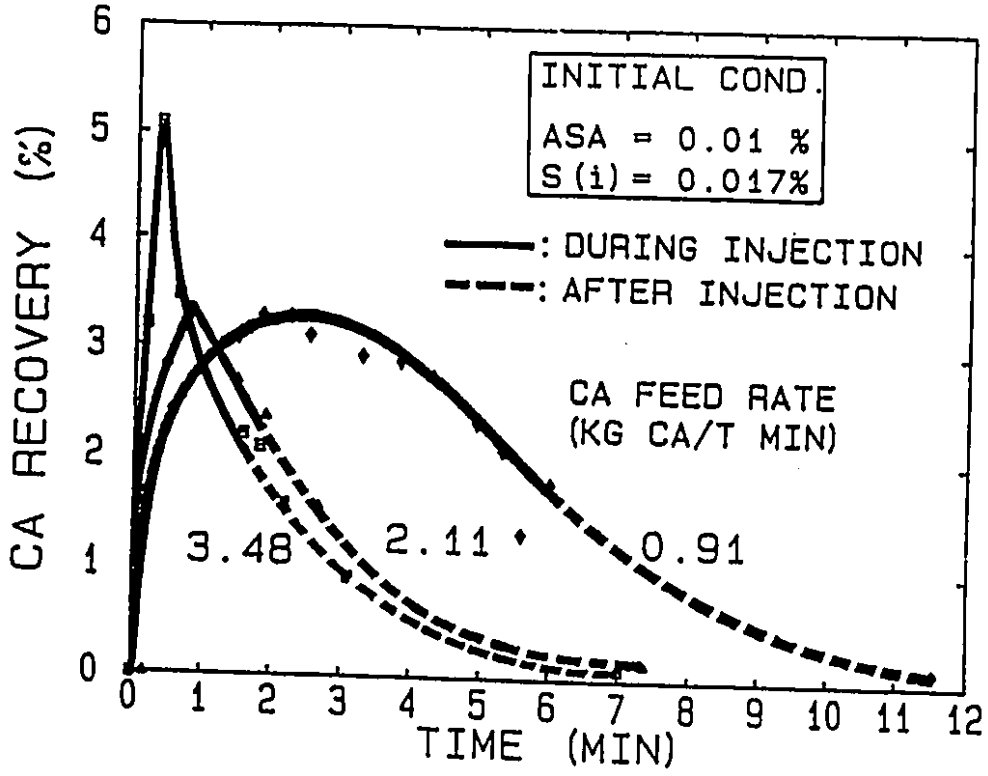

Figure 5.55 The calcium recovery as a function of time for three different injection rates.

CHAPTER 6

KINETICS, MECHANISMS AND MODELLING

6.1. INTRODUCTION

During calcium wire injection into the molten steel, calcium vaporizes at the tip of the wire, and comes in contact with the steel in the cavity produced by the vapour. As calcium dissolves into the liquid, it reacts with oxygen and sulphur to form CaO and CaS,

$$\underline{Ca} + \underline{O} = CaO \qquad (6.1)$$

$$\underline{Ca} + \underline{S} = CaS \qquad (6.2)$$

resulting in the reduction of the dissolved oxygen and sulphur in the melt.

Dissolved calcium can also react with the primary oxide Al_2O_3 inclusions in the melt to modify it from Al_2O_3 to CA_x to CaO in the following sequence: Al_2O_3-CA_6-CA_2-CA-$C_{12}A_7$-C_3A-CaO. These different phases of CA_x are indicated in CaO-Al_2O_3 phase

diagram (Figure 2.12):

$$\underline{Ca} + \underline{O} + x(Al_2O_3) = (CaO)\cdot x(Al_2O_3) \qquad (6.3)$$

Calcium can also modify MnS into (Ca,Mn)S:

$$\underline{Ca} + \underline{S} + MnS = (Ca,Mn)S \qquad (6.4)$$

The modified oxide CA_x and sulphide (Ca,Mn)S can also interact with each other to form the complex oxy-sulphide inclusion $(Ca,Mn)S\cdot CA_x$, which is also in coexistence in the melt with pure CaO, CaS, CA_x, (Ca,Mn)S, Al_2O_3 and MnS inclusions (Figures 5.16 to 5.20).

In such a complicated system, it is necessary to know where and when each of the above reactions (Equations 6.1-6.4) takes place during and after calcium injection in the steel, before a comprehensive kinetic model can be developed to quantitatively interpret the present experimental data.

6.2. THE KINETICS AND MECHANISM OF CALCIUM DISSOLUTION

To begin, the most important question is how calcium comes into the melt.

There are two possible hypotheses to explain the

mechanism of calcium dissolution into steel: 1) one hypothesis is calcium dissolution with no or negligible reactions in the liquid film, and 2) the other hypothesis is calcium dissolution with reactions in both the liquid film and the bulk. Both cases were introduced and discussed in the literature review (see section 2.7.1).

6.2.1 Calcium Dissolution with no or Negligible Reactions in the Liquid Film

The hypothesis of calcium dissolution with no or negligible reactions in the liquid film suggests that the reaction between the gas absorbants, Ca, and the reactants, S and O, in the liquid film and gas-liquid interface is very slow or negligible. This hypothesis of calcium dissolution with no or negligible reactions in the liquid film also indicates that the calcium dissolution rate is independent of the chemical components in the melt, and the calcium mass transfer rate through the gas-liquid boundary is solely a function of the physical hydrodynamic parameters. However, it was found from Figures 5.7 and 5.8 that both sulphur and oxygen enhanced the calcium mass transfer rate in our experiments. This means that calcium dissolution into the liquid steel under the present conditions is not a simple dissolution process.

6.2.2 Calcium Dissolution with Reactions in the Liquid Film

Irons and Guthrie's work [119] on magnesium desulphurization in molten iron found that there was a strong reaction between the dissolving magnesium gas and sulphur at the gas-liquid interface (the concentration profiles are shown in Figure 6.1). From the thermodynamic analysis in section 2.4.1 and Figure 2.8, it is shown that calcium is a much stronger desulphurizer and deoxidizer than magnesium. Therefore, the strong reactions between the dissolving calcium with sulphur and oxygen in the liquid film are inevitable. According to this hypothesis of calcium dissolution with reactions in the liquid film, the concentration profiles of Ca, S and O in the liquid film are schematically shown in Figure 6.2. The strong calcium deoxidation and desulphurization reactions in the liquid film will change the calcium concentration profile from a straight line to a curve, and push it closer to the gas-liquid interface, thus resulting in a steeper slope ij, rather than the slope ik for the simple dissolution. A higher value of the effective mass transfer coefficient $k_{L,E}$ is then obtained in comparison with the coefficient k_L for the simple dissolution. As a result, the calcium mass transfer rate is enhanced by the presence of sulphur and oxygen in the melt. This is in qualitative agreement with the results in Figures 5.7 and 5.8.

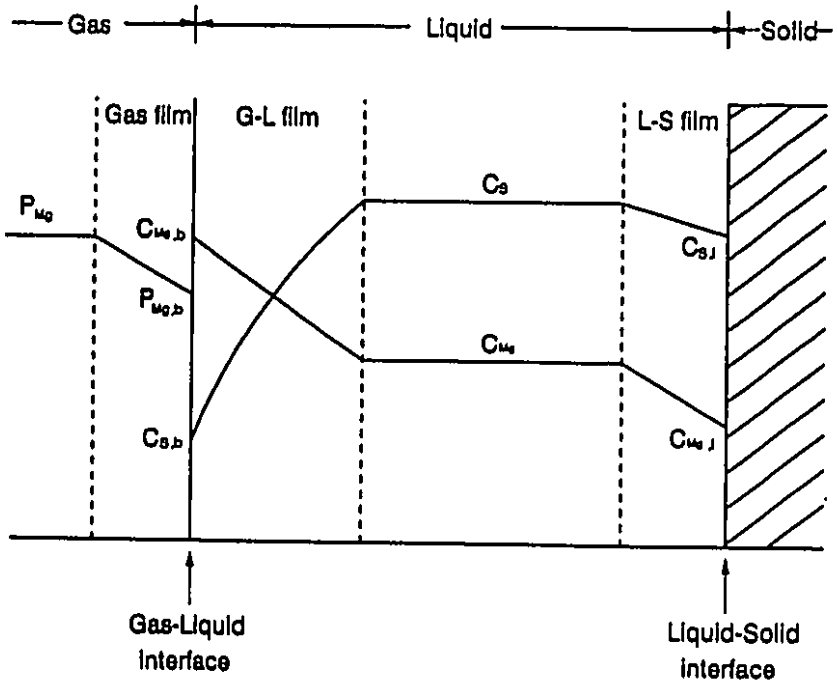

Figure 6.1 The schematic concentration profiles of magnesium and sulfur in the liquid iron film for magnesium desulphurization [119].

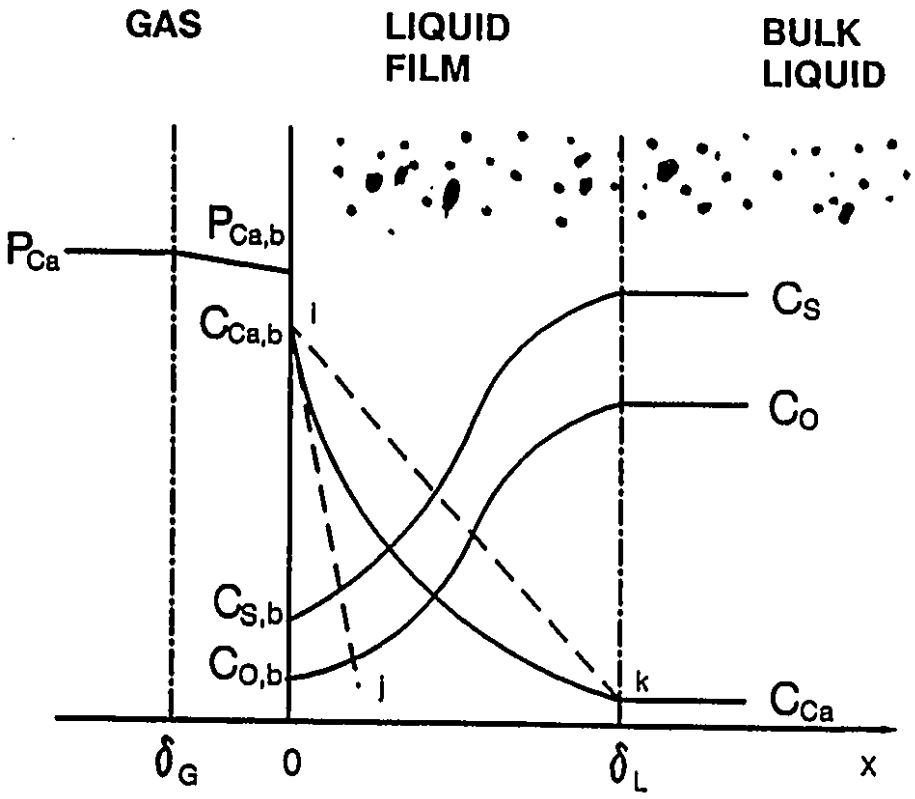

Figure 6.2 The schematic concentration profiles of calcium, oxygen and sulfur for calcium dissolution with Ca deoxidation and desulphurization reactions occurring at inclusions in the gas-liquid film. The ratio of slope ij to ik represents the enhancement factor over calcium dissolution without reactions in film.

However, quantitatively it is essential to know how significant it is for the reactions to affect the calcium concentration profile in the liquid film, and whether it is possible for most of calcium to be consumed in the liquid film.

A Film Conversion Parameter, M, [98] is adopted to define the ratio of the rate of calcium reactions at inclusions in the film to the rate of calcium diffusion through the film:

$$M = \frac{Maximum\ possible\ reaction\ rate\ in\ Film}{Maximum\ Diffusion\ rate\ through\ Film} \quad (6.5)$$

If M >> 1, the calcium reaction rate, $r_{Ca,reac}$, (reactions at the inclusions in the liquid film) is larger than the calcium diffusion rate, $r_{Ca,diff}$, (diffusion through the film). Therefore there would be enough sites to explain a high reaction rate in the film. Consequently, chemical reactions with sulphur and oxygen could enhance the rate of calcium dissolution.

The calcium reaction rate, $r_{Ca,reac}$, is the rate at which calcium would diffuse through the boundary layers of inclusions which are inside the film at the gas liquid interface. The rate is:

$$r_{Ca,reac} = \int_0^{\delta_L} k_i z_{CA_x} (C_{Ca,x} - C_{Ca,i}) A_L dX \qquad (6.6)$$

where A_L is the gas-liquid interfacial area, and x is the distance from the gas liquid interface. $(C_{Ca,i} - C_{Ca,x})$ is the driving force for diffusion to the inclusion interface, i.e. the calcium concentration at any position x minus the concentration in equilibrium with the inclusion. $k_i z_{CA_x}$ is the mass transfer rate constant for the inclusions in the liquid phase. For the present conditions, it is calculated according to Equation (2.75) [120] :

$$k_i z_{CA_x} = 2\pi D_{Ca} d_i n_i$$
$$= 2.5 - 25 \quad (s^{-1}) \qquad (6.7)$$

where d_i is the inclusion diameter. For the present experiments, the average volumetric inclusion diameter is relatively constant (Figure 5.38). $k_i z_{CA_x}$ varies from 2.5 to 25 (s^{-1}) as the number of inclusions varies from 10^{14} to 10^{15} ($/m^3$) (Figures 5.32-33). The detailed calculation of $k_i z_{CA_x}$ is given in Appendix C. For the maximum calcium reaction in the film, $C_{Ca,i}$ can be assumed to be zero at the inclusion interface. The calcium concentration profile is also assumed to be linear across the film, so that $C_{Ca,x}$ is given as:

$$C_{Ca,x} = \left(1 - \frac{X}{\delta}\right) C_{Ca,b} \qquad (6.8)$$

The maximum calcium reaction at the inclusions in the liquid film is then given by:

$$r^{max}_{Ca,reac} = \int_0^{\delta_L} k_i z_{CA_x}\left(1-\frac{X}{\delta_L}\right)C_{Ca,b}A_L dX$$

$$= \frac{k_i z_{CA_x}}{2} C_{Ca,b}A_L\delta_L \qquad (6.9)$$

The calcium diffusion rate, $r_{Ca,diff}$, through the liquid film is given by:

$$r_{Ca,diff} = \frac{D_{Ca}}{\delta_L}(C_{Ca,b}-C_{Ca})A_L \qquad (6.10)$$

To maximize the diffusion rate, the bulk calcium term, C_{Ca}, can be regarded as zero, and a linear concentration profile is again applied across the film. Then the maximum calcium diffusion in the film is given as:

$$r^{max}_{Ca,diff} = \frac{D_{Ca}}{\delta_L} C_{Ca,b}A_L \qquad (6.11)$$

From Equations (6.8) and (6.10), the film conversion parameter is calculated as:

$$M = \frac{r^{max}_{Ca,reac}}{r^{max}_{Ca,diff}} = \frac{k_i z_{CA_x}\delta_L^2}{2D_{Ca}} \qquad (6.12)$$

where calcium diffusivity D_{Ca} was estimated as $3*10^{-9}$ m^2/s. The liquid film thickness is estimated by applying the film model to the Baird-Davidson [107] relationship for the mass transfer coefficient to bubbles which was found to apply to magnesium dissolution in iron [120].

$$\delta = \frac{D_{Ca}}{k} \doteq \frac{3*10^{-9}}{4.6*10^{-5}} = 6.5*10^{-5} \quad m \qquad (6.13)$$

Note that the gas-liquid film thickness is of the order of 65 μm, whereas the inclusions are of the order of 2 μm. Substituting into Equation 6.12, one obtains:

$$M = \frac{k_1 z_{CA_x} \delta_L^2}{2D_{Ca}}$$

$$= \frac{(2.5 \sim 25)*(6.5*10^{-5})^2}{2*3*10^{-9}} \qquad (6.14)$$

$$= 1.8 \sim 18$$

In the present calculations, M is always greater than one, which indicates that there are enough inclusions in the melt and gas liquid film to carry out the chemical reactions at a faster rate than that of the calcium diffusion through the film. Therefore, significant enhancement is possible. M was calculated assuming the maximum rate of reaction (i.e. $C_{Ca,i}$=0). Even with this assumption, M was not orders of magnitude greater than one. Consequently, not all of the calcium is expected to be consumed in the film.

From Figure 6.2, it can be seen that the calcium mass transfer rate with chemical reactions across the film is given by:

$$r_{Ca,E} = D_{Ca} \cdot A_L \cdot \left.\frac{dC_{Ca}}{dx}\right|_{x=0} \qquad (6.15)$$

The calcium mass transfer rate without chemical reactions is:

$$r_{Ca} = k_G \cdot A_L \cdot (P_{Ca} - P_{Ca,b}) = k_L \cdot A_L \cdot (C_{Ca,b} - C_{Ca}) \qquad (6.16)$$

Therefore, the enhancement factor, E, the increased ratio of mass transfer rate with chemical reactions to mass transfer rate without reactions in the film, is then given as:

$$E = \frac{r_{Ca,E}}{r_{Ca}} = \frac{\left.\frac{dC_{Ca}}{dx}\right|_{x=0}}{\frac{C_{Ca} - C_{Ca,b}}{\delta_L}} = \frac{slope(ij)}{slope(ik)} \qquad (6.17)$$

where the slope ij for the case of calcium mass transfer with reactions in film, and slope ik for the case of mass transfer without reactions are indicated in Figure 6.2.

6.2.3 An Instantaneous Reaction Mechanism for Calcium Dissolution

Although the general solution of Equation 6.16 for enhanced dissolution does not exist, the enhanced calcium mass transfer rate, $r_{Ca,E}$, can be determined analytically in special cases. Nine reaction regimes are classified by the dimensionless groups in Table 2.11 [123]. From Table 2.11, if Ha > 3, the reaction in the liquid film is considered as fast or instantaneous. Since M and Ha have the similar physical

significance: the ratio of conversion rate in film to diffusion rate through film of the dissolving gas, high M values in the present calculation indicate the fast and instantaneous nature of calcium reactions with sulphur and oxygen in the liquid. Therefore, the general case of Figure 6.2 can be simplified with an instantaneous reaction two-film model: during calcium injection, calcium dissolves through the gas-liquid boundary layer and is met by oxygen and sulphur diffusing towards the gas-liquid interface. The concentration profiles are shown schematically in Figure 6.3. Where these fluxes meet, reactions between calcium with oxygen and sulphur occur in the liquid film. These strong calcium deoxidation and desulphurization reactions in the liquid film result in a steep slope and faster mass transfer rate. This explains the enhancement of calcium absorption by higher initial sulphur and oxygen contents in the melt. The following assumptions are made to develop a model for the enhanced calcium dissolution:

1) These reactions are assumed to be so fast that the dissolving calcium reacts instantaneously with oxygen and sulphur at a plane δ_r from the interface, controlled by the rates of diffusion,
2) chemical equilibrium exists at the gas-liquid interface, and the plane for both calcium deoxidation and desulphurization reactions, and

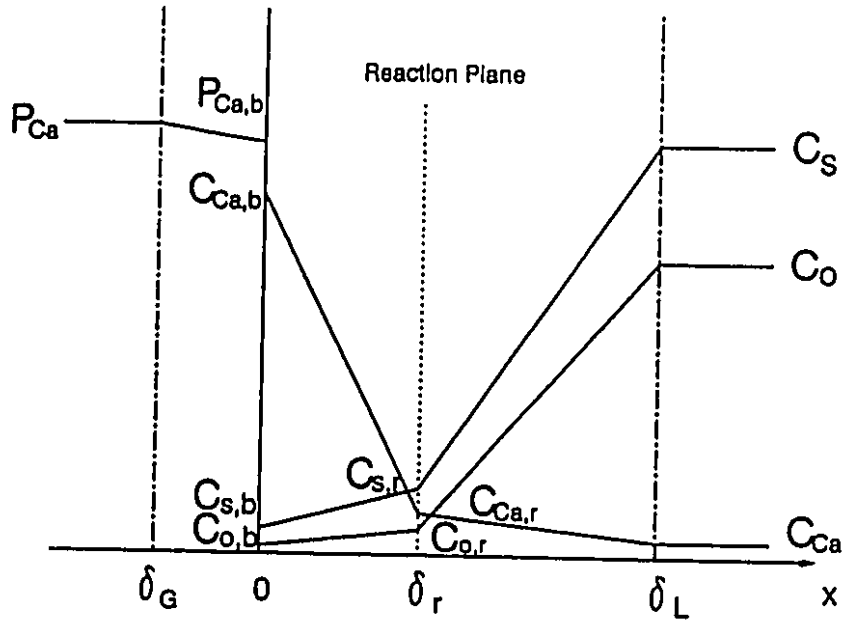

Figure 6.3 The two-film model for calcium dissolution with its instantaneous reactions with oxygen and sulphur at a reaction plane in the liquid film. The concentration profiles of calcium, oxygen and sulphur in the boundary layer are assumed to be linear.

3) the concentration profiles of calcium, oxygen and sulphur in the boundary layer are assumed to be linear.

Using thses assumptions, and Fick's Law, the following relationships can be developed:

1) the effective thickness, δ_r, for the reaction plane is determined by the balance of the fluxes for calcium against sulphur and oxygen:

$$\frac{D_O(C_O-C_{O,r})}{\delta_L-\delta_r}+\frac{D_S(C_S-C_{S,r})}{\delta_L-\delta_r}=\frac{D_{Ca}}{\delta_r}(C_{Ca,b}-C_{Ca,r}) \qquad (6.18)$$

where $C_{Ca,r}$, $C_{S,r}$ and $C_{O,r}$ are the equilibrium concentrations of calcium, sulphur and oxygen at the reaction plane.

2) Equilibrium exists at the reaction plane δ_r and at the gas-liquid interface:

$$\begin{aligned} C_{Ca,r}\cdot C_{O,r}&=K_{CaO}, \quad & C_{Ca,r}\cdot C_{S,r}&=K_{CaS} \\ C_{Ca,b}\cdot C_{O,b}&=K_{CaO}, \quad & C_{Ca,b}\cdot C_{S,b}&=K_{CaS} \end{aligned} \qquad (6.19)$$

3) The remain unreacted calcium diffuses through the outer portion of the liquid film into the bulk as dissolved calcium which contributes to inclusions modification:

$$\frac{dC_{Ca}}{dt}=\frac{D_{Ca}}{\delta_L-\delta_r}\frac{A_L}{V}(C_{Ca,r}-C_{Ca}) \qquad (6.20)$$

where A_L is the calcium gas-liquid interface area, and V is the volume of the liquid melt.

Since the equilibrium constants for both deoxidation (K_{CaO}) and (K_{CaS}) are very small [6] (in the order of 10^{-8} from Table 2.7), the equilibrium concentrations at the reaction plane can be ignored in comparison with the other concentration terms in Equation (6.18). δ_r can then be calculated in terms of boundary layer thickness, δ_L:

$$\delta_r = \left(\frac{D_{Ca} C_{Ca,b}}{D_O C_O + D_S C_S + D_{Ca} C_{Ca,b}} \right) \delta_L \qquad (6.21)$$

The equilibrium calcium concentration at the instantaneous reaction plane, $C_{Ca,r}$, can be obtained by substituting Equation (6.21) into Equation (6.18):

$$C_{Ca,r} = \sqrt{\frac{D_O K_{CaO} + D_S K_{CaS}}{D_O C_O + D_S C_S} C_{Ca,b}} \qquad (6.22)$$

For a typical heat condition (%O = 0.001 and %S = 0.01), $\%Ca_r$ is calculated to be 0.0003 from the above equation, which is three orders of magnitude smaller than that of the interfacial calcium concentration at the vapour-liquid interface ($\%Ca_b$ = 0.024). The equilibrium concentrations of oxygen and sulfur at the reaction plane are then obtained from the equilibrium constants [6] in Table 2.7:

$$\%S_r = \frac{K_{CaS}}{\%Ca_r} = \frac{1.96*10^{-7}}{0.0003} = 6*10^{-4} \qquad (6.23)$$

$$\%O_r = \frac{K_{CaO}}{\%Ca_r} = \frac{7*10^{-9}}{0.0003} = 2.3*10^{-5} \qquad (6.24)$$

Again by comparison, the equilibrium concentrations of sulfur and oxygen at the reaction plane in the liquid film are about 3 orders of magnitude smaller than the bulk concentrations. Therefore, the assumptions regarding the equilibrium concentrations at the reaction plane are reasonable.

It is then convenient to define an enhancement factor, E_{Ca}, which is the rate of calcium dissolution with chemical reactions in the liquid film compared to that for the simple dissolution:

$$E_{Ca} = \frac{k_{L,E}}{k_L} = \frac{D_{Ca}/\delta_r}{D_{Ca}/\delta_L} = 1 + \frac{D_O C_O + D_S C_S}{D_{Ca} C_{Ca,b}} \qquad (6.25)$$

Inserting the initial concentrations of oxygen and sulphur into Equation (6.25), the enhancement factor E_{Ca}^0 at the very beginning of injection is calculated in Table 6.1 for all the injection heats.

The total calcium pick-up rate from the instantaneous reactions with oxygen and sulphur in the liquid boundary is given by the following equation:

$$\frac{dC_{Ca,T}}{dt} = \frac{D_{Ca}z_L}{\delta}\left(1+\frac{D_OC_O+D_SC_S}{D_{Ca}C_{Ca,b}}\right)C_{Ca,b} - k_{Ca}z_LE_{Ca}(C_{Ca,b}-C_{Ca,I}) \approx k_{Ca}z_LE_{Ca}C_{Ca,b} \qquad (6.26)$$

where z_L is the calcium gas-liquid interface area per unit volume of the melt ($z_L = A_L/V$)

Since most of the total calcium in the melt is combined in the inclusions, and the inclusion flotation (elimination) is the major contributor to the decay of total calcium, the total calcium mass balance is written as:

$$\frac{dC_{Ca,T}}{dt} = k_{Ca}z_LE_{Ca}C_{Ca,b} - k_ez_eC_{Ca,T} \qquad (6.27)$$

At the very beginning of calcium injection, the elimination term for the above equation can be ignored, i.e. $C_{Ca,T} = 0$, so that the tangent of the calcium concentration curve at $t \to 0$, should be the term of the total calcium pick-up rate, i.e.,

TABLE 6.1

The Calculation Results of $dC_{Ca,T}/dt|_{t=0}$, z_L/δ_L and kz_L at Different E_{Ca}^0

Heat #	Case #	MEASURED			CALCULATED				
		C_s^0 (mol/m^3)	C_o^0 (mol/m^3)	$dC_{Ca,T}/dt\|_{t=0}$ (mol/m^3·s)	E_{Ca}^0	z_L/δ_L (m)	$k_{Ca}z_L$ *10^3 (s^{-1})	k_sz_L *10^3 (s^{-1})	k_oz_L *10^3 (s^{-1})
H6R1	1	31	8	0.009	2.46	33.8	1.01	1.45	1.05
H6R2		7	2	0.022	1.31	55.5	1.66	2.38	1.72
H7R1		38	43	0.032	3.75	78.3	2.35	3.37	2.43
H8R1		25	15	0.022	2.43	84.9	2.55	3.65	2.63
H8R2		20	5	0.021	1.94	99.7	2.99	4.29	3.09
H9R1		34	27	0.059	3.13	175.8	5.27	7.56	5.45
H3R1	2	64	1	0.0072	3.58	18.6	0.56	0.80	0.58
H4R1		33	1	0.0047	2.34	18.5	0.55	0.79	0.57
H5R1		20	3	0.0695	1.88	341.8	10.25	14.7	10.59
H7R2		22	2	0.0085	1.93	70.5	2.11	3.03	2.19
H9R2	3	2	11	0.0054	1.30	35.8	1.07	1.54	1.11
H9R3	4	0.9	1	0.0071	1.06	61.8	1.85	2.66	1.91

where

$D_{Ca} = 3*10^{-9}$ m^2/s (from Appendix B)
$D_s = 4.3*10^{-9}$ m^2/s (from Appendix B)
$D_o = 3.1*10^{-9}$ m^2/s (from Appendix B)
$C_{Ca,b} = 36.0$ mole/m^3
$E_{Ca}^0 = 1 + (D_oC_o^0 + D_sC_s^0)/(D_{Ca}C_{Ca,b})$
$k_{Ca}*z_L = D_{Ca}*z_L/\delta_L$
$k_s*z_L = D_s*z_L/\delta_L$
$k_o*z_L = D_o*z_L/\delta_L$

$$\left.\frac{dC_{Ca,T}}{dt}\right|_{t=0} = \frac{D_{Ca}z_L}{\delta_L}\left(1+\frac{D_OC_O^0+D_SC_S^0}{D_{Ca}C_{Ca,b}}\right)C_{Ca,b}$$

$$= \left[\frac{D_{Ca}z_L}{\delta_L}\right] E_{Ca}^0\ C_{Ca,b} \qquad (6.28)$$

$$= k_{Ca}\ z_L\ E_{Ca}^0\ C_{Ca,b}$$

For the same injection conditions, the product of the mass transfer coefficient and area, $k_{Ca}z_L$, should be the same. Consequently, the initial calcium pick-up rate should increase linearly with the initial enhancement factor, E_{Ca}^0. When the calcium pick-up rate is plotted against the postulated enhancement factor according to Equation 6.28, the experiment results fall into line very well with this model (Figure 6.4).

The hydrodynamic term in Equation 6.28, z_L/δ_L, which is independent of the chemical parameters, can be determined by rearranging Equation 6.28:

$$\frac{z_L}{\delta_L} = \frac{\left.\frac{dC_{Ca,T}}{dt}\right|_{t=0}}{D_{Ca}\left(1+\frac{D_OC_O^0+D_SC0}{D_{Ca}C_{Ca,b}}\right)C_{Ca,b}} \qquad (6.29)$$

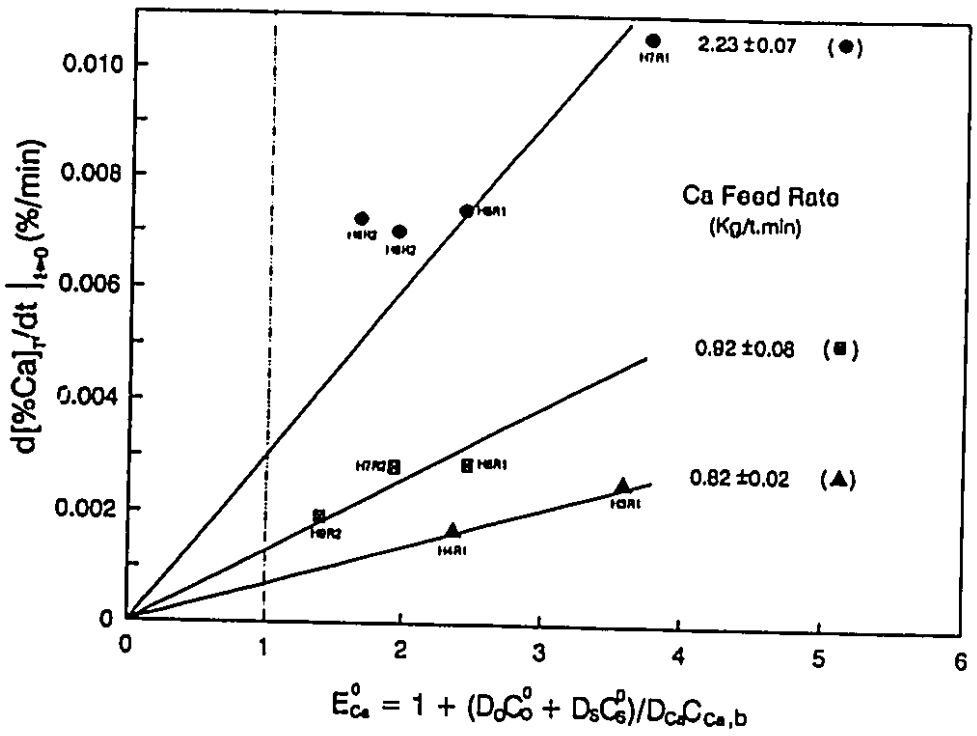

Figure 6.4 The relationship between the initial calcium pick-up rate, $d[\%Ca]_T/dt|_{t=0}$ and the initial enhancement factor, E_{Ca}^0, for three different calcium injection rates. Lines are from the instantaneous reaction model for calcium dissolution (Equation 6.28).

The mass transfer rate constants for dissolution without reactions, $k_{Ca}z_L$, $k_o z_L$ and $k_s z_L$ for calcium, oxygen and sulphur at the gas-liquid boundary are then obtained by:

$$k_{Ca}z_L\text{-}D_{Ca}\left(\frac{z_L}{\delta_L}\right) \quad , \quad k_o z_L\text{-}D_o\left(\frac{z_L}{\delta_L}\right) \quad , \quad k_s z_L\text{-}D_s\left(\frac{z_L}{\delta_L}\right) \qquad \textbf{(6.30)}$$

Both the hydrodynamic term, z_L/δ_L, and mass transfer rate constants for simple dissolution, $k_{Ca}z_L$, $k_o z_L$ and $k_s z_L$ are calculated in Table 6.1.

The calcium mass transfer rate constant, $k_{Ca}z_L$, can also be independently estimated. Mucciardi [43] has obtained an empirical equation (Equation 2.39) to estimate aluminum wire penetration depth in steel. Since both aluminum and calcium are exothermic in their dissolution in the melt, the above empirical equation can be used to estimate the calcium wire penetration. At a low calcium wire feed rate, 0.02 m/s, the calcium wire penetration depth was calculated to be 0.045 m, and at a high feed rate, 0.06 m/s, the penetration depth is 0.065 m. For such a relatively shallow penetration of calcium wire, there is a great possibility that a gas cavity or dimple would be formed, since a high volume of calcium vapour has to escape to the atmosphere. Assuming calcium gas forms a open cylinder, the volume of the cylinder can be obtained from the gas flow (escaping) rate, so that the calcium gas-liquid interfacial area, A_L, and area per volume of melt, z_L, can be calculated.

Mass transfer at the gas-liquid interface in the cavity formed by the jet was studied by Walkelin [109], who obtained the following equation (Equation 2.51) for local mass transfer coefficient.

Equation 2.51 is used here to estimate the calcium mass transfer coefficient, k_{Ca}, at the gas-liquid interface. The calculated calcium mass transfer rate constants, $k_{Ca}z_L$, are then compared in Figure 6.5 with the experimentally measured rate constants which are taken from Table 6.1. Most of the calculated values are within 35% to 75% of the experimentally determined. In comparison with aluminum wire, calcium wire generates gas in its contact with the melt, so that there is an uncertainty in applying Equation (2.39) to estimate the calcium wire penetration depth in steel, and also Walkelin's [109] Equation (2.51) was for shallow dimples. These uncertainties might cause the difference between the estimation and the experimental data in Figure 6.5.

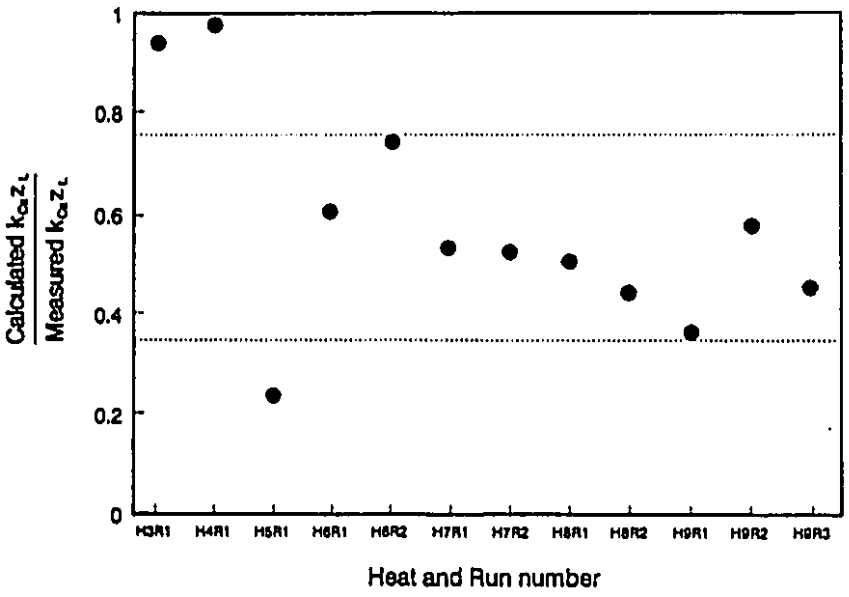

Figure 6.5 The comparison between the calculated and the experimentally determined calcium mass transfer rate constant at gas-liquid interface. Note that most of the calculated values are 35% to 75% of the experimental results.

6.3 KINETICS AND MECHANISMS OF INCLUSION MODIFICATION

Before calcium addition to steel, there are mainly two kinds of non-metallic inclusions: oxide Al_2O_3 and sulfide MnS. Al_2O_3 is a direct product of aluminum deoxidation and solid in the liquid steel. MnS inclusion usually forms at the grain boundaries during solidification of steel.

As calcium injection progresses, both oxide and sulfide morphologies change towards calcium-rich components (Figures 5.41-51). Al_2O_3 transformation to calcium-rich aluminate is favoured by increased calcium treatment (Figures 5.41-43), low acid soluble aluminum content (Figure 5.44), and low sulphur (Figure 5.45). MnS transformation to calcium-rich sulphide inclusions is favoured by increased calcium treatment (Figures 5.47 and 5.48), high acid soluble aluminum (Figure 5.49) and low sulphur (Figure 5.50). Higher initial h_s/h_o tends to favour sulphide modification and lower initial h_s/h_o tends to favour oxide inclusion modification (Figures 5.46 and 5.51).

During the continuous morphology change of oxide and sulphide by calcium injection, large amounts of "primary" CaO and CaS were found to come from the gas-liquid film (Figures 5.25-28), as discussed in the previous section. Reactions may continue at those primary inclusions in the bulk. However, in the same sample, there also exist unmodified Al_2O_3 and

unmodified MnS inclusions, as shown in Figure 5.25-28.

There is also a strong relationship between oxide and sulphide inclusions (Figures 5.46 and 5.51). This reflects the nature of the simultaneous modification of both oxide and sulphide inclusions by calcium addition in the melt. However, the individual modification mechanisms for both oxide and sulphide inclusions must be studied first, before their interactions and the system reaction paths can be fully explored.

6.3.1 Alumina (Al_2O_3) modification

As the dissolved calcium diffuses towards the solid Al_2O_3 inclusions, the following overall reaction contributes to the modification of Al_2O_3 into calcium aluminate CA_x.

$$\underline{Ca} + \frac{1}{3}(Al_2O_3) = (CaO) + \frac{2}{3}\underline{Al} \qquad (6.31)$$

where the species within the parentheses are dissolved in the aluminate phase (CA_x). If equilibrium is reached at the inclusion interfaces, the activity ratio of the CaO and Al_2O_3 components in CA_x is a function of the ratio of the calcium and aluminum activities:

$$\frac{a_{CaO}}{a_{Al_2O_3}^{1/3}} = \frac{K_{Al_2O_3}}{K_{CaO}}\left(\frac{h_{Ca}}{h_{Al}^{2/3}}\right) \qquad (6.32)$$

where $K_{Al_2O_3}$ and K_{CaO} are the equilibrium constants for aluminum and calcium deoxidation in the melt, $a_{Al_2O_3}$ and a_{CaO} are the activities of Al_2O_3 and CaO, using pure solid as the standard state, and h_{Ca} and h_{Al} are the calcium and aluminum activities, using 1 wt% as the standard state. For the same aluminum activity, the activity ratio of CaO to Al_2O_3 in Equation (6.32) or the chemistry of CA_x depends solely on the calcium activity. With increasing concentration of dissolved calcium in the melt during injection, the CA_x changes from alumina-rich towards calcia-rich aluminates.

The oxide inclusions formed during calcium treatment will be richer in CaO than those precipitating during liquid metal cooling and solidification. However, from the literature survey [87], the average composition of CA_x observed at room temperature is not very different from that calculated at high temperature, since the ratio of $a_{CaO}/(a_{Al_2O_3})^{1/6}$ changes only within 20% with temperature during cooling from 1600 to 1500 ^{0}C [6,53]. The solidification of the liquid metal in the small samplers used in the present experiments is so fast that there is very little time for the solid state reactions to take place. Therefore, the oxide CA_x composition analyzed in the solid samples are believed to reflect its composition at high temperature.

6.3.2 Manganese sulphide (MnS) modification

The thermodynamics for MnS formation is [164]:

$$MnS = \underline{Mn} + \underline{S} \qquad (6.33)$$

$$\log \frac{h_{Mn}\, h_S}{a_{MnS}} = -\frac{8194}{T} + 4.96 \qquad (6.34)$$

For the present conditions, MnS does not exist in the liquid steel due to the low sulfur and manganese contents in the melt; it forms during solidification.

From CaS-MnS phase diagram in Figure 2.15, at 1600 ^{0}C, calcium reacts with manganese and sulfur to form the solid ($X_{CaS} > 0.65$) or liquid ($0 \leq X_{CaS} \leq 0.65$) calcium-manganese sulfide, (Ca,Mn)S. This solid or liquid calcium-manganese sulfide may exist as a single phase, (Ca,Mn)S, or in combination with the oxy-sulphide complex inclusions, (Ca,Mn)S·CA_x. In the present experiments, it was found that most of calcium-maganese sulphide existed as a single phase, with only minor amounts of oxy-sulphide complex present (Figures 5.25-28). The composition of sulfide changed from MnS-rich towards CaS-rich (Ca,Mn)S (Figures 5.47 and 5.48) as injection progresses, but it did not change substantially during the holding period.

The formation of oxy-sulphide complex can be explained as

the following: as calcium dissolves into steel, it reacts with Al_2O_3 and changes it towards lime-rich CA_x.

$$\underline{Ca} + \frac{1}{3}(Al_2O_3) = (CaO) + \frac{2}{3}\underline{Al} \qquad (6.35)$$

When CA_x reaches a certain composition, it reacts with sulfur and manganese to form complex (Ca,Mn)S.CA_x inclusions, so that the reactions occurring on CA_x inclusions are the following:

$$(CaO) + \frac{2}{3}\underline{Al} + \underline{S} = (CaS) + \frac{1}{3}(Al_2O_3) \qquad (6.36)$$

where the species within the parentheses are part of either oxide CA_x, or sulfide (Ca,Mn)S.

During calcium injection, there is also a continuous supply of the primary CaO and CaS inclusions from the calcium gas-liquid boundary. Manganese and sulfur can diffuse to and react with them to form the single phase (Ca,Mn)S. The overall thermodynamic relation for (Ca,Mn)S formation in equilibrium with its components can be written as:

$$\underline{Ca} + (MnS) = (CaS) + \underline{Mn} \qquad (6.37)$$

where the species within the parentheses are part of the sulfide phase (Ca,Mn)S. The equilibrium calcium-manganese sulfide composition relates to the manganese and calcium activities. The equilibrium activity ratio of CaS and MnS components in (Ca,Mn)S is then:

$$\frac{a_{CaS}}{a_{MnS}} = \frac{K_{MnS}}{K_{CaS}} \frac{h_{Ca}}{h_{Mn}} \qquad (6.38)$$

where K_{MnS} and K_{CaS} are the equilibrium constants for reactions of MnS and CaS formation in the melt, and a_{CaS} and a_{MnS} are the activities of CaS and MnS, using pure solid as the standard state, and h_{Ca} and h_{Mn} are the calcium and manganese activities, using 1 wt% as the standard state. For the same manganese activity, the activity ratio in Equation (6.38), or the chemistry of (Ca,Mn)S depends solely on the calcium activity.

According to CaS-MnS activity diagrams in Figures H2-H4 in Appendix H, the ratio of a_{CaS}/a_{MnS} changes within 25% in the temperature range of 1600 to 1500 ^{0}C. This means that the composition of (Ca,Mn)S does not change substantially during cooling from 1600 ^{0}C to the steel solidification temperature, 1500 ^{0}C. When the sample solidifies, some of the MnS inclusions might precipitate on the primary inclusions in the melt, but most MnS were found to form as a single phase at the grain boundaries from the last solidifying liquid. No obvious MnS ring was found on either CA_x or CaS and CaO inclusions, and the inclusions observed were uniform and homogenous in nature. This indicates that in the present experiments that observable quantities of (Ca,Mn)S do not form during solidification by precipitation of Mn and S on the primary CaS and CaO inclusions. Furthermore, the samples were cooled down

and solidified in seconds, so that there was not enough time for significant solid state reactions to take place within the sulphide inclusions. Therefore, the data analyzed from SEM are believed to reflect the composition of sulfide in the liquid steel.

As more sulphur reacted and tied up calcium and manganese in the (Ca,Mn)S inclusions, less MnS was available to precipitate at the grain boundaries during solidification as shown in Figures 5.25-28.

6.3.3 The relationship between oxide and sulphide inclusions

Calcium changes the compositions of both oxide and sulfide inclusions simultaneously during its injection. At any injection time, the compositions of both CA_x and (Ca,Mn)S inclusions are directly related to the initial conditions (see Figures 5.41-51). There exists a strong relationship between the oxides, CA_x, and the sulphides, (Ca,Mn)S. This relationship is shown in Figure 6.6, by plotting the CA_x composition (CaO% in CA_x) on the x-axis against the (Ca,Mn)S composition (CaS% in (Ca,Mn)S) on the y-axis for the same samples. The results show that the higher initial h_s/h_o ratio shifts the experimental results towards the left corner; that means, sulphide modification precedes the oxide modification, whereas at the lower initial h_s/h_o oxide modification precedes

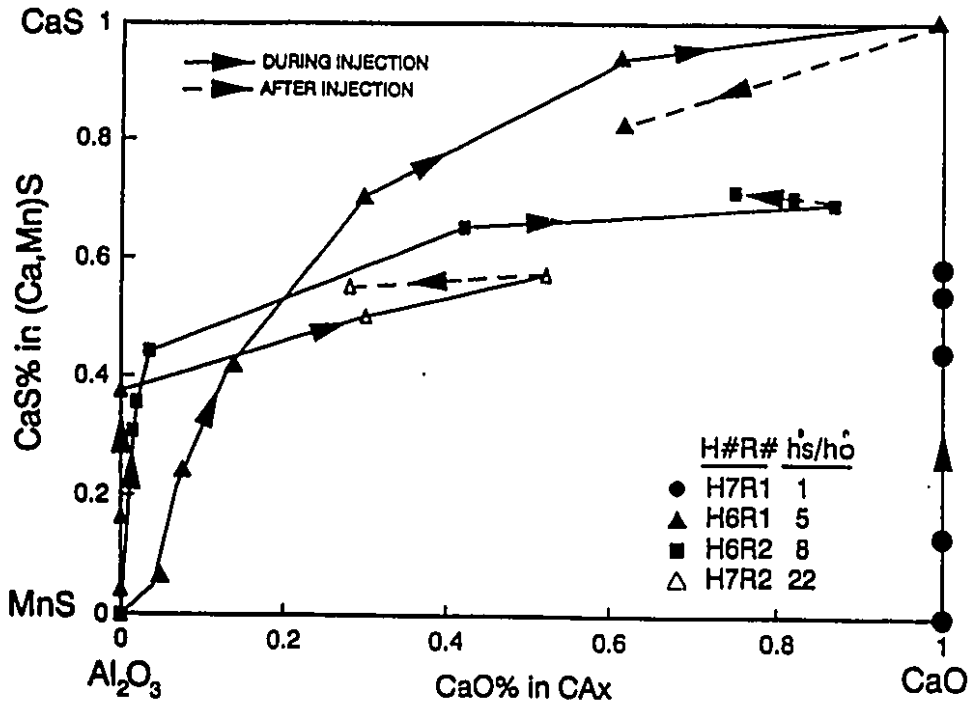

Figure 6.6 The relationship or interaction between CA_x and (Ca,Mn)S, showing the CaS% in the sulphide phase against the CaO% in the oxide phase during and after injection, for four different injections.

the sulphide. However, the pattern diminishes in the later stages of injection. This relationship between simultaneous oxide and sulphide modification is studied in detail in the next section.

6.3.4 System kinetic paths during and after injection

Figure 6.7 shows the relationship and interaction between deoxidation, desulphurization, and simultaneous oxide and sulphide modification in the bulk by calcium. The left-hand side represents the CaO component in oxide (either as pure CaO or CA_x), and the right-hand side represents the CaS component in sulfide (either as pure CaS or (Ca,Mn)S). The oxide and sulfide interact with S and O in the bulk. Therefore, this overall interaction between oxide and sulfide can be represented as:

$$(CaO) + \underline{S} = (CaS) + \underline{O} \qquad (6.39)$$

The species in the parentheses are either in pure state or dissolved in the oxide or sulphide inclusions. If the above equation reaches equilibrium with the bulk, the relationship between oxide and sulphide, and the related bulk chemistry is given by:

$$\frac{a_{CaO}}{h_o} = \left(\frac{K_{CaS}}{K_{CaO}}\right) \frac{a_{CaS}}{h_s} \qquad (6.40)$$

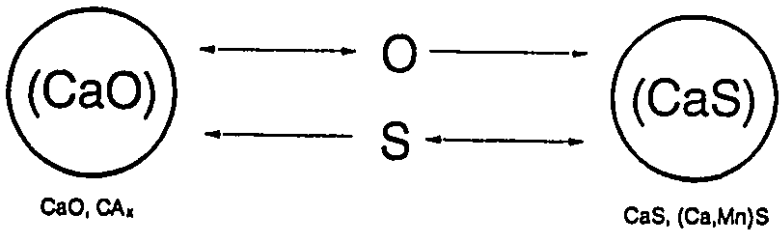

$$(CaO) + \underline{S} = (CaS) + \underline{O}$$

$$\log\frac{a_{CaS}}{h_S} = \log K + \log\frac{a_{CaO}}{h_O}$$

Figure 6.7 The interactions between oxide (CaO and CA_x) and sulfide (CaS and (Ca,Mn)S) inclusions with the melt, and their overall reaction as (CaO) + $\underline{S}$ = (CaS) + $\underline{O}$.

During calcium injection, the activities of CaO and CaS will increase simultaneously with the modification of both oxide and sulfide towards calcium-rich inclusions. In order to apply above equation to interpret the data in Figures 5.46, 5.51 and 6.6, the activities of CaO and CaS must be evaluated at various inclusion compositions. CaO activities in the calcium aluminate system have been previously evaluated [1,13], but CaS activities in the CaS-MnS system have not been reported to the best of our knowledge. However, the CaS and MnS activities can be calculated from CaS-MnS phase diagram (Figure 2.15). The calculation of CaS and MnS activities is given in Appendix H by applying a regular solution model to the solid solution and an ideal model to the liquid phase. The calculated results for CaS-MnS activities at three steelmaking temperatures and their applications to calcium treatment of steel have been published recently [164].

It is now possible to trace the thermodynamic behaviour of the system in terms of variations of activities as a function of injection of calcium. Instead of plotting individual activities, it has been found that to show the deviation from equilibrium of reaction 6.39 is most informative. This is done by plotting $\log(a_{CaS}/h_s)$ against $\log(a_{CaO}/h_o)$ as shown in Figure 6.8.

This form of presentation has 3 advantages:

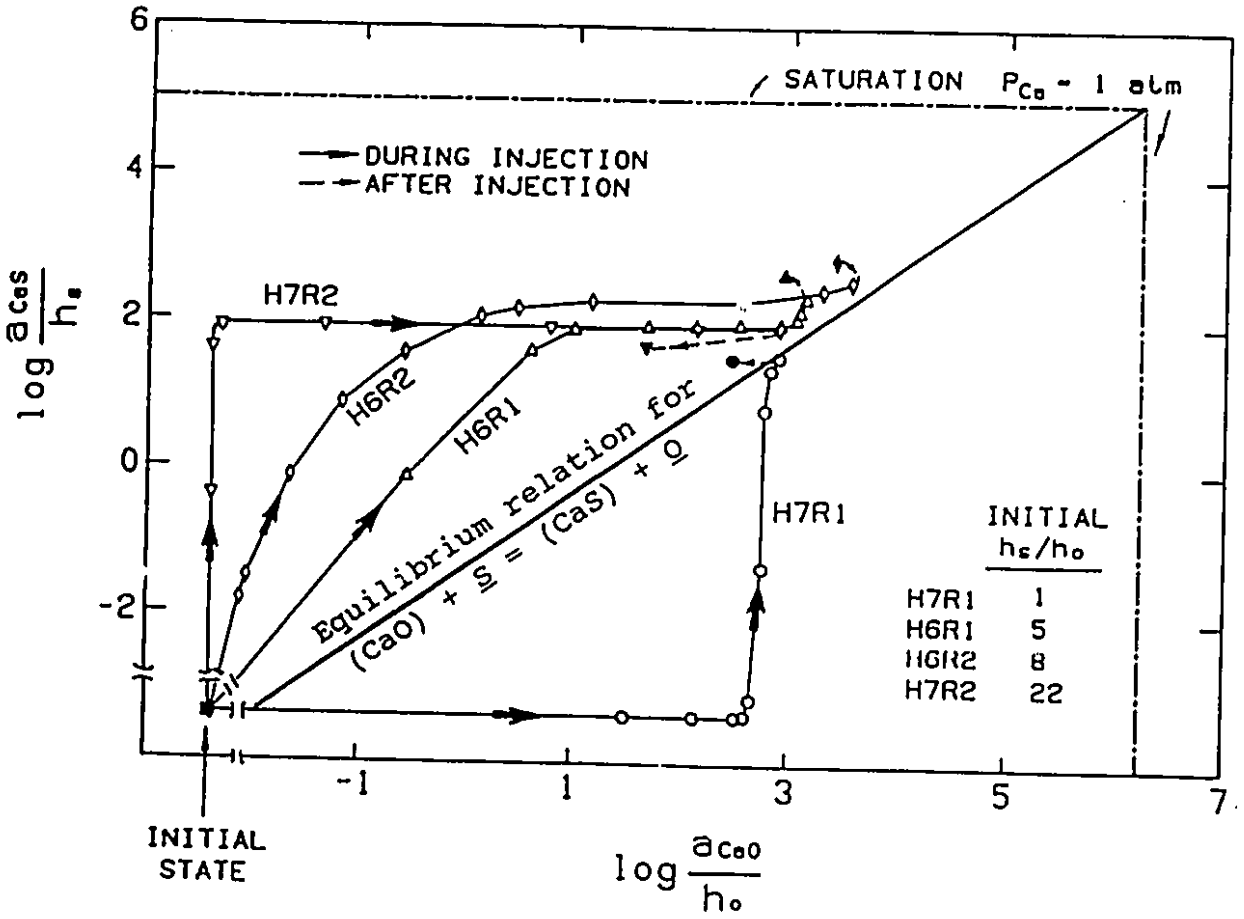

Figure 6.8 The system reaction paths for calcium treatment of steel, plotted as $\log(a_{CaS}/h_S)$ against $\log(a_{CaO}/h_O)$ for the same injections as Figure 6.6. For various initial sulphur and oxygen activities the results eventually converge on the equilibrium between (CaS) and (CaO) (Equation 6.41).

(1) It is based on Equation 6.40, i.e. log (a_{CaS}/h_s) = log (a_{CaO}/h_o) + log K. Therefore, the equilibrium relation is represented by the diagonal line in Figure 6.8.

(2) The y-axis relates to the calcium activity in equilibrium with (Ca,Mn)S, or the extent of sulfide modification. The x-axis reflects the calcium activity in equilibrium with CA_x, or the extent of oxide modification.

(3) The reaction paths of the system which describe the evolution of the system from the initial state to the final equilibrium state under the condition of continuing calcium injection are shown by the solid lines. The drifting of the system after the completion of injection is also shown by the dashed lines and the closed data points.

The trends in Figures 5.46, 5.51 and 6.6 are difficult to discern. However, when this set of data is plotted in Figure 6.8, a pattern presents itself. It appears that the initial conditions determine the paths towards equilibrium. High initial h_s/h_o shifts the reaction path towards the upper left corner of the diagram. On this path the ratio of a_{CaS}/h_s increases faster than a_{CaO}/h_o. In other words, higher initial h_s/h_o favours the modification of sulphide inclusions, while lower initial h_s/h_o favours oxide modification.

In all experiments, the inclusion compositions eventually approached the equilibrium state given by Equation 6.39. The system did not drift far away from the equilibrium state prevailing at the point injection was terminated, except in the case H7R2, in which reoxidation pushed the system away from the equilibrium state and towards the left of the diagram.

Since the y-axis is proportional to the equilibrium calcium activity with (Ca,Mn)S and the x-axis with CA_x, the diagonal equilibrium line indicates that both oxide and sulfide have the same equilibrium value of calcium activity. The path shown above and to the left of the diagonal line indicates higher equilibrium calcium activity with sulfide than that with oxide. The path shown below and to the right of the diagonal line indicates higher equilibrium calcium activity with oxide than that with sulfide.

In Figure 6.8, the two broken lines represent saturation with one atmosphere of calcium vapour. For the present conditions, the maximum, calcium solubility is 0.024% [1,6]. The broken line parallel to the y-axis is given by:

$$\left(\log\frac{a_{CaO}}{h_o}\right)^{Sat} - \log h_{Ca}^{Sat} + \log K_{CaO} \qquad (6.41)$$

where h_{Ca}^{Sat} is the saturation calcium activity and the equilibrium constant, K_{CaO}, for calcium deoxidation (Equation 6.1) is given by:

$$K_{CaO} = \frac{a_{CaO}}{h_O h_{Ca}} \qquad (6.42)$$

Similar expressions also apply for the broken line parallel to the x-axis. The saturation lines define the feasible range of operation for the process. It can be inferred that the actual dissolved calcium content is approximately three orders of magnitude lower than its solubility value, even though equilibrium with respect to Equation 6.39 is reached near the end of calcium injection. Thus the effective dissolved calcium content is less than 1 ppm, even though the total calcium is approximately 120 ppm (Figures 5.46 and 5.51). This very low activity of dissolved calcium in the bulk implies a major calcium concentration profile drop from 240 ppm Ca at the gas-liquid interface to less than 1 ppm. This finding supports the instantaneous two-film reaction model.

Most of the present heats were "over-treated" with calcium compared to the amount of calcium addition to steel in industry (see section 6.5.1). Therefore, for industrial cases, the dissolved calcium in the bulk near the end of injection would be expected to be even lower, assuming the initial conditions are similar.

6.4 THE MATHEMATICAL MODEL

Having studied and understood the kinetics and mechanisms of calcium dissolution at the gas-liquid interface, and of the oxide and sulfide inclusions modification in the melt, one is then able to construct an overall reaction and mathematical model for the whole system. The model would trace the sources and sinks for each dissolved component in the system during and after injection. Therefore, the rate of deoxidation and desulphurization and the change of dissolved calcium concentration in the melt could be calculated. The model would also monitor the rate of diffusion of components to the oxide and sulfide inclusions; thus the rate of oxide and sulfide modification could be calculated.

The basis for the mathematical model is shown schematically in Figure 6.9. Calcium vaporizes when it is injected. Most of it escapes to the argon atmosphere, while the remainder dissolves in the liquid through the gas-liquid boundary, where it encounters oxygen and sulphur, accounting for most of the deoxidation and desulphurization. The reaction products CaO and CaS are then mixed into the melt, while the unreacted calcium dissolves into the melt to react with existing alumina to transform it to calcium-rich CA_x. The modified CA_x reacts with S and Mn to form complex oxy-sulphide inclusions, when the bulk S and Mn concentrations

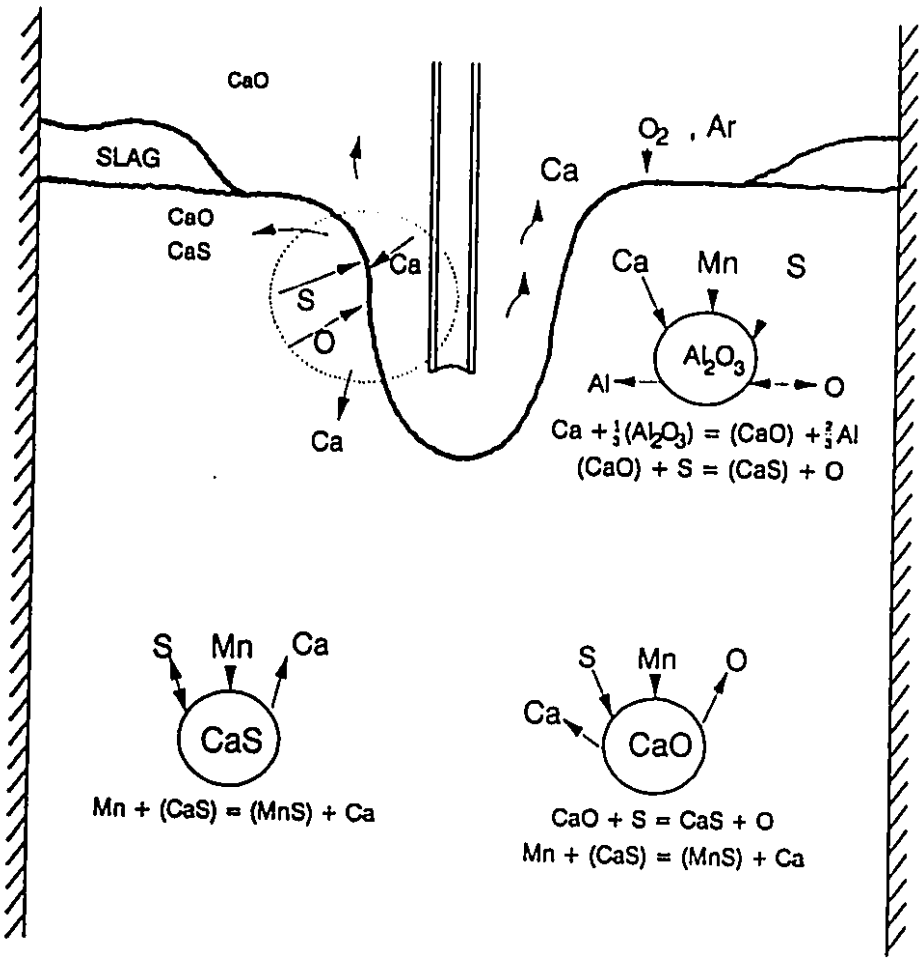

Figure 6.9 The schematic representation of the overall reaction and kinetic model for calcium absorption, deoxidation and desulphurization, and inclusions modifications and their interactions.

exceed their equilibrium values with respect to CA_x. Manganese and sulphur also diffuse to the CaO and CaS inclusions to form calcium-manganese sulphide inclusions. Desulphurization also occurs at the slag-melt interface, while dissolved oxygen originates from the free surface and the crucible lining.

6.4.1 Reactions involved in the system

According to Figure 6.9, the individual reaction involved in the system and its reaction site and the reaction conditions is summarized below:

1) Instantaneous reactions between calcium with sulfur and oxygen at a reaction plane in the liquid film:

$$\underline{Ca} + \underline{S} = CaS \qquad (6.43)$$

$$\underline{Ca} + \underline{O} = CaO \qquad (6.44)$$

2) reoxidation from the atmosphere and lining:

$$\frac{1}{2}O_2 = \underline{O} \qquad (6.45)$$

3) slag desulphurization at the slag-metal interface:

$$\underline{S} = (S)^{-2} + 2e \qquad (6.46)$$

4) calcium modification of CA_x on CA_x inclusion in the melt, and desulphurization by the modified CA_x when the bulk sulfur exceeds its equilibrium value with CA_x:

$$\underline{Ca} + \frac{1}{3}(Al_2O_3) = (CaO) + \frac{2}{3}\underline{Al} \qquad (6.47)$$

$$(CaO) + \frac{2}{3}\underline{Al} + \underline{S} = (CaS) + \frac{1}{3}(Al_2O_3) \qquad (6.48)$$

5) diffusion of manganese and sulphur to form (Ca,Mn)S on the primary CaO, CaS inclusions in the melt:

$$\underline{Ca} + (MnS) = (CaS) + \underline{Mn} \qquad (6.49)$$

6.4.2 Model assumptions

The following assumptions are made to develop the model:

(a) The inclusions are small enough that diffusion within the inclusions is fast enough that each inclusion is a single homogenous phase.

(b) The chemical reactions are fast compared to diffusion in the melt, so that chemical equilibrium is achieved at all interfaces.

(c) The inclusion interfacial area is taken from the quantitative image analysis results.

6.4.3 Rate equations for the dissolved elements

A mass balance for the dissolved calcium can be written:

$$\frac{dC_{Ca}}{dt} = -k_{Ca} z_L \frac{E}{E-1}(C_{Ca,r} - C_{Ca}) - k_{Ca,i} z_{CA_x}(C_{Ca} - C_{Ca,i}) - k_{Ca,i} z_{CaO}(C_{Ca} - C_{Ca,p}) - k_{Ca,i} z_{CaS}(C_{Ca} - C_{Ca,p}) - k_e z_e (C_{Ca} - 0) \quad (6.50)$$

where the first term on the right is the dissolution term including the enhancement factor discussed earlier. The remaining terms consume dissolved calcium; the second on the right represents calcium diffusion to CA_x inclusions; the third and fourth represent diffusion to primary CaO and CaS inclusions respectively; the final term accounts for evaporation of calcium. The evaporation rate constant, $k_e z_e$, was determined in Appendix D, based on previous work [119]. $C_{Ca,p}$ is the equilibrium concentration with (Ca,Mn)S. The mass transfer coefficient for the inclusions, k_{Ca}, is calculted in Appendix C, based on a Sherwood Number of 2, and is relatively constant in the experiments since the inclusion size does not change dramatically during treatment. The inclusion interfacial area per unit volume, z_{CAx}, z_{CaS} and z_{CaO} for the CA_x, CaS and CaO inclusions, respectively were taken from the quantitative image analysis.

A similar balance can be constructed for the dissolved sulfur:

$$-\frac{dC_s}{dt} = k_s z_L \frac{E}{E-1}(C_s - C_{s,r}) + k_{sl} z_{sl}(C_s - C_s') + \gamma (k_{s,i} z_{CA_x})(C_s - C_{s,i}) + k_{s,i} z_{CaS}(C_s - C_{s,p}) + k_{s,i} z_{CaO}(C_s - C_{s,p}) \quad (6.51)$$

where the first term on the right hand side represents enhanced diffusion of sulphur to the calcium vapour interface; the second term is diffusion to the top slag where the rate constant, $k_{sl}z_{sl}$, is estimated in Appendix E from previous work [120,117]; the third term represents desulphurization at calcium aluminates (γ is normally 1, but if there is no sulphur in the aluminate, and the bulk sulphur content is lower than the calculated interfacial value, γ is set to zero), and the final two terms account for desulphurization at CaS and CaO inclusions, respectively.

The dissolved oxygen equation is very similar to the sulphur equation:

$$-\frac{dC_o}{dt} = k_o z_L \frac{E}{E-1}(C_o - C_{o,r}) + (k_{o,i} z_{CA_x})(C_o - C_{o,i}) + k_{o,i} z_{CaO}(C_o - C_{o,p}) + k_{ro} z_{ro}(C_{o,ro} - C_o) \quad (6.52)$$

where the final term is due to reoxidation from the atmosphere and refractory, and the rate constant $k_{ro}z_{ro}$ is estimated in Appendix F from the previous work [117,119].

The dissolved aluminum equation is given as:

$$\frac{dC_{Al}}{dt} = -k_{Al,i}z_{CA_x}(C_{Al} - C_{Al,i}) - k_{ro}(D_{Al}/D_o)\,z_{ro}(C_{Al} - C_{Al,ro}) \qquad (6.53)$$

where the first term on the right is diffusion to or from calcium aluminate inclusions and the second term is aluminum being consumed due to reoxidation.

Table 6.2 lists the input and output variables for the model calculations. Some variables are explained below.

TABLE 6.2 INPUT AND OUTPUT VARIABLES FOR MODEL CALCULATIONS

INPUT	C_{Ca}^0	C_s^0	C_o^0	Inj. Time		d_i^v	n_{Al2O3}^0
OUTPUT	C_{Ca}	C_s	C_o	X_{CaO}	X_{CaS}	$C_{Ca,T}$	$n_i, z_i, k_i z_i$

6.4.4 Calculation of CA_x and (Ca,Mn)S inclusion compositions

CA_x Composition

Assuming the number of the initial oxide inclusions per uint volume of melt is $n_{Al_2O_3}$ and the average inclusion diameter is d_i, the amount of oxygen combined in the initial Al_2O_3 inclusions is then

$$C_{o,Al_2O_3} = 3n_{Al_2O_3}\left(\frac{\pi}{6}d_i^3\right)\frac{\rho_{Al_2O_3}}{M_{Al_2O_3}} \qquad (6.54)$$

and the amount of Al_2O_3 inclusions (mole per unit volume) is then given by:

$$C_{Al_2O_3} = \frac{1}{3}C_{o,Al_2O_3} \qquad (6.55)$$

The rate of reaction of oxygen at the inclusion is given by:

$$r_{o,CA_x} = k_{o,i}z_{CA_x}(C_o - C_{o,i}) \qquad (6.56)$$

The integration of the oxygen flux to or from CA_x over an injection time t is then given as:

$$C_{o,CA_x} = \int_0^t k_{o,i}z_{CA_x}(C_o - C_{o,i})\,dt \qquad (6.57)$$

Similar expression would also apply to the dissolved aluminum in the melt.

$$r_{Al,CA_x} = k_{Al,i} z_{CA_x} (C_{Al} - C_{Al,i}) \qquad (6.58)$$

At any instant time interval, the flux of calcium to the inclusion is:

$$r_{Ca,CA_x} = k_{Ca,i} z_{CA_x} (C_{Ca} - C_{Ca,i}) \qquad (6.59)$$

The integration of the total calcium flux to the CA_x inclusion over the injection time t is then:

$$C_{Ca,CA_x} = \int_0^t k_{Ca} z_{CA_x} (C_{Ca} - C_{Ca,i})\, dt \qquad (6.60)$$

As assumed earlier, the fluxes of both oxygen and calcium are completely mixed ir the CA_x to form a single phase; at any integration time t, the composition of CA_x can therefore be calculated by the following equations:

$$X_{Al_2O_3} = \frac{C_{Al_2O_3} + \frac{1}{3}(C_{O,CA_x} - C_{Ca,CA_x})}{C_{Al_2O_3} + \frac{1}{3}(C_{O,CA_x} - C_{Ca,CA_x}) + C_{Ca,CA_x}} \qquad (6.61)$$

$$X_{CaO} = 1 - X_{Al_2O_3} \qquad (6.62)$$

The activities of Al_2O_3 and CaO are then calculated according to the work of Kay et al [6]:

$$a_{Al_2O_3} = X^3_{Al_2O_3} \qquad (6.63)$$

$$\begin{aligned} a_{CaO} &= 1, && X_{Al_2O_3} \leq 0.268 \\ a_{CaO} &= 2.5485(1-X_{Al_2O_3})^3, && 0.268 \leq X_{Al_2O_3} \leq 0.85 \\ a_{CaO} &= 0.002, && 0.85 \leq X_{Al_2O_3} \leq 1 \end{aligned} \qquad (6.64)$$

Assuming the interfacial oxygen activity is in equilibrium with CA_x, it is then expressed:

$$h_{o,i} = K_{Al_2O_3} \frac{h^{2/3}_{Al,i}}{a^{1/3}_{Al_2O_3}} \qquad (6.65)$$

The equilibrium interfacial calcium concentration is then given as:

$$h_{Ca,i} = K_{CaO} \frac{a_{CaO}}{h_{o,i}} \qquad (6.66)$$

(Ca,Mn)S Composition

As described in section 6.3.2, The mechanism of sulphide inclusion modification is given as:

$$\underline{Ca} + (MnS) = (CaS) + \underline{Mn} \qquad (6.67)$$

and the equilibrium activity ratio of CaS to MnS in the sulphide phase (Ca,Mn)S, is given by the following equation:

$$\frac{a_{CaS}}{a_{MnS}} = \frac{K_{MnS}}{K_{CaS}} \frac{h_{Ca}}{h_{Mn}} \qquad (6.68)$$

Since the ratio of CaS to MnS is a function of the composition of calcium manganese sulphide (Ca,Mn)S at a specific temperature [164], (see Figures H2-H4 in Appendix H), the sulphide phase composition can then be determined by the above a_{CaS}/a_{MnS} ratio. For example, at 1500^0C the composition of sulfide phase (Ca,Mn)S is determined from:

$$\frac{a_{CaS}}{a_{MnS}} = \left(\frac{1}{X_{MnS}} - 1\right) e^{\frac{\Omega}{RT}(2X_{MnS}-1)} \qquad (6.69)$$

$$X_{CaS} = 1 - X_{MnS} \qquad (6.70)$$

X_{MnS} is then determined by the iteration process at a certain a_{CaS}/a_{MnS} ratio. Then X_{CaS} and the individual activities, a_{CaS} and a_{MnS} can also be determined.

6.4.5 Calculation of Total Calcium

Having calculated the compositions of CA_x and (Ca,Mn)S, the amount of calcium combined in oxides and sulfides inclusions can then be calculated. The total calcium is then the sum of all the calcium combined in the inclusions and the dissolved calcium.

6.4.6 Methods of Model Calculation

The numerical solutions to the first order ordinary differential equations (6.50 to 6.53) were generated using a Runge-Kutta subroutine (DVERK) based on Verner's Fifth and Sixth Order approximations [165] with the initial conditions.

A computer program is written for the calculations and is shown in Appendix I. The program is also used to calculate the inclusions composition and total calcium content. The calculation was performed on a 386 PC in Fortran 77. The average calculation time for a typical heat is about two to three minutes.

6.4.7 Model Results

The results of the model calculations are shown in Figures 6.10 to 6.17 for four injections. In these Figures, only the heats with the detailed inclusion analysis are used for the comparison with the model results, because a) the number of inclusions is needed for the model calculation; and b) the sulfur content for comparison is the dissolved sulfur which is the total sulfur minus the sulfur in the inclusions.

The dissolved oxygen, sulphur and total calcium contents of the steel are shown in Figure 6.10 for injection H6R1, and the corresponding inclusion compositions are shown in Figure 6.11. Similar results for injections H6R2, H7R1 and H7R2 are given in Figures 6.12-17. (H7R1 had no experimental data on CA_x for comparison, because it had no pre-deoxidation by aluminum). It can been seen that the model calculations agree well with the experimental results. However, the model predicts a faster sulfide modification rate than observed. This is maybe due to a complication in the formation of the solid sulfide inclusions late in the injection. The diffusional resistance within the solid inclusions may also slow the overall sulphide modification rate.

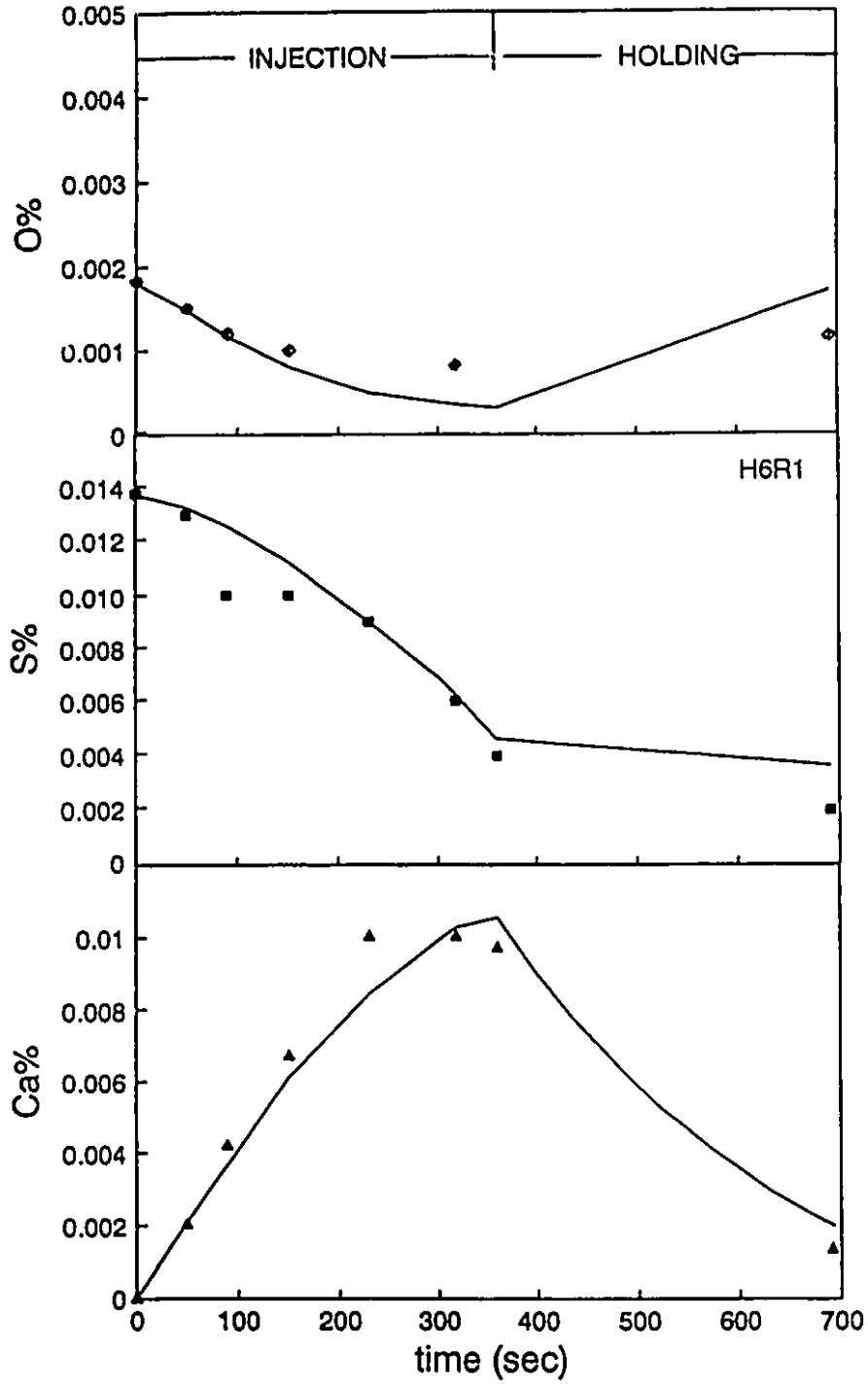

Figure 6.10 Model results for oxygen, sulfur and total calcium contents as a function of time compared with results from H6R1

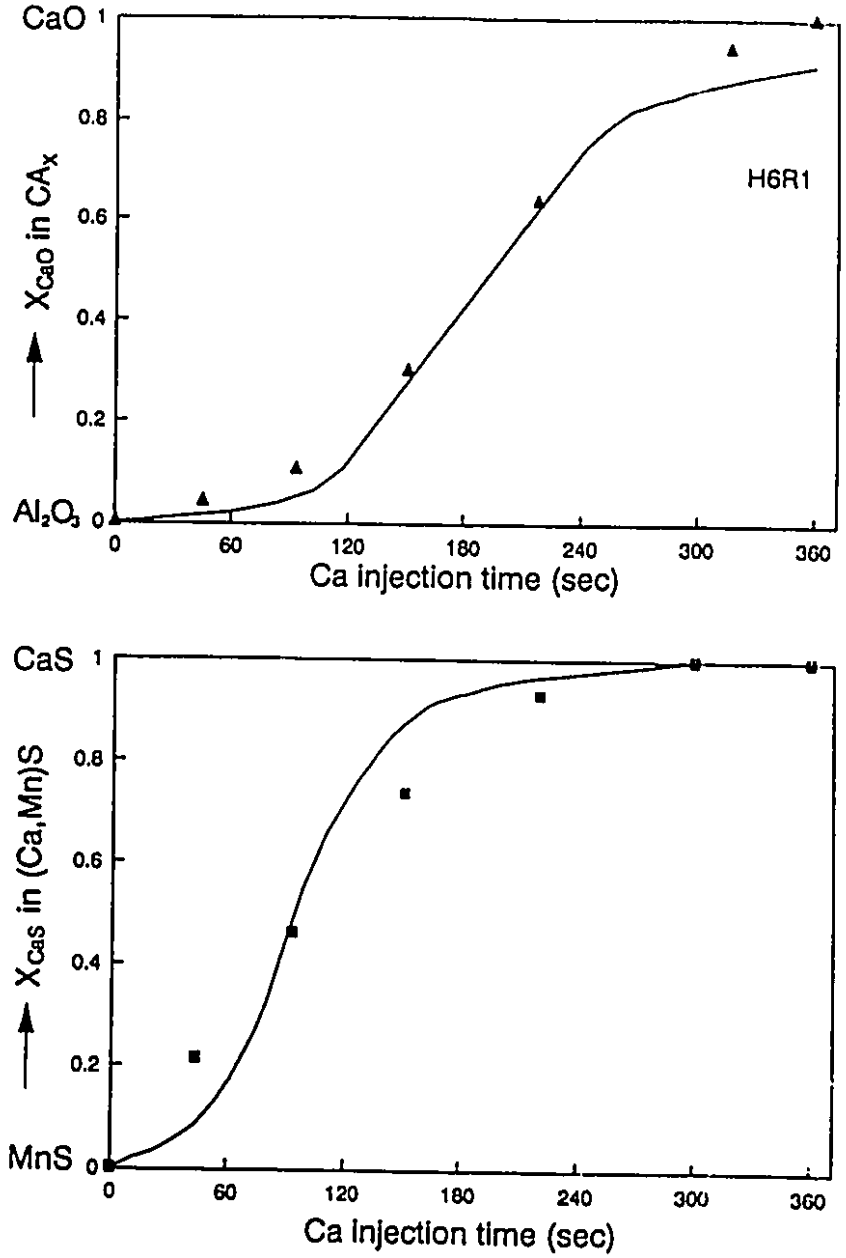

Figure 6.11 Model results for the compositions of CA_x and (Ca,Mn)S as a function of injection time compared with results from H6R1

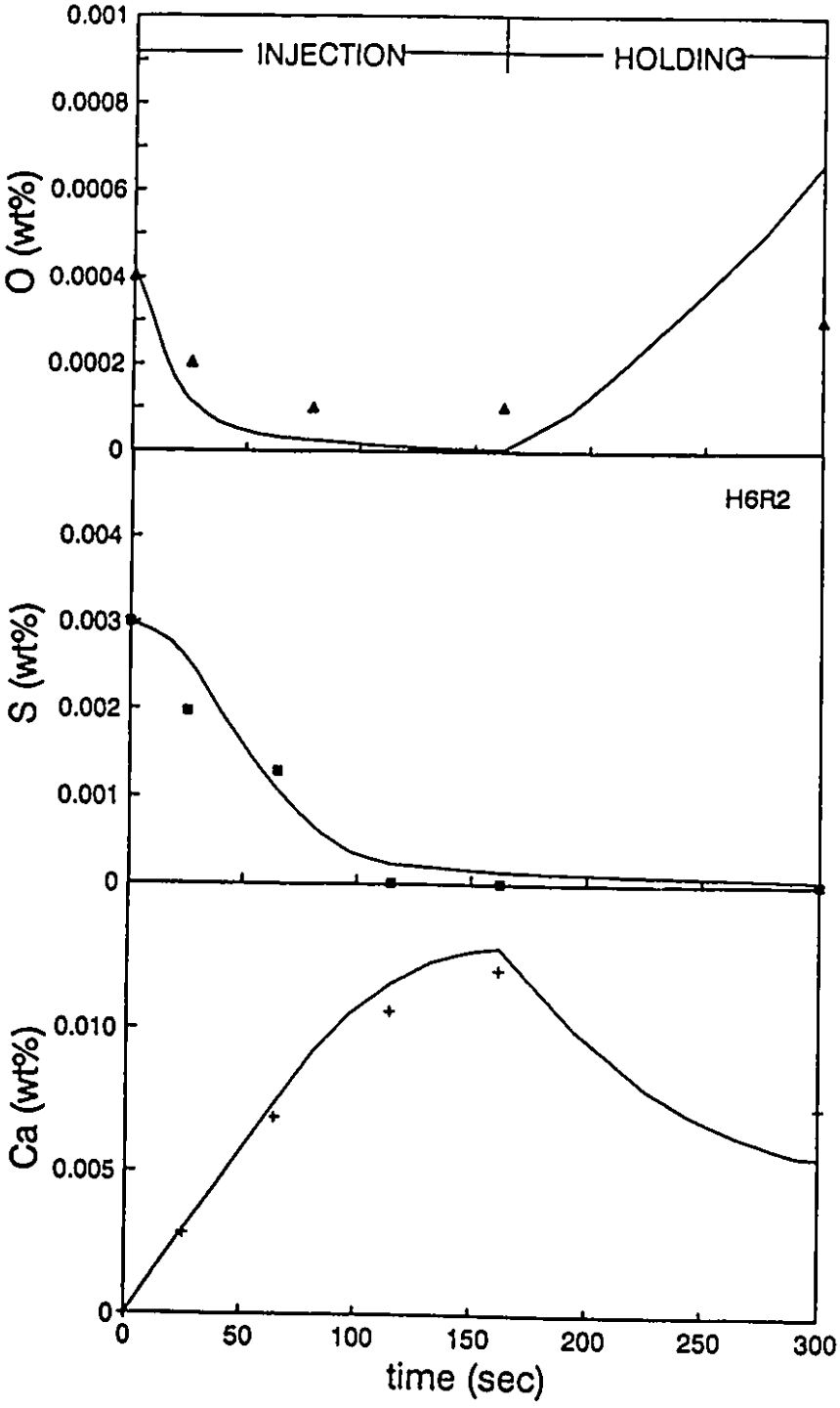

Figure 6.12 Model results for oxygen, sulfur and total calcium contents as a function of time compared with results from H6R2

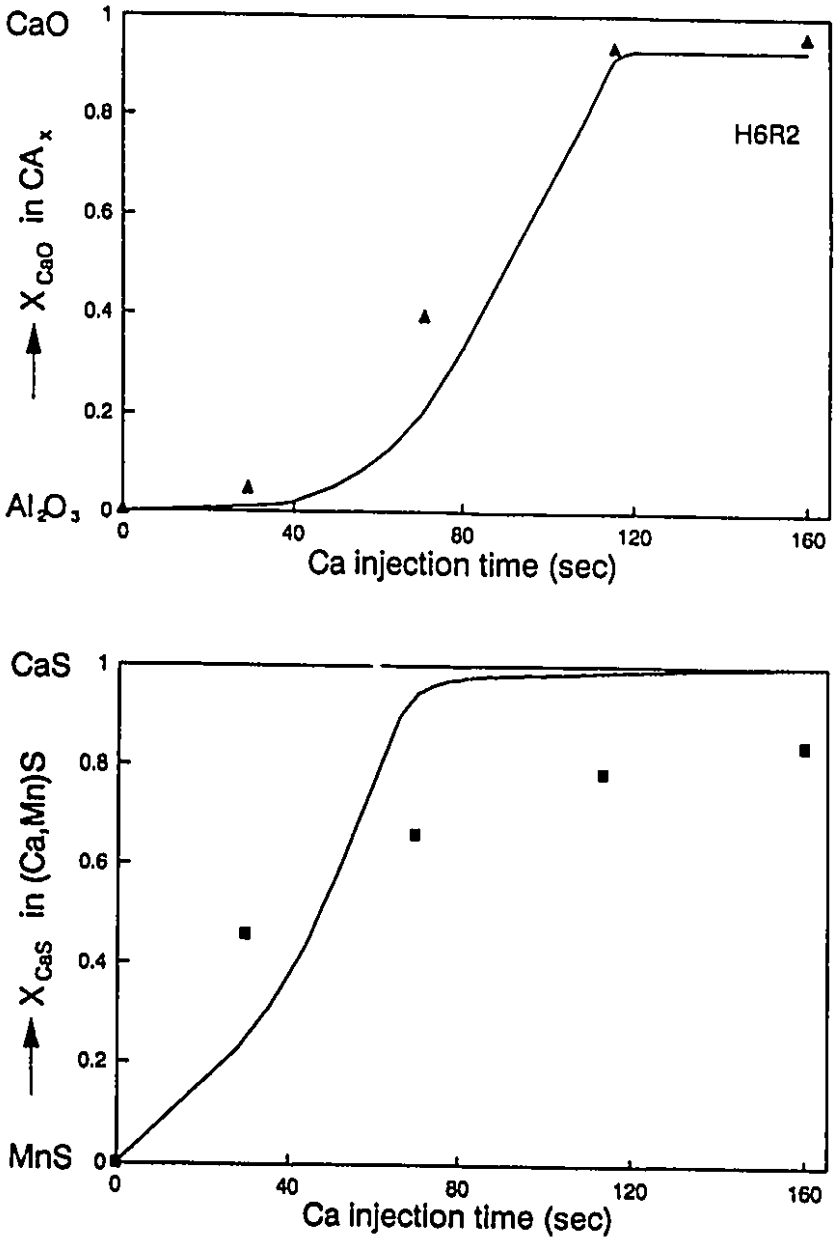

Figure 6.13 Model results for the compositions of CA_x and (Ca,Mn)S as a function of injection time compared with results from H6R2.

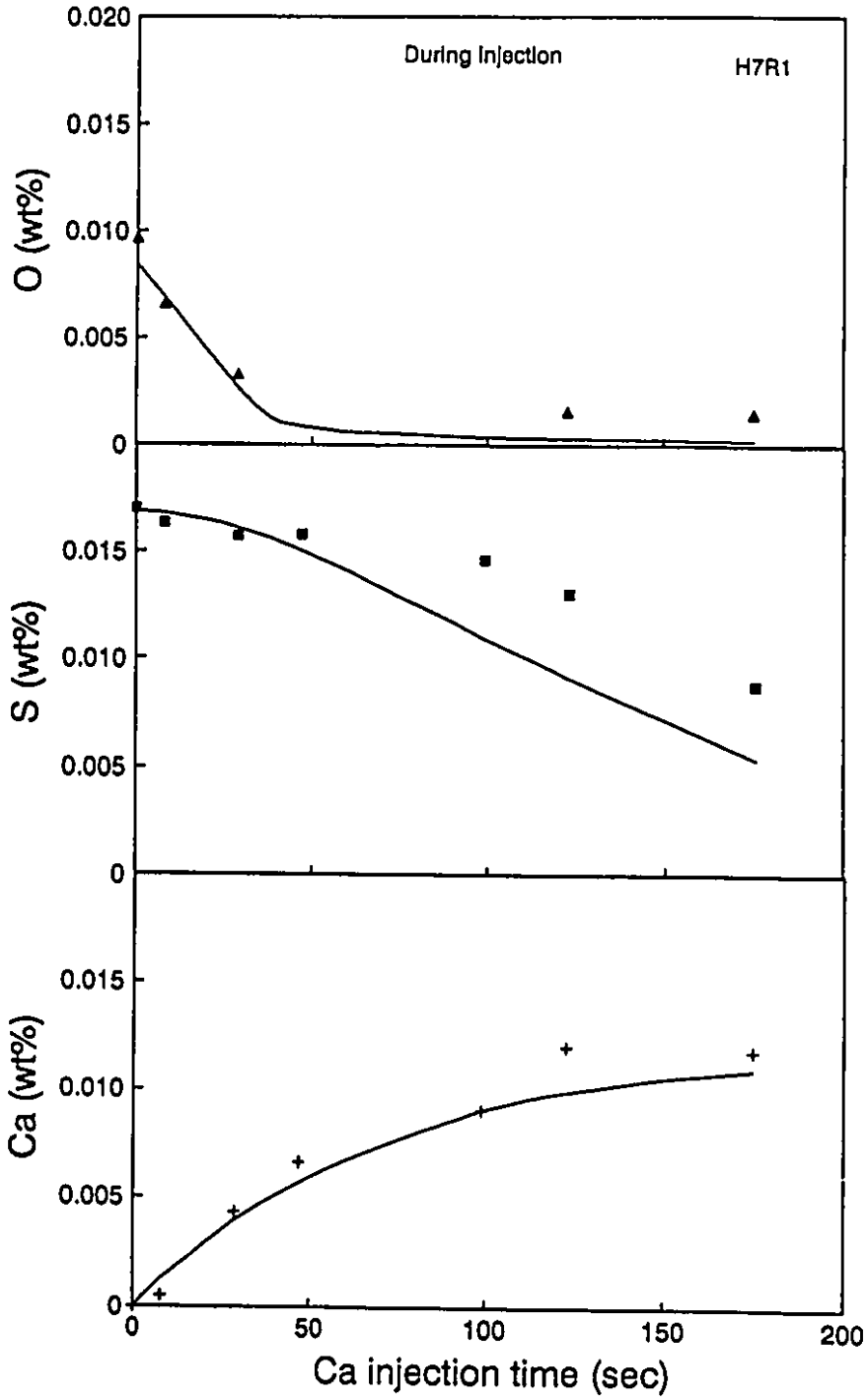

Figure 6.14 Model results for oxygen, sulfur and total calcium contents as a function of time compared with results from H7R1.

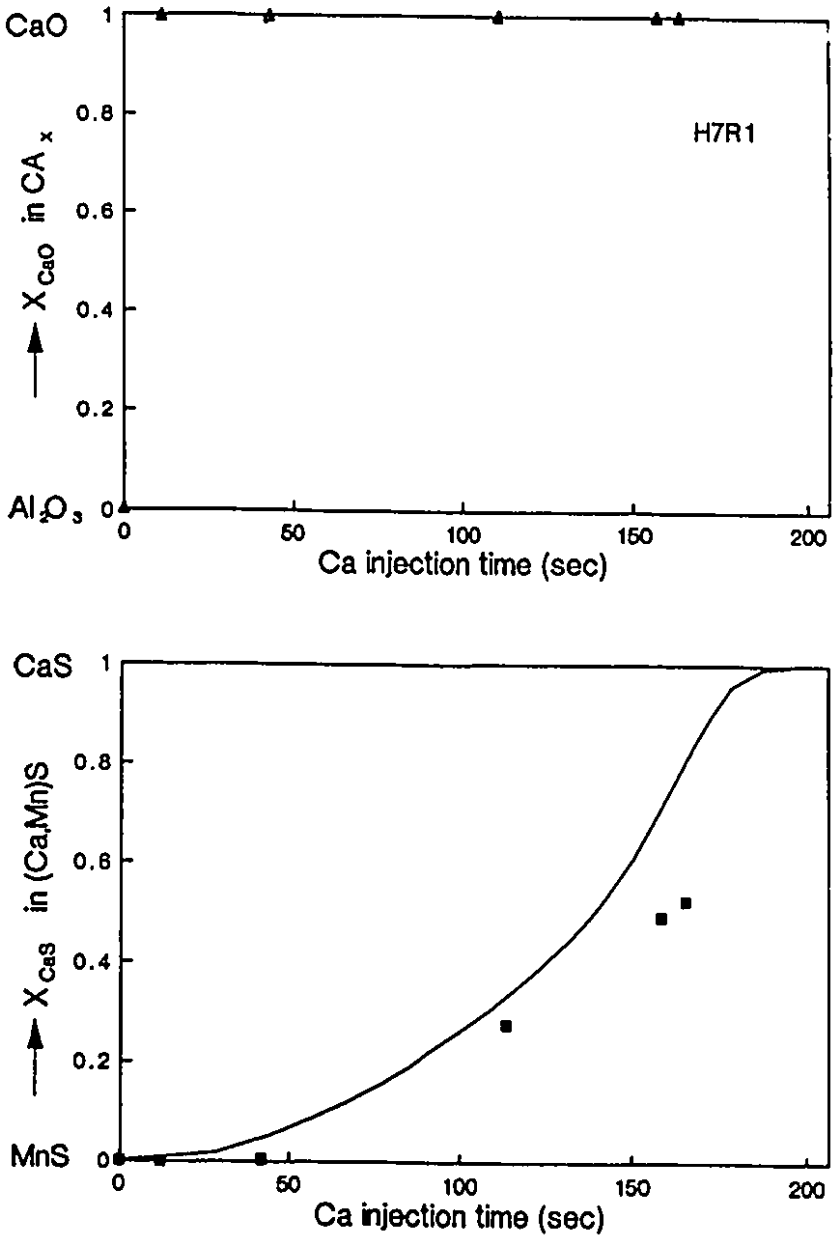

Figure 6.15 Model results for the composition of (Ca,Mn)S as a function of injection time compared with results from H7R1.

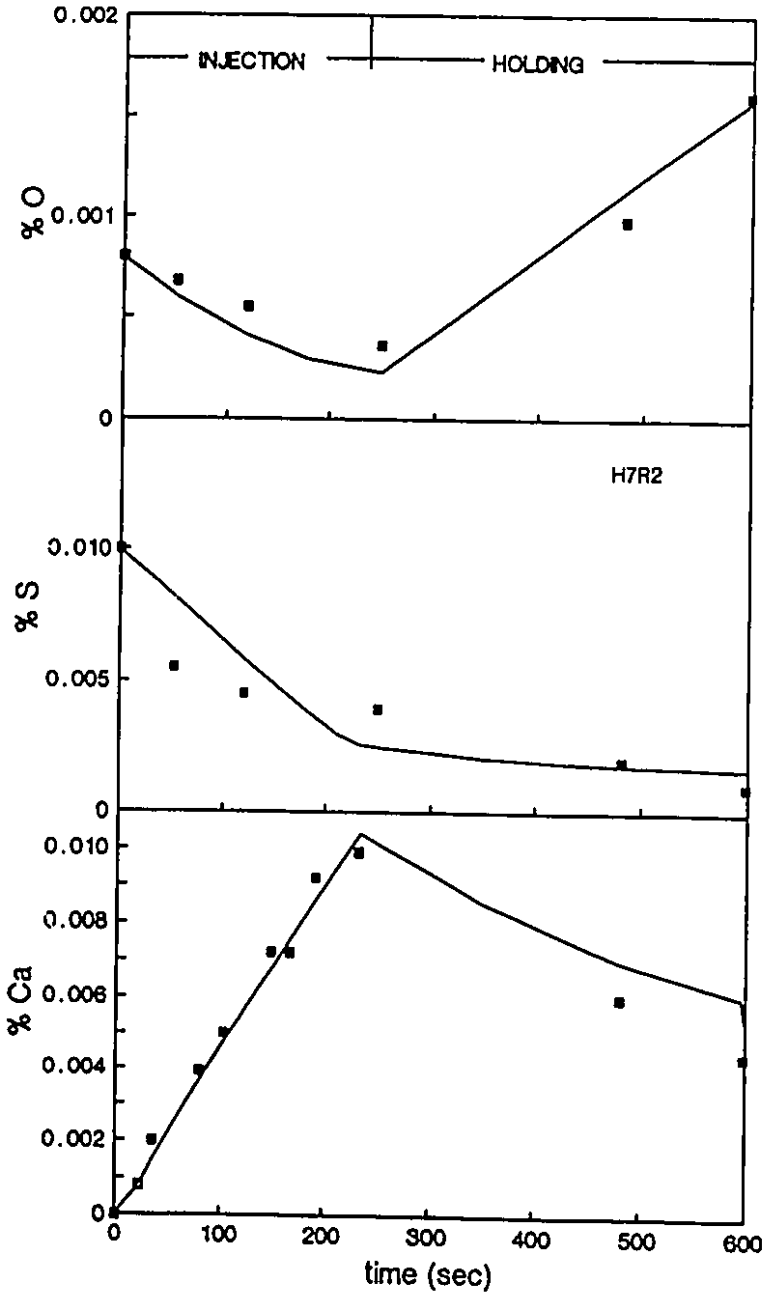

Figure 6.16 Model results for oxygen, sulfur and total calcium contents as a function of time compared with results from H7R2.

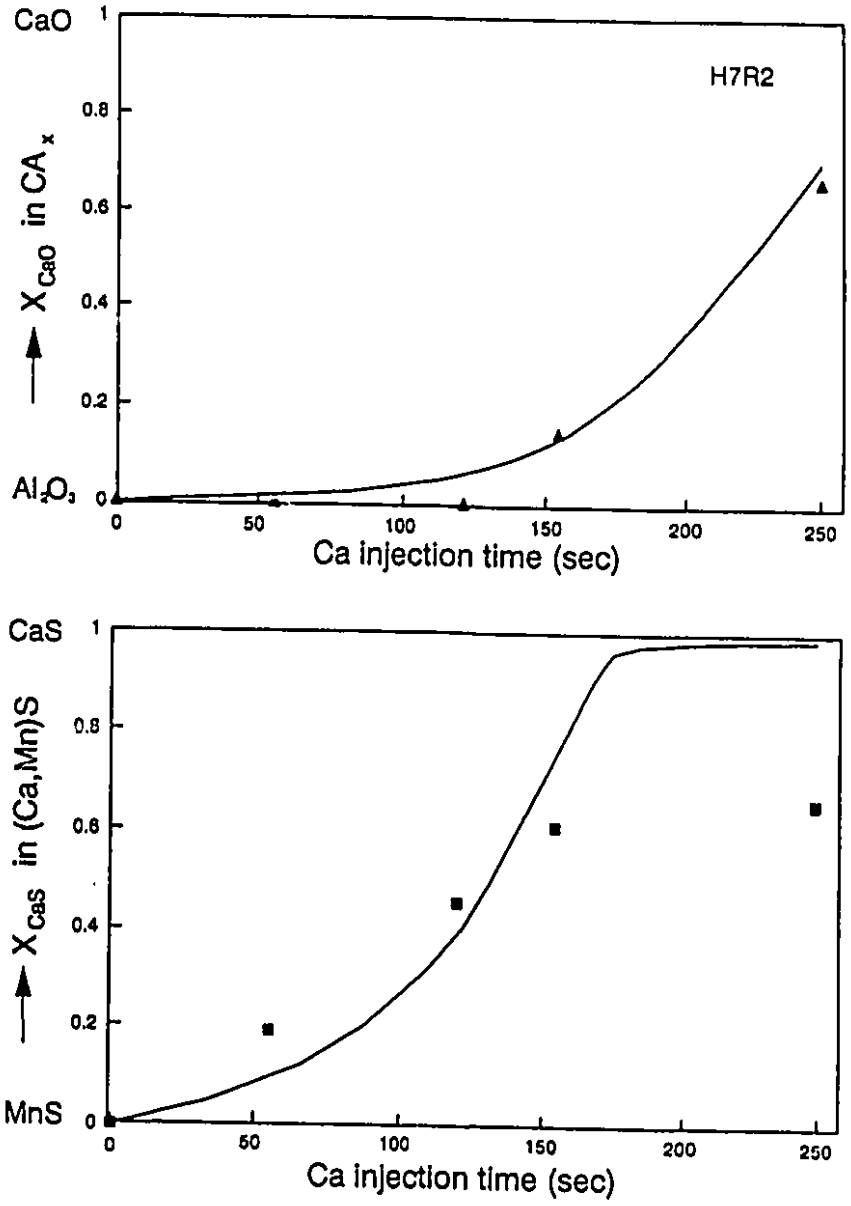

Figure 6.17 Model results for the compositions of CA_x and (Ca,Mn)S as a function of time compared with results from H7R2.

4.6.8 Model Predictions

Having established the validity of the model, it is possible to use the model to predict the behaviour in other situations. H6R1 was used as the reference heat. Figure 6.18 shows the effect of the initial sulphur content on the dissolved sulphur, oxygen and total calcium. It can be seen that higher initial sulphur enhanced the calcium dissolution rate and desulphurization rate, but reduced the deoxidation rate. More calcium is used for sulphide modification than for oxide modification. Figure 6.19 shows the effect of the initial sulphur content on both oxide and sulphide modification rate. It can be seen that higher initial sulphur content reduced the modification rate for both oxide and sulphide inclusions, particularly for oxide inclusions. This is because the dissolved calcium term, which is responsible for inclusion modification, is smaller with more sulphur present at the liquid film, thus the inclusion modification rate is reduced.

The effect of the injection rate (three different rates 0.455, 0.91 and 1.82 kg/t.min) on the model calculation results is shown in Figure 6.20 for oxygen, sulfur and total calcium contents, and in Figure 6.21 for the compositions of CA_x and (Ca,Mn)S. Both deoxidation and desulphurization, calcium pick-up rate and its steady-state value, and both

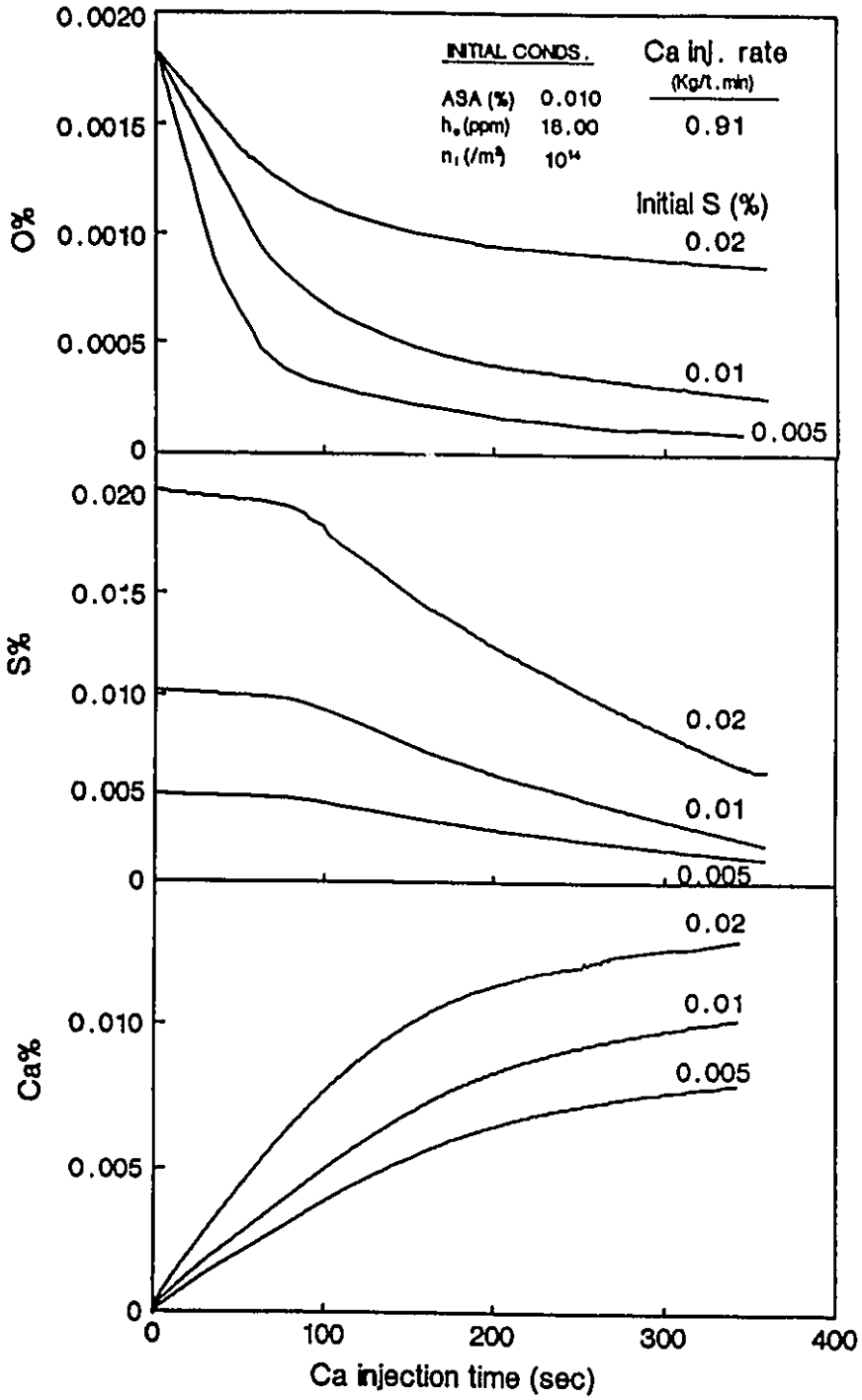

Figure 6.18 The model prediction for the effect of the initial sulphur content on oxygen, sulphur and total calcium contents during injection.

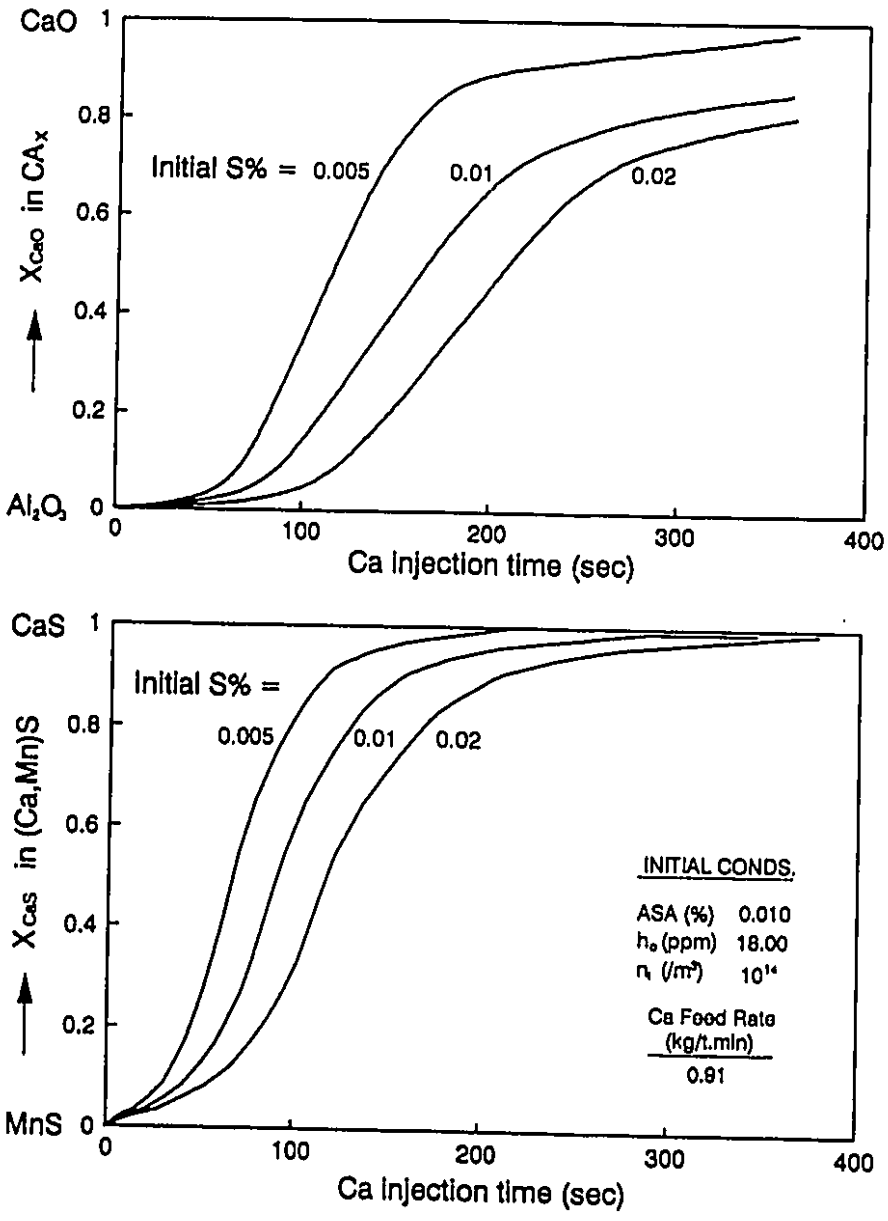

Figure 6.19 The model prediction for the effect of the initial sulphur content on the extent of oxide and sulphide inclusion modification during calcium injection.

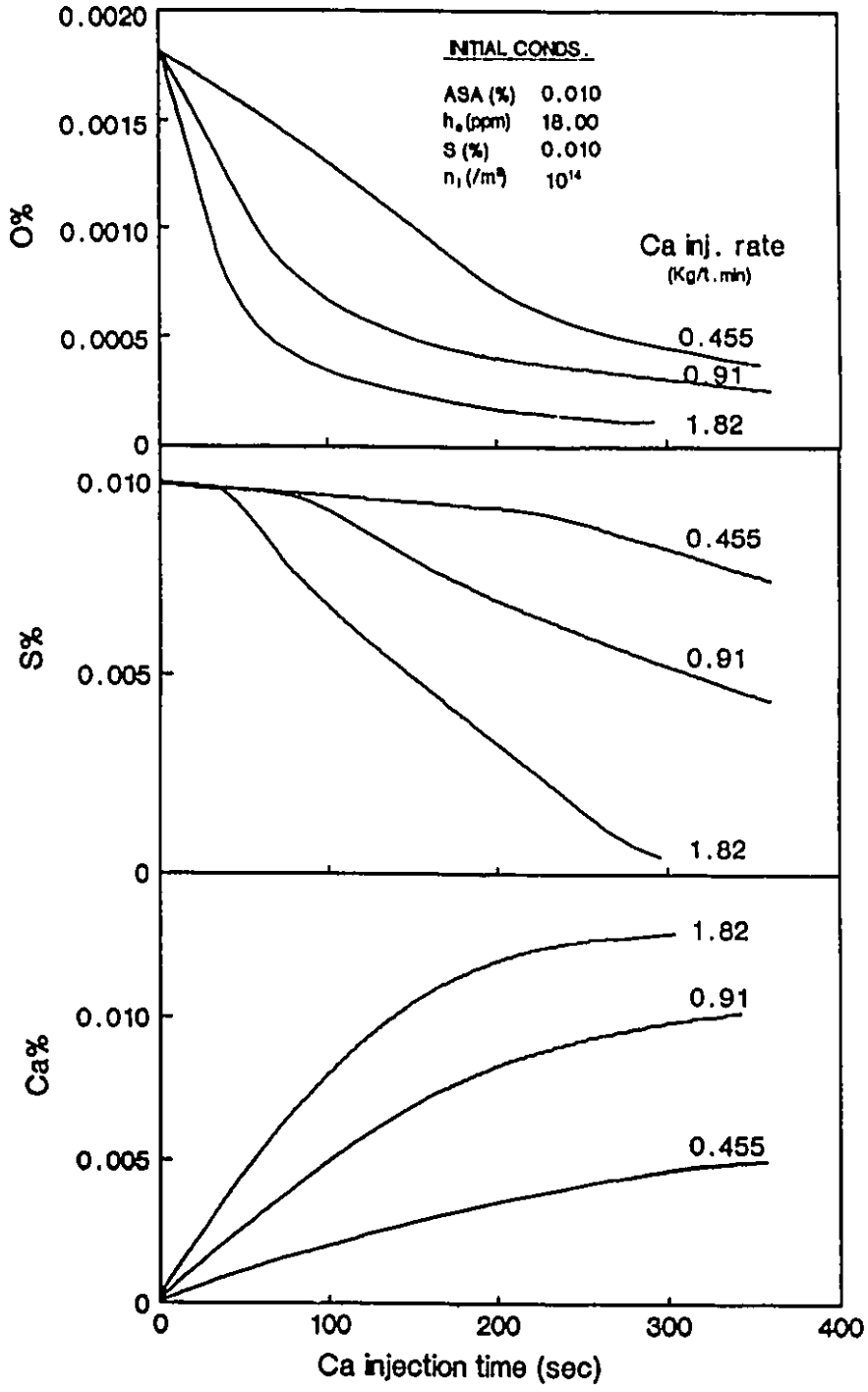

Figure 6.20 The model prediction for the effect of calcium injection rate on oxygen, sulphur and total calcium contents during injection.

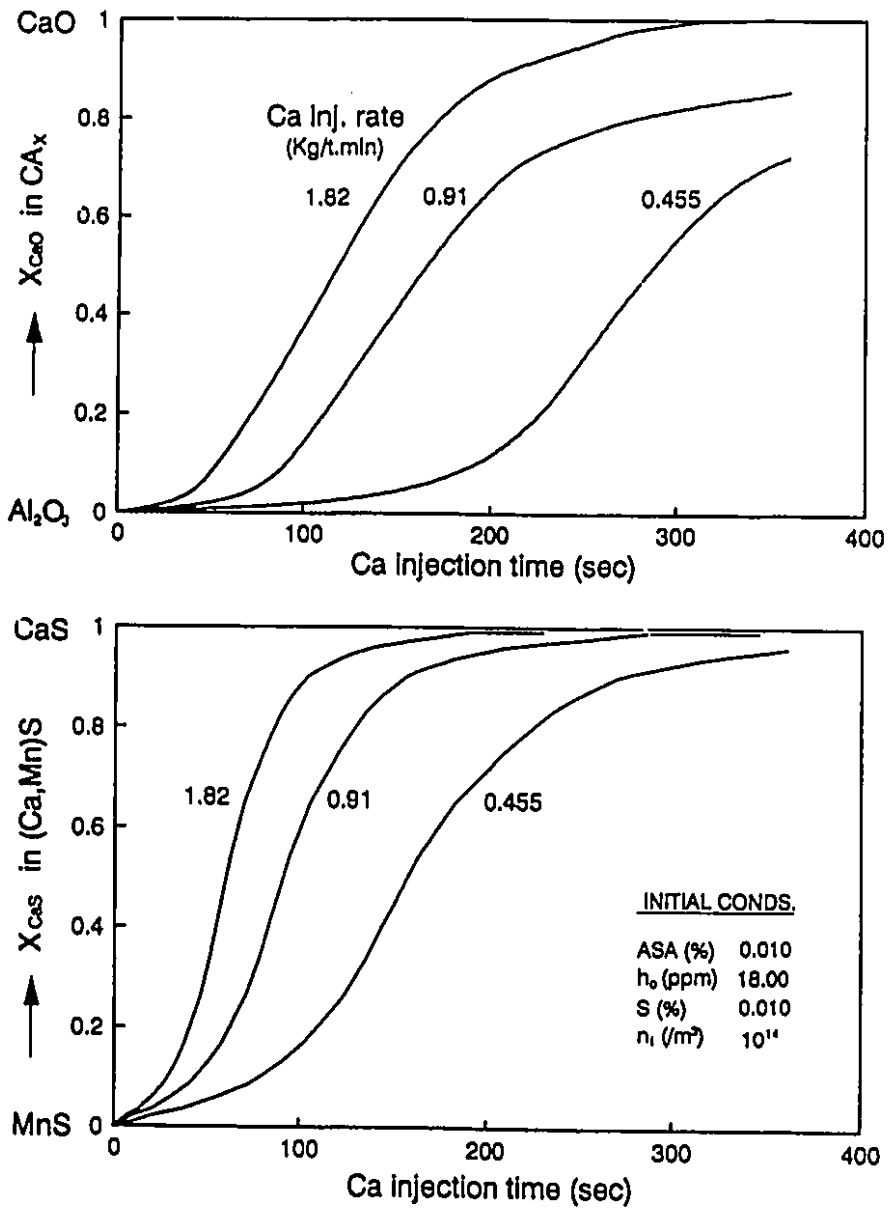

Figure 6.21 The model prediction for the effect of calcium injection rate on the extent of oxide and sulphide inclusion modification during injection.

oxide and sulphide inclusions modification increase dramatically with the calcium injection rate. However, Figure 6.20 shows that the deoxidation precedes desulphurization at a lower injection rate. At lower injection rate, the rates of both deoxidation and desulphurization at the gas-liquid interface are relatively slow, so that the term of interaction between oxygen, sulphur and inclusions in the bulk becomes important in the rate equations (6.53-54). According to thermodynamics of calcium oxide and sulphide (Table 2.6), sulphur starts to decrease dramatically only when oxygen has reached to a certain level, if the bulk is close to the equilibrium with oxide and sulphide inclusions (Equ. 6.41).

The effect of the initial number of alumina inclusions or the initial cleanliness of the steel on the dissolved sulphur and oxygen and total calcium contents is shown in Figure 6.22, and the effect on the compositions of both oxide CA_x and sulphide (Ca,Mn)S inclusions is shown in Figure 6.23. It can be seen that with fewer oxide inclusions or cleaner steel in the steel, deoxidation, desulphurization and inclusions modification rates are increased. Based on the mass balance, this is reasonable since fewer inclusions imply that there is less modification to be done; the effect is more dramatic for the oxide inclusions.

Figures 6.24 and 6.25 show the effect of the initial

average alumina inclusion size on the bulk chemistry and the extent of both oxide and sulphide modification. Figure 6.24 shows that larger initial oxide inclusions reduced the diffusion of calcium and oxygen to/from CA_x inclusions. Therefore, deoxidation and oxide modification rates are reduced. More dissolved calcium is available at the primary inclusions (CaO and CaS) for desulphurization and sulphide modification. Figure 6.25 shows that the initial alumina size has little effect on the sulphide modification; CaS and CaO inclusion formation at the gas-liquid film is relatively independent of the initial oxide size which explains the almost constant transformation rate at the different initial alumina size. In industrial practice inclusions are much larger than observed in the present experiments; it would be interesting to apply the present model to industrial data.

Figures 6.26 and 6.27 shows the effect of top slag coverage on the bulk chemistry and inclusions composition during injection. The slag coverage varies from 70%, 20% (reference heat H6R1) to 5%. Higher slag coverage increases the slag desulphurization rate and reduces reoxidation from the free surface. Therefore, both deoxidation and desulphurization are increased as shown in Figure 6.26. More dissolved calcium would be available for modifying the inclusions, and the modification rates for both oxide and sulphide are increased as shown in Figure 6.27. However, the

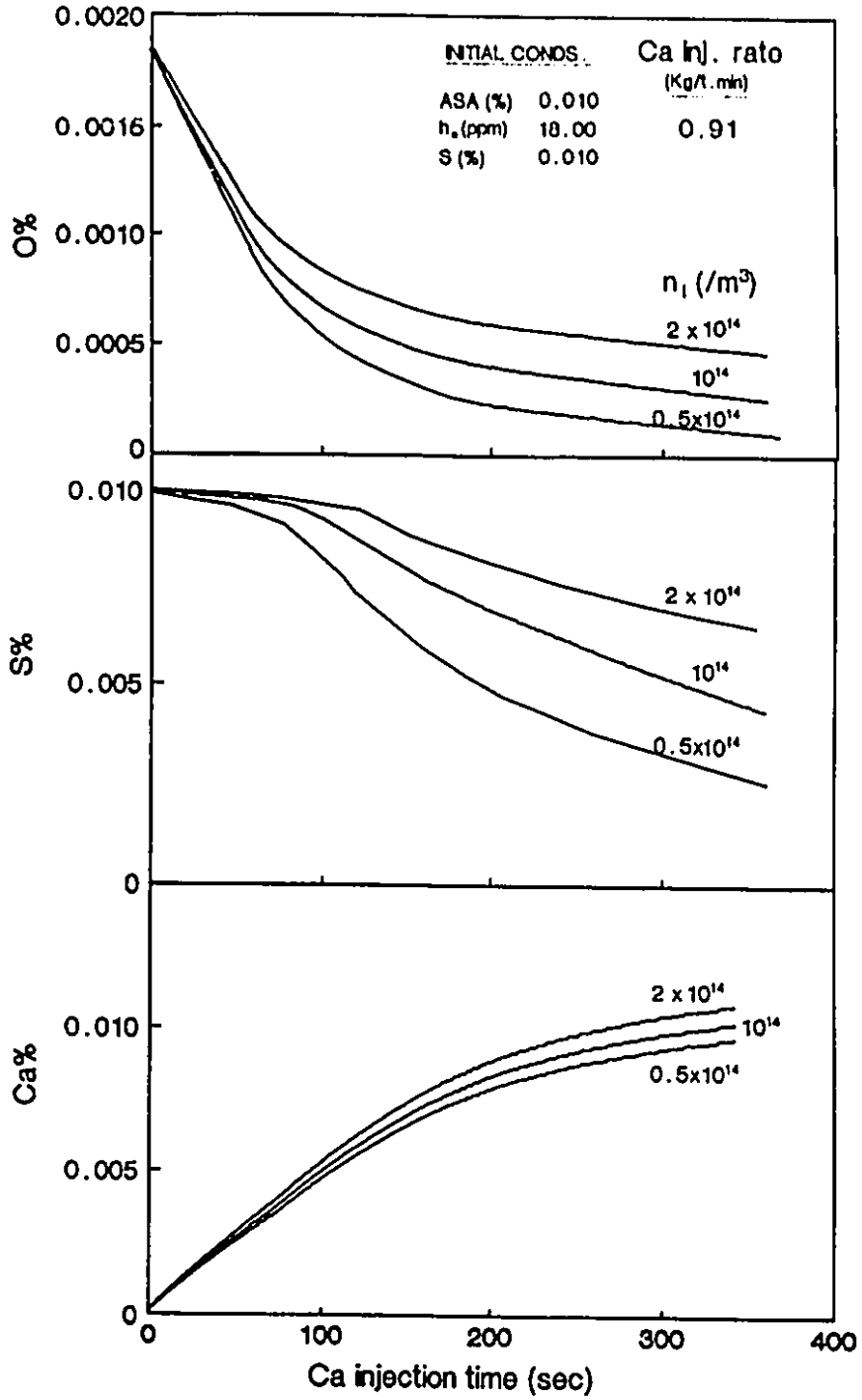

Figure 6.22 The model prediction for the effect of the initial number of oxide inclusions on oxygen, sulfur and total calcium contents during injection.

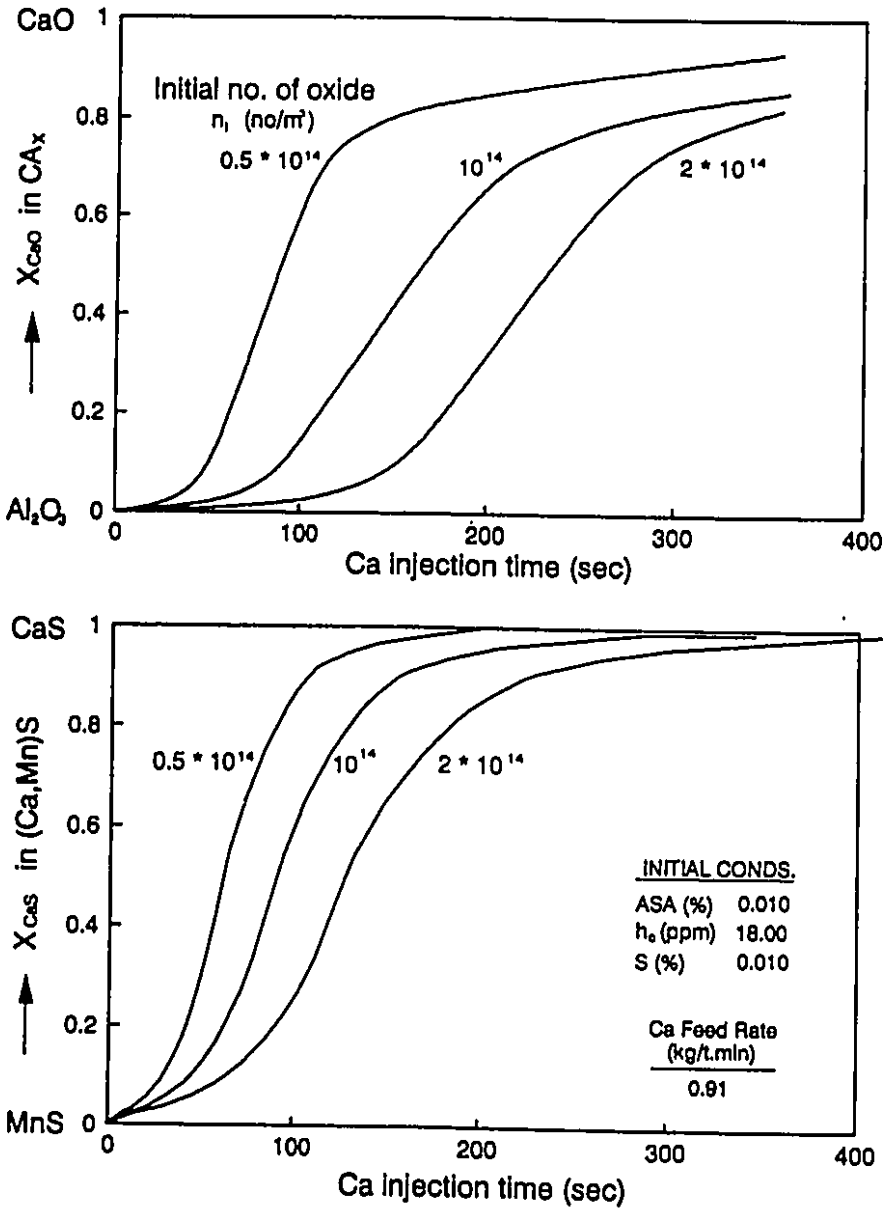

Figure 6.23 The model prediction for the effect of the initial number of oxide inclusions on the compositions of CA_x and (Ca,Mn)S during injection.

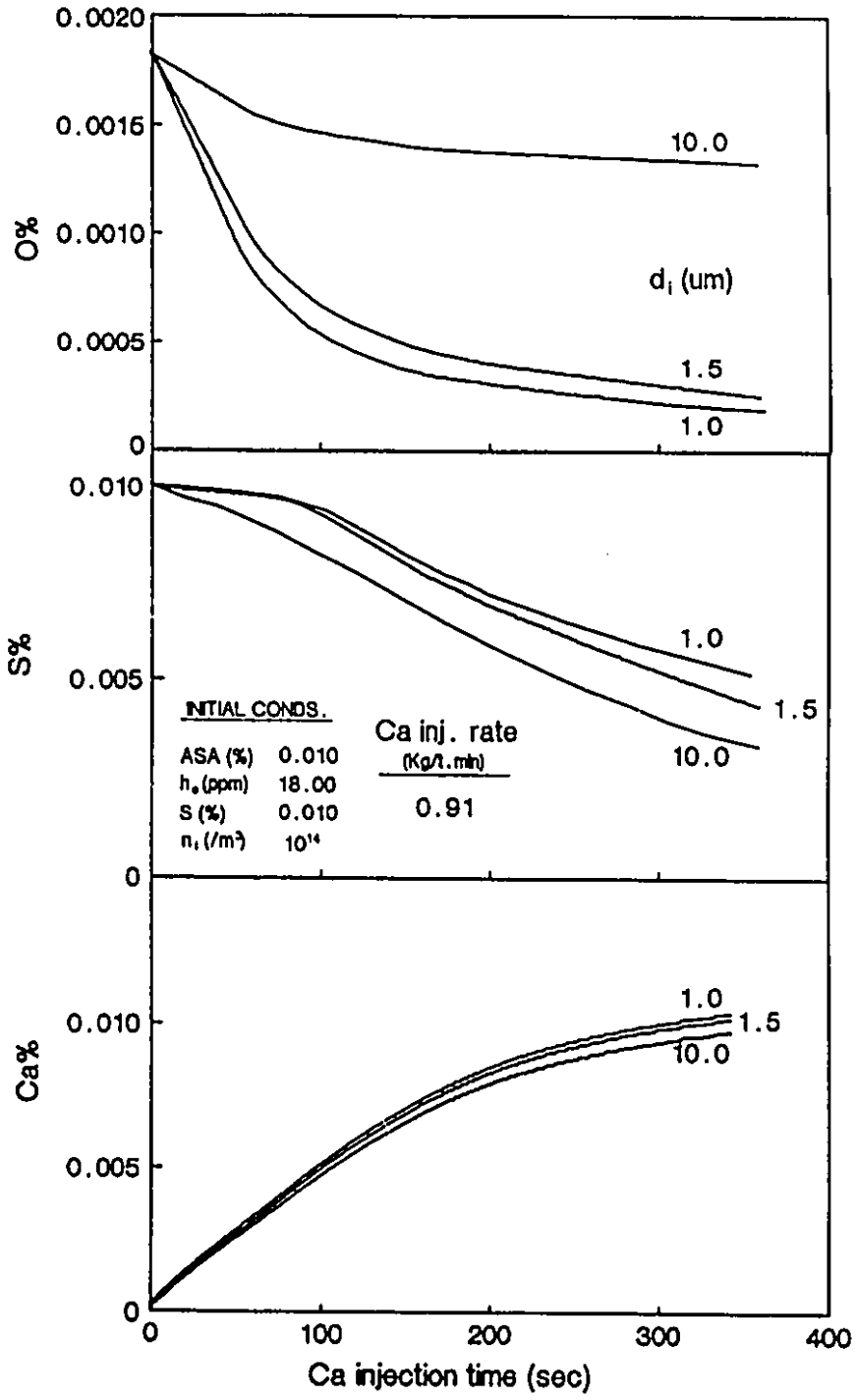

Figure 6.24 The model prediction for the effect of the diameter of the initial oxide inclusions on oxygen, sulphur and total calcium contents during injection.

EAF\dl2.drw

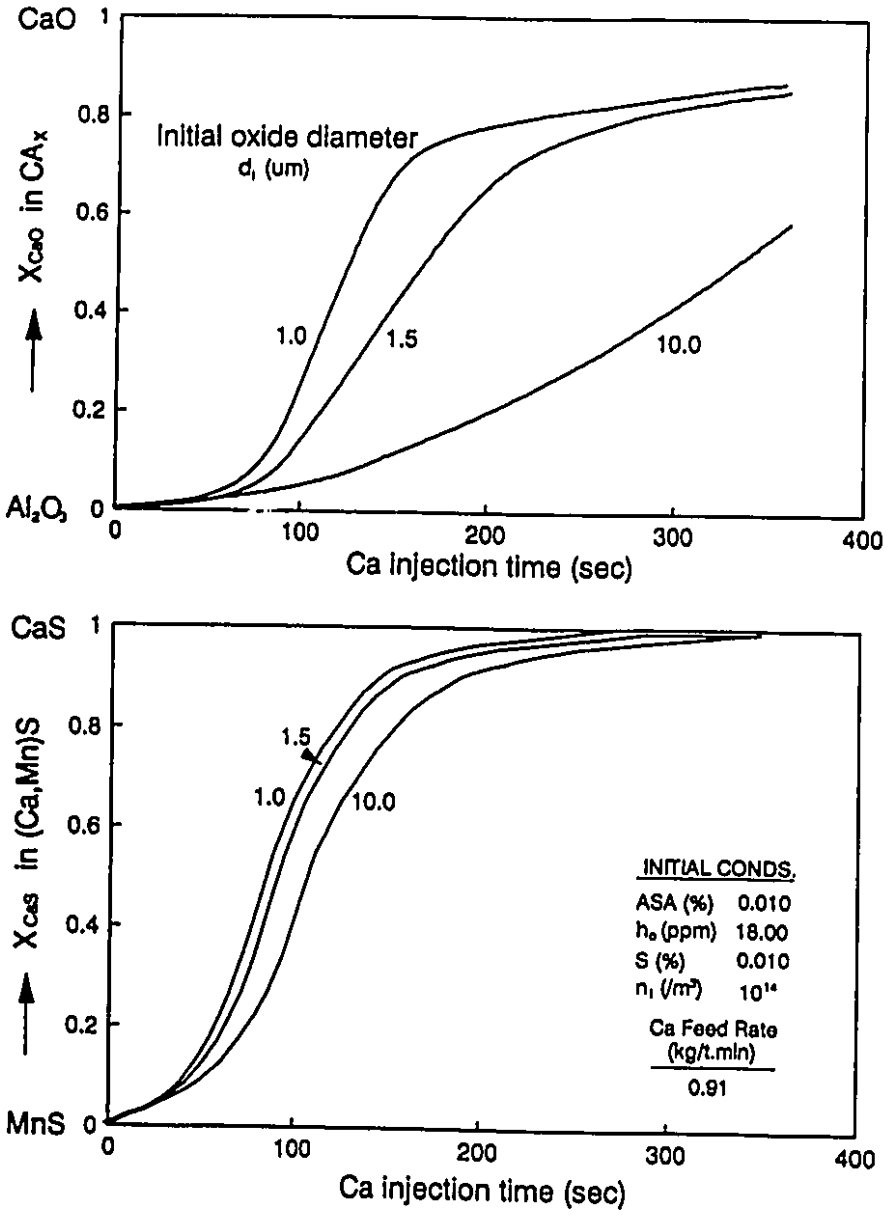

Figure 6.25 The model prediction for the effect of the diameter of the initial oxide inclusions on the compositions of CA_x and (Ca,Mn)S during injection.

effect of slag coverage on the extent of inclusions modification is quite small.

Figures 6.28 and 6.29 show the effect of inclusion flotation rate on the bulk chemistry and inclusions composition. The faster the inclusions float out from the melt, fewer inclusions will remain to be modified by calcium. Thus deoxidation, desulphurization and inclusion modification rates are increased. However, the degree of these increases due to a faster inclusion flotation rate is relatively minor as shown in the Figures 6.28 and 6.29.

6.5 INDUSTRIAL IMPLICATIONS

6.5.1 Comparison with Full-scale Practices

There are several differences between the present experiments and full-scale injection processes. Table 6.3 compares the injection rates. While the linear rate of wire feeding is much slower than full-scale, the specific injection rate per tonne is higher. This is due to the small melt volume. Consequently, in the present experiments the amounts of calcium added are greater than full-scale. This resulted in "over-treatment" of the steel which would have deleterious effects in practice. For example, Figure 5.51 shows that for

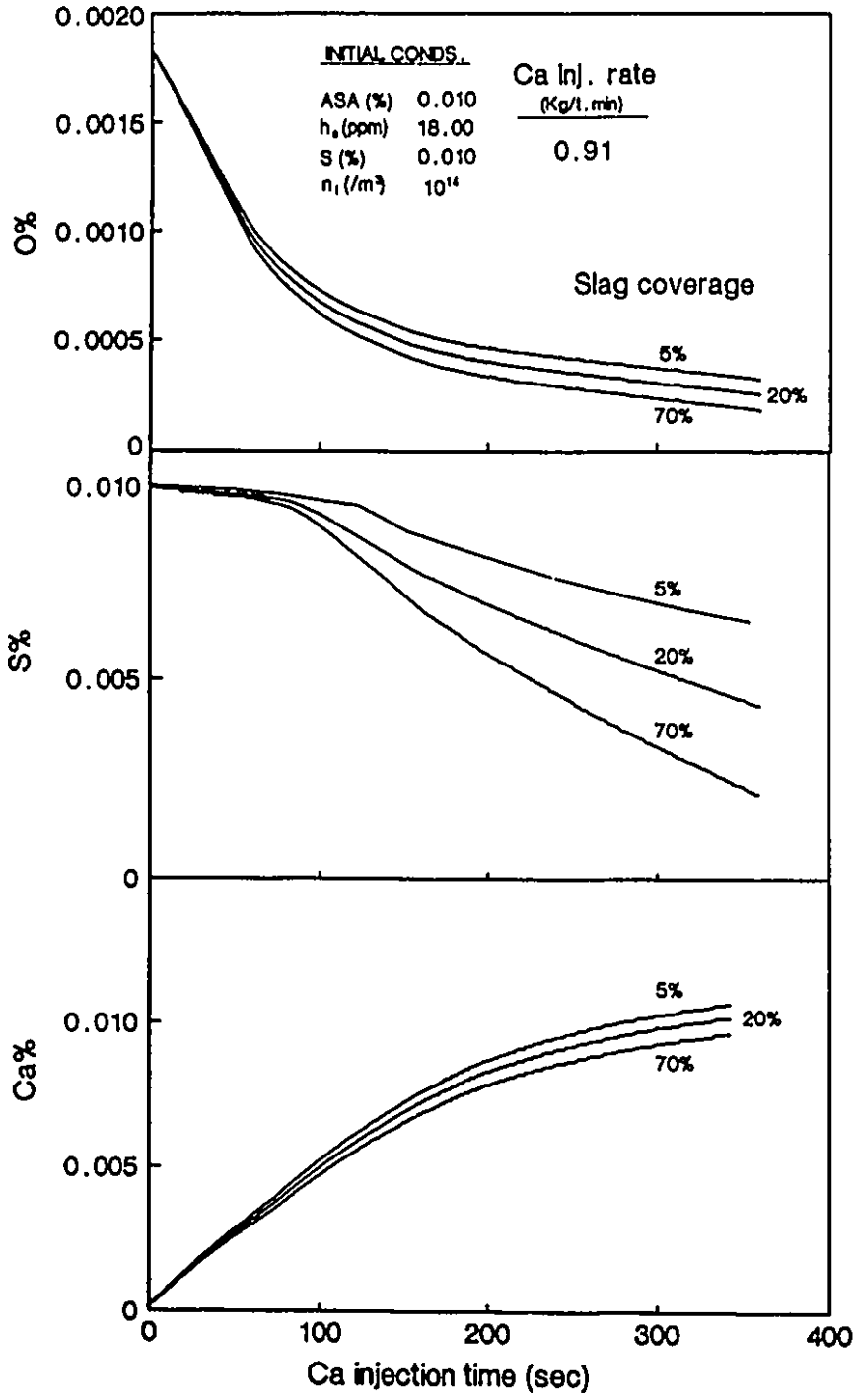

Figure 6.26 The model prediction for the effect of the slag coverage on oxygen, sulphur and total calcium contents during injection.

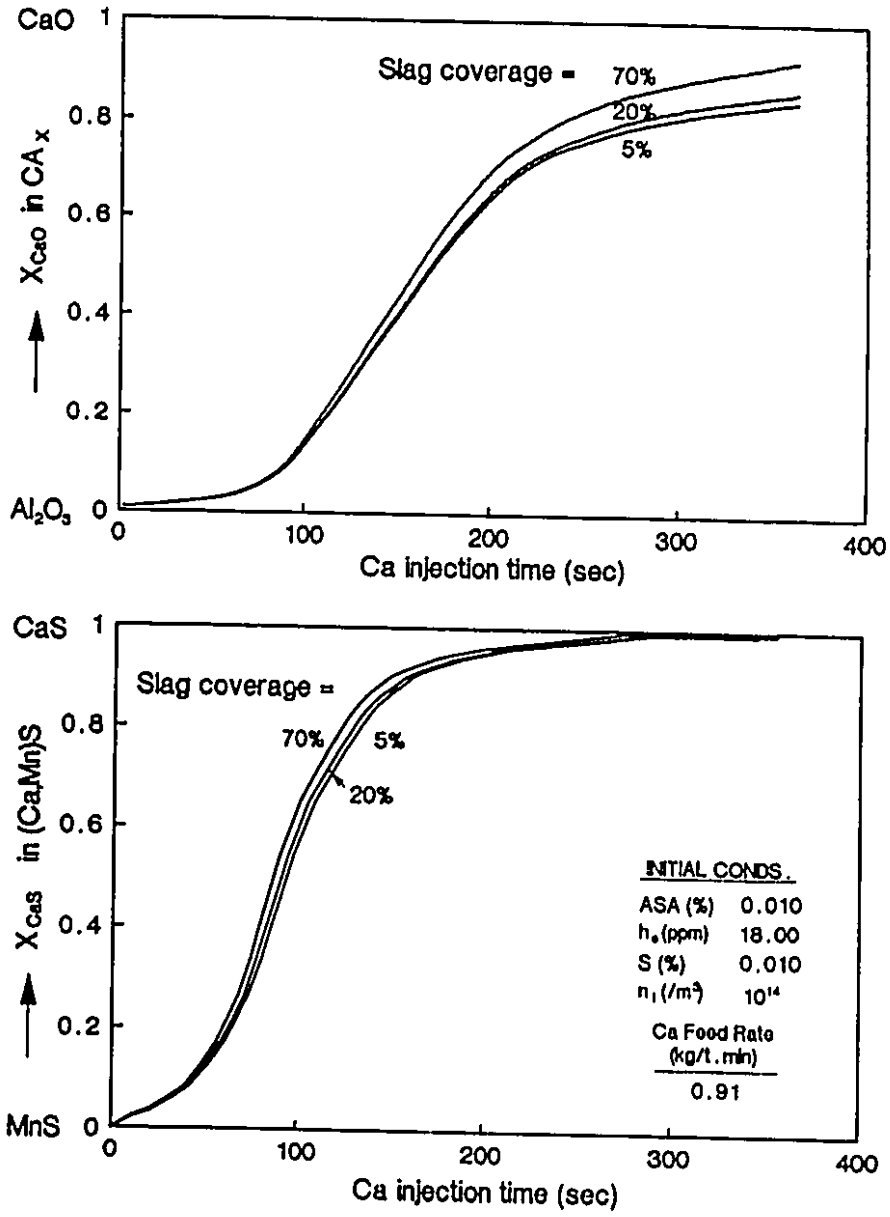

Figure 6.27 The model prediction for the effect of the slag coverage on the composition of CA_x and (Ca,Mn)S during injection.

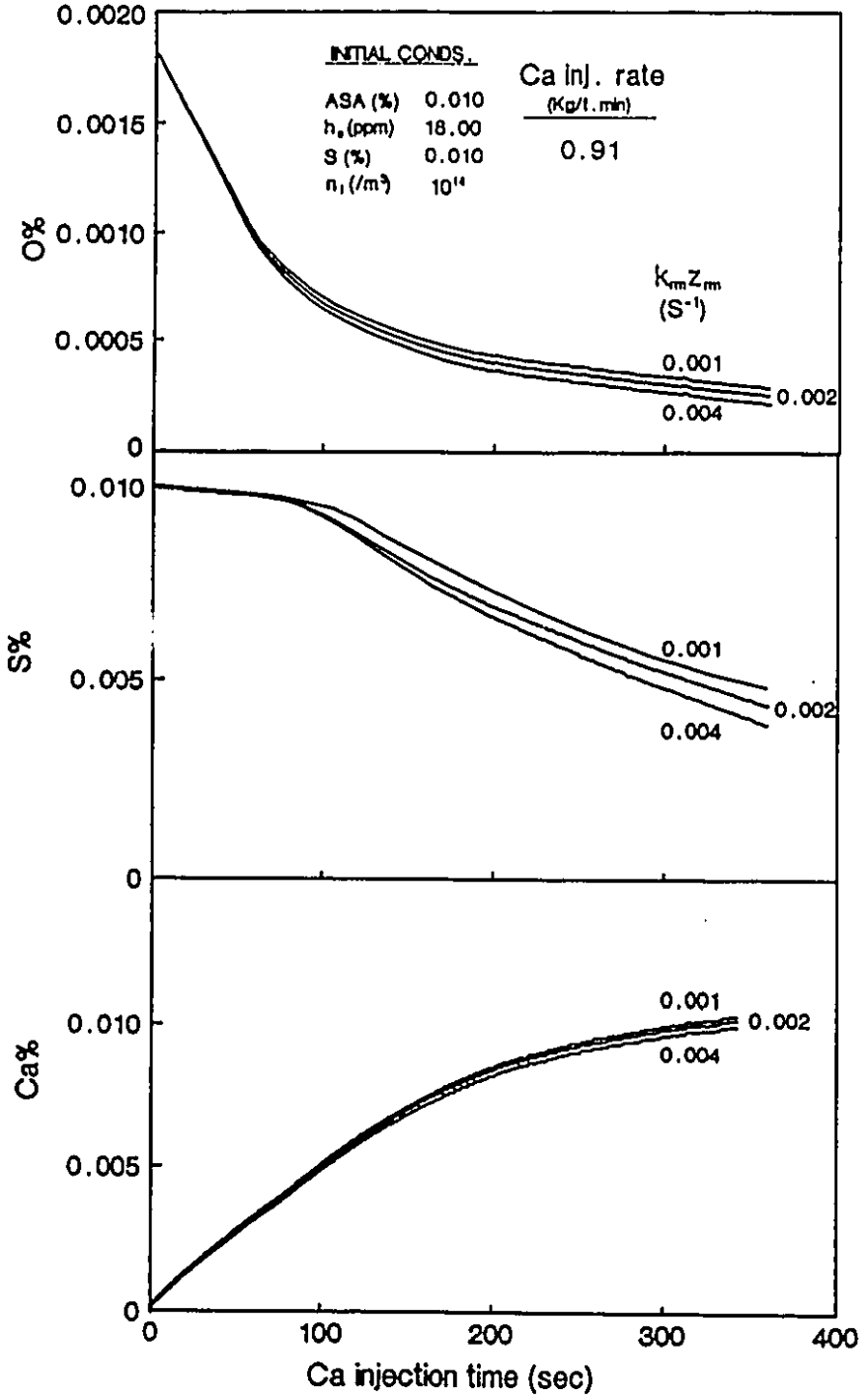

Figure 6.28 The model prediction for the effect of the inclusion flotation rate on oxygen, sulphur and total calcium contents during injection.

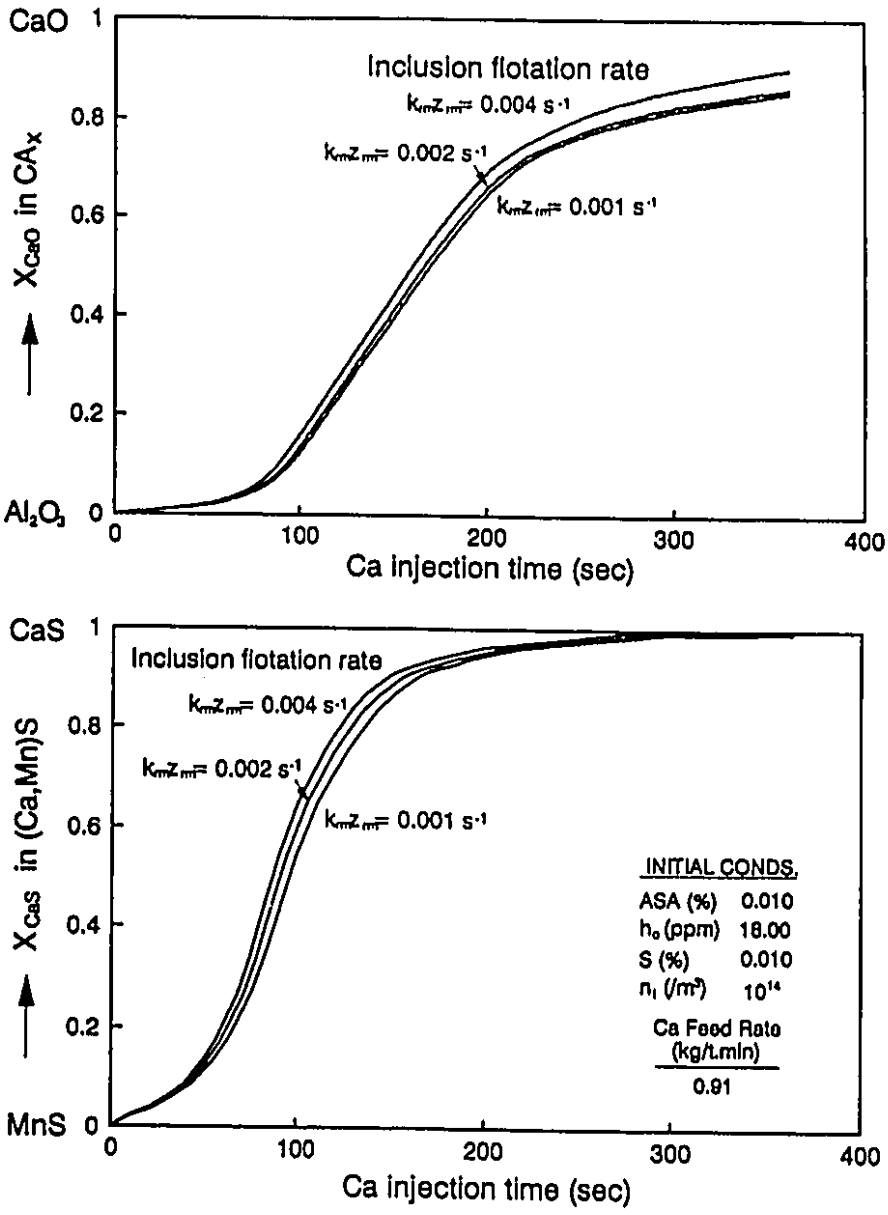

Figure 6.29 The model prediction for the effect of the inclusion flotation rate on the compositions of CA_x and (Ca,Mn)S during injection.

well-deoxidized heats and high sulfur and calcium contents, solid calcium sulfides were formed. Similarly, Figure 5.46 shows that at high levels of calcium, solid lime rather than liquid calcium aluminates are formed.

TABLE 6.3

COMPARISON ON CALCIUM FEED RATES WITH FULL-SCALE PROCESSES

	Calcium Feed Rates	
	Linear (m/s)	Specific (Kg Ca/tonne/min)
Present work	0.02 - 0.10	0.8 - 4.8
Full - scale	1 - 5	0.02 - 1.0

In addition, because of the small melt volume the conditions in the present experiments are more characteristic of what would be expected near the injection point in a full-scale process. It is believed that this is reason that this is the first time that large amounts of primary CaO and CaS have been observed.

The present experiments were more susceptible to reoxidation than full-scale operations in spite of the argon atmosphere because the synthetic slag cover was usually ejected from the melt during injection and because the proportion of surface area to volume of the melt is comparatively large.

6.5.2 Industrial Implications

The present study has several implications for the industrial practice of calcium treatment of steel:

1) Calcium recovery is a function of calcium injection rate and sampling time (Figure 5.55). It continues to decrease over the time during the holding period. Therefore, calcium recoveries must be carefully interpreted, and comparisons between widely different practices may not yield a useful measure of the effectiveness of inclusion modification using different techniques.

2) The solubility of dissolved calcium with 1 atm of calcium vapour for the present conditions is about 240 ppm, whereas the results (Figure 6.8) demonstrate that the actual dissolved calcium near the end of calcium injection is three order of magnitude smaller (about 0.2 ppm). It is this very small concentration of calcium that is responsible for modification of inclusions, thus there is tremendous potential for the improvement of reaction rate and efficiency of calcium utilization in steel.

3) Figure 6.4 shows that the dissolution rate is considerably enhanced by the presence of sulphur and oxygen; previous work has demonstrated that solubility can be enhanced

by aluminum silicon, carbon and nickel which is purely an equilibrium phenomenon [1,4].

4) The present work provides a fundamental thermodynamic and kinetic framework to interpret calcium dissolution, and oxide and sulphide inclusion modification. It was shown to accurately re-produce the bulk chemistry and inclusion composition with given the initial inclusion size and numbers. The model is now ready for application to full-scale heats; some experimental work would be required to characterize the inclusion distributions in such heats, but it is expected that melt chemistry and inclusion distributions could be better controlled by using the present model framework.

5) Higher initial h_s/h_o favours sulfide modification and lower initial h_s/h_o favours oxide modification. This interaction of oxide and sulfide with the melt governs the final equilibrium state. When calcium is used for oxide modification, the interaction from the sulfide has to be considered, and visa versa.

6) Reoxidation should be avoided after calcium injection in order to prevent the system from drifting away from the final equilibrium state.

CHAPTER 7

CONCLUSIONS

Steel-clad calcium wire was fed into 40 kg heats of AISI steel with various sulphur and aluminum contents under argon atmosphere. Samples were taken continuously during and after calcium injection for chemical and inclusion analysis. After analysis of the experimental results from more than twelve heats of injection, the following conclusions were drawn.

(1) During calcium wire injection there was an initial rapid rise of total calcium content to a steady-state level. Both the dissolution rate and the steady-state level increased with calcium feed rate and the initial sulfur and oxygen (dissolved) contents in the bulk. After injection, calcium decreased rapidly and exponentially with the holding time, apparently following the first-order kinetics.

(2) Both desulphurization and deoxidation rates decreased

with the initial oxygen activity, but increase with the calcium feed rate.

(3) Analysis of inclusions obtained during calcium injection indicated that large amounts of CaO and CaS were formed, and coexisted with both modified oxide (CA_x), sulfide (Ca,Mn)S, oxy-sulfide (($CaS \cdot CA_x$), (Ca,Mn)$S \cdot CA_x$, unmodified oxide (Al_2O_3), and sulfide (MnS) inclusions.

(4) Alumina inclusions tended to be transformed to calcium-rich aluminate CA_x by increased calcium treatment, decreased acid soluble aluminum content and decreased sulfur content.

(5) Manganese sulphide inclusions tended to be transformed to calcium-rich (Ca,Mn)S inclusions with increased calcium treatment, increased acid soluble aluminum and decreased sulfur content.

(6) Higher initial h_s/h_o ratio favoured the sulfide inclusion modification, and lower initial h_s/h_o favoured the oxide inclusion modification.

(7) Most of the bulk total calcium content was found to be calcium obtained as inclusions. The dissolved calcium (0.2 ppm) at the end of injection was found to be three-order of magnitude smaller than the saturation calcium

content (240 ppm) in equilibrium with 1 atmosphere of calcium vapour.

(8) The calcium recovery was found to vary with time and the calcium injection rate. The total calcium recovery and calcium to aluminum ratio were found to be not good measures of the extent of inclusion modification.

(9) Calcium dissolution was found to be enhanced by instantaneous reactions with oxygen and sulfur in the boundary layer. The unreacted calcium dissolved through the gas-liquid into the melt to modify inclusions.

(10) The overall interaction between oxides and sulphides with the bulk tended to drive towards the equilibrium of (CaO) + $\underline{S}$ = (CaS) + $\underline{O}$.

(11) The CaS and MnS activities at three steelmaking temperatures were calculated by applying a regular solution model to the solid phase and an ideal model to the liquid phase of the CaS-MnS phase diagram. The results showed moderately large positive deviations from ideality which may be attributed to differences in the lattice parameters for CaS and MnS.

(12) A mathematical model for the multiphase kinetics was developed to interpret the calcium dissolution,

deoxidation and desulphurization, and inclusion modification. The implications for full-scale operation were also discussed.

CLAIM TO ORIGINALITY

Several aspects of this Thesis constitute, in the Author's opinion, new and distinct contributions to knowledge. The major contributions are:

1. While calcium treatment of steel has gained much importance for improving the castibility of molten steel and quality of the final products, this is the first well-controlled laboratory research conducted to study and understand the kinetics and mechanism of the process through continuous monitoring and sampling during and after calcium injection.

2. This is the first time that the calcium dissolution in the steel during injection was found to be enhanced by the initial sulphur and oxygen contents. An instantaneous reaction theory has been put forward to explain this enhancement phenomenon, and it is consistent with the experimental results.

3. This is the first time that large amounts of CaS and CaO inclusions were found to coexist with both modified and

unmodified oxide and sulphide inclusions during and after injection.

4. This is the first time that the activities of CaS and MnS have been calculated by applying an ideal solution model for the liquid phase and a regular model to the solid phase of the CaS-MnS phase diagram at various steelmaking temperatures. The calculated a_{CaS}-a_{MnS} diagrams are believed to provide metallurgists with a more complete tool for understanding and control of the calcium injection process, especially for sulphide modification and interaction between oxide and sulphide inclusions.

5. The system kinetic paths have been constructed and were found to drive towards the equilibrium condition of the following governing equation: (CaO) + $\underline{S}$ = (CaS) + $\underline{O}$.

6. This is the first time that a comprehensive mathematical model has been developed to successfully interpret calcium dissolution, deoxidation, desulphurization, oxide and sulphide inclusion modification. The model provides a framework exploring similar reactions in full-scale systems.

REFERENCES

1. D. Sponseller and R.A. Flinn: Trans. AIME, 230, 1964, pp. 876.
2. T. Ototani, Y. Katamura and T. Degawa: Trans. ISIJ, No. 16, 1976, pp. 275-282.
3. G.M. Faulring and S. Ramalingam: Metall. Trans. B, Vol. 11B, 1980, pp. 125-132.
4. M. Kohler, H. Engell and D. Janke: Steel Research, No. 8, 1985, pp. 413-423.
5. M. Nadif and C. Gatellier: IRSID Report, June 1985.
6. D.A.R. Kay and S.V. Subramanian: Second International Symposium on the Effects and Controls of Inclusions and Residuals in Steel, CIM, Toronto, 1986, pp. I25-I43.
7. T. Ototani: Calcium Clean Steel, 1986, Springer-Verlag, pp. 4-7.
8. I.S. Kulikov: Russian Met., No. 6, 1985, pp. 6-13.
9. E. Schürmann, P. Fünders and H. Litterscheidt: Arch. Eisenhüttenw, 45, 1974, pp. 433.
10. H.M. Howe: The Metallurgy of Steel, 1890, Scientific Publishing, New York, pp. 89.

11. O.P. Watts: J. Am. Chem. Soc., 28, 1906, pp. 152.

12. W.O. Philbrook, K.M. Goldman and M.H. Henzel: Trans. AIME, 188, 1950, pp. 361.

13. R.A. Grange, F.J. Shortsleeve, D.C. Hilty, W.O. Binder, G.T. Motock and C.M. Offenhauer: B, Ca, Cb and Zr in Iron and Steel, Wiley and Sons, New York, 1957.

14. T. Kusakawa, H. Tagawa and H. Kamio: Tetsu-to-Hagane, 58, 1972, pp. S398.

15. Y. Miyashita and K. Nishilawa: Tetsu-to-Hagane, 51, 1971, pp. 1969-1975.

16. T. Ototani and Y. Kataura: Sci. Rep. RITU, A21, 1969, pp.2.

17. B. Tivelius and T. Sohlgren: 1979 McMaster Symp. on Iron and Steelmaking, (ed. by K.S. Kirkaldy), May 1979, pp. 3.1-3.17.

18. K. Ogawa, S. Koyama, R. Yamanaka, Y. Suzuki and T. Sasaki: Kobe Steel Ltd., Japan, 1991, Private Comm.

19. G. Carlsson and L.W. Helle: Scan. J. Met., 14, 1985, pp. 18-24.

20. L.W. Helle, B. E. Gabrielsson and G. Carlsson: Scan J. Met., 15, 1986, pp. 9-15.

21. H. Sir Davy: Phil. Trans. Roy. Soc., 98, 1808, pp. 333.

22. H. Goldschmidt: Z. Elektrochem., 14, 1908, pp. 558.

23. T. Geilenkirchen: Stahl und Eisen, 28, 1908, pp. 593.

24. W.S. Anderson: Raw Mater., 4, 1921, pp. 51.

25. I.M. Espana: Rass. Min. Metall. Chim., 66, 1927, pp. 55.

26. W. Ziehler: Arch. Eisenhüttenw, 5, 1931, pp. 299.

27. C.L. Mantell and C. Hardy: Met. Progr., 21, 1932, pp.60.

28. J. Chipman: Trans. ASM, 22, 1934, pp. 385.

29. W. Kroll: Trans. Electrochem. Soc., 46, 1934, pp. 81.

30. C.E. Sims amd F.B. Dahle: Trans. Am. Foundryman's Assoc., 46, 1938, pp. 65.

31. W. Crafts, J.J. Egan and W.D. Forgen: Trans. AIME, 140, 1940, pp. 233.

32. J. N. Ludwig: Proc. Elect. Furn. Steel Conf. AIME, 6, 1948, pp. 208.

33. C.L. Mantell and C. Hardy: Calcium Metallurgy and Technology, Reinhold Publishing, New York, 1945.

34. SCANINJECT I-V: Int. Conf. on Inj. Met., Luleå, Sweden, 1979-1989.

35. 1st Int. Ca Treatment Symp., the Inst. of Metals, Glasgow, Scotland, June 1988.

36. D.J. Naylor, D.M. Keane and D.T. Llewellyn: Bethlehem Steel, 1974, Private Comm.

37. E. Förster, W. Klapdar, H. Richter, H.W. Rommerswinkel, E. Spetzler and J. Wendorff: Stahl und Eisen, 94, 1975, pp. 474.

38. K.E. Oeberg, F.J. Weiss: 36th EAF Conf., Toronto, Dec. 5-8, 1978.

39. Nemoto, Kawawa, Sazashima and Sato: Testu-to-Hagane, 56, 1970, pp. 430.

40. T. Ototani and Y. Kataura: Testu-to-Hagane: 57, 1971, pp. 1573.

41. Y. Kataura and D. Oelschlägel: Stahl und Eisen, 100, 1980, pp. 200.

42. S.A. Argyropoulos and R.I.L. Guthrie: Steelmaking Proceedings, Pittsburgh, PA, Vol. 65, 1982, pp. 156-167.

43. F.A. Mucciardi: Master's Theisis, Dept. of Mining and Metallurgical Eng., McGill University, Jan. 1977.

44. F.A. Mucciardi: Canadian Metallurgical Quaterly, Vol. 26, No. 4, 1987, pp. 351-357.

45. A. Gueussier, F. Pellicani and R. Szezesny: SCANINJECT V, Part II, June 6-8, 1989, pp. 395.

46. J.G. Kaiser: American Magazine, 33, June 30, 1983.

47. F.D. Richardson and J.H.E. Jeffes: J. Iron Steel Inst., 160, 1948, pp. 261; 164, 1952, pp. 165.

48. O. Kubaschewski and C.B. Alcock: Metallurgical Thermochemistry, 5th Ed., Pergamon Press, 1979, pp. 378.

49. M. W. Chase, Jr., A. A. Davies, J. R. Downey, Jr., D. J. Frurip, R. A. McDonad and A. N. Syverud: J. Phys. Chem. Ref. Data, 3rd ed., JANAF Thermochemical Tables, 1985, vol. 14, supp. 1.

50. D. M. Edmunds and J. Taylor: J. Iron Steel Inst., 1972, vol. 210, pp.280-83.

51. T. Wakasugi and N. Sano: Metall. Trans., vol. 20B, 1989, PP.431-33.

52. R.V. Kumar and D.A.R. Kay: Metall. Trans., Vol. 16B, 1985, pp. 287-294.

53. J.F. Elliott, M. Gleiser and V. Ramakrishna: Thermochemistry for Steelmaking, Vol. II, Addison-Wesley Press Inc. Reading, Mass., 1963.

54. N. Nadif and C. Gatellier: IRSID Report, 1108, BIS Juin 1985.

55. T. Fujisawa and H. Sakao: CSIRA/ISIJ Japan-Canada Seminar, Tokyo, 1985.

56. H. Han: Beijing University of Iron and Steel, 1989, Private Comm.

57. V.S. Kobayashi, Y. Omori and K. Sanbongi: Trans. ISIJ, 11, 1971, pp. 260-269.

58. K. Suzuki, A. Ejima and K. Sanbongi: Testsu-to-Hagane, 66, 1979, pp. SS85.

59. S. Gustaffsson: Ph.D. Thesis, The Royal Institute of Technology, Stockholm, Sweden, 1982.

60. C. Gatellier, M. Olette, R. Vasse and M. Devaux: 25éme Colloque de métallurgie de Saclay, INSTN, 23-25 June 1982.

61. H.M. Pielet and D. Bhattacharya: Metall. Trans., 15B, 1984, pp. 547-56.

62. S.Y. Kitamura, K. Miyamura and I. Fukuoka: ISIJ, 27, 1987, pp. 344-350.

63. B. Mintz, Z. Mohamed and R. Abu-shosha: Materials Science and Technology, 5, 1989, pp. 682-686.

64. T. Takenouchi and K. Suzuki: Tetsu to Hagane, 63, 1977, pp. 1653.

65. A. Nordgren and A. Melander: Materials Science and Technology, 5, Sept. 1989, pp. 940-951.

66. H. Nashiwa, A. Mori, S. Ura, T. Ikeda, H. Matsuno and R. Ishikawa: 25, ISIJ, 1977, pp. 81.

67. A. Ishii, A. Ishikawa and Y. Nakamura: Interceram, 1987, pp. 70-74.

68. I.G. Davies and P.C. Morgan: Ironmaking & Steelmaking, 2, 1985, pp. 176-184.

69. K.J. Handerhan, W.C. Beringer and A.V. Hinkel: Iron and Steel Maker, Dec. 1989, pp. 41-52

70. Slag Atlas, Verlag Stahleisen m.b.H, Dusseldorf, 1981.

71. H. Nashiwa, A. Mori, S. Ura, T. Ikeda, H. Matsuno and R. Ishikawa: The sixth Japan-USSR Joint Symp. on Physical Chemistry of Metallurgical Processes, ISIJ, Tokyo, No.25, 1977, pp. 81.

72. D.C. Hilty and J.W. Farrel: Iron and Steelmaker, 1975, May, pp. 17-20 and June, pp. 20-27.

73. W.Y. Weh, C.L. Chou, F.S. Shyr, P.S. Yang, Y.I. Kuo and W.S. Wang: SCANINJECT IV, Part II, 1986, pp. P6:1-P6:21.

74. W.Y. Weh, C.L. Chou, F.S. Shyr, P.S. Yang, Y.I. Kuo and W.E. Wang: SCANINJECT IV, Part II, 1986, pp. P7:1-P7:29.

75. L. Holappa and H. Ylonen: SCANINJECT III, 1985, pp. 47:1-23.

76. G.J.W. Kor: 1st Int. Ca Treatment Symposium, The Inst. of Metals, Glasgow, Scotland, 1988, pp. 5:1-17.

77. C.P. Church, T.M. Krebs and J.P. Rowe: J. of Metals, 18, 1966, pp. 62-68.

78. W.J.M. Salter and F.R. Pickering: J. of Iron & Steel Institute, 207, 1969, pp. 992-1002.

79. R. Kiessling and C. Westman: J. of Iron & Steel Institute, 208, 1970, pp. 699-700.

80. B.J. Skinner and F.D. Luce: American Mineralogist, 56, 1971, pp. 1269-1298.

81. C.H. Leung and L.H. Van Vlack: J. of American Ceramic Soc., 62, 1979, pp. 613-616.

82. Oyama, Tanaka and Kitamura: Tetsu-to-Hagane, 63, 1977, pp. 159.

83. Takenouchi and Suzuki: Testu-to-Hagane, 63, 1977, pp. 1653.

84. Hirahara, Marukawa, Yamazaki, Takahashi and Shiroda: Testu-to-Hagane, 64, 1978, pp. 122.

85. Umeda, Ikeda, Kawai and Sugisawa: Testu-to-Hagane, 65, 1979, pp. A29.

86. J.I. Takamur and S. Mizoguchi: Proc. of the sixth Intern. Iron and Steel Congress, Nagoya, Japan, 1990, pp. 591-97.

87. C. Gatellier, H. Gaye and J. Lehmann: IRSID Report, France, 1991, Private Comm.

88. G.M. Faulring, J.W. Farrell and D.C. Hilty: Iron and Steelmaker, 7, 1980, pp. 14.

89. M.J. Heesom: 1st Int. Ca Treatment Symposium, The Inst. of Metals, Glasgow, Scotland, 1988, pp. 69-81.

90. T.A. Engh and N. Lindskog: Scand. J. Metallurgy, 4, 1975, pp. 49-58.

91. K. Torsell: Trans. Iron and Steel Inst. Japan, 8, 1968, pp. 203-219.

92. Y. Sundberg: ASEA J., 44, 1971, pp. 71-80.

93. K. Nakanishi, T. Fujii and J. Szekely: Ironmaking and Steelmaking, 3, 1975, pp. 193-197.

94. K.W. Lange, K. Okohira, D. Papamantellos and H. Schenck: Arch. Eisenhüttenw, 42, 1971, pp. 1-4.

95. O.J. Ilegbusi and J. Szekely: Metall. Trans., Vol. 19B, 1988, pp. 557-562.

96. U. Lindborg and K. Torssel: Trans. Metall. Soc. AIME, 242, 1968, pp. 94-102.

97. P.A. Ramachandran and R.V. Chaudhai: Three-phase Catalytic Reactions, Gordon and Breach Science Publishers Inc., London, 1983.

98. K.R. Westerterp, W.P.M. van Swaaij and A.A.C.M. Beenackers: Chemical Reactor Design and Operation, Jhon Wiley and Sons, 1984.

99. Y.T. Shah: Gas-Liquid-Solid Reactor Design, McGraw-Hill Int. Bookd Co., 1979.

100. Mass Transfer with Chemical Reactions in Multiphase System, Vol.II: Three-phase System, Ed. by E. Alper, NATO ASI Series, Martinus Nijhoff Publishers, 1983.

101. Froment and Bischoff: Chemical Reactor Anaysis and Design,

102. G.A. Irons: Ph.D. Thesis, McGill University, 1978.

103. R. Higbie: Trans. A.I.Ch.E., Vol. 31, 1935, pp. 365-87.

104. J.H.C. Coppus: Thesis, Eindhoven Univ. of Tech., the Netherlands, 1977.

105. A.I. Johnson et al: Can. J. Chem. Eng., Vol. 47, 1969, pp. 559.

106. A.C. Lochiel and P.H. Caldebank: Chem. Eng. Soc., Vol.19, 1964, pp. 471-484.

107. M.H.I. Baird and J.F. Davidson: Chem. Eng. Soc., Vol. 17, 1962, pp. 87-93.

108. M.E. Weber: Chem. Eng. Soc., Vol. 30, 1975, pp. 1507-10.

109. D.H. Waklin: Ph.D. Thesis, Imperial College, University of London, 1966.

110. J. Szekely and N.J. Themelis: Rate Phenomena in Process Metallurgy, Wiley, New York, 1971, pp. 724-734.

111. P. Kozalevitch: Surface Phenomena of Metals, London, 1968, pp.233-45.

112. G.R. Belton: Metall. Trans., Vol. 7B, 1976, pp. 35-42.

113. T. Deb Roy, N.H. El-kaddah and D.G.C. Roberston: Metall. Trans., Vol. 8B, 1977, pp. 271-77.

114. F.D. Richardson: Phys. Chem. of Metals in Met., Vol. 2, 1974, pp. 474.

115. A.V. Bradshaw and F.D. Richardson: "Chemical Engineering in the Iron and Steel Industry", A Symposium, Institute

of Chemical Engineers, 1970, pp. 130.

116. R.B. Bird, W.E. Stewart and E.N. Lightfoot: Trans. A.F.S., 1962, pp. 508-512.

117. E.S. Machlin: Trans. AIME, Vol. 218, 1960, pp. 314-26.

118. G.A. Irons: M. Sc. Thesis, McGill University, 1975.

119. G.A. Irons and R.I.L. Guthrie: Can. Metall. Quart., Vol. 15, No. 4, 1976, pp. 325-32.

120. G.A. Irons et al: Metall. Trans., Vol. 9B, 1978, pp. 151-54.

121. M. Joyant and C. Gatellier: IRSID Reprot, PCM-RE, 1108, Mai, 1984.

122. P.V, Danckwerts: Gas-Liquid Reaction, McGraw-Hill, New York, 1970.

123. J.C. Charpentier: Adv. Chem. Eng., 11, 1981, pp. 1-133.

124. O. Levenspiel: Chemical Reaction Engineering, 2nd ed., John Wiley & Sons, New York, 1972, pp. 409-59.

125. P.A. Ramachandran and M.M. Sharma: Chem. Eng. Sci., Vol. 24, 1969, pp. 1681-86.

126. E. Alper, B. Wichtendahl and W.-D. Deckwer: Chem. Eng. Sci., Vol. 35, 1980, pp. 217-222.

127. B.H. Al-Ubaidi, M.S. Selin and A.A. Shaikh: AICHE J., Vol. 36, No. 1, 1990, pp. 141-146.

128. E.T. Turkdogan, P. Grieveson and L.S. Darken: J. Phys. Chem., 67, 1963, pp. 1647-54.

129. J.H. Zong and J.K. Yoon: Metall. Trans., Vol. 21B, 1990, pp. 49-57.

130. W.E. Ranz and W.R. Marshall: Chem. Engng. Prog., 48, 1952, pp. 141-146, 173-180.

131. J. Szekely: Fluid Flow Phenomena in Metals Processing, Academic Press, New York, 1979, pp. 140-141.

132. J.C. Fulton and J. Chipman: The Physical Chemistry of Steelmaking, Chapman and Hall, London, 1958, pp. 113.

133. G.R.St. Pierre and J. Chipman: AIME Trans., Vol. 226, 1956, pp. 1474.

134. L.S. Darken abd B.M. Larsen: AIME Trans., Vol. 150, 1942, pp. 87.

135. E.W. Filer and L.S. Darken: J. of Metals, 1961, pp. 672.

136. Y. Tomita: Metall. Trans., Vol. 21A, 1990, pp. 2739-46.

137. M. Wahlster, A. Choudhury, L.E. Rohde, H. Knahl and A. Freissmuth: Stahl und Eisen, 90, 1970, pp. 1013.

138. E. Kucharski and C. G. Mickleson: Proc. Electric Furnace Conf., 25, 1967, pp. 34.

139. F.C. Hackett and J. Melver: Proc. Electric Furnace Conf., 29, 1971, pp. 117.

140. I.P. Volchok and Yu.A. Shul'te: Russian Casting Prod., 9, 1965, pp. 402.

141. H.A. Young: Proc. Electric Furnace Conf., 6, 1948, pp. 189.

142. N. Otoya and Y. Kataura: Nippon Kinzoku, 33, 1969, pp. 736.

143. K. Mineura and K. Tanaka: Mat. Sci. & Tech., Vol. 6, 1990, pp. 743-748.

144. H. Opitz and W. König: Arch. Eisenhüttenw, 33, 1962, pp. 851.

145. H. Opitz, M. Gappisch, W. König, R. Pape and A. Wicher: Arch. Eisenhüttenw, 33, 1962, pp. 841.

146. Teledyne Analytical Instruments; Instruction Manual for Oxygen Analyzer, Model 320P-4, p. 7.

147. C. Wagner; Advances in electrochemistry and electrochemical Engineering, 1966, Vol. 4, pp. 1-46.

148. P.H. Scaife, D.A.J. Swinkels and S.R. Richards; High temperature Science, Vol. 8, 1976, pp. 34-47.

149. M. Iwase, E. Ichise, M. Takeuchi and Yamasaki; Trans. Japan Inst. Metals, Vol. 25, No.1, 1984, pp. 43-52.

150. M.J.U.T. van Wijnggaarden, Je.M.A. Geldenhuis and R.J. Dippenaar; I&SM, April 1988, pp. 35-44, 67.

151. D. Janke and H. Richter; Arch. Eisenhuttenwes., Vol. 50, 1979, pp. 93-99.

152. Electro-Nite; Hamilton, Ontario, Private comm. 1985.

153. Leco Analytical Instruments for the Analysis of Metals and Inorganic Materials; Model TC-136, 1985, p. 8.

154. Leco Analytical Instruments; Model 518 Semi-Automatic Sulfur Titrator.

155. O.P. Bhargava, G.F. Pitt, J.F. Donovan and W.G. Hines; Technicon International Congress, Nov. 1970, in New York.

156. ICAP 7000 Operation Manual;

157. LINK System; DIGISCAN/FDC Operators Manual, SR2-500-FDC-0784, 1985.

158. M.R. Hoover, E.W. White, J. Lebiedzik and G.G. Jhonson, Jr.; Pro. 10th Ann. MAS Conf., 1975, pp. 54A-54B.

159. R.J. Lee, F.E. Huggins and G.P. Huffman; Scanning Electron Microscopy, 1978, Vol. I, pp. 561-568.

160. R.J. Lee and J.F. Kelly; Scanning Electron Microscopy, 1980, Vol. I, pp. 303-310.

161. J.I. Goldstein et al; Scanning Electron Microscopy and X-Ray Microanalysis, 1981, Plenum Press, pp. 305-392.

162. D.A.R. Kay and D. Ghosh; J. Electrochem. Soc., Vol. 124, 1977, pp. 1836-45.

163. E.E. Underwood; in Quantitative Microscopy, ed. by R.T. de Hoff and F.N. Rhines, 1968, McGraw-Hill, New York, pp. 149.

164. D-Z. Lu, G.A. Irons and W-K. Lu; Ironmaking & Steelmaking, The Institute of Metals, London, 1991, Vol. 18, No. 5, pp. 342-346.

165. T.E. Hull, W.H. Enright and K.R. Jackson; "DVERK, a R-K Procedure for Nonstiff ODEs," 1990, Department of Computer Science, University of Toronto, Canada.

Appendix A

Raw Data

BULK CHEMICAL RESULTS

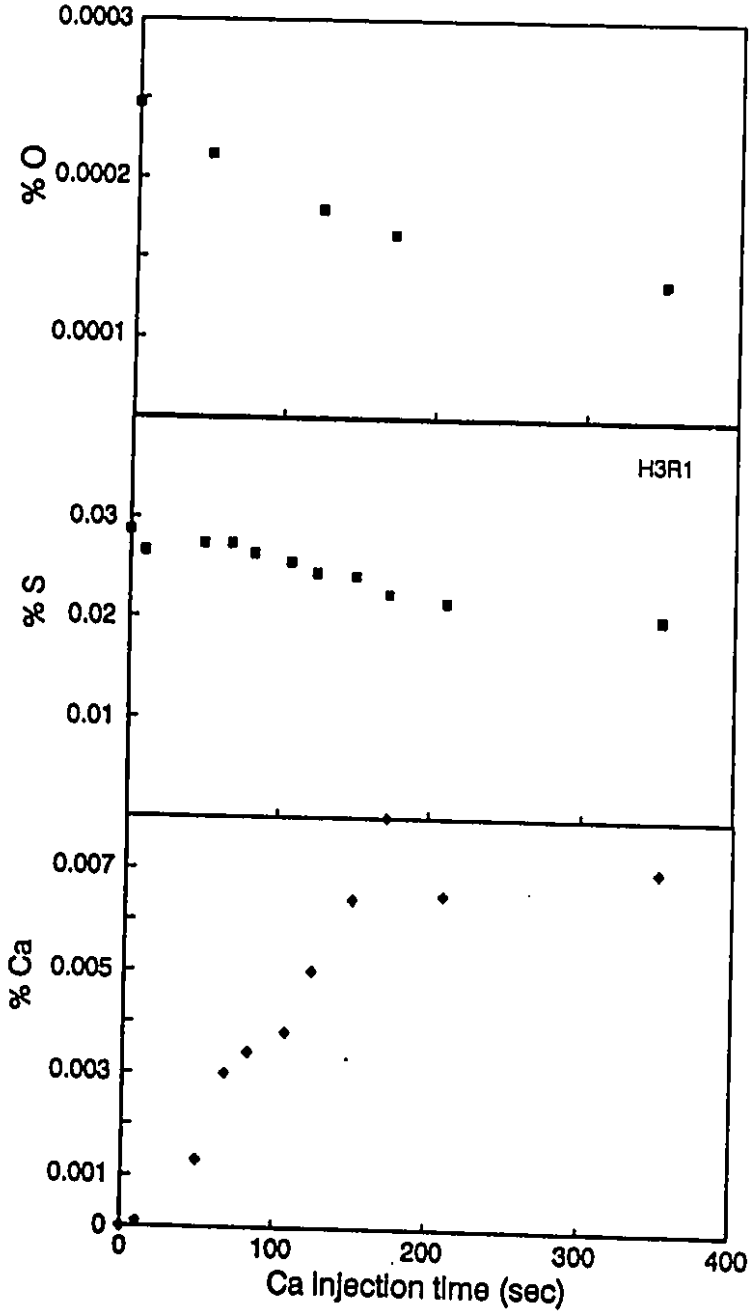

Figure A.1 Oxygen (dissolved), sulfur and calcium contents during injection in H3R1

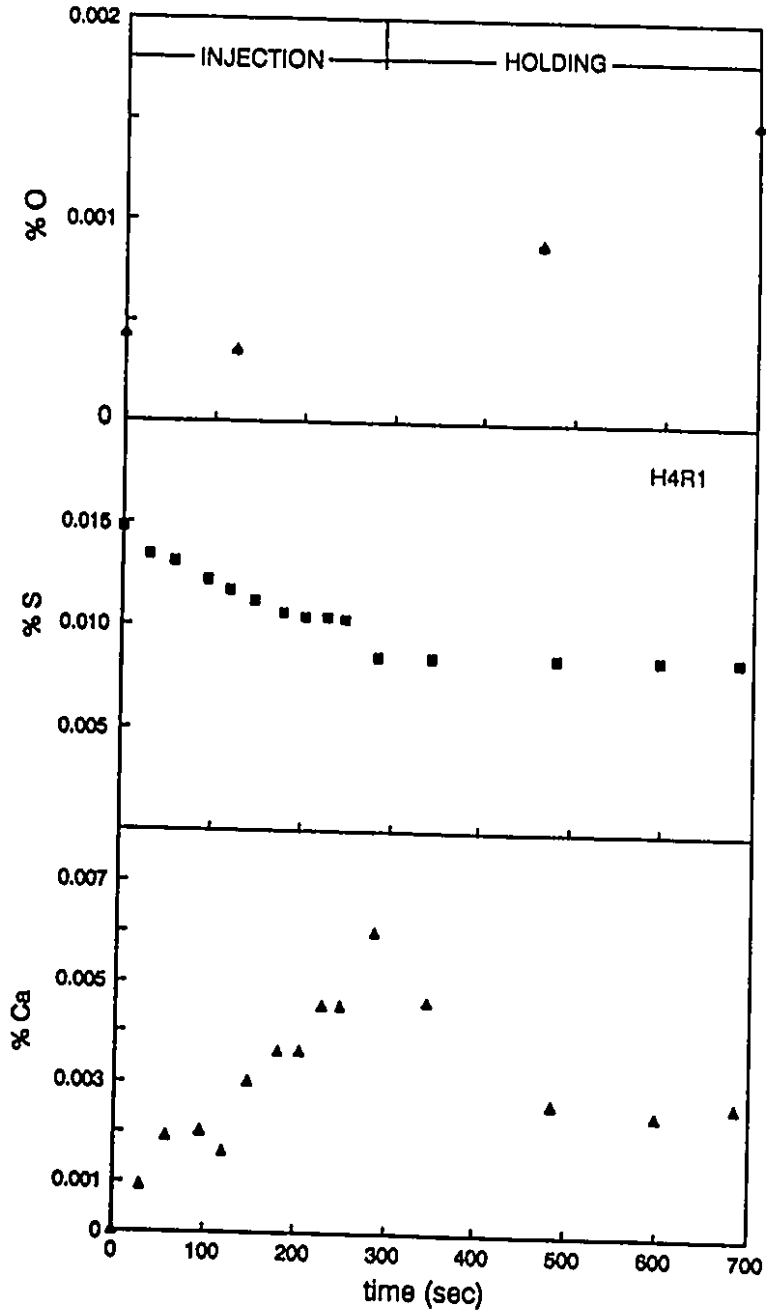

Figure A.2 Oxygen (dissolved), sulfur and calcium contents during and after injection in H4R1

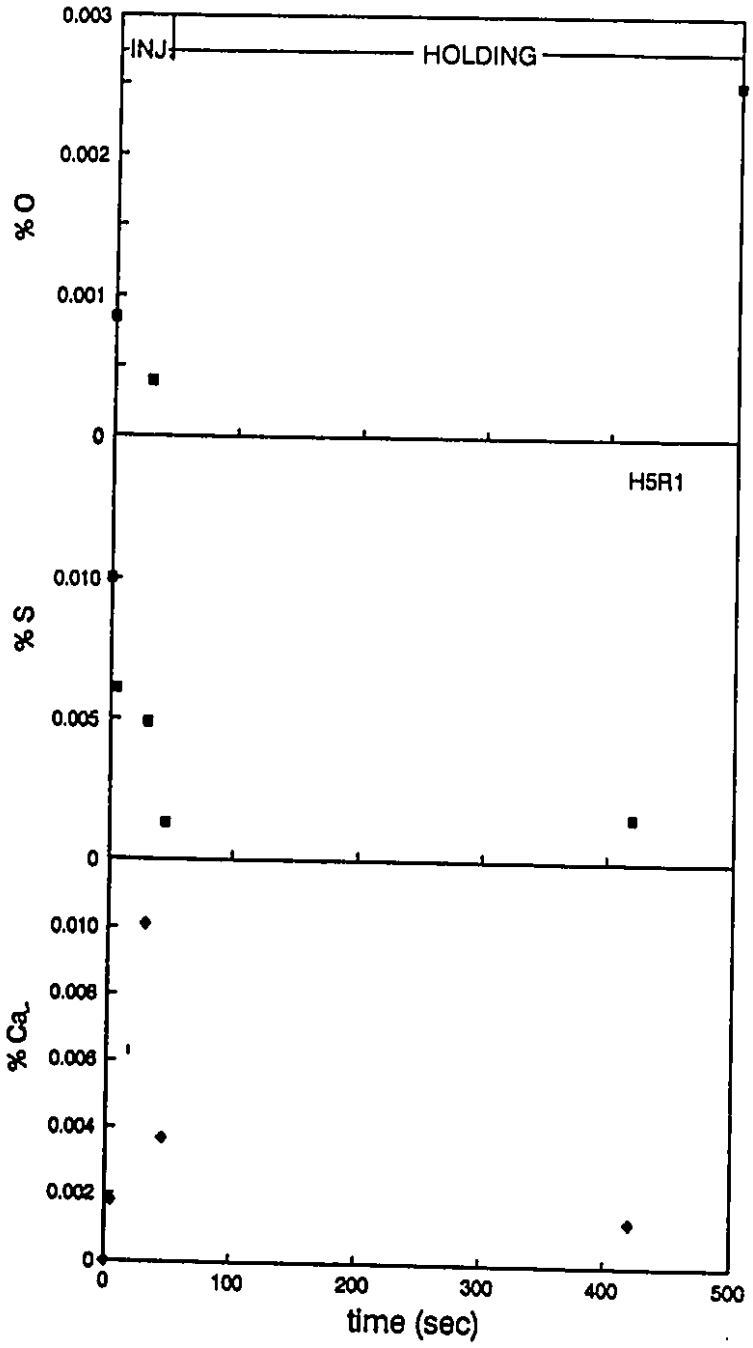

Figure A.3 Oxygen (dissolved), sulfur and calcium contents during and after injection in H5R1

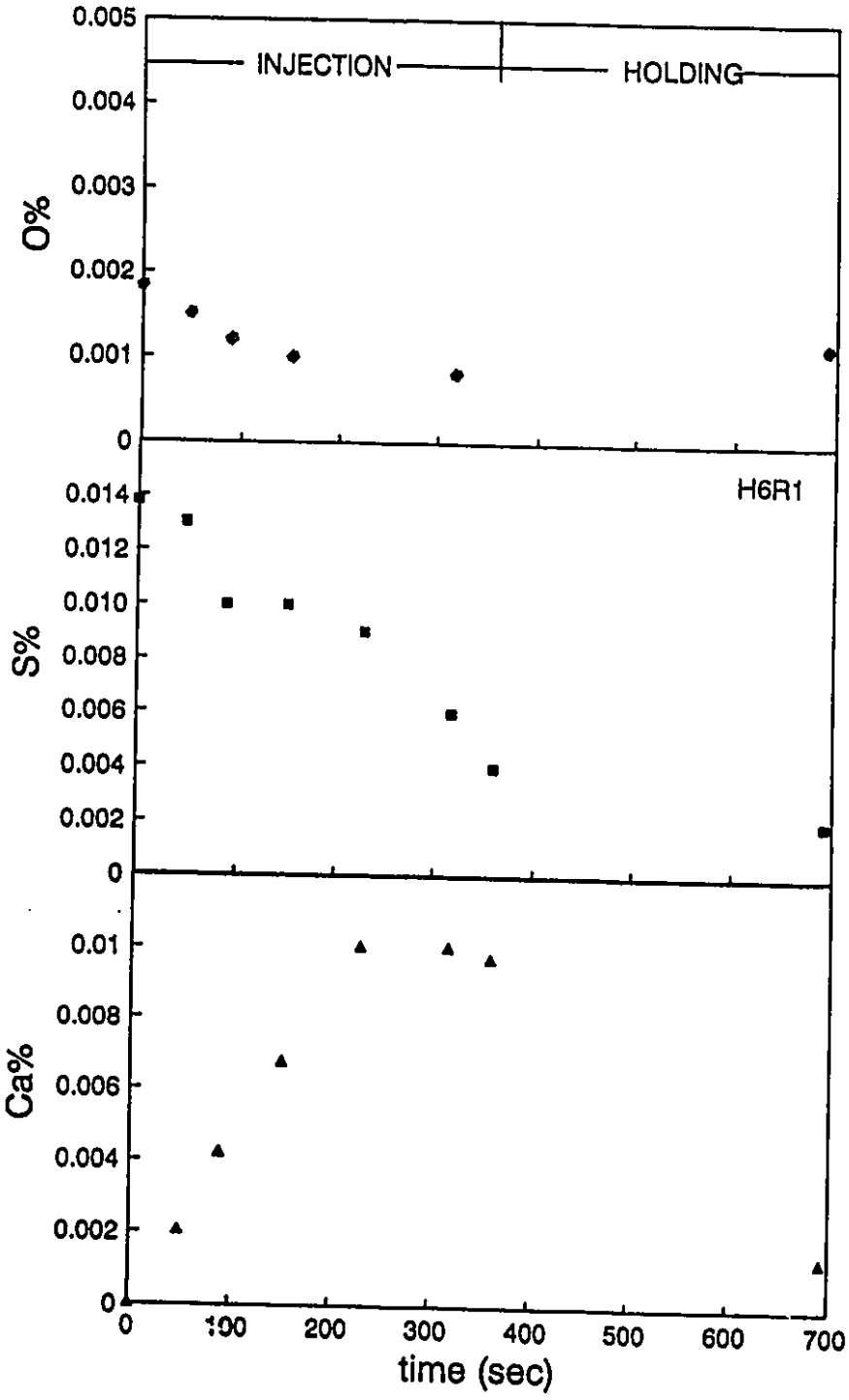

Figure A.4 Oxygen (dissolved), sulfur and calcium contents during and after injection in H6R1

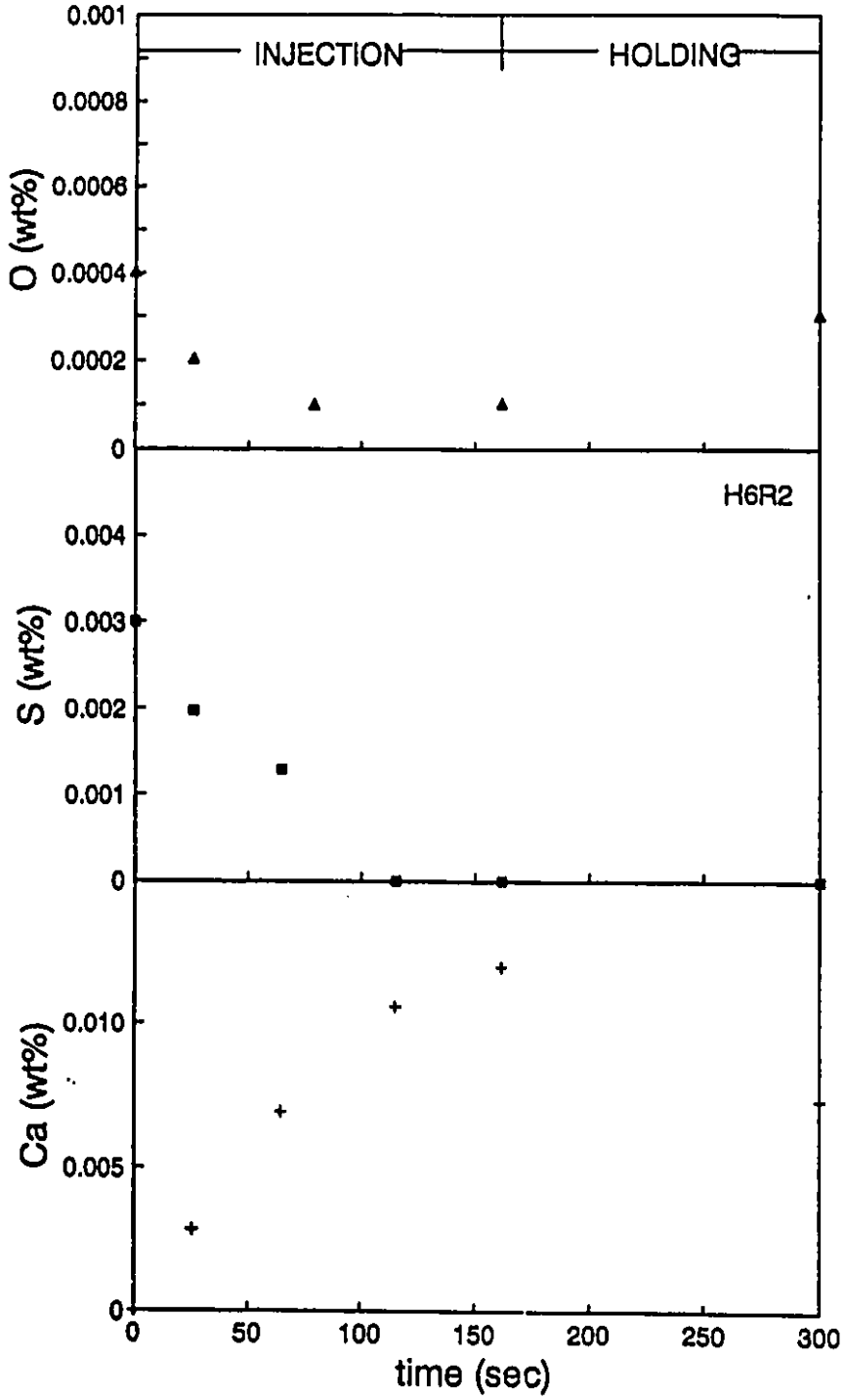

Figure A.5 Oxygen (dissolved), sulfur and calcium contents during and after injection in H6R2

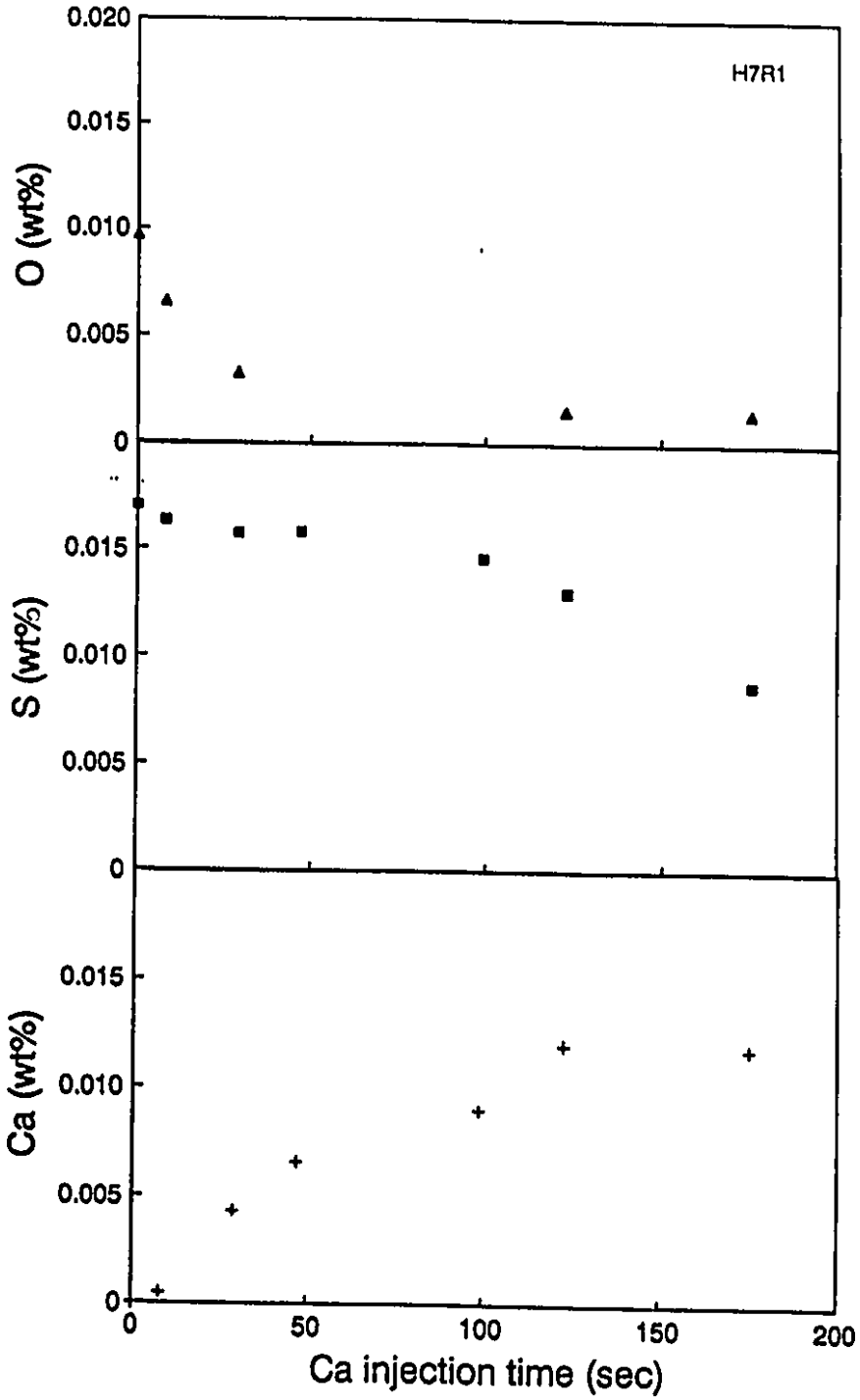

Figure A.6 Oxygen (dissolved), sulfur and calcium contents during injection in H7R1

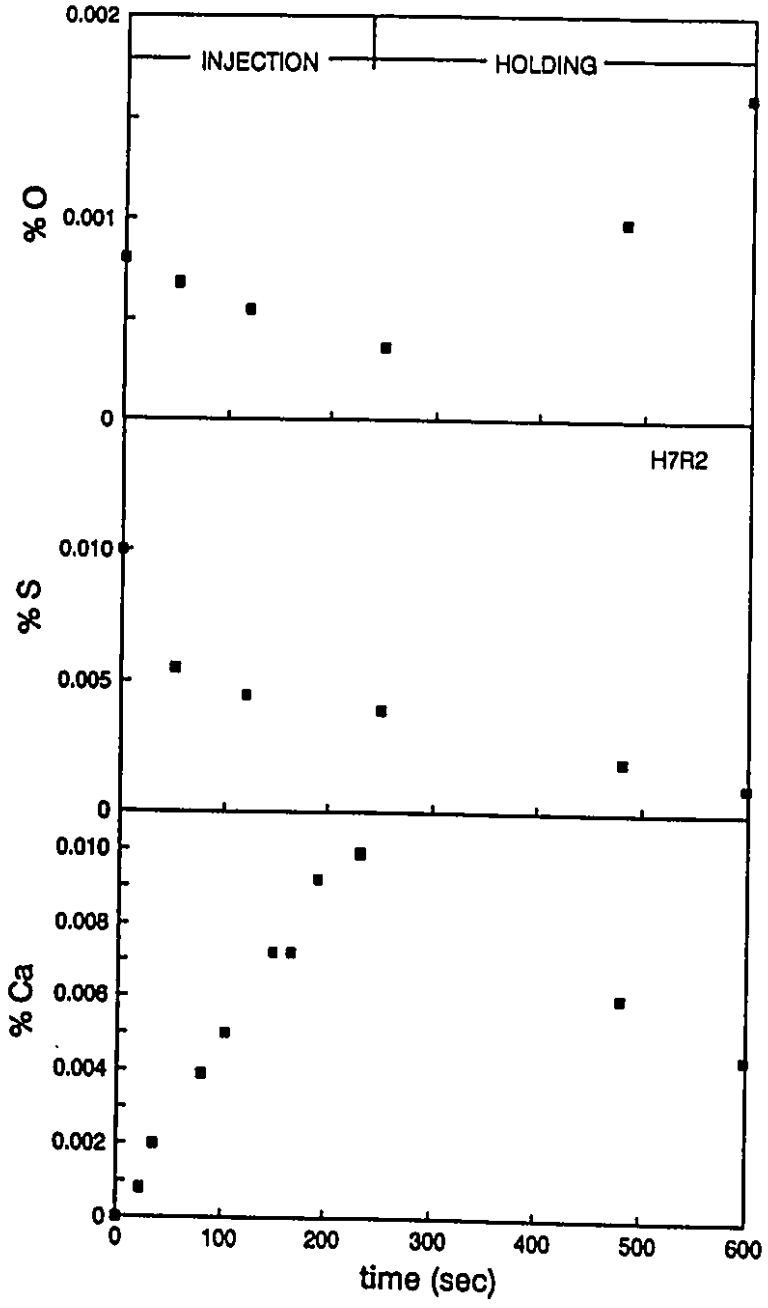

Figure A.7 Oxygen (dissolved), sulfur and calcium contents during and after injection in H7R2

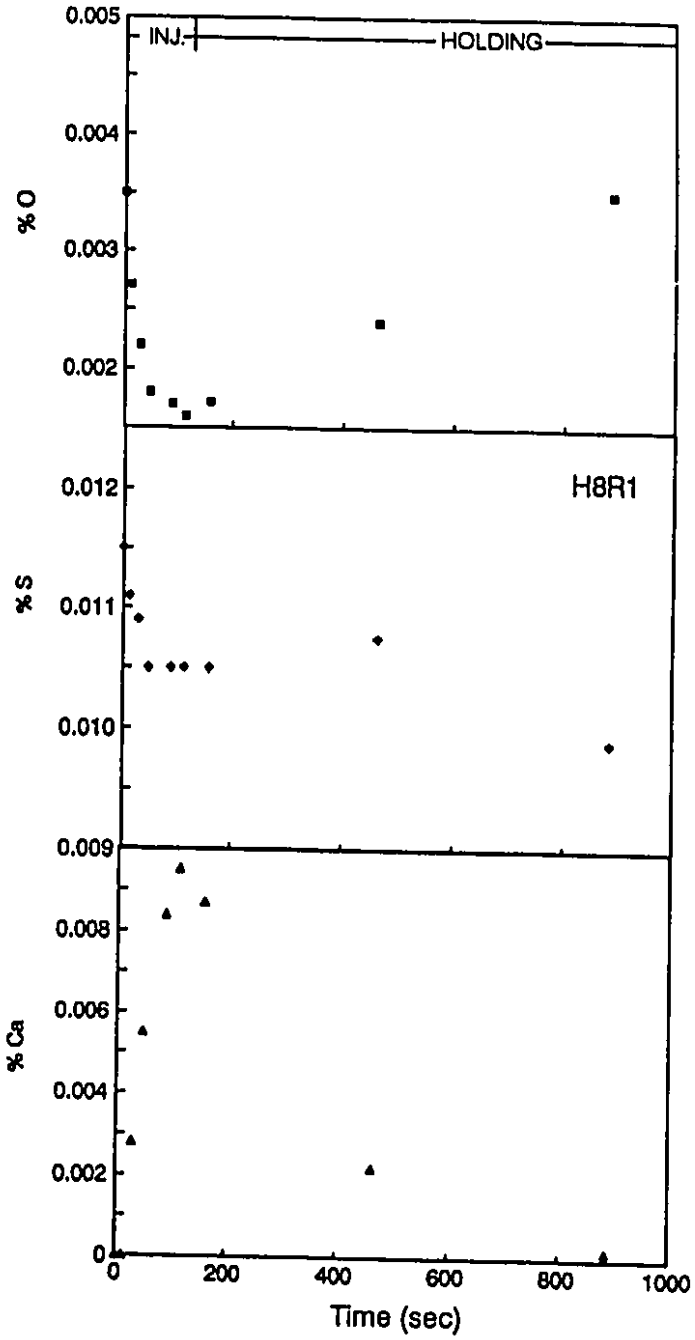

Figure A.8 Oxygen (dissolved), sulfur and calcium contents during and after injection in H8R1

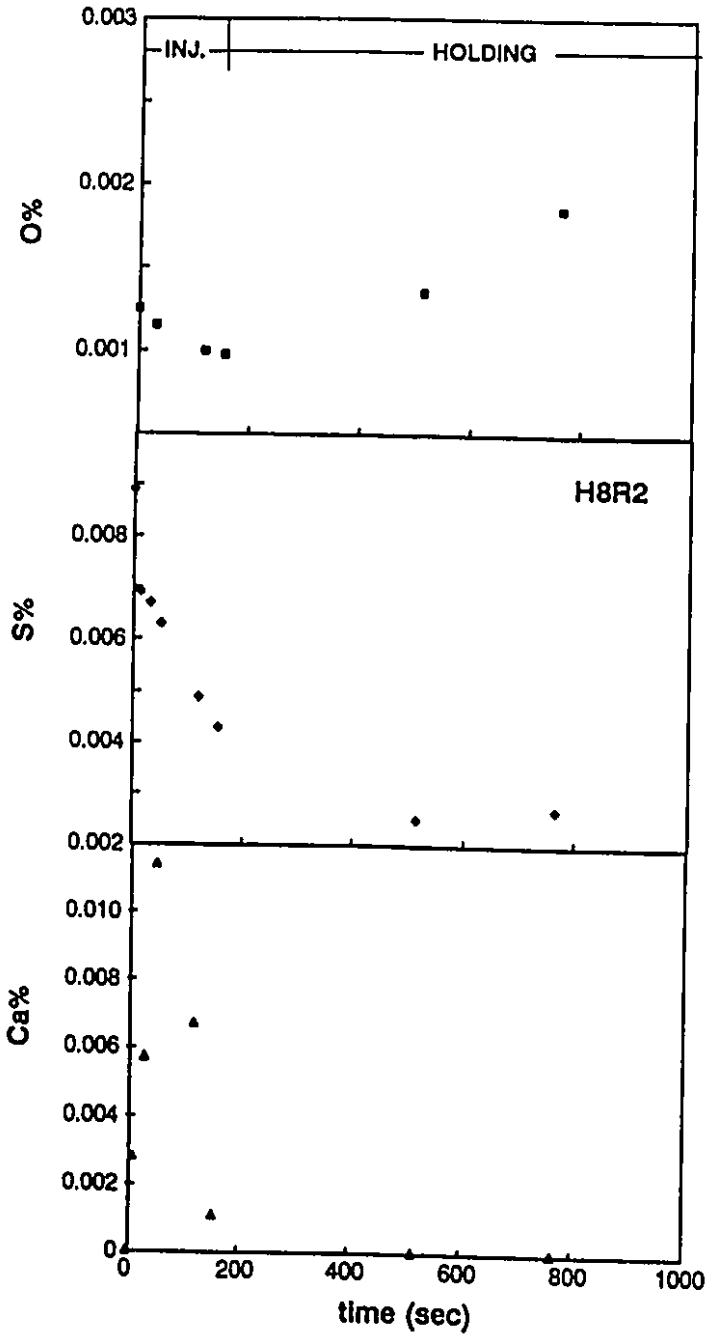

Figure A.9 Oxygen (dissolved), sulfur and calcium contents during and after injection in H8R2

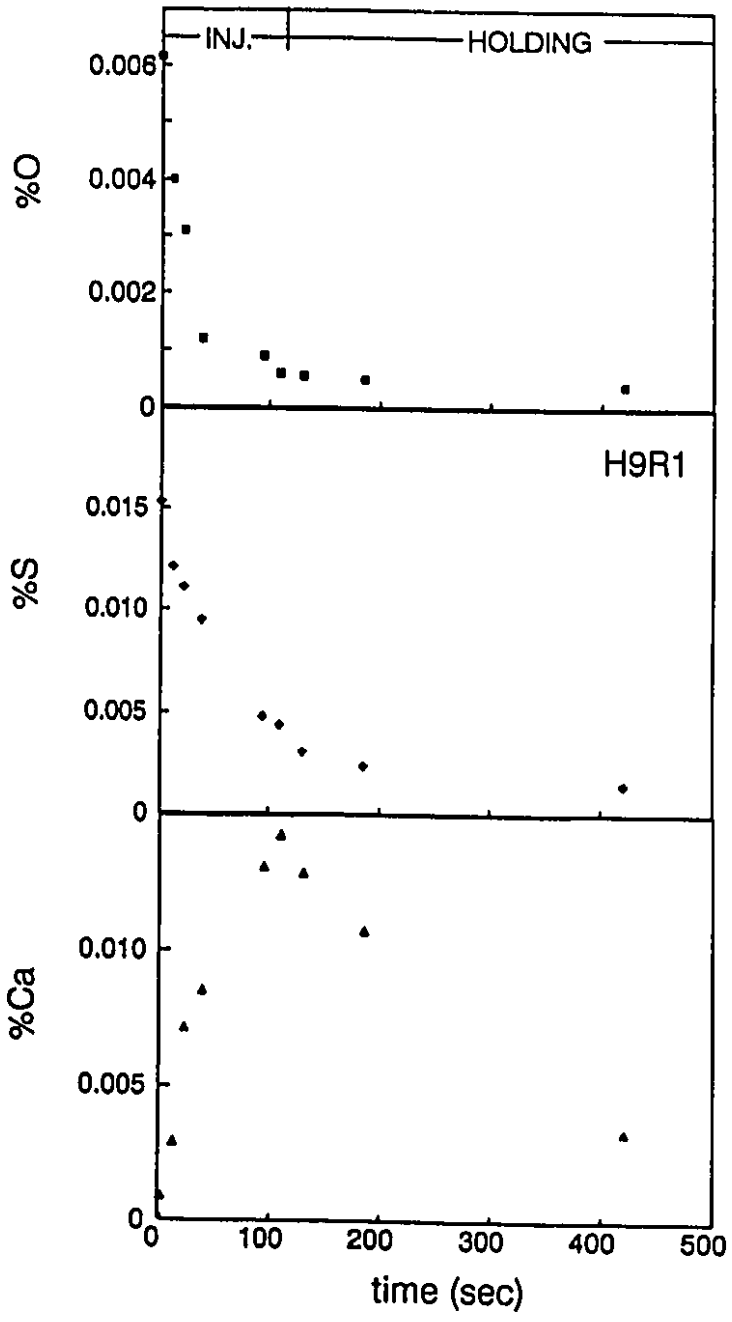

Figure A.10 Oxygen (dissolved), sulfur and calcium contents during and after injection in H9R1

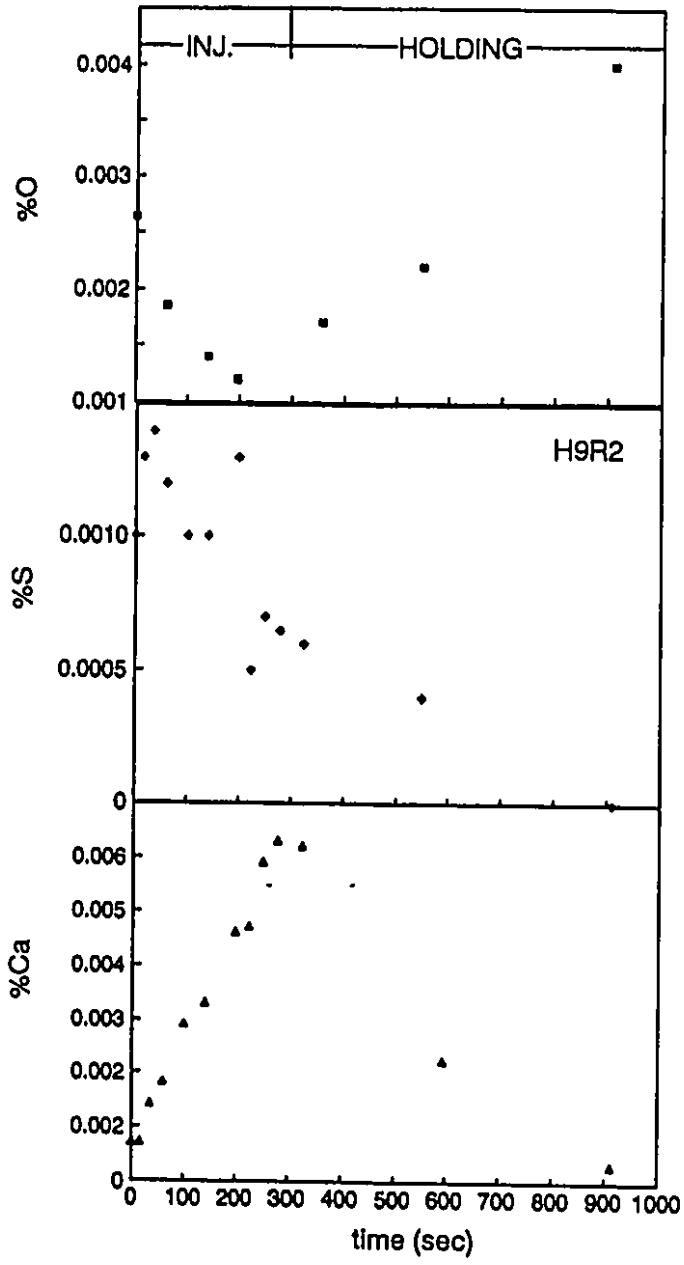

Figure A.11 Oxygen (dissolved), sulfur and calcium contents during and after injection in H9R2

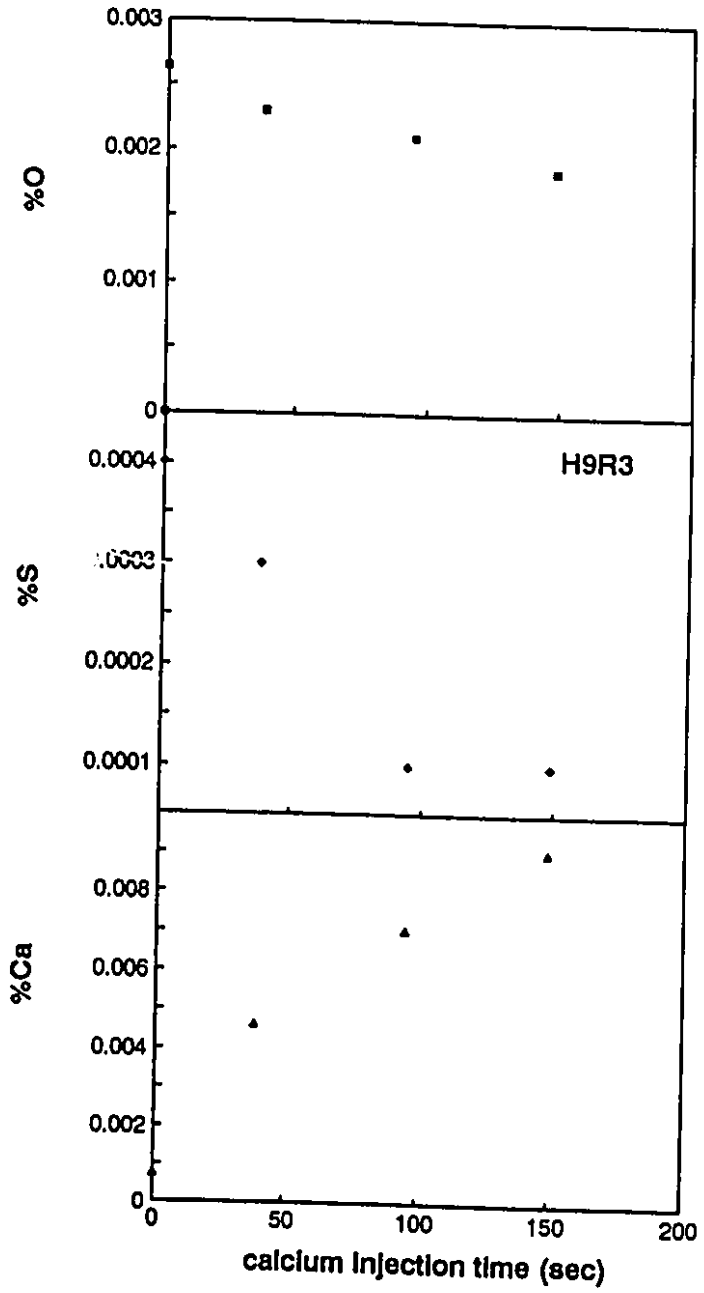

Figure A.12 Oxygen (dissolved), sulfur and calcium contents during injection in H9R3

INCLUSIONS DISTRIBUTION AND CHEMICAL ANALYSIS

TABLE A.1

STATISTICAL SUMMARY OF INCLUSIONS FROM A TYPICAL SAMPLE

Heat no. = H6R1, Sample no. = 11, X-Ray window file = MnSAlCa, Standards file = Mac, 20 Fields analyzed.

MEAN DIAMETER DISTRIBUTION (μm)		
BIN	RANGE (μm)	AREA%
1	0 to 0.5	0.0221
2	0.5 to 1.0	0.0301
3	1.0 to 1.5	0.0135
4	1.5 to 2.0	0.0119
5	2.0 to 2.5	0.0106
6	2.5 to 3.0	0.0104
7	3.0 to 3.5	0.0083
8	3.5 to 4.0	0.0000
9	4.0 to 4.5	0.0000
10	greater than 4.5	0.0000
Total		0.1068

CHEMICAL CLASSIFICATION:	
INCLUSION CLASS	AREA %
1: MnS	0.0053
2. CaS	0.0234
3. CaO	0.0212
4. Al2O3	0.0058
5. (Ca,Mn)S	0.0217
6. CAx	0.0014
7. CaS·CAx	0.0084
8. (Ca,Mn)S·CAx	0.0043
9. unclassified	0.0153
Total	0.1068

HISTOGRAM SUMMARY

CLASS	BIN NO. = 1	2	3	4	5	6	7	8	9	10
MnS	32	9	2	1	0	0	0	0	0	0
CaS	18	30	7	1	2	1	0	0	0	0
CaO	97	26	2	0	0	0	1	0	0	0
Al2O3	36	12	1	0	0	0	0	0	0	0
(Ca,Mn)S	19	22	2	3	1	2	0	0	0	0
CAx	6	6	0	0	0	0	0	0	0	0
CaS·CAx	5	4	3	2	1	0	0	0	0	0
(Ca,Mn)S·CAx	1	3	2	0	1	0	0	0	0	0
unclassified	94	22	1	0	0	0	0	0	0	0
Total	308	134	20	7	5	3	1	0	0	0

TABLE A.2

TYPICAL EDS ANALYSIS RESULTS OF AN INCLUSION

Inclusion ID: H7R2S4, Inc3 LIVE TIME (spec.) = 100

OPERATING PARAMETERS

ENERGY	RES	AREA
13.0	102.43	77642

TOTAL AREA = 297979

ELMT	APP. CONC	ERROR(WT%)
S	1.446	0.104
Mn	1.791	0.196
Ca	0.283	0.053
Al	1.109	0.074
Si	0.334	0.074

25.00 kv TILT = 45.00 ELEV = 0.00 AZIM = 45.00 COSINE=1.00

SPECTRUM

All elements analysed, normalised

ELM	ZAF	%ELM	ATOM.%
S K: 0	0.961	23.748	25.75
Mn K: 0	0.863	32.756	20.726
Ca K: 0	1.045	10.128	12.533
Al K: 0	0.609	28.730	37.017
Si K: 0	0.521	4.279	3.711
Mg K: 0	0.698	0.000	0.000
TOTAL		100.004	100.00

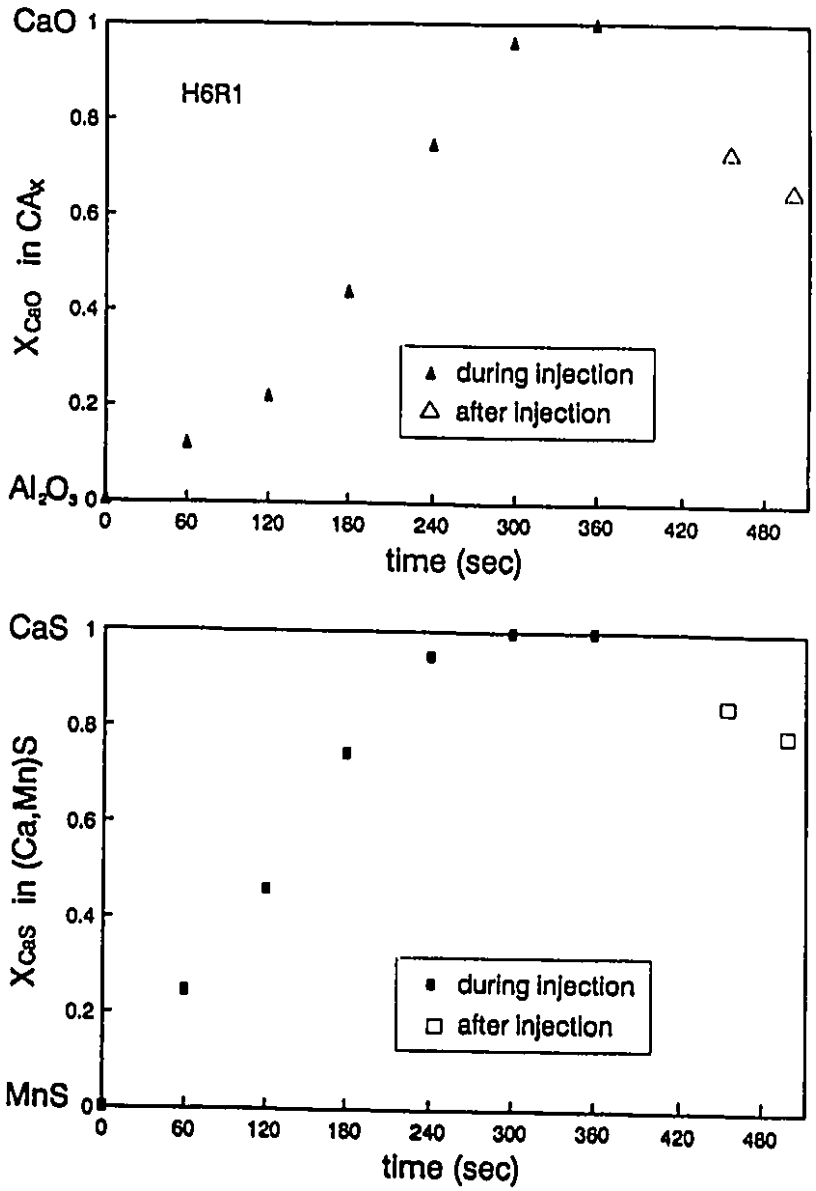

Figure A.13 The composition changes of oxide CA_x (TOP) and sulphide (Ca,Mn)S (BOTTOM) during and after calcium injection in H6R1

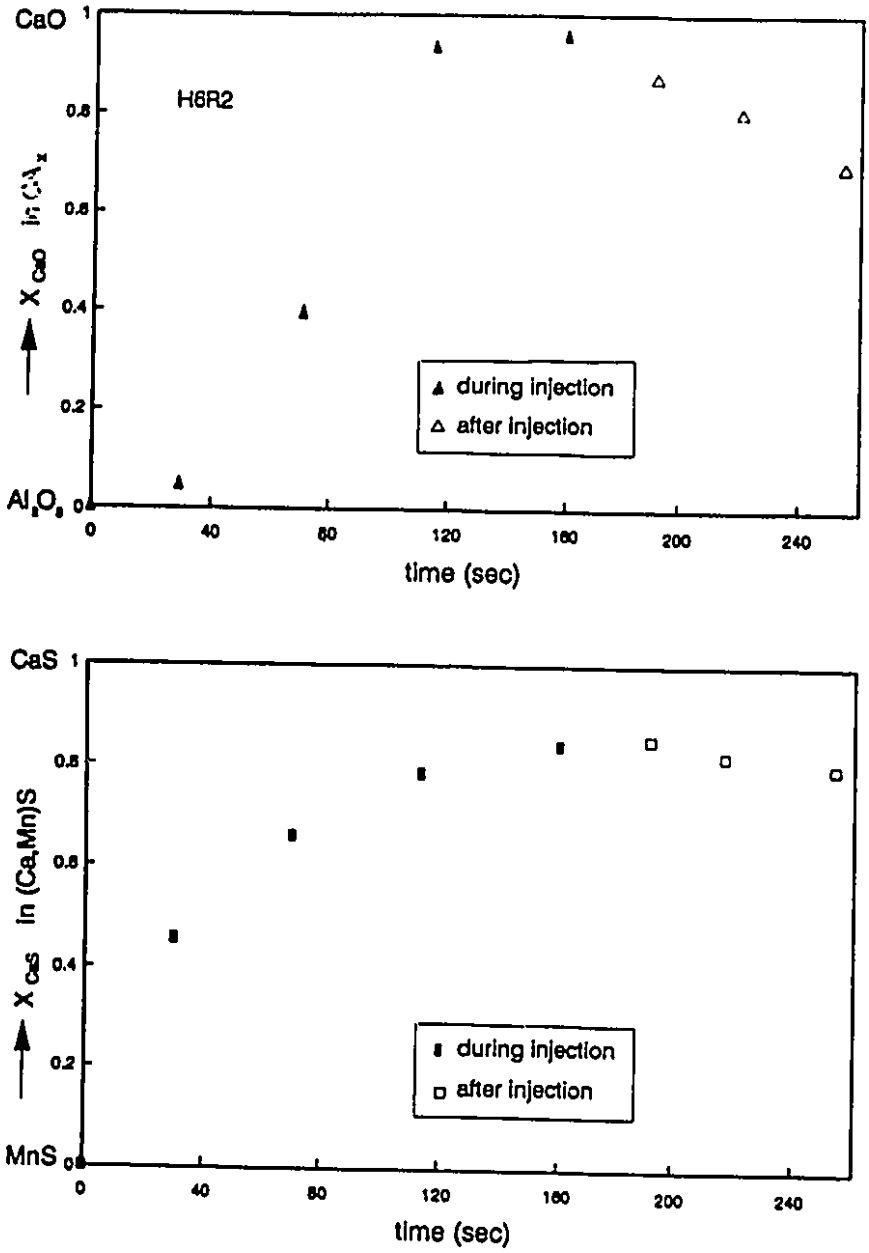

Figure A.14 The composition changes of oxide CA_x (TOP) and sulphide (Ca,Mn)S (BOTTOM) during and after calcium injection in H6R2

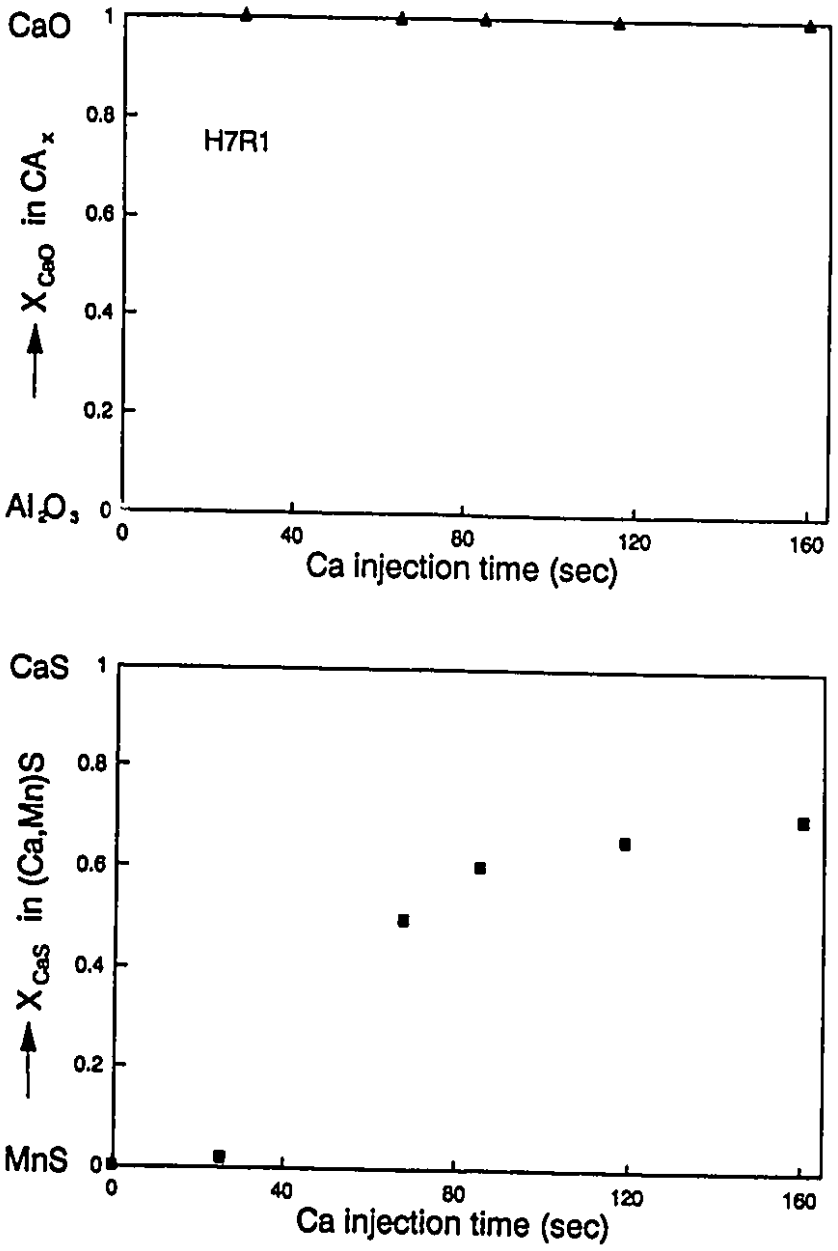

Figure A.15 The composition changes of oxide CA_x (TOP) and sulphide (Ca,Mn)S (BOTTOM) during calcium injection in H7R1

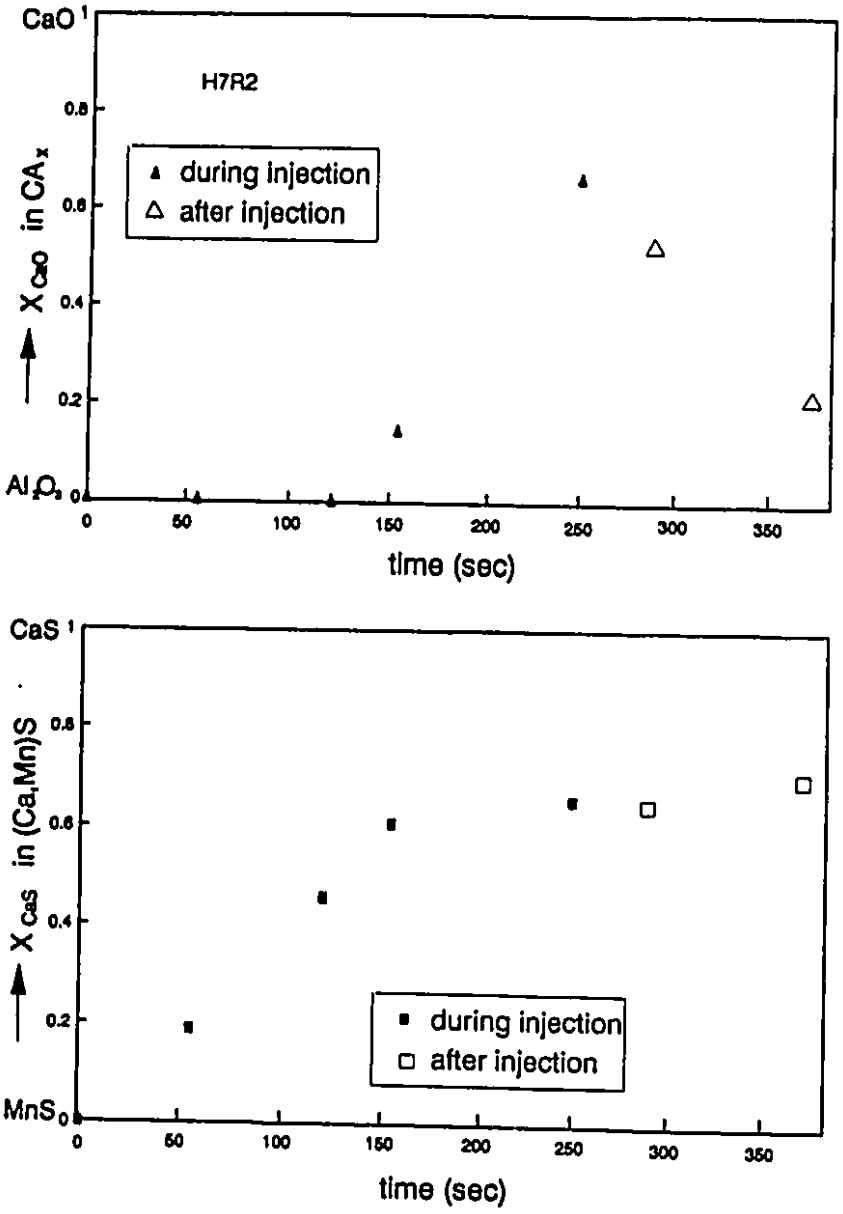

Figure A.16 The composition changes of oxide CA_x (TOP) and sulphide (Ca,Mn)S (BOTTOM) during and after calcium injection in H7R2

Appendix B

Estimation of D_{Ca}, D_S and D_O

APPENDIX B

Estimation of D_{Ca}, D_S and D_O

Estimation of D_{Ca}

As discussed in Chapter 2 Literature Review, Joyant and Gatellier [1] tried to measure the calcium diffusivity in the liquid Fe and Fe-Ni alloys, by using Machlin's theory [2] for alloy vaporization. Their results (Table 2.10) show that there is nearly two order of magnitude of difference in D_{Ca} between pure Fe and Fe-20%Ni. Although this may be explained by the different experimental systems, it is rather reasonable to consider that some errors in measuring the dissolved calcium in the melt account for this difference. Since most of calcium is tied up in the non-metallic inclusions, using total calcium in their experiments to estimate the calcium diffusivity from Machlin's theory [2] might create the errors.

However, there are several "Hydrodynamic" models available to predict the diffusivities of the solutes in liquid metals, such as those of Stokes-Einstein [3], Sutherland [4], Li and Chang [5], Eyring [6], Walls and Upthegrove [7]. None of these theories is capable of accurately predicting the diffusivities of light elements, such as carbon, oxygen, nitrogen and hydrogen, in liquid iron [8]. However, Irons [9] used the "hydrodynamic" models to predict the diffusivity of

magnesium in liquid iron which is a somewhat heavier element. Since calcium is heavier that magnesium, these models were therefore used here to predict the calcium diffusivity in liquid steel for the present experiments. The estimated results of D_{Ca} are shown in Table B.1.

Table B.1

Estimates of Calcium diffusivity in Liquid Iron at 1600^{0}C

Theory	Form of D_L	$D_{Ca} * 10^9$ (m^2/s)	Reference
Stokes-Einstein	$\frac{kT}{6\pi r\mu}$	2.03	3
Sutherland	$\frac{kT}{4\pi r\mu}$	3.05	4
Eyring	$\frac{kT}{2\delta r\mu}$	3.19	5
Li and Chang	$\frac{(\alpha-\beta)kT}{2\alpha(2r\mu)}$	3.19	6
Walls and Upthegrove	$\frac{kT}{2\pi r(2b+1)\mu}$	3.46	7

where D is the diffusivity of the solute, calcium, μ the viscosity of the solvent, k the Boltzmann constant, T the absolute temperature, and r the radius of the diffusing molecules. The most likely ionic radius for calcium, r_{Ca+2},

was taken as 0.99×10^{-10} m [10]. α and β are the number of closest nearest neighbours in all directions and in one plane, numerically 6 and 4, respectively, for simple cubic liquids [10]. δ is the number of nearest neighbours of the diffusing species, perpendicular to their plane of motion, six in this case [10]. The parameter, b, is the ratio of the solute ionic radius to the solvent interatomic space. This was estimated to be 0.38 on the basis of the atomic diameter of pure iron (δ) at 1550^0C being $2\ 56 \times 10^{-10}$ m [11]. The values for the diffusivity of calcium in liquid iron from Table B.1 are in the vicinity of 3×10^{-9} m^2/s and this will be used as the estimate.

Estimation of D_S

Kawai [12-13] used a diffusion couple technique to measure the sulfur diffusivity in which two cylindrical specimens, one containing sulfur and the other with negligible sulfur concentration, were joined together and held in a refractory capillary. After an experiment, the sample was quenched and the concentration distribution of the solute determined, and the sulfur diffusivity calculated. His experimental results of D_S for two different liquid iron mediums were shown in Table B.2.

Table B.2

Estimates of D_S in Liquid iron at 1600^{0}C [12-13]

Author(s)	$D_S * 10^9$ (m^2/s)	Medium	Reference
Kawai Y.	3.73	0.08-0.64%S in Fe-C	12
Kawai Y.	4.86	0.96-1.25%S in Fe	13
Average	4.3±0.57		

From Table B.2, the sulfur diffusivity in liquid steel for the present conditions was estimated as 4.3×10^{-9} m^2/s.

Estimation of D_O

Solar and Guthrie [15] tested several theoretical models for predicting the diffusivity of oxygen in liquid iron. They found that all models tested were incapable of doing that, and concluded that the major discrepancies between various theoretical predictions and experimental values for those systems may well be due to a lack of knowledge of the physical state of solutes in liquid metals. However, experimentally, the oxygen diffusivity has been measured very extensively. The diffusivity has been obtained in two different ways, namely, by capillary reservoir method [16-17], and by measurement of slag formation rate on rotating silica disk [18]. The typical measured results from different methods are listed in

Table B.3. The results from both methods seem to be in consistent, and D_0 is in the vicinity of 3.1 x 10^{-9} m^2/s.

Table B.3

Estimates of D_0 in liquid iron at 1600^{0}C

Author(s)	D_0 * 10^9 (m^2/s)	Method	Reference
Belton and McCarron	2.50	Capillary	16
Suzuki and Mori	2.96	Capillary	17
Shurygin and Krjuk	4.10	rotating disk	18
average	3.10		

REFERENCES

1. M. Joyant and C. Gatellier: IRSID Report, PCM-RE, 1108, Mai, 1984.
2. E.S. Machlin: Trans. AIME, Vol. 218, 1960, pp. 314-26.
3. R.B. Bird, W.E. Stewart and E.N. Lightfoot: Transport Phenomena, John Wiley and Sons, New York, 1966.
4. J.B. Edwards, E.E. Hucke and J.J. Martin: Metals Mater., 1968, Met. Rev. 120 (Part I and II).
5. J.C.M. Li and P. Chang: J. Chem. Phs., 23, No. 3, 1955, pp. 518-520.

6. H. Eyring, T. Ree, D.M. Grant and R.C. Hirst: Z. Eleketrochem., 64, 1960, pp. 146-152.

7. H.A. Walls and W.R. Upthegrove: Acta Met., 12, 1964, pp. 461-471.

8. M.Y. Solar and R.I.L. Guthrie: Met. Trans., 3, 1972. pp. 2007-9.

9. G.A. Irons: M. Sc. Thesis, McGill University, 1975.

10. Handbook of Physics and Chemistry, 51st edition, ed. R.C. Weast, Chemical Rubber Company, Cleveland, 1970.

11. W. Hume-Rothery: The Structure of Alloys in Iron, Permagon Press, London, 1966.

12. Y. Kawai: Sci. Repts. Res. Inst., Tohoku Uni. Ser. A9, 1957, pp. 520.

13. Y. Kawai: Sci. Repts. Res. Inst., Tohoku Uni. Ser. A9, 1957, pp. 78.

14. J.F. Elliot, M. Gleiser and V. Ramakrishna: Thermochemistry for Steelmaking, Vol. II, Addison-Wesley Publishing Company, New York, 1963.

15. M.Y. Solar and R.I.L. Guthrie: Met. Trans., 3, 1972, pp. 2007.

16. G.R. Belton and R.L. McCarron: Trans. Met. Soc. AIME, 245, 1969, pp. 1161.

17. K. Suzuki and K. Mori: Tetsu-to-Hagane, 57, 1971, pp. 2219.

18. P.M. Shurygin and V.I. Krjuk: Russ. Met. Mining., No. 3, 53, 1963, pp. 47.

Appendix C

Estimation of k_j, z_{CAx}, z_{CaS} and z_{CaO}

APPENDIX C

ESTIMATION OF k_i, z_{CaX}, z_{CaS} and z_{CaO}

The rate of precipitation on inclusions and the interfacial area per unit volume are needed to be known in order to integrate the differential Equations (6.52-72) in the model calculation.

Estimation of k_i

The rate of precipitation on inclusions in liquid steel should normally be diffusion-controlled, since rates of chemical reaction are very fast at high temperature. Consequently, the dimensionless mass transfer to a spherical inclusion particle should be given by the well-known Ranz-Marshall relation [1]:

$$Sh = \frac{k_i d_i}{D_L} = 2 + 0.6 Re^{1/2} Sc^{1/3} \qquad \text{(C.1)}$$

where k_i is the mass transfer rate coefficient, d_i the inclusion diameter, D_L the solute diffusivity in the melt, Re the Reynolds number and Sc the Schmidt number.

For micro-size inclusions, the terminal settling velocity is negligible [2]. So that the mass transfer coefficient is given by:

$$k_i = \frac{2D_L}{d_i} \qquad \text{(C.2)}$$

The smaller the inclusion size, the larger the mass transfer coefficient. For a average size of d_i = 1.35 μm, for calcium diffusion (D_{Ca} = 3 x 10^{-9} m/s) to the inclusion, the mass transfer coefficient k_i is 0.0044 m/s.

Estimation of z_{CA_x}, z_{CaS} and z_{CaO}

There are mainly three primary inclusions existed during injection, namely, CA_x, CaS and CaO. Each inclusion surface area per unit volume of steel is related to the inclusion size, d_i, the number of inclusions per unit volume, n_i, and the inclusion size distribution.

As we can see from our experimental results, the number of initial oxide inclusions per unit volume is relatively high and in the range of:

$$n_i = 10^{14} - 10^{15} \ no/m^3 \qquad \text{(C.3)}$$

From the size distribution of inclusions (Figure 5.38), most of the inclusions are very small and near 1.35 μm range.

The average volumetric diameter of the inclusions is [3]:

$$d_i^V = \frac{\pi}{2} d_i^a \qquad \text{(C.4)}$$

where d_i^a is the average area diameter of inclusions, which is from EDS inclusion analysis:

$$d_i^a = \frac{\sum_{j=1}^{N} n_i d_i}{\sum_{j=1}^{N} n_i} \qquad \text{(C.5)}$$

d_i^V varies from 1.2 to 1.5 μm for the present conditions (Figure 5.38). For a average of d_{iV} = 1.35 μm, the average inclusion interfacial area per unit volume would be:

$$\begin{aligned} z_i &= n_i \pi (d_i^V)^2 \\ &= (10^{14} \sim 10^{15}) \pi * ((1.35 * 10^{-6})^2 \\ &= 572.5 \sim 5725 \quad (m^2/m^3) \end{aligned} \qquad \text{(C.6)}$$

Calculation of z_{CA_x}

The interfacial area per unit volume of the initial oxide inclusions can also be calculated by mass balance.

Assuming the amount of CA_x is C_{CA_x} in mole/m^3, the number of oxide inclusions per unit volume will be:

$$n_{CA_x} = C_{CA_x} * \frac{M_{CA_x}}{\rho_{CA_x}} * \left(\frac{1}{\frac{1}{6}\pi d_{CA_x}^3} \right) \qquad \text{(C.7)}$$

where the average diameter d_{CA_x} is 1.35 μm and assumed as a constant, M_{CA_x} and ρ_{CA_x} are the molar weight and density of CA_x inclusion. Inputting Equation C.7 into Equation C.6, the interfacial oxide inclusion area per unit volume, z_{CA_x}, can then be calculated:

$$z_{CA_x} = \pi (d_{CA_x})^2 * \frac{M_{CA_x}}{\rho_{CA_x}} * C_{CA_x} \left(\frac{1}{\frac{1}{6}\pi d_{CA_x}^3} \right) \qquad \text{(C.8)}$$

Calculations of z_{CaS} and z_{CaO}

Similar principle can also be used to calculated the interfacial area per unit volume for CaS (z_{CaS}) and CaO (z_{CaO}) inclusions:

$$z_{CaS} = \pi (d_{CaS})^2 * \frac{M_{CaS}}{\rho_{CaS}} * C_{CaS} * \left(\frac{1}{\frac{1}{6}\pi d_{CaS}^3} \right) \qquad \text{(C.9)}$$

$$z_{CaO} = \pi (d_{CaO})^2 * \frac{M_{CaO}}{\rho_{CaO}} * C_{CaO} * \left(\frac{1}{\frac{1}{6}\pi d_{CaO}^3} \right) \qquad \text{(C.10)}$$

where M and ρ are the molar weight and density of inclusion CaS or CaO, C_{CaS} and C_{CaO} are the amount of CaS and CaO inclusions formed (in mole/m^3), and d_{CaO} and d_{CaS} are the average diameters for CaO and CaS inclusions. They are considered to be equal and constant (1.35 μm).

REFERENCES

1. W.E. Ranz and W.R. Marshall: Chem. Engng. Prog., 48, 1952, pp. 141-146, 173-180.
2. G.A. Irons and R.I.L. Guthrie: Can. Metall. Quart., Vol. 15, No. 4 ,1976, pp. 325-32.
3. E.E. Underwood: in Quantitative Microscopy, ed. R.T. de Hoff and F.N. Rhines, 1968, McGraw-Hill, New York, pp. 149.

Appendix D

Estimation of $k_e z_e$

APPENDIX D

Estimation of $k_e z_e$

The magnitude of $k_e z_e$ is determined by the liquid circulation pattern. In the induction furnace, the flow is in the shape of a single toroid, up-welling at the centre and going down at the sides [1].

On the basis of the similarity to the experimental conditions of Irons' work [1], the mean radical velocity of the melt surface (U) was estimated as 0.2 m/s.

The mass transfer coefficient from the free-surface, k_e, was estimated based on Machlin's model of an inductively-stirred bath [2].

$$k_e = 2\left(\frac{D_{Ca}U}{\pi R}\right)^{1/2} \qquad \text{(D.1)}$$

where

D_{Ca} = Ca diffusion coefficient (3×10^{-9} m^2/s from Appendix B)

R = crucible radius (0.09 m)

U = mean radial velocity of melt surface (0.2 m/s)

The interfacial area per unit volume, z_e, is simply the inverse of the bath depth (H), thus the rate constant for the

mass transfer to the free-surface is then:

$$
\begin{aligned}
k_e z_e &= \frac{k_e}{H} \\
&= 2\left(\frac{D_{Ca}U}{\pi R}\right)^{1/2}/H \\
&= 2\left(\frac{3*10^{-9}*0.2}{\pi*0.09}\right)^{1/2}/H \\
&= 0.000092/H
\end{aligned}
\qquad \text{(D.2)}
$$

For the average H = 0.18 m, k_e = 0.000092 m/s, the calculated average $k_e z_e$ equals to 5.05×10^{-4} s^{-1}.

REFERENCES

1. G.A. Irons and R.I.L. Guthrie: Can. Metall. Quart., Vol. 15, No. 4, 1976, pp. 325-32.
2. E.S. Machlin: Trans. AIME, Vol. 218, 1960, pp. 314-26.

Appendix E

Estimation of k_{sl} and z_{sl}

APPENDIX E

Estimation of k_{sl} and z_{sl}

For the slag desulphurization, the mass transfer rate of sulfur to the slag-metal interface, k_{sl}, is given as [1]:

$$k_{sl} = 2\left(\frac{D_S\, U}{\pi\, R}\right)^{1/2} \qquad \text{(E.1)}$$

where D_S is sulfur diffusion coefficient (4.1×10^{-9} m^2/s from Appendix B), R the crucible radius (0.09 m), and U the mean radical velocity of melt (0.2 m/s). So that k_{sl} is then equal to 0.00011 m/s calculated from the above equation.

Before injection, most of the free-surface was covered by the slag. However, when injection starts, the slag is immediately pushed to the side. From the video camera recording, the slag coverage at the moment of starting injection is almost same as that after injection, and it is about 20% coverage of total surface. So that it is assumed that the slag coverage is constant during and after injection, and then the slag-metal interfacial area per unit volume is:

$$z_{sl} = \frac{0.2}{H} \qquad \text{(E.2)}$$

So that the rate constant for the slag desulphurization at the slag-metal interface is then:

$$k_{sl} z_{sl} = \frac{0.000022}{H} \qquad \text{(E.3)}$$

REFERENCE

1. E.S. Machlin: Trans. AIME, Vol. 218, 1960, pp. 314-26.

Appendix F

Estimation of k_{ro} and z_{ro}

APPENDIX F

Estimation of k_{ro} and z_{ro}

Even though the present experiments were conducted under the argon atmosphere, there is still considerate reoxidation, which is seen from the increase of oxygen activity during the holding period. Reoxidation from the atmosphere and the refractory wall is a very complicated issue. Here some assumptions are made in order to estimate the rate of oxygen input into the melt:

1. The reoxidation is controlled by the oxygen diffusion in the liquid phase.
2. The interfacial equilibrium oxygen, C_{ro}, is constant during and after injection.

Then the reoxidation rate, r_{ro}, is given as:

$$r_{ro} = k_{ro} z_{ro} (C_{ro} - C_o) \qquad \textbf{(F.1)}$$

C_o is the bulk oxygen content, $k_{ro}z_{ro}$ is the mass transfer rate constant, and the mass transfer coefficient, k_{ro}, is calculated as k_e:

$$k_{ro} = 2\left(\frac{D_O\, U}{\pi\, R}\right)^{1/2} = 0.000094 \ \ m/s \qquad \textbf{(F.2)}$$

The free-surface exposed to the atmosphere, z_{ro}, is the total surface minus the surface by the slag (20% of total):

$$z_{ro} = \frac{0.8}{H} \tag{F.3}$$

So that the rate constant for reoxidation is

$$k_{ro}z_{ro} = \frac{0.000075}{H} \qquad (s^{-1}) \tag{F.4}$$

After injection, the dissolved oxygen (oxygen activity) increases with the holding time due to mainly reoxidation. From Equation F.1, the oxygen activity at holding time t, is then written as:

$$\ln \frac{C_O - C_{ro}}{C_O^0 - C_{ro}} = - k_{ro}z_{ro}t \tag{F.5}$$

where C_0^0 is the initial oxygen content at the time of stopping injection, C_{ro} is the hypothetical interfacial oxygen concentration.

Appendix G

Estimation of $k_{rm}z_{rm}$

APPENDIX G

Estimation of $k_{rm}z_{rm}$

A number of studies show that the concentration of oxide inclusions, or the oxygen content combined in the oxide, decreases with time down to a constant plateau value. This is found for various kinds of agitation, electromagnetic [1-3], mechanical [4], and gas purging [5-6].

This exponential relationship may be interpreted to mean that removal rates are proportional to oxygen concentration (concentration of inclusions) [1]:

$$\frac{dC_i}{dt} = - k_{rm}z_{rm}C_i \qquad \text{(G.1)}$$

or

$$C_i = C_i^0 \exp(-k_{rm}z_{rm}t) \qquad \text{(G.2)}$$

where C_i^0 and C_i are the inclusion concentration at initial state and time t, respectively. $k_{rm}z_{rm}$ is the rate constant for the inclusion removal.

The same first-order inclusion removal is also applied to the inclusions during and after calcium injection. Since most of calcium are in the form of inclusions, and the oxygen in the inclusions are hard to obtain, the total calcium is used in above equations to obtain the inclusion removal rate, $k_{rm}z_{rm}$, after injection:

$$\ln\frac{C_{Ca}}{C_{Ca}^{0}} = - k_{rm}z_{rm}t \qquad \text{(G.3)}$$

where C_{Ca}^{0} and C_{Ca} are the total calcium content at the point at which injection was terminated and at the holding time, t, respectively. After inserting this equation to the experimental data (Figure 5.10), $k_{rm}z_{rm}$ is evaluated and $k_{rm}z_{rm} = K_2'$ as shown in Figure 5.9. Its numerical value ranges from 0.000018 ± 0.000001 to 0.00003 ± 0.000002 s^{-1}.

REFERENCES

1. T.A. Engh and N. Lindskog: Scand. J. Metallurgy, 4, 1975, pp. 49-58.
2. K. Torssell: Trans. Iron Steel Inst. Japan, 8, 1968, pp. 203-219.
3. Y. Sundberg: ASEA J., 44, 1971, pp. 71-80.
4. R. Ando and T. Fukushima: Proc. ICSTIS, Suppl. Trans. Iron Steel Inst. Japan, 11, 1971, pp. 179-183.
5. K.W. Lange, K. Okohira, D. Papamantellos and H. Schenck: Arch. Eisenhüttenw, 42, 1971, pp. 1-4.
6. U. Lindberg and K. Torssell: Trans. Met. Soc. AIME, Vol. 242, 1968, pp. 94-102.

Appendix H

Calculation of CaS and MnS activities

APPENDIX H

CALCULATION OF CaS and MnS ACTIVITIES

The following calculation was taken from a recent publication [1].

INTRODUCTION

Sulphide inclusions with varying amounts of Mn and Ca in solid solution have been observed in different grades of calcium treated steel [2-6]. These (Ca,Mn)S inclusions may exist as a single phase inclusion, however they usually occur surrounding calcium aluminate inclusions. Church et al [7] were among the early ones to find (Ca,Mn)S inclusions in vacuum-degassed, bearing steel. Salter and Pickering [8] reported an extensive solid solubility range in the ternary system: MnS, CaS, and FeS, containing up to 19% MnS and 4% FeS in CaS. A continuous series of solid solution was not found, so they concluded that there is a miscibility gap in the system. Kiessling and Westman [9] obtained the approximate extent of the miscibility gap. This gap was also observed by Skinner and Luce [10] in solid solutions of (Ca,Mg,Mn,Fe)S. It was Leung and van Vlack [11] who constructed a complete phase diagram for the CaS-MnS binary system, shown in Figure H.1 (or Figure 2.15), among other chalcogenide systems.

During calcium injection, the activities of CaO and CaS will increase simultaneously, as both deoxidation and desulphurization reactions progress. In order to correctly interpret the data in Figures 5.51 and 5.46, the activities of CaO and CaS must be evaluated at various compositions. CaO activities in the calcium aluminate system have been previously evaluated [2,12], however CaS activities in the CaS-MnS system have not been reported to the best of our knowledge. In fact, most thermodynamic calculations for the Al_2O_3 modification by calcium have been based on the assumption that the oxide phase was saturated with CaS, i.e. a_{CaS} is unity. This assumption may be partially responsible for the large discrepancy between thermodynamic predictions and the experimental results for oxide and sulphide modification [13-15]. Furthermore, there has been no adequate explanation for the conditions under which a solid (Ca,Mn)S phase will form to clog continuous casting nozzles [16-18]. In order to further our understanding of these important problems, the activities of CaS and MnS at different compositions are required.

CALCULATIONS OF CaS AND MnS ACTIVITIES

As a first order approximation, for systems with miscibility gaps in the solid phase, a regular solution model for the solid solution and an ideal one for the liquid phase are usually employed to calculate activities [19-20]. These

assumptions are proposed for the following calculations for the CaS-MnS phase diagram in Figure H.1.

Binary Solid Sulphide Solutions

For a binary regular solution, the enthalpy change on mixing is represented by:

$$\Delta H_{mix} = \Omega X_{CaS} X_{MnS} \qquad \text{(H.1)}$$

where Ω is a constant, given by:

$$\Omega = 2RT_c \qquad \text{(H.2)}$$

T_c is the critical temperature for the miscibility gap, which is taken to be 1130°C from Figure H.1.

The entropy change in a regular solution is assumed to be the same as that in an ideal solution, thus the Gibbs Free Energy change on mixing is:

$$\Delta G_{mix} = \Omega X_{CaS} X_{MnS} + RT(X_{CaS} ln X_{CaS} + X_{MnS} ln X_{MnS}) \qquad \text{(H.3)}$$

in which the activities of CaS and MnS are defined in the following equations:

$$\ln\left(\frac{a_{CaS}}{X_{CaS}}\right) = \frac{\Omega}{RT}(1-X_{CaS})^2 \qquad \text{(H.4)}$$

$$\ln\left(\frac{a_{MnS}}{X_{MnS}}\right) = \frac{\Omega}{RT}(1-X_{MnS})^2 \qquad \text{(H.5)}$$

Equations H.4 and H.5 are used to calculate the activities of CaS and MnS in their solid solutions at the steelmaking temperatures.

Liquid Sulphide Solutions

In the previous section, the stable pure solids were used as the standard states, consequently, activities in the liquid solution must be related to the same standard states for comparison and consistency. The pure solids are stable at all temperatures relevant to steelmaking, consequently, the activities of components in the ideal liquid solution with respect to hypothetic solid standard states may be expressed as:

$$a_{CaS}^{(l)} = X_{CaS}^{(l)} \exp\left[\frac{\Delta G_{m(CaS)}}{RT}\right] \qquad \text{(H.6)}$$

where $\Delta G_{m(Cas)}$ is the free energy of fusion for pure CaS.

For an ideal solution:

$$\Delta G_{m(CaS)} = \Delta H_{m(CaS)}\left[\frac{T_{m(CaS)}-T}{T_{m(CaS)}}\right] \qquad \text{(H.7)}$$

where $\Delta H_{m(CaS)}$ is the heat of melting of CaS at its melting point, $T_{m(CaS)}$. Its value has not been measured, nevertheless, it may be estimated for the ideal liquid solution using Kracek's [19,21] method based on:

$$\log X_{CaS(liq)} = -\frac{\Delta H_{m(CaS)}}{2.303R}\left(\frac{T_{m(CaS)}-T_{liq}}{T_{m(CaS)}T_{liq}}\right) \qquad \text{(H.8)}$$

where $X_{CaS(liq)}$ is the mole fraction of CaS on the binary liquidus at a temperature T_{liq}, near the melting point of CaS. Thus, a plot of the bracketed term against log $X_{CaS(liq)}$ should yield a straight line with a slope of $-\Delta H_{m(CaS)}/2.303R$. As can be seen in Figure H.2, such an approach appears to be valid for $X_{CaS(liq)}$ less than 0.5. In this range, the estimated value of $\Delta H_{m(CaS)}$ is 35500 $\pm$ 4200 J/mole. In Figure H.2, the solid line and the points are calculated from the measured liquidus line and points from Figure H.1. The dashed line is calculated from the extension of the measured liquidus to the melting point of CaS.

Combining Equations (H.7) and (H.8), one arrives at an expression for the activity of CaS in liquid solutions with respect to the hypothetic solid Raoultian standard state:

$$a_{CaS}^{(l)} = X_{CaS}^{(l)} \exp\left[\frac{\Delta H_{m(CaS)}}{R}\left(\frac{T_{m(CaS)}-T}{T_{m(CaS)}T}\right)\right] \qquad \text{(H.9)}$$

An identical expression applies for MnS, but in this case $\Delta H_{m(MnS)}$ has been measured at the melting point; it is 26100 J/mole [12].

CALCULATED RESULTS AND DISCUSSION

The calculations for CaS-MnS activities were performed at three temperatures relevant to steelmaking: 1500, 1550 and 1600°C, and are summarized in Figures H.3 to H.5, respectively. At 1500°C, only a solid solution exists, as shown in Figure H.3. There are moderately large positive deviations from ideality which may be attributed to differences in the lattice parameters for CaS and MnS: 0.5683 and 0.5226 nm,respectively.

For temperatures at which solid and liquid co-exist, the results of the calculations are shown in Figures H.4 and H.5. The activities of CaS and MnS in the solid solution are shown by the solid lines which were computed according to the regular model, while the activities in liquid solution are represented by the dashed lines, based on the ideal model. (Here the liquid solution uses the hypothetic solid state as the standard state). It should be noted that there is reasonably good agreement between the independently computed solid and liquid activity curves at the liquidus composition. This demonstrates that the independent activity calculations

for the solid and liquid solutions are compatible. It also provides confidence in the extension of the liquidus to the melting point of pure solid CaS in Figures H.1 and H.2, required for the estimation of $\Delta H_{m(CaS)}$.

These calculated CaS-MnS activities may provide the guidelines for understanding the interactions between oxide and sulphide inclusions during their simultaneous modifications by calcium injection, and thereby provide metallurgists with a more complete tool for control of the process of calcium injection into steel. A procedure for using these activities, in conjunction with existing oxide activity data [2,12], is illustrated in Chapter 6.

NOMENCLATURE

a	activity in solid solution based on pure solid as
the	standard state
$a^{(l)}$	activity in liquid solution based on pure solid as
the	standard state
ASA	Acid soluble aluminum
Ca	dissolved calcium
f_s	sulphur activity coefficient
ΔG_m	ΔG of melting of pure compound
ΔG_{mix}	the Gibbs free energy change on mixing (J/mole)
ΔH_m	Heat of melting at the melting point (J/mole)

ΔH_{mix}	the internal energy of mixing (J/mole)
h	activity based on 1 wt% as the standard state
h_{Ca}^{Sat}	calcium activity at its solubility
$\underline{O}$	dissolved oxygen
R	gas constant
$\underline{S}$	dissolved sulphur
T	temperature (K)
T_c	the critical temperature at the miscibility gap (K)
T_m	the melting point (K)
T_{liq}	the liquidus temperature (K)
X	molar fraction in solid solution
$X^{(l)}$	molar fraction in liquid solution
(CaO)	CaO component in calcium aluminate
(CaS)	CaS component in (Ca,Mn)S inclusion
X_{liq}	molar fraction on the liquidus
Ω	constant defined by Equation (H.2)

LIST OF FIGURES

solid lines, while liquid solutions are with dotted lines. Note that there is good agreement between the solid and liquid activities at the liquidus compositions.

H.5 Calculated activities of calcium sulphide and manganese sulphide at 1600°C. Solid solutions are indicated with solid lines, while liquid solutions are with dotted lines. Note that there is good agreement between the solid and liquid activities at the liquidus compositions.

REFERENCES

1. D.-Z. Lu, G.A. Irons and W.-K. Lu: Ironmaking & Steelmaking,
1. D. A. R. Kay and S. V. Subramanian: Second International Symposium in Effects and Controls of Inclusions and Residuals in Steel, CIM, 1986, pp. I:25-43.
2. S. Y. Kitamura, K. Miyamura and I. Fukuoka: ISIJ, **27**, 1987, pp. 344-350.
3. B. Mintz, Z. Mohamed and R. Abu-shosha: Materials Science and Technology, **5**, 1989, pp. 682-686.
4. T. Takenouchi and K. Suzuki: Tetsu to Hagane, **63**, 1977, pp. 1653.
5. A. Nordgren and A. Melander: Materials Science and Technology, **5**, Sept. 1989, pp. 940-951.
6. H. Nashiwa, A. Mori, S. Ura, T. Ikeda, H. Matsuno and R.

Ishikawa: ISIJ, **25**, 1977, pp. 81.

7. C. P. Church, T. M. Krebs and J. P. Rowe: J. of Metals, **18**, 1966, pp. 62-68.
8. W. J. M. Salter and F. R. Pickering: J. of Iron & Steel Institute, **207**, 1969, pp. 992-1002.
9. R. Kiessling and C. Westman: J. of Iron & Steel Institute, **208**, 1970, pp. 699-700.
10. B. J. Skinner and F. D. Luce: American Mineralogist, **56**, 1971, pp. 1269-1298.
11. C. H. Leung and L. H. Van Vlack: J. of American Ceramic Soc., **62**, 1979, pp. 613-616.
12. J. F. Elliot and M. Gleiser: Thermochemistry for Steelmaking, 1960, Addison-Wesley Publishing Company.
13. H. M. Pielet and D. Bhattacharya: Metall. Trans., **15B**, 1984, pp. 547-562.
14. L. Holappa and H. Ylonen: Scaninject III Conference, Lulea, (Sweden), 1985, pp. 47:1-23.
15. G. J. W. Kor: International Calcium Treatment Symposium, 1988, the Institute of Metals, pp. 5:1-17.
16. A. Ishii, A. Ishikawa and Y. Nakamura: Interceram, 1987, pp. 70-74.
17. I. G. Davies and P. C. Morgan: Ironmaking & Steelmaking, **2**, 1985, pp. 176-184.
18. K. J. Handerhan, W. C. Beringer and A. V. Hinkel: Iron and Steel Maker, Dec. 1989, pp. 41-52.
19. D. R. Gaskell: Introduction to Metallurgical

Thermodynamics, 1981, McGraw-Hill book company.

20. D. A. Porter and K. E. Easterling: Phase Transformations in Metals and Alloys, 1987, Van Nostrand Reinhold (UK).

21. F. C. Kracek: J. of American Chem. Soc., **52**, 1930, pp. 1436-1442.

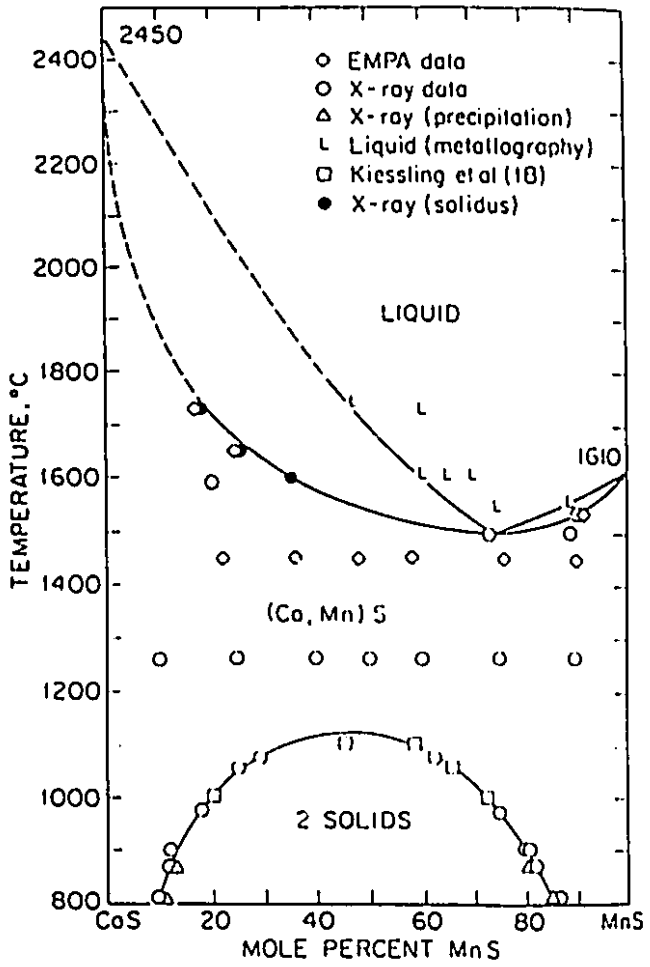

Figure H.1 The CaS-MnS phase diagram [H11].

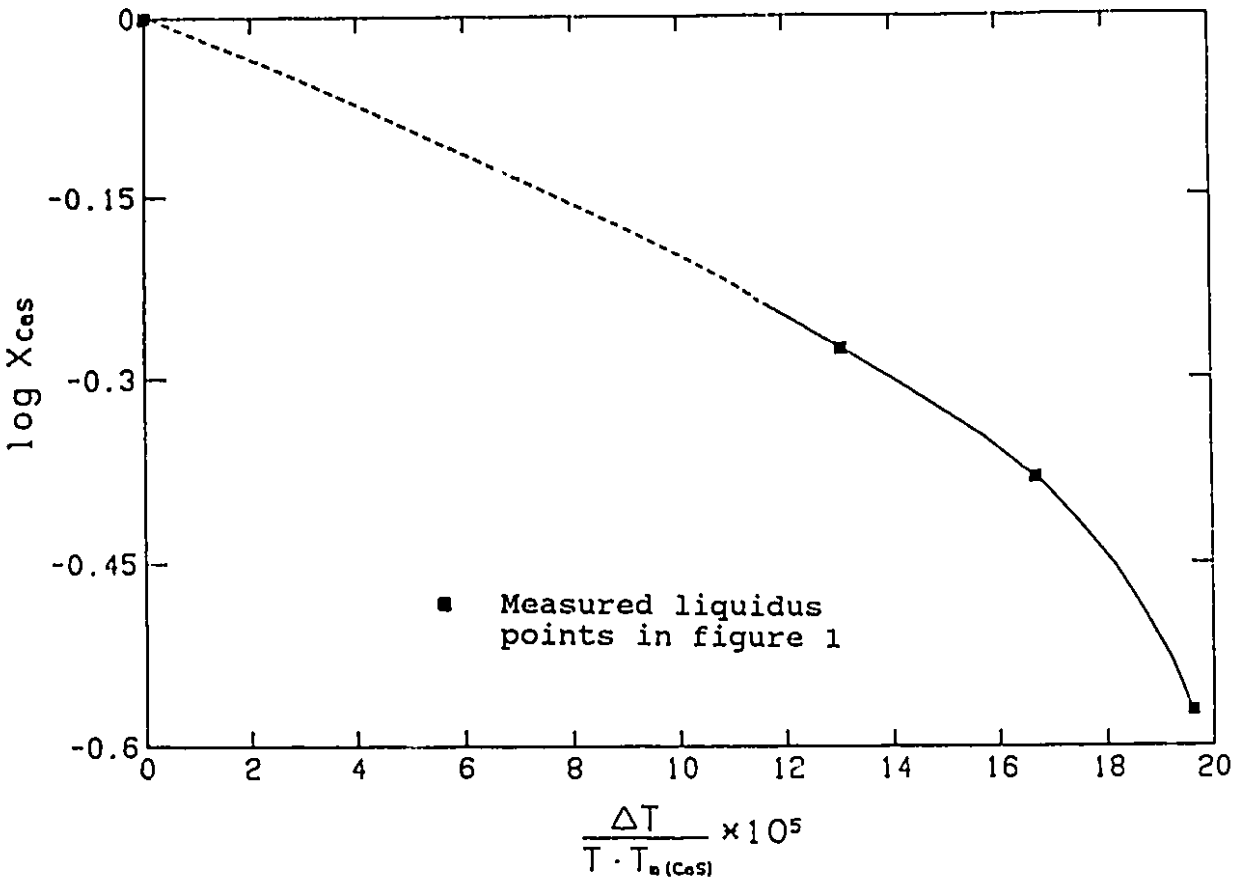

Figure H.2 A plot of log X_{CaS} against $\Delta T/(T.T_{m(CaS)})$, according to Kracek's method [22]

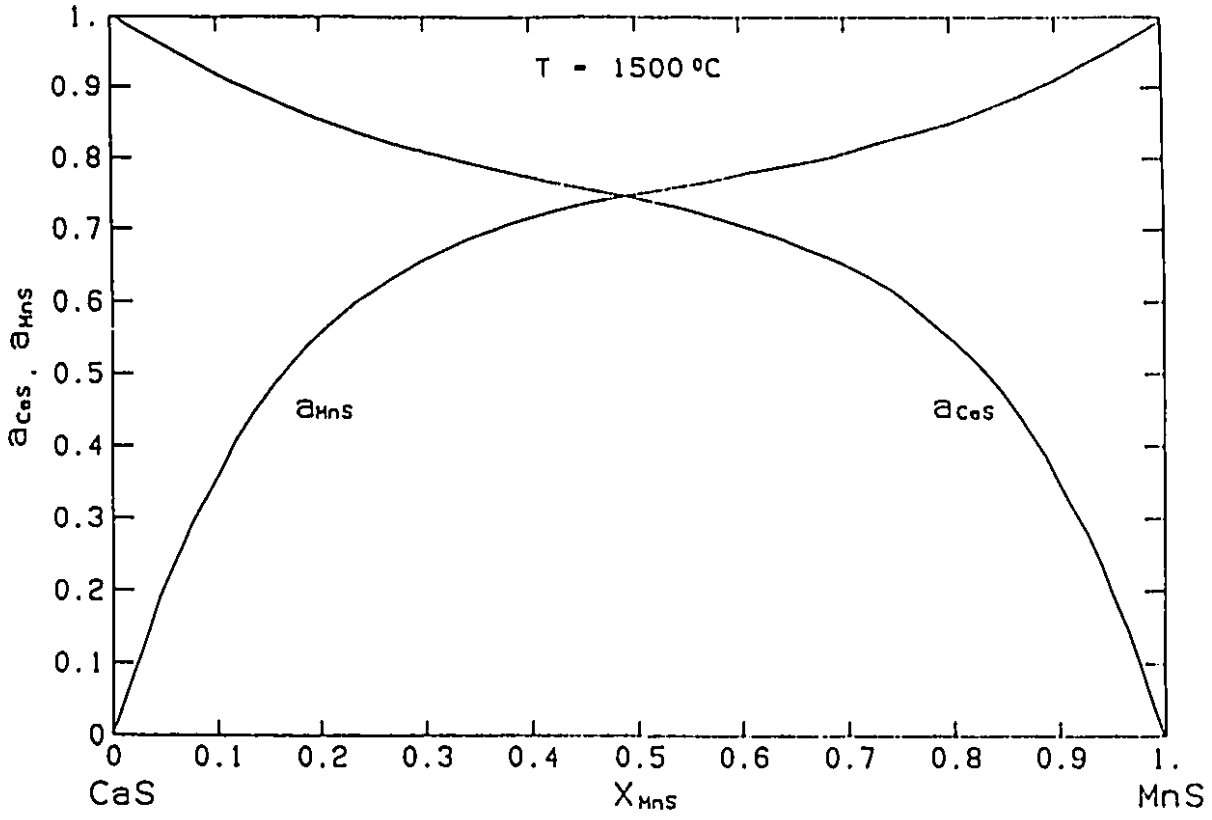

Figure H.3 Calculated activities of calcium sulphide and manganese sulphide at 1500 ^{0}C

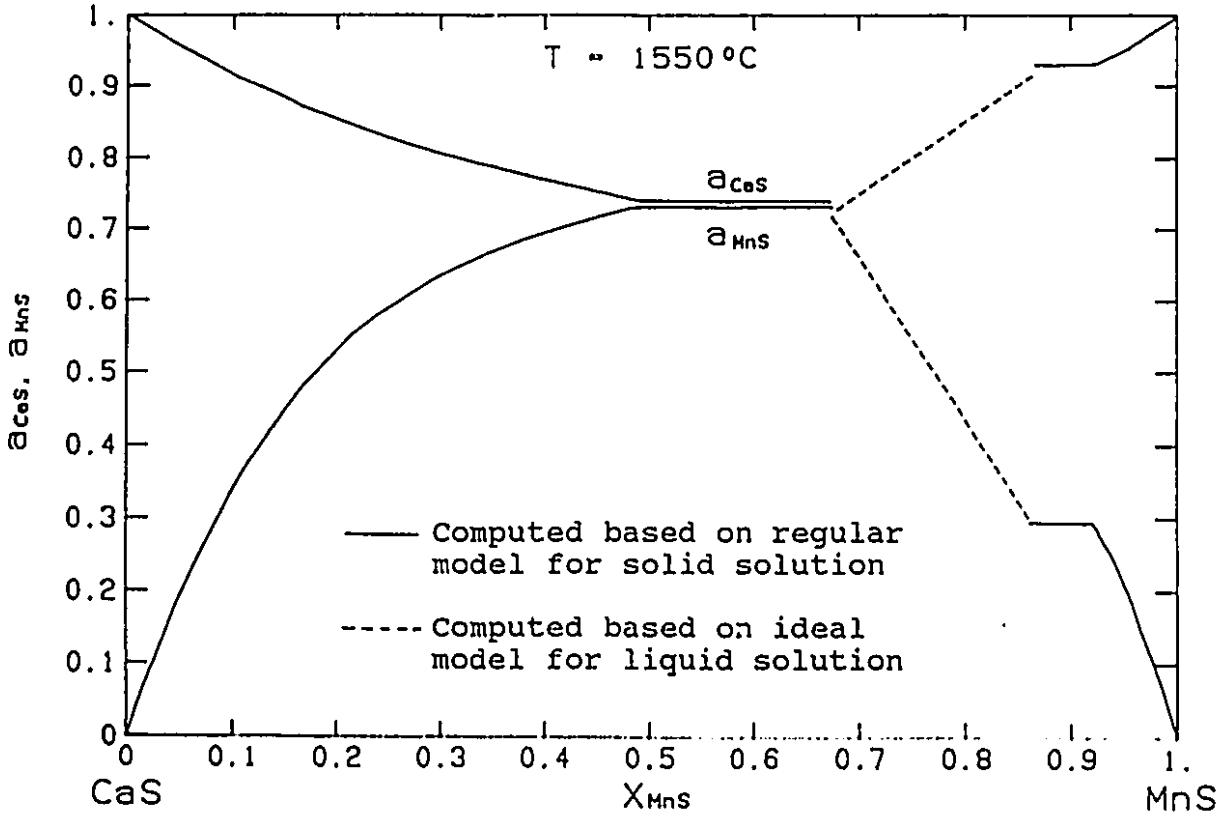

Figure H.4 Calculated activities of calcium sulphide and manganese sulphide at 1550 ^{0}C. Solid solutions are indicated with solid lines, while liquid solutions are with dotted lines. Note that there is good agreement between the solid and liquid activities at the liquidus compositions

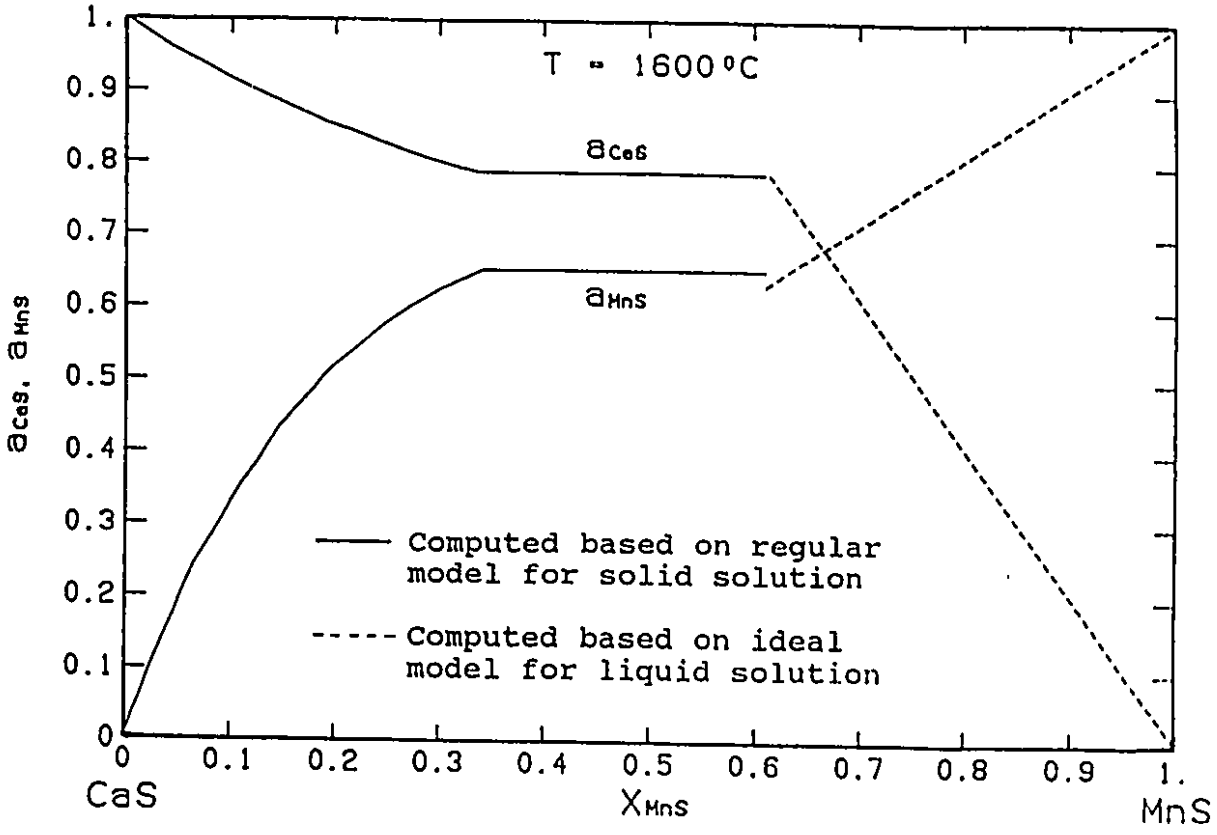

Figure H.5 Calculated activities of calcium sulphide and manganese sulphide at 1600 ^{0}C. Solid solutions are indicated with solid lines, while liquid solutions are with dotted lines. Note that there is good agreement between the solid and liquid activities at the liquidus compositions

Appendix I

The Computer Program

```
      PROGRAM  CAINJ
C
C*************************************************************************
C     This program uses DVERK [1] subroutine to calculate the concentrations of  *
C     dissolved sulfur Y(1), oxygen Y(2), calcium Y(3) and aluminum Y(4), and    *
C     the compositions and amount of oxide and sulphide inclusions in the melt   *
C     as a function of Ca injection time (X).                                    *
C                                                                                *
C     - The calculation is based on Equations (6.52-72).                         *
C                                                                                *
C     © Copyright Dennis Lu, 1992.  All rights reserved.                         *
C*************************************************************************
C
      INTEGER N, NW, IND, K
      DOUBLE PRECISION X, XEND, Y(4), TOL, C(24), W(4,9)
      DOUBLE PRECISION ERROR(2),yy,f1,f2,aeas,XMnS,Xeas,aMns,aCaO,aAlO
      DOUBLE PRECISION Dca,Do,Ds,DAl,Ceab,Cro,Ca,kca,ks,ko,kAl,zCaO
      DOUBLE PRECISION KCaO,KCaS,KAlO,Kro,Ksl,Krm,Ke,Cea0,Cs0,Co0,zCaS
      DOUBLE PRECISION zCAx,hAl,Coi,CeaT,CAli,Ceap,Csp,Cop,XCaO,XAl
      DOUBLE PRECISION CAlO,CaS,CaO,CaSi,CaOi,CAx,CAxi,Ceai,Csi,Coi,CAli
      EXTERNAL FCN
      INTEGER TM
      CHARACTER*4 LU
C
C INITIALIZE THE VARIABLES.
C
      N  = 4
      NW = 4
      IND = 1
      X  = 0.D0
      TOL = 1.D-11
C
C INPUT OF KCi VALUES AND INITIAL DATA
C
      OPEN(UNIT=4,FILE='KCi.DAT',STATUS='OLD')
      READ(4,*) Dca,Do,Ds,DAl,Ceab,Cro,ni,di
      READ(4,*) Cea0,Cs0,Co0,A,Ksl,Kro,Krm,Ke,TM
      READ(4,*) zCAx,hAl,CAx,KCaS,KCaO,KAlO
      READ(4,*) LU
      CLOSE(UNIT=4)
C
C OUTPUT THE HEADING.
C
      Y(1) = Cs0
      Y(2) = Co0
      Y(3) = Cea0
      Y(4) = hAl/27.*7.2/100.
      Ca   = Dca*Ceab
      Coi  = Co0
      kCa  = 2.*Dca/di
      ks   = 2.*Ds/di
      ko   = 2.*Do/di
      kAl  = 2.*DAl/di
      CAlO = 3.1415/6.*ni*3.4/102.D0*di**3.
C
```

```
C PARAMETER OUTPUT
C
C OUT.DAT contains the headings and the bulk concentrations in the melt
C INT.DAT contains the interfacial concentrations at inclusions
C COM.DAT contains the compositions and activities of oxide and sulphide inclusions
C QUA.DAT contains the quantity of different inclusions and total Ca content
C
      OPEN(UNIT=5,FILE='OUT.DAT',STATUS='unknown')
      OPEN(UNIT=7,FILE='INT.DAT',STATUS='unknown')
      OPEN(UNIT=8,FILE='COM.DAT',STATUS='unknown')
      OPEN(UNIT=9,FILE='QUA.DAT',STATUS='unknown')
C
C INITIAL OUTPUT OF INPUT VARIABLES
C
      WRITE (5,*) '                H#R#  =   ', LU
      WRITE (5,*) '                **********'
      WRITE (5,*) '    '
      WRITE (5,77)
 77     FORMAT(1X,'Dca=',3X,'Do=',3X,'Ds=',3X,'DAl=',3X,'ni=',
     +          3X,'di=')
      WRITE (5,79) Dca, Do, Ds, DAl, ni, di
 79     FORMAT(1x, 6D8.3)
      WRITE (5,78)
 78     FORMAT(1X,'A=z/delta',3X,'Ksl =',2X,'Kro =',2X,'Krm =',
     +          2x,'kca=',2x,'ks=',2x,'ko=',2x,'kAl=')
      WRITE (5,74) A, Ksl, Kro, Krm, kca, ks, ko, kAl
 74     FORMAT(2X, 8D8.3)
      WRITE (5,76)
 76     FORMAT(1x,'Cs0 =',2x,'Co0=',2x,'Ccab=',1X,'Cro=',1x,'zCAx=',
     +          1x,'INJ.Time=')
      WRITE (5,73) Cs0, Co0, Ccab, Cro, zCAx, TM
 73     FORMAT(1x, 5D8.3, 3x, I5)
C
      WRITE (5,1)
 1     FORMAT(/// 20x,'  OUTPUT RESULTS FROM  CAINJ.FOR '
     +    // 2X, 't(sec)', 1X,'Y(1)=Cs', 3X, 'Y(2)=Co',
     +                3X,'Y(3)=Cca',3x, 'Y(4)=CAl'
     +     / 2X, '------', 4(3X, '--------') )
C
      WRITE (7,98)
 98     FORMAT(//2x, 't(sec)', 4X,'Ccai=',3x,'Coi=',3x,'Csi=',
     +                 3x,'Ccap=',3x,'Cop=',3x,'Csp='
     +     / 2x, '------', 6(3x, '--------') )
C
      WRITE(8,67)
 67     FORMAT(//2x,'t =',5x,'Xcao =',6x,'Xcas =',
     +        6x,'aCaO =',5x,'aAl2O3 =',
     +        5x,'aCaS =',6x,'aMnS ='
     +      / 2x, '------', 6(3X, '--------') )
C
      WRITE(9,88)
 88     FORMAT(//2x,'t(sec)',3x,'CAxi=',3x,'CaSi=',3x,'CaO=',
     +        3x,'CcaT='
     +      / 2x, '------', 4(3X, '--------') )
C
```

```
C INITIAL VALUES
C
      WRITE (5,2)  x, Y(1),Y(2),Y(3),Y(4)
      WRITE (7,99) x,Ceai,Coi,Csi,Ceap,Cop,Csp
      WRITE (8,68) x,Xcao,Xcas,aCao,aAlO,aCas,aMnS
      WRITE (9,89) x,CAxi,CaSi,CaOi,CeaT
C
C CALCULATE AND OUTPUT THE SOLUTION AT EACH SECOND OF INJECTION
C t = 1, 2, 3, ... Inj.TM (sec).
C
      DO 10 K = 1, TM
      XEND = DFLOAT(K)
C
C CALL THE SUBROUTINE DVERK
C
      CALL DVERK(N,FCN,X,Y,XEND,TOL,IND,C,NW,W )
        IF ( IND .EQ. 3 ) THEN
C
C INTEGRATION SUCCESSFUL - COMPUTE ERRORS AND PRINT RESULTS
C
C CALCULATE THE CONCENTRATIONS AT THE REACTION PLANE IN THE
C GAS-LIQUID FILM
C
      Cear = SQRT((Do*KCaO+Ds*KCaS)/(Do*Y(2)+Ds*Y(1))*Ceab)
      Csr  = KCaS/Cear
      Cor  = KCaO/Cear
C
C AMOUNT OF CALCIUM AND OXYGEN DIFFUSE TO CAx INCLUSIONS
C AT TIME INTERVAL, t+dt, [dt = 1 (sec)]
C
      AA = kca*zCAx*(Y(3)-Ceai)*1.D0
      AB = AB + AA
      OO = ko*zCAx*(Y(2)-Coi)*1.D0
      AO = AO + OO
C
C CALCULATE THE COMPOSITION OF CAx
C
      xAl = (CAlO+(AO-AB)/3.)/(CAlO+(AO-AB)/3.+AB)
      xCaO = 1. - xAl
C
C CALCULATE THE ACTIVITIES OF CAx AND ITS INTERFACIAL CONCENTRATIONS
C
      aAlO = 1.D0*(xAl)**3.
      Coi = Co0*(aAlO)**0.3333D0
      hoi = Coi*16./7.2*100.D0
      hAli = SQRT(aAlO/KAlO/(hoi)**3)
      CAli = hAli*27./7.2*100.
      if(xAl.LT.0.268) then
       aCaO = 1.D0
      ELSE
       aCaO = 2.5485D0*(1.-xAl)**3.
      End if
      heai = aCaO/hoi*7.D-09
      Ceai = heai/40.*7.2/100.
      hsi  = aCaS/heai*1.69D-07
```

```
      Csi  = hsi/32.*7.2/100.D0
C
C TO CHECK IF Cs > Csi at CAx, IF YES, r IS SET TO 1
C
      r = 0.
      if(Y(1).GT.Csi) r = 1.
C
C THE ACITVITY OF CALCIUM IN THE BULK USING 1WT% AS STANDARD STATE
C
      hCa = Y(3)*40./7.2*100.D0
C
C CALCULATE THE SULPHIDE COMPOSITION
C
      hMn = 0.75D0
C
C      YY  = aCaS/aMnS
C
      YY = 1.02D7*hCa/hMn
      DO 22 I = 140, 10, -1
      V = -(DREAL(I)-50.D0)/10.D0
      XMnS = 1.D0/(1.D0+ 10.**V)
      f1 = 1.498D0*(2.*XMnS - 1.)-Dlog(yy)
      f2 = -DLOG(1./XMnS - 1.)
      f = f2 / f1
      IF (f.GT.1.05) goto 22
      IF (f.GT.0.95) goto 23
 22    continue
 23    XMnS = XMnS
      XCaS = 1.D0 - XMnS
C
C CALCULATE THE ACTIVITIES OF THE SULPHIDE
C
      aCaS = Xcas*DEXP(1.498D0*XMnS**2.)
      aMnS = XMnS*DEXP(1.498D0*XCaS**2.)
C
C CALCULATE THE INTFACIAL CONCENTRATIONS ON (Ca,Mn)S INCLUSIONS
C
      hop = 1./hca*7.D-09
      hsp = aCaS/hca*1.69D-07
      Ccap= hca/40.*7.2/100.D0
      Cop = hop/16.*7.2/100.D0
      Csp = hsp/32.*7.2/100.D0
C
C CALCULATE AMOUNT OF CaS and CaO INCLUSIONS
C
      CaS  = CaS
     +      + Ds*A*(1.+Ca/(Ds*Y(1)+Do*Y(2)))*(Y(1)-Csr)
      CaO  = CaO
     +      + Do*A*(1.+Ca/(Ds*Y(1)+Do*Y(2)))*(Y(2)-Cor)
      CaSi = CaS*DEXP(-Krm*X)
      CaOi = CaO*DEXP(-Krm*X)
C
C CALCULATE VOLUMETRIC AREA OF CaS AND CaO INCLUSIONS
C
      zCaS = 8.6486D5*CaSi
```

```
      zCaO = 7.4495D5*CaOi
C
C CALCULATE VOLUMETRIC AREA AND NUMBER OF CAx OXIDE INCLUSIONS
C
      CAx = CAx+ko*zCAx*(Y(2)-Coi)/3.
      CAxi= CAx*DEXP(-Krm*X)
      zCAx= 8.60D5*CAxi
      ni  = 6./3.1415/(di**3.)*CAxi*(56.*XCaO+102.*XAl)/3.1
C
C CALCULATE TOTAL CALCIUM CONTENT
C
      CcaT = Y(3) + (CaSi+kca*zCaS*(Y(3)-Ccap))
     +       + (CaOi+kca*zCaO*(Y(3)-Ccap)) + AB
C
C CALCULATE THE REACTION PATH
C
      hs  = Y(1)*32./7.2*100.D0
      ho  = Y(2)*16./7.2*100.D0
      gas = 0.D0 + DLOG10(aCas/hs)
      gao = 0.D0 + DLOG10(aCao/ho)
C
C PRINT THE RESULTS AT EACH INTEGRATION TIME, X, ON SCREEN
C AND WRITE TO THE ASSIGNED FILES
C
      Print*,    x,Y(1),Y(2),Y(3), Y(4)
      WRITE(5,2)  x,Y(1),Y(2),Y(3),Y(4)
 2     FORMAT(2X, F5.1, 4(3x, D8.3))
      WRITE(7,99) x,Ccai,Coi,Csi,Ccap,Cop,Csp
 99    FORMAT(2x, F5.1, 6(3x, D8.3))
      WRITE(8,68) x,Xcao,Xcas,aCaO,aAlO,aCas,aMnS
 68    FORMAT(2x, F5.1, 6(3x, D8.3))
      WRITE(9,89) x,CAxi,CaSi,CaOi,CcaT
 89    FORMAT(2x, F5.1, 4(3x, D8.3))
C
       ELSE
C         INTEGRATION UNSUCCESSFUL - PRINT MESSAGE AND STOP
C
         WRITE (5,3) X, IND
 3        FORMAT(/// ' INTEGRATION STOPPED AT X =', F7.3,
     +              ' WITH IND =', I5 )
      Close(UNIT=9)
      Close(UNIT=8)
      Close(UNIT=7)
      CLOSE(UNIT=5)
         STOP
        END IF

 10    CONTINUE
C
      STOP
      END
C
```

```
C
      SUBROUTINE FCN ( N, X, Y, YPRIME )
C
      INTEGER N, TM
      DOUBLE PRECISION X, Y(N), YPRIME(N), A,AB,AO,AA,OO
      DOUBLE PRECISION yy,f1,f2,acas,XMnS,Xcas,aMns,XCaO,XAl,aCaO,aAlO
      DOUBLE PRECISION Dca,Do,Ds,DAl,Ccab,Cro,Ca,kca,ks,ko,kAl,zCaO
      DOUBLE PRECISION KCaO,KCaS,KAlO,Kro,Ksl,Krm,Ke,Cca0,Cs0,Co0,zCaS
      DOUBLE PRECISION zCAx,hAl,Coi,CcaT,CAli,Ccap,Csp,Cop
      DOUBLE PRECISION CAlO,CaS,CaO,CaSi,CaOi,CAx,CAxi,Ccai,Csi,Coi,CAli
      CHARACTER*4 LU
C
      OPEN(UNIT=4,FILE='KCi.DAT',STATUS='OLD')
      READ(4,*) Dca,Do,Ds,DAl,Ccab,Cro,ni,di
      READ(4,*) Cca0,Cs0,Co0,A,Ksl,Kro,Krm,Ke,TM
      READ(4,*) zCAx,hAl,CAx,KCaS,KCaO,KAlO
      READ(4,*) LU
      CLOSE(UNIT=4)
C
      Ca   = Dca*Ccab
      kCa  = 2.*Dca/di
      ks   = 2.*Ds/di
      ko   = 2.*Do/di
      kAl  = 2.*DAl/di
      CAlO = 3.1415/6.*ni*3.4/102.D0*di**3.
C
      AA = kca*zCAx*(Y(3)-Ccai)*1.D0
      AB = AB + AA
      OO = ko*zCAx*(Y(2)-Coi)*1.D0
      AO = AO + OO
      xAl = (CAlO+(AO-AB)/3.)/(CAlO+(AO-AB)/3.+AB)
      aAlO = 1.D0*(xAl)**3.D0
      Coi = Co0 * (aAlO)**0.3333333D0
      hoi = Coi*16./7.2*100.D0
      hAli = SQRT(aAlO/KAlO/(hoi)**3)
      CAli = hAli*27./7.2*100.
      if(xAl.LT.0.268) then
       aCao =1.D0
      ELSE
       aCao =2.5485D0*(1.-xAl)**3.
      END IF
      hCai = aCaO/hoi*7.D-09
      Ccai = hCai/40.*7.2/100.
C
      r = 0.
      if(Y(1).GT.Csi) r = 1.
C
      hCa = Y(3)*40./7.2*100.D0
      hMn = 0.75D0
      yy = 1.02D7*hCa/hMn
C
C     yy = aCaS/aMnS
      DO 33 I = 140, 10, -1
      V = -(DREAL(I)-50.D0)/10.D0
      XMnS = 1.D0/(1.D0+10.**V)
```

```
      f1 = 1.489D0*(2.*XMnS - 1.)-Dlog(yy)
      f2 = -DLOG(1.D0/XMnS -1.D0)
      f = f2 / f1
      if(F.GT.1.05) goto 33
      if(f.GT.0.95) goto 34
33    continue
34    XMnX = XMnS
      XCas = 1. - XMnS
      aCaS = Xcas *DEXP(1.489D0*XMnS**2.)
      hsp = aCaS/hCa*1.69D-07
      hop = 1./hCa*7.D-09
      Csp = hsp/32.*7.2/100.D0
      Cop = hop/16.*7.2/100.D0
      Ccap = hCa/40.*7.2/100.D0
C
      Ccar = SQRT((Do*KCaO+Ds*KCaS)/(Do*Y(2)+Ds*Y(1))*Ccab)
      Csr  = KCaS/Ccar
      Cor  = KCaO/Ccar
C
      CrAl = KAlO/Cro
C
C THE MASS BALANCE EQUATION FOR SULPHUR
C
      YPRIME(1) = - (Ds*A*(1.+Ca/(Do*Y(2)+Ds*Y(1)))*(Y(1)-Csr)
     +          + Ksl*(Y(1)-0)
     +          + r*ks*zCAx*(Y(1)-Csi)
     +          + ks*zCaS*(Y(1)-Csp)
     +          + ks*zCaO*(Y(1)-Csp) )
C
C THE MASS BALANCE EQUATION FOR OXYGEN
C
      YPRIME(2) = - (Do*A*(1.+Ca/(Do*Y(2)+Ds*Y(1)))*(Y(2)-Cor)
     +          + ko*zCAx*(Y(2)-Coi)
     +          + ko*zCaO*(Y(2)-Cop)
     +          + Kro*(Y(2)-Cro) )
C
C THE MASS BALANCE EQUATION FOR DISSOLVED CALCIUM
C
      YPRIME(3) = - (Dca*A*(1+Ca/(Do*Y(2)+Ds*Y(1)))*(Y(3)-Ccar)
     +          + kca*zCAx*(Y(3)-Ccai)
     +          + kca*zCaS*(Y(3)-Ccap)
     +          + kca*zCaO*(Y(3)-Ccap)
     +          + Ke*(Y(3)-0) )
C
C THE MASS BALANCE EQUATION FOR SOLUBLE ALUMINUM
C
      YPRIME(4) = - (kAl*zCAx*(Y(4)-CAli)
     +          + DAl/Do*Kro*(Y(4)-CrAl) )
C
C THE MASS BALANCE OF CaS, CaO AND CAx INCLUSIONS
C
      DO 333 K = 1, TM
      IF(X.NE.DFLOAT(K)) GOTO 333
      CaS  = CaS
     +     + Ds*A*(1.+Ca/(Do*Y(2)+Ds*Y(1)))*(Y(1)-Csr)
```

```
      CaSi = CaS*DEXP(-Krm*X)
      CaO  = CaO
     +     + Do*A*(1.+Ca/(Do*Y(2)+Ds*Y(1)))*(Y(2)-Cor)
      CaOi = CaO*DEXP(-Krm*X)
      CAx  = CAx+ko*zCAx*(Y(2)-Coi)/3.
      CAxi = CAx*DEXP(-Krm*X)
      ni  = 6./3.1415/(di**3.)*CAxi*(56.*XCaO+102.*XAl)/3.1
      zCaS = 8.6486D5*CaSi
      zCaO = 7.4495D5*CaOi
      zCAx = 8.60D5*CAxi
  333 continue
      RETURN
      END
C
C The following subroutine DVERK was supplied by Department of Computer
C Science of McMaster University, and the program was written by:
C T.E. Hull, W.H. Enright and K.R. Jackson; "DVERK, a R-K Procedure
C for Nonstiff ODEs," 1990, Department of Computer Science,
C University of Toronto, Canada.
C
      SUBROUTINE DVERK (N, FCN, X, Y, XEND, TOL, IND, C, NW, W)
      INTEGER N, IND, NW, K
      DOUBLE PRECISION X, Y(N), XEND, TOL, C(32), W(3,9), TEMP
C
C .....ABORT IF IND OUT OF RANGE 1 TO 6
      IF (IND.LT.1 .OR. IND.GT.6) GO TO 500
C
C     CASES - INITIAL ENTRY, NORMAL RE-ENTRY, INTERRUPT RE-ENTRIES
      GO TO (5, 5, 45, 1111, 2222, 2222), IND
C     CASE 1 - INITIAL ENTRY (IND .EQ. 1 OR 2)
C .....ABORT IF N.GT.NW OR TOL.LE.0
    5   IF (N.GT.NW .OR. TOL.LE.0.D0) GO TO 500
        IF (IND.EQ. 2) GO TO 15
C         INITIAL ENTRY WITHOUT OPTIONS (IND .EQ. 1)
C         SET C(1) TO C(9) EQUAL TO 0
          DO 10 K = 1, 9
            C(K) = 0.D0
   10     CONTINUE
          GO TO 35
   15   CONTINUE
C         INITIAL ENTRY WITH OPTIONS (IND .EQ. 2)
C         MAKE C(1) TO C(9) NON-NEGATIVE
          DO 20 K = 1, 9
            C(K) = DABS(C(K))
   20     CONTINUE
C         MAKE FLOOR VALUES NON-NEGATIVE IF THEY ARE TO BE USED
          IF (C(1).NE.4.D0 .AND. C(1).NE.5.D0) GO TO 30
            DO 25 K = 1, N
              C(K+30) = DABS(C(K+30))
   25       CONTINUE
   30     CONTINUE
   35   CONTINUE
C       INITIALIZE RREB, DWARF, PREV XEND, FLAG, COUNTS
        C(10) = 2.d0**(-56)
        C(11) = 1.D-35
```

```
C       SET PREVIOUS XEND INITIALLY TO INITIAL VALUE OF X
        C(20) = X
        DO 40 K = 21, 24
          C(K) = 0.D0
 40     CONTINUE
        GO TO 50
C      CASE 2 - NORMAL RE-ENTRY (IND .EQ. 3)
C .....ABORT IF XEND REACHED, AND EITHER X CHANGED OR XEND NOT
 45     IF (C(21).NE.0.D0 .AND.
     +              (X.NE.C(20) .OR. XEND.EQ.C(20))) GO TO 500
C       RE-INITIALIZE FLAG
        C(21) = 0.D0
        GO TO 50
C      CASE 3 - RE-ENTRY FOLLOWING AN INTERRUPT (IND .EQ. 4 TO 6)
C      END CASES
 50   CONTINUE
C
C   END INITIALIZATION, ETC.
C
C   ******************************************************************
C
99999  CONTINUE
C
C
C***********ERROR RETURN (WITH IND=-1) IF NO OF FCN EVALS TOO GREAT
        IF (C(7).EQ.0.D0 .OR. C(24).LT.C(7)) GO TO 100
          IND = -1
          RETURN
 100    CONTINUE
C
C       CALCULATE SLOPE (ADDING 1 TO NO OF FCN EVALS) IF IND .NE. 6
        IF (IND .EQ. 6) GO TO 105
          CALL FCN(N, X, Y, W(1,1))
          C(24) = C(24) + 1.D0
 105    CONTINUE
C
C       CALCULATE HMIN - USE DEFAULT UNLESS VALUE PRESCRIBED
        C(13) = C(3)
        IF (C(3) .NE. 0.D0) GO TO 165
C         CALCULATE DEFAULT VALUE OF HMIN
C         FIRST CALCULATE WEIGHTED NORM Y - C(12) - AS SPECIFIED
C         BY THE ERROR CONTROL INDICATOR C(1)
          TEMP = 0.D0
          IF (C(1) .NE. 1.D0) GO TO 115
C           ABSOLUTE ERROR CONTROL - WEIGHTS ARE 1
            DO 110 K = 1, N
              TEMP = DMAX1(TEMP, DABS(Y(K)))
 110        CONTINUE
            C(12) = TEMP
            GO TO 160
 115        IF (C(1) .NE. 2.D0) GO TO 120
C            RELATIVE ERROR CONTROL - WEIGHTS ARE 1/DABS(Y(K)) SO
C            WEIGHTED NORM Y IS 1
            C(12) = 1.D0
            GO TO 160
```

```
 120      IF (C(1) .NE. 3.D0) GO TO 130
C          WEIGHTS ARE 1/MAX(C(2),ABS(Y(K)))
         DO 125 K = 1, N
           TEMP = DMAX1(TEMP, DABS(Y(K))/C(2))
 125       CONTINUE
         C(12) = DMIN1(TEMP, 1.D0)
         GO TO 160
 130     IF (C(1) .NE. 4.D0) GO TO 140
C          WEIGHTS ARE 1/MAX(C(K+30),ABS(Y(K)))
         DO 135 K = 1, N
           TEMP = DMAX1(TEMP, DABS(Y(K))/C(K+30))
 135       CONTINUE
         C(12) = DMIN1(TEMP, 1.D0)
         GO TO 160
 140     IF (C(1) .NE. 5.D0) GO TO 150
C          WEIGHTS ARE 1/C(K+30)
         DO 145 K = 1, N
           TEMP = DMAX1(TEMP, DABS(Y(K))/C(K+30))
 145       CONTINUE
         C(12) = TEMP
         GO TO 160
 150     CONTINUE
C          DEFAULT CASE - WEIGHTS ARE 1/MAX(1,ABS(Y(K)))
         DO 155 K = 1, N
           TEMP = DMAX1(TEMP, DABS(Y(K)))
 155       CONTINUE
         C(12) = DMIN1(TEMP, 1.D0)
 160     CONTINUE
       C(13) = 10.D0*DMAX1(C(11),C(10)*DMAX1(C(12)/TOL,DABS(X)))
 165   CONTINUE
C
C      CALCULATE SCALE - USE DEFAULT UNLESS VALUE PRESCRIBED
       C(15) = C(5)
       IF (C(5) .EQ. 0.D0) C(15) = 1.D0
C
C      CALCULATE HMAX - CONSIDER 4 CASES
C      CASE 1 BOTH HMAX AND SCALE PRESCRIBED
        IF (C(6).NE.0.D0 .AND. C(5).NE.0.D0)
   +                      C(16) = DMIN1(C(6), 2.D0/C(5))
C      CASE 2 - HMAX PRESCRIBED, BUT SCALE NOT
        IF (C(6).NE.0.D0 .AND. C(5).EQ.0.D0) C(16) = C(6)
C      CASE 3 - HMAX NOT PRESCRIBED, BUT SCALE IS
        IF (C(6).EQ.0.D0 .AND. C(5).NE.0.D0) C(16) = 2.D0/C(5)
C      CASE 4 - NEITHER HMAX NOR SCALE IS PROVIDED
        IF (C(6).EQ.0.D0 .AND. C(5).EQ.0.D0) C(16) = 2.D0
C
C**********ERROR RETURN (WITH IND=-2) IF HMIN .GT. HMAX
       IF (C(13) .LE. C(16)) GO TO 170
         IND = -2
         RETURN
 170   CONTINUE
C
C      CALCULATE PRELIMINARY HMAG - CONSIDER 3 CASES
       IF (IND .GT. 2) GO TO 175
C      CASE 1 - INITIAL ENTRY - USE PRESCRIBED VALUE OF HSTART, IF
```

```
C          ANY, ELSE DEFAULT
           C(14) = C(4)
           IF (C(4) .EQ. 0.D0) C(14) = C(16)*TOL**(1./6.)
           GO TO 185
 175       IF (C(23) .GT. 1.D0) GO TO 180
C          CASE 2 - AFTER A SUCCESSFUL STEP, OR AT MOST ONE FAILURE,
C            USE MIN(2, .9*(TOL/EST)**(1/6))*HMAG, BUT AVOID POSSIBLE
C            OVERFLOW. THEN AVOID REDUCTION BY MORE THAN HALF.
           TEMP = 2.D0*C(14)
           IF (TOL .LT. (2.D0/.9D0)**6*C(19))
     +                  TEMP = .9D0*(TOL/C(19))**(1./6.)*C(14)
           C(14) = DMAX1(TEMP, .5D0*C(14))
           GO TO 185
 180       CONTINUE
C          CASE 3 - AFTER TWO OR MORE SUCCESSIVE FAILURES
           C(14) = .5D0*C(14)
 185       CONTINUE
C
C          CHECK AGAINST HMAX
          C(14) = DMIN1(C(14), C(16))
C
C          CHECK AGAINST HMIN
          C(14) = DMAX1(C(14), C(13))
C
C**********INTERRUPT NO 1 (WITH IND=4) IF REQUESTED
          IF (C(8) .EQ. 0.D0) GO TO 1111
            IND = 4
            RETURN
C          RESUME HERE ON RE-ENTRY WITH IND .EQ. 4  .....RE-ENTRY..
 1111      CONTINUE
C
C          CALCULATE HMAG, XTRIAL - DEPENDING ON PRELIMINARY HMAG, XEND
          IF (C(14) .GE. DABS(XEND - X)) GO TO 190
C            DO NOT STEP MORE THAN HALF WAY TO XEND
            C(14) = DMIN1(C(14), .5D0*DABS(XEND - X))
            C(17) = X + DSIGN(C(14), XEND - X)
            GO TO 195
 190        CONTINUE
C            HIT XEND EXACTLY
            C(14) = DABS(XEND - X)
            C(17) = XEND
 195        CONTINUE
C
C          CALCULATE HTRIAL
          C(18) = C(17) - X
C
C        END STAGE 1
C
C        ***************************************************************
C        * STAGE 2 - CALCULATE YTRIAL (ADDING 7 TO NO OF FCN EVALS). *
C        * W(*,2), ... W(*,8) HOLD INTERMEDIATE RESULTS NEEDED IN *
C        * STAGE 3. W(*,9) IS TEMPORARY STORAGE UNTIL FINALLY IT HOLDS *
C        * YTRIAL.                                                    *
C        ***************************************************************
C
```

```
      TEMP = C(18)/1398169080000.D0
C
      DO 200 K = 1, N
        W(K,9) = Y(K) + TEMP*W(K,1)*233028180000.D0
 200    CONTINUE
      CALL FCN(N, X + C(18)/6.D0, W(1,9), W(1,2))
C
      DO 205 K = 1, N
        W(K,9) = Y(K) + TEMP*(   W(K,1)*74569017600.D0
     +                 + W(K,2)*298276070400.D0  )
 205    CONTINUE
      CALL FCN(N, X + C(18)*(4.D0/15.D0), W(1,9), W(1,3))
C
      DO 210 K = 1, N
        W(K,9) = Y(K) + TEMP*(   W(K,1)*1165140900000.D0
     +                 - W(K,2)*372845088000.D0
     +                 + W(K,3)*349542270000.D0 )
 210    CONTINUE
      CALL FCN(N, X + C(18)*(2.D0/3.D0), W(1,9), W(1,4))
C
      DO 215 K = 1, N
        W(K,9) = Y(K) + TEMP*( - W(K,1)*3604654659375.D0
     +                 + W(K,2)*1281654990000.D0
     +                 - W(K,3)*9284716546875.D0
     +                 + W(K,4)*1237962206250.D0 )
 215    CONTINUE
      CALL FCN(N, X + C(18)*(5.D0/6.D0), W(1,9), W(1,5))
C
      DO 220 K = 1, N
        W(K,9) = Y(K) + TEMP*(   W(K,1)*3355605792000.D0
     +                 - W(K,2)*11185352640000.D0
     +                 + W(K,3)*9172628850000.D0
     +                 - W(K,4)*427218330000.D0
     +                 + W(K,5)*482505408000.D0  )
 220    CONTINUE
      CALL FCN(N, X + C(18), W(1,9), W(1,6))
C
      DO 225 K = 1, N
        W(K,9) = Y(K) + TEMP*( - W(K,1)*770204740536.D0
     +                 + W(K,2)*231163954560O.D0
     +                 - W(K,3)*1322092233000.D0
     +                 - W(K,4)*453006781920.D0
     +                 + W(K,5)*326875481856.D0  )
 225    CONTINUE
      CALL FCN(N, X + C(18)/15.D0, W(1,9), W(1,7))
C
      DO 230 K = 1, N
        W(K,9) = Y(K) + TEMP*(   W(K,1)*2845924389000.D0
     +                 - W(K,2)*9754668000000.D0
     +                 + W(K,3)*789711037500O.D0
     +                 - W(K,4)*192082660000.D0
     +                 + W(K,5)*400298976000.D0
     +                 + W(K,7)*201586000000.D0  )
 230    CONTINUE
      CALL FCN(N, X + C(18), W(1,9), W(1,8))
```

```
C
C       CALCULATE YTRIAL, THE EXTRAPOLATED APPROXIMATION AND STORE
C         IN W(*,9)
        DO 235 K = 1, N
          W(K,9) = Y(K) + TEMP*(   W(K,1)*104862681000.D0
     +                   + W(K,3)*545186250000.D0
     +                   + W(K,4)*446637345000.D0
     +                   + W(K,5)*188806464000.D0
     +                   + W(K,7)*15076875000.D0
     +                   + W(K,8)*97599465000.D0   )
  235   CONTINUE
C
C       ADD 7 TO THE NO OF FCN EVALS
        C(24) = C(24) + 7.D0
C
C     END STAGE 2
C
C
C       CALCULATE THE UNWEIGHTED ABSOLUTE ERROR ESTIMATE VECTOR
        DO 300 K = 1, N
          W(K,2) = (   W(K,1)*8738556750.D0
     +             + W(K,3)*9735468750.D0
     +             - W(K,4)*9709507500.D0
     +             + W(K,5)*8582112000.D0
     +             + W(K,6)*95329710000.D0
     +             - W(K,7)*15076875000.D0
     +             - W(K,8)*97599465000.D0)/1398169080000.D0
  300   CONTINUE
C
C       CALCULATE THE WEIGHTED MAX NORM OF W(*,2) AS SPECIFIED BY
C       THE ERROR CONTROL INDICATOR C(1)
        TEMP = 0.D0
        IF (C(1) .NE. 1.D0) GO TO 310
C         ABSOLUTE ERROR CONTROL
          DO 305 K = 1, N
            TEMP = DMAX1(TEMP,DABS(W(K,2)))
  305       CONTINUE
          GO TO 360
  310   IF (C(1) .NE. 2.D0) GO TO 320
C         RELATIVE ERROR CONTROL
          DO 315 K = 1, N
            TEMP = DMAX1(TEMP, DABS(W(K,2)/Y(K)))
  315       CONTINUE
          GO TO 360
  320   IF (C(1) .NE. 3.D0) GO TO 330
C         WEIGHTS ARE 1/MAX(C(2),ABS(Y(K)))
          DO 325 K = 1, N
            TEMP = DMAX1(TEMP, DABS(W(K,2))
     +                 / DMAX1(C(2), DABS(Y(K))) )
  325       CONTINUE
          GO TO 360
  330   IF (C(1) .NE. 4.D0) GO TO 340
C         WEIGHTS ARE 1/MAX(C(K+30),ABS(Y(K)))
          DO 335 K = 1, N
            TEMP = DMAX1(TEMP, DABS(W(K,2))
```

```
     +                 / DMAX1(C(K+30), DABS(Y(K))) )
 335   CONTINUE
       GO TO 360
 340   IF (C(1) .NE. 5.D0) GO TO 350
C       WEIGHTS ARE 1/C(K+30)
       DO 345 K = 1, N
         TEMP = DMAX1(TEMP, DABS(W(K,2)/C(K+30)))
 345   CONTINUE
       GO TO 360
 350   CONTINUE
C       DEFAULT CASE - WEIGHTS ARE 1/MAX(1,ABS(Y(K)))
       DO 355 K = 1, N
         TEMP = DMAX1(TEMP, DABS(W(K,2))
     +                 / DMAX1(1.D0, DABS(Y(K))) )
 355   CONTINUE
 360   CONTINUE
C
C      CALCULATE EST - (THE WEIGHTED MAX NORM OF W(*,2))*HMAG*SCALE
C        - EST IS INTENDED TO BE A MEASURE OF THE ERROR  PER  UNIT
C        STEP IN YTRIAL
      C(19) = TEMP*C(14)*C(15)
C
C     END STAGE 3
C
C     ******************************************************************
C     * STAGE 4 - MAKE DECISIONS.                                      *
C     ******************************************************************
C
C      SET IND=5 IF STEP ACCEPTABLE, ELSE SET IND=6
      IND = 5
      IF (C(19) .GT. TOL) IND = 6
C
C***********INTERRUPT NO 2 IF REQUESTED
      IF (C(9) .EQ. 0.D0) GO TO 2222
        RETURN
C      RESUME HERE ON RE-ENTRY WITH IND .EQ. 5 OR 6  ...RE-ENTRY..
 2222   CONTINUE
C
      IF (IND .EQ. 6) GO TO 410
C        STEP ACCEPTED (IND .EQ. 5), SO UPDATE X, Y FROM XTRIAL,
C          YTRIAL, ADD 1 TO THE NO OF SUCCESSFUL STEPS, AND SET
C          THE NO OF SUCCESSIVE FAILURES TO ZERO
        X = C(17)
        DO 400 K = 1, N
          Y(K) = W(K,9)
 400    CONTINUE
        C(22) = C(22) + 1.D0
        C(23) = 0.D0
C**************RETURN(WITH IND=3, XEND SAVED, FLAG SET) IF X .EQ. XEND
        IF (X .NE. XEND) GO TO 405
          IND = 3
          C(20) = XEND
          C(21) = 1.D0
          RETURN
 405    CONTINUE
```

```
          GO TO 420
 410      CONTINUE
C           STEP NOT ACCEPTED (IND .EQ. 6), SO ADD 1 TO THE NO OF
C             SUCCESSIVE FAILURES
          C(23) = C(23) + 1.D0
C***************ERROR RETURN (WITH IND=-3) IF HMAG .LE. HMIN
          IF (C(14) .GT. C(13)) GO TO 415
            IND = -3
            RETURN
 415        CONTINUE
 420      CONTINUE
C
C      END STAGE 4
C
     GO TO 99999
C    END LOOP
C
C  BEGIN ABORT ACTION
  500 CONTINUE
C
     WRITE(6,505) IND, TOL, X, N, C(13), XEND, NW, C(16), C(20),
    +     C(22), C(23), C(24), (Y(K), K = 1, N)
  505 FORMAT( /// 1H0, 58HCOMPUTATION STOPPED IN DVERK WITH THE FOLLOWIN
    +G VALUES -
    +   / 1H0, 5HIND =, I4, 5X, 6HTOL  =, 1PD13.6, 5X, 11HX       =,
    +         1PD22.15
    +   / 1H , 5HN   =, I4, 5X, 6HHMIN =, 1PD13.6, 5X, 11HXEND    =,
    +         1PD22.15
    +   / 1H , 5HNW  =, I4, 5X, 6HHMAX =, 1PD13.6, 5X, 11HPREV XEND =,
    +         1PD22.15
    +   / 1H0, 14X, 27HNO OF SUCCESSFUL STEPS    =, 0PF8.0
    +   / 1H , 14X, 27HNO OF SUCCESSIVE FAILURES =, 0PF8.0
    +   / 1H , 14X, 27HNO OF FUNCTION EVALS      =, 0PF8.0
    +   / 1H0, 23HTHE COMPONENTS OF Y ARE
    +   // (1H , 1P5D24.15)                              )
C
     STOP
C
C  END ABORT ACTION
C
     END
```

REFERENCE

1. T.E. Hull, W.H. Enright and K.R. Jackson; "DVERK, a R-K Procedure for Nonstiff ODEs," 1990, Department of Computer Science, University of Toronto, Canada.